

Geochemical, petrophysical and geomechanical properties of stratigraphic sequences in  
Horn River Shale, Middle and Upper Devonian, Northeastern British Columbia, Canada

by

TIAN DONG

A thesis submitted in partial fulfillment of the requirements for the degree of

Doctor of Philosophy

Department of Earth and Atmospheric Sciences

University of Alberta

© Tian Dong, 2016

## ABSTRACT

The Middle and Upper Devonian Horn River Shale, comprising the Evie and Otter Park members and the Muskwa Formation, northeast British Columbia, Canada is recognized as a significant shale gas reservoir in the Western Canada Sedimentary Basin. However, many aspects of this shale formation have not been adequately studied, and the published geochemical, petrophysical and geomechanical data are limited. This work aims to document the controls of geochemical composition variation on petrophysical and geomechanical properties and the relationship of rock composition to lithofacies and stratigraphic sequences. A detailed core-based sedimentological and wireline log analysis was conducted by my colleague Dr. Korhan Ayranci as a parallel study, in order to classify lithofacies, interpret depositional environments and establish sequence stratigraphic framework across the basin.

Major and trace elements concentrations, key trace element ratios and  $C_{org}$ -Fe-S relationships were used to understand the effect of sea level fluctuation on detrital flux, redox conditions, productivity and therefore organic carbon enrichment patterns. Detrital sediment flux indicated by the concentration of aluminum and titanium to the basin was found to be higher during transgressions than regressions. Redox conditions, exhibiting strong correlation to TOC content, were the primary controls on the organic carbon deposition. The bottom water conditions are more anoxic during transgressions than regressions. The presence of biogenic silica, identified by crossplot of silica versus zirconium concentrations, makes the use of total silica problematic as a detrital proxy;

biogenic silica concentrations may be useful as a proxy for productivity. The depositional environments for the Evie and Muskwa intervals, depositing during high sea level, represented favorable conditions for organic matter accumulation, including anoxic bottom water conditions, high primary productivity and less clastic dilution. The Otter Park Member, deposited during sea level falling stage, has relatively low organic matter concentrations, which may have been due to high clastic dilution and dysoxic to oxic bottom water conditions.

Geochemical controls on petrophysical properties (porosity, permeability, pore morphology, pore size and pore throat size distribution) within Horn River shale reservoirs were investigated by an integrated analysis of porosity and permeability measured by helium pycnometry and GRI method, nitrogen adsorption analysis, mercury injection analysis, scanning electron microscopy (SEM) and transmission electron microscopy (TEM). Porosity ranges from 0.62% to 12.04%, and the measured matrix permeability values increase with increasing porosity, ranging between 1.7 and 42.8 nanodarcy. Among the organic matter and inorganic components, TOC content exerts the strongest control on porosity and permeability. Pore size and pore throat size distribution are strongly associated with TOC content, decreasing with increasing TOC content. SEM and TEM images suggest that several kinds of sites for porosity development are present, including organic matter, pyrite framboids, clay platelets, quartz rims, carbonate grains and microfractures. High porosity and permeability are associated with specific depositional facies. Massive and pyritic mudstones, which are

rich in TOC and quartz, have relatively high porosity and permeability. Laminated mudstone, bioturbated mudstone and carbonate, which are rich in clay and carbonate content, have relatively low porosity and permeability.

Rock mechanical properties were evaluated by hardness measurements and Young's modulus, Poisson's ratio and brittleness calculated from dipole sonic and density log data. Clay content is the most significant factor controlling the brittleness of shale rocks. The effect of quartz content on rock mechanical properties depends on the type of the quartz present in the rock. Authigenic quartz is positively correlated with brittleness, but detrital quartz has little or no effect. Factor analysis indicates that carbonate increases brittleness, while no obvious correlation between TOC content and brittleness was observed in this study. Brittleness in Horn River Shale shows both geographic and stratigraphic variability. Increasing brittleness in the northwest part of the basin largely results from greater distance from the sediment source and decreased clay content. The Otter Park member represents a period of major relative sea level fall and is more ductile than the underlying Evie Member and the overlying Muskwa Formation because of its high clay content.

## **PREFACE**

This thesis is an original work by Tian Dong, participating in an ongoing project funded by consortium of oil companies and the NSERC (Natural Sciences and Engineering Research Council of Canada). T. Dong was primarily responsible for the work, which was also contributed by coauthors, including Drs. Nicholas B. Harris, Korhan Ayranci, as well as Cory E. Twemlow, Brent R. Nassichuk, Julia M. McMillan and Sheng Yang. It is impossible for the completeness of SEM and TEM work without the assistance from Drs. Peng Li and Nathan Gerein. Randy Kofman and Dr. Nancy Zhang gave great assistance to the mercury injection and nitrogen adsorption work. The main body of this thesis is consisting of four chapters, described as following:

Chapter 2 of this thesis will be submitted to GSA Bulletin, as Dong, T., Harris, N.B., Ayranci, K. "Sea level fluctuation and organic matter accumulation in Honr River Shale, Northeastern British Columbia, Canada: Insights into redox conditions, productivity and sediment flux from major and trace element geochemistry". Core description and lithofacies classification was conducted by K. Ayranci. Sample cutting, processing and crushing were conducted by T. Dong, assisted by N.B. Harris. T. Dong analyzed the major and trace elements data with assistance from N.B. Harris. N.B. Harris assisted with the data collection and contributed to manuscript edits. T. Dong created the figures and wrote the initial manuscript. N.B. Harris was the supervisory author and was involved with the data analysis. T. Dong submitted the manuscript and was responsible for every stage of the revision and editing.

Chapter 3 of this thesis has been published as Dong, T., Harris, N.B., Ayranci, K., Twemlow, C.E., Nassichuk, B.R., "Porosity characteristics of the Devonian Horn River shale, Canada: Insights from lithofacies classification and shale composition," International Journal of Coal Geology 141-142 (2015), 74-90. Core description and lithofacies classification was conducted by K. Ayranci. Sample cutting, processing and crushing were conducted by T. Dong with assistance from N.B. Harris. Porosity

measurement was carried out by C.E. Twemlow and B.R. Nassichuk. Nitrogen adsorption, SEM and TEM work were carried out by T. Dong. T. Dong created the figures and wrote the initial manuscript. N.B. Harris assisted with the data collection and contributed to manuscript edits. T. Dong submitted the manuscript and was responsible for every stage of the revision and editing.

Chapter 4 of this thesis has been submitted to Marine and Petroleum Geology, as Dong, T., Harris, N.B., Ayranci, K., Twemlow, C.E., Nassichuk, B.R., "The controls of geochemical composition on pore throat size distribution and permeability in a high maturity shale: an example in Middle and Upper Devonian Horn River Shale, northeastern British Columbia, Canada". Core description and lithofacies classification was conducted by K. Ayranci. Sample cutting, processing and crushing were conducted by T. Dong with assistance from N.B. Harris. Permeability measurement was carried out by C.E. Twemlow and B.R. Nassichuk. Mercury injection and SEM work were carried out by T. Dong. T. Dong created the figures and wrote the initial manuscript. N.B. Harris assisted with the data collection and contributed to manuscript edits. T. Dong submitted the manuscript and was responsible for every stage of the revision and editing.

Chapter 5 of this thesis has been submitted to AAPG Bulletin as Dong, T., Harris, N.B., Ayranci, K., Yang, S., "The impact of rock composition on geomechanical properties in a shale formation: Middle and Upper Devonian Horn River Shale, Northeast British Columbia, Canada". K. Ayranci. completed the core description, lithofacies classification and depositional environment interpretation. T. Dong. was responsible for the sample cutting and processing. All the SEM and cathodoluminescence work was completed by T. Dong. T. Dong carried out the hardness measurements with assistance from S. Yang and K. Ayranci. N.B. Harris assisted with the data collection and contributed to manuscript edits. T. Dong created the figures and the initial manuscript composition. T. Dong submitted the manuscript and was responsible for every stage of the revision and editing.

The ideas present here are my own with assistance from N.B. Harris. All the coauthors contributed to the data analyzing and discussion work.

## ACKNOWLEDGEMENT

How time flies! I have been in University of Alberta for five years. At first, I did not like the winter weather here and I was not adapted to the food, culture as well as living habit. Today, about to leave after a couple of months, I find that I actually do not want to leave this place.

First and foremost, I would like to thank my supervisor, Dr. Nicholas Harris who gave me a big influence on my academic career. I would like to thank you for encouraging my research with his industry experience and professional knowledge. In the past five years, he not only gave academic guidance to me, but also care and concern on my life. In my final year, thank you for your time and patience on my every paper manuscript, from which I learned a lot. Again, I would like to give my most sincere gratitude to you, my advisor, Dr. Nicholas Harris.

Secondly, I would like to thank the Natural Sciences and Engineering Research Council of Canada, and consortium of oil companies, including ConocoPhillips Canada, Devon Canada, Husky Energy, Imperial, Nexen-CNOOC, and Shell Canada, for providing funding to support our research work.

I would also like to thank my committee members, Professor Doug Schmitt and Professor Robert A. Creaser for giving constructive comments and advices on the progress of my research work. In the past five years, I have had the pleasure to work with every member in our group, Korhan Ayranci, Noga Vaisblat, Levi Knapp, Julia McMillan and Martin Schwangler. I am grateful to Drs. Peng Li in the National Institute for Nanotechnology, Nathan Gerein in the Scanning Electron Lab, Department of Earth and Atmospheric Sciences, Nancy Zhang in the Integrated Nanosystems Research Facility and Randy Kofman in the Department of Physics for their assistance and training during my experiments. I would like to thank all the faculties and staff in the Department of Earth and Atmospheric Sciences for their help on my thesis and Ph.D. education.

Special thanks to my family. They are the most important people in my world and I

dedicate this thesis to them. I would like to thank my wife, Wenliang Ge, for her support and encouragement throughout my research work. Whenever I felt lost, confused or facing difficulties, she was always careful and patient to answer my queries. I also want to extend my thanks to my parents, my mother-in-law and father-in-law for their taking care of my little son. I also thank my friends for providing support and friendship that I needed.

## TABLE OF CONTENTS

<b>CHAPTER 1 INTRODUCTION.....</b>	<b>1</b>
1.1 Overview.....	1
1.2 Study Area.....	5
1.3 Organization of the thesis.....	8
1.4 References.....	9
<b>CHAPTER 2 SEA LEVEL FLUCTUATION AND ORGANIC MATTER ACCUMULATION IN HORN RIVER SHALE, NORTHEASTERN BRITISH COLUMBIA, CANADA: INSIGHTS INTO REDOX CONDITIONS, PRODUCTIVITY AND SEDIMENT FLUX FROM MAJOR AND TRACE ELEMENT GEOCHEMISTRY.....</b>	<b>15</b>
2.1 Introduction.....	16
2.2 Geological setting.....	18
2.3 Methodology.....	20
2.3.1 Samples.....	20
2.3.2 Analytical methods.....	21
2.4 Results.....	24
2.4.1 Core description and sequence stratigraphy.....	24
2.4.2 Organic matter enrichment.....	25
2.4.3 Terrestrial input proxies.....	26
2.4.4 Redox proxies.....	32
2.4.5 Productivity proxies.....	35
2.5 Discussion.....	38
2.5.1 Effect of sea level change on detrital flux, redox conditions and productivity.....	38
2.5.2 Models for organic carbon deposition.....	46

2.5.3 Effect of sea level change on organic matter deposition.....	50
2.6 Conclusions.....	53
2.7 References.....	55

**CHAPTER 3 POROSITY CHARACTERISTICS OF THE DEVONIAN HORN RIVER SHALE, CANADA: INSIGHTS FROM LITHOFACIES CLASSIFICATION AND SHALE COMPOSITION..... 65**

3.1 Introduction.....	66
3.2 Geological setting.....	68
3.3 Methodology.....	70
3.3.1 Samples and datasets.....	70
3.3.2 Methods.....	70
3.4 Results.....	73
3.4.1 Lithofacies classification.....	73
3.4.2 Geochemical composition.....	87
3.4.3 Porosity.....	89
3.4.4 Pore microstructure.....	91
3.5 Discussion.....	100
3.5.1 Contributors to pore development.....	100
3.5.2 Pore structure and models for pore system.....	102
3.6 Conclusions.....	104
3.7 References.....	105

**CHAPTER 4 SHALE COMPOSITION, PORE THROAT SIZE AND PERMEABILITY IN A HIGH MATURITY SHALE: AN EXAMPLE IN MIDDLE AND UPPER DEVONIAN HORN RIVER SHALE, NORTHEASTERN BRITISH COLUMBIA, CANADA..... 112**

4.1 Introduction.....	113
4.2 Geological setting.....	115
4.3 Methodology.....	117
4.4 Results.....	122
4.4.1 Lithofacies classification.....	122
4.4.2 TOC content, major oxides concentration and mineralogy.....	124
4.4.3 Permeability.....	127
4.4.4 Pore system.....	127
4.4.5 Pore throat size distribution.....	133
4.5 Discussion.....	136
4.5.1 Relationship between porosity and permeability.....	136
4.5.2 Relationship between shale composition and pore throat size distribution.....	137
4.5.3 Shale composition and permeability.....	138
4.6 Conclusions.....	142
4.7 References.....	143

**CHAPTER 5 THE IMPACT OF ROCK COMPOSITION ON  
GEOMECHANICAL PROPERTIES IN A SHALE FORMATION: MIDDLE AND  
UPPER DEVONIAN HORN RIVER SHALE, NORTHEAST BRITISH  
COLUMBIA,**

<b>CANADA.....</b>	<b>150</b>
5.1 Introduction.....	151
5.2 Geological setting.....	152
5.3 Methodology.....	155
5.3.1 Materials.....	155
5.3.2 Methods.....	155

5.4 Results.....	159
5.4.1 Lithofacies.....	159
5.4.2 Abundance of organic matter and major oxides.....	162
5.4.3 Scanning electron microscopy-cathodoluminescence (SEM-CL).....	166
5.4.4 Hardness.....	171
5.4.5 Dynamic rock mechanical properties.....	171
5.5 Discussion.....	172
5.5.1 Hardness- a proxy for brittleness in shale formation.....	172
5.5.2 Effect of shale composition on rock geomechanical properties.....	175
5.5.3 Links between lithofacies and mechanical properties.....	181
5.5.4 Depositional environment and its influence in the geomechanical properties.....	184
5.6 Conclusions.....	187
5.7 References.....	188
<b>CHAPTER 6 CONCLUSIONS.....</b>	<b>195</b>
6.1 The effect of sea level change on organic matter accumulation.....	195
6.2 The characteristics of porosity and permeability and their controlling factors. ....	196
6.3 The impact of geochemical composition on geomechanical properties.....	198
6.4 Recommendations for future studies.....	199
<b>Bibliography.....</b>	<b>200</b>
<b>APPENDICES</b>	
Appendix 1 Major oxides concentrations for Horn River Shale samples .....	222
Appendix 2. Petrophysical data for Horn River Shale samples.....	235

## LIST OF TABLES

### CHAPTER 2

TABLE 2.1: Major, trace and minor elements concentration of cody shale, replicate sample and recommend values (U.S. Geological Survey Standards, SCo-1).....	22
--	----

### CHAPTER 3

TABLE 3.1: Porosity, TOC content, inorganic geochemical composition and Rock-Eval data for selected samples.....	75
TABLE 3.2: TOC content, major mineralogical components, and pore size at half pore volume from nitrogen adsorption.....	80
TABLE 3.3: Statistics on porosity, TOC content, major oxides for selected samples.....	83

### CHAPTER 4

TABLE 4.1: Geochemical composition for the 13 samples selected for SEM imaging analysis.....	120
TABLE 4.2: X-Ray Diffraction (XRD) analyzed mineralogy of the four samples from EOG Maxhamish and Imperial Komie well.....	121

### CHAPTER 5

TABLE 5.1: Major elements concentration of Cody Shale (USGS, SCo-1), replicate sample and the recommended values.....	158
TABLE 5.2: Five shale samples and their geochemical composition data.....	159
TABLE 5.3: Factor analysis results showing the first two factors.....	180

## LIST OF FIGURES

### CHAPTER 1

FIGURE 1.1: Map of Horn River Basin and adjacent areas.....	6
FIGURE 1.2: Middle and Upper Devonian paleogeography of Horn River Basin and Western Canada Sedimentary Basin.....	6
FIGURE 1.3: Stratigraphy column, depositional history, and interpreted relative sea level curve.....	7

### CHAPTER 2

FIGURE 2.1: Map of Horn River Basin and adjacent areas (Liard Basin and Cordova Embayment), showing well location.....	19
FIGURE 2.2: Middle and Upper Devonian stratigraphy of the Liard Basin, Horn River Basin and Cordova Embayment.....	20
FIGURE 2.3: Stratigraphic distribution of lithofacies, gamma-ray log, TOC contents and geochemical indices for EOG Maxhamish core.....	27
FIGURE 2.4: Stratigraphic distribution of lithofacies, gamma-ray log, TOC contents and geochemical indices for Nexen Gote core.....	28
FIGURE 2.5: Stratigraphic distribution of lithofacies, gamma-ray log, TOC contents and geochemical indices for ConocoPhillips McAdam core.....	29
FIGURE 2.6: Stratigraphic distribution of lithofacies, gamma-ray log, TOC contents and geochemical indices for Imperial Komie core.....	29
FIGURE 2.7: Stratigraphic distribution of lithofacies, gamma-ray log, TOC contents and geochemical indices for Arc Snake core.....	30
FIGURE 2.8: Correlation between $TiO_2$ and $Al_2O_3$ .....	31
FIGURE 2.9: C-S-Fe relationship.....	34
FIGURE 2.10: Ba-Al crossplots for the five cores.....	37
FIGURE 2.11: Crossplots of Zr versus $SiO_2$ for the Horn River Shale.....	40

FIGURE 2.12: U-EF versus Mo-EF for Horn River Shale samples..... 43

FIGURE 2.13: Correlation between concentrations of Cd and Mo..... 45

FIGURE 2.14: Relationship between TOC content and proxies for detrital fluxes, TiO<sub>2</sub>..... 47

FIGURE 2.15: Relationship between TOC content and proxies for redox conditions, Th/U..... 48

FIGURE 2.16: Relationship between TOC content and proxies for productivity, biogenic silica..... 49

**CHAPTER 3**

FIGURE 3.1: Map of Horn River Basin and adjacent areas (Liard Basin and Cordova Embayment), showing well locations..... 69

FIGURE 3.2: Middle and Upper Deonian stratigraphy of the Liard Basin, Horn River Basin and Cordova Embayment..... 70

FIGURE 3.3: Representative core photographs of the Horn River Group lithofacies..... 84

FIGURE 3.4: Gamm ray log, core description and porosity data for Maxhamish and Imperial Komie well..... 86

FIGURE 3.5: Gamm ray log, core description and porosity data for Nexen Gote and McAdam well..... 87

FIGURE 3.6: Ternary diagram showing the variation of major oxides among different lithofacies..... 89

FIGURE 3.7: The relationship between TOC content and quartz content..... 89

FIGURE 3.8: Histogram showing differences in porosity among different lithofacies..... 90

FIGURE 3.9: The relationship between porosity and TOC content, concentration of SiO<sub>2</sub>, Al<sub>2</sub>O<sub>3</sub> and CaO+MgO, representing quartz, clay and carbonate content,

respectively.....	91
FIGURE 3.10: Nitrogen adsorption and desorption isotherms for four representative samples.....	92
FIGURE 3.11: Pore size distribution of representative shale samples determined from nitrogen adsorption using BJH model.....	93
FIGURE 3.12: Plot of pore volume versus pore size derived from nitrogen adsorption isotherm for representative samples.....	94
FIGURE 3.13: Pore size at half pore volume versus shale composition.....	95
FIGURE 3.14: Field emission scanning electron microscope (FE-SEM) images of shale samples from Maxhamish well.....	97
FIGURE 3.15: Field emission scanning electron microscope (FE-SEM) images of shale samples from Imperial Komie well.....	98
FIGURE 3.16: Transmission electron microscope (TEM) images of focused ion beam-milled sample from the Muskwa Formation, Imperial Komie well.....	100

#### **CHAPTER 4**

FIGURE 4.1: Map of Horn River Basin and adjacent areas, showing well locations.....	116
FIGURE 4.2: Middle and Upper Devonian stratigraphy of the Liard Basin and Horn River Basin.....	117
FIGURE 4.3: Core description, gamma ray and permeability profile for EOG Maxhamish well and Imperial Komie well.....	122
FIGURE 4.4: Core description, gamma ray and permeability profile for Nexen Gote well and ConocoPhillips McAdam well.....	123
FIGURE 4.5: QEMSCAN images showing the mineral distribution and fabric of representative samples from the five lithofacies.....	124
FIGURE 4.6: Correlation between selected major oxides (SiO <sub>2</sub> , Al <sub>2</sub> O <sub>3</sub> and CaO) and	

mineralogy from XRD analysis (quartz, clay and carbonate).....	125
FIGURE 4.7: The relationship between permeability and TOC content, concentrations of major oxides, SiO <sub>2</sub> , Al <sub>2</sub> O <sub>3</sub> , CaO, representing quartz, clay and carbonate, respectively.....	126
FIGURE 4.8: Correlation between porosity and permeability for Horn River Shale samples.....	126
FIGURE 4.9: SEM images showing pore structure of organic-rich shale samples.....	128
FIGURE 4.10: SEM images showing pore structure of quartz-rich shale samples.....	130
FIGURE 4.11: SEM images showing pore structure of clay-rich shale samples and carbonate-rich samples.....	132
FIGURE 4.12: Histogram of pore throat size distribution calculated from mercury injection data.....	134
FIGURE 4.13: The relationship between median pore throat diameter calculated from mercury injection data and shale composition.....	135
FIGURE 4.14: Effective porosity calculated from mercury injection data versus TOC content.....	135
FIGURE 4.15: Statistics on the permeability data among the five lithofacies.....	141
FIGURE 4.16: Correlation between TOC content and permeability among different drilling wells.....	142

## CHAPTER 5

FIGURE 5.1: Map of Horn River Basin and adjacent areas.....	154
FIGURE 5.2: Middle and Upper Devonian stratigraphy of the Liard Basin, Horn River Basin and Cordova Embayment.....	154
FIGURE 5.3: Representative core photos of the Horn River Group lithofacies.....	160

FIGURE 5.4: Core description, profiles of TOC content, major oxides, Young's modulus, Poisson's ratio, brittleness and hardness for EOG Maxhamish.....	163
FIGURE 5.5: Core description, profiles of TOC content, major oxides, Young's modulus, Poisson's ratio, brittleness and hardness for Imperial Komie.....	164
FIGURE 5.6: Core description, profiles of TOC content, major oxides, Young's modulus, Poisson's ratio, brittleness and hardness for Nexen Gote.....	165
FIGURE 5.7: Core description, profiles of TOC content, major oxides, Young's modulus, Poisson's ratio, brittleness and hardness for ConocoPhillips McAdam.....	166
FIGURE 5.8 Crossplots of selected major oxide and mineral contents.....	166
FIGURE 5.9: SEM-CL images for massive mudstone and pyritic mudstone samples.....	168
FIGURE 5.10: SEM-CL images for the laminated mudstone.....	169
FIGURE 5.11: SEM-CL images for a bioturbated mudstone and carbonate.....	170
FIGURE 5.12: Cross-plot of hardness versus dynamic Young's modulus and Poisson's ratio for EOG Maxhamish and Imperial Komie wells.....	174
FIGURE 5.13: Cross-plot of brittleness versus hardness for EOG Maxhamish and Imperial Komie wells.....	174
FIGURE 5.14: Cross-plot of hardness versus TOC content and major oxides for EOG Maxhamish core.....	176
FIGURE 5.15: Cross-plot of hardness versus TOC content and major oxides for Imperial Komie core.....	176
FIGURE 5.16: Cross-plot of hardness versus TOC content and major oxides for Nexen Gote core.....	177
FIGURE 5.17: Cross-plot of hardness versus TOC content and major oxides for ConocoPhillips McAdam core.....	177
FIGURE 5.18: Cross-plot of Si versus Zr for all samples.....	181
FIGURE 5.19: Ternary plot of SiO <sub>2</sub> , Al <sub>2</sub> O <sub>3</sub> and CaO of samples belonging to different	

lithofacies..... 182

FIGURE 5.20: Cross-plot of Young's modulus versus Poisson's ratio of samples from different lithofacies..... 182

FIGURE 5.21: Box and whisker plots showing brittleness and hardness of shale samples differentiated by lithofacies..... 183

FIGURE 5.22: Geographic distribution of Young's modulus, Poisson's ratio and brittleness..... 187

## CHAPTER 1 INTRODUCTION

### 1.1 Overview

Shales or mudstones are fine-grained sedimentary rocks, predominantly composed of sedimentary materials less than 62.5 microns in diameter. Mudrocks, including mudstones and shales are widely distributed across the world, comprising 65% of all sedimentary rocks (Broichhausen et al., 2005). Over the past ten years, with the advancement of horizontal well drilling and hydraulic fracturing technology, oil and gas stored in shale reservoirs have become increasingly important as an emerging fossil fuel sources that been ignored previously. It has been demonstrated that gas shales and oil shales now typically not only serve as source rocks or seals, but also reservoirs for hydrocarbons (Curtis, 2002; Jarvie et al., 2007; Ross and Bustin, 2008; Slatt, 2011; Curiale and Curtis, 2015).

In the United States, natural gas has been produced from shales and mudrocks since 1821 (Curtis, 2002) and will account for a progressively increasing proportion of natural gas supply in the future (U.S. EIA, 2012). By 2013, there were over 40000 producing shale gas wells spread across the United States (Rivard et al., 2014). Gas production from Canadian shale started in 2005 and has significantly increased since 2007 (B.C. Oil and Gas Commission, 2014). A number of prospective shale gas deposits have been found in various stages of exploration and exploitation, including Middle to Upper Devonian Horn River Shale in northeastern British Columbia (Ross and Bustin, 2008; B.C. Ministry of Energy and Mines, 2011; Dong et al., 2015), Upper Devonian Duvernay Formation in Alberta (Rivard et al., 2014; Knapp et al., 2015), Lower Triassic Montney Formation (tight gas and shale gas) (National Energy Board, 2013; Vaisblat et al., 2015; Wood et al., 2015). Other shale plays are currently being evaluated including the Upper Ordovician Utica Shale in southern Quebec and the Mississippian Frederick Brook Shale in New Brunswick (Rivard et al., 2014). By the end of 2012, more than 1100 wells had

been drilled for shale gas exploration and exploitation in Canada, with the majority of them drilled in British Columbia and Alberta (Rivard et al., 2014). Both the shale gas production and estimated in-place gas resources will increase sharply in the next few decades with the increasing demand of natural gas and decreasing trend of conventional gas resource in Canada.

This thesis presents four studies of the Horn River Shale reservoir using diverse methodologies to investigate the geochemical, petrophysical and geomechanical characterization and correlate them to sequence stratigraphic framework.

Sequence stratigraphic analysis is of significant importance in formation correlation in conventional hydrocarbon exploration and production like sandstone and carbonate reservoirs. A stratigraphic sequence is a relatively conformable, genetically related succession of strata bounded by unconformities or their correlative conformities (Van et al., 1990). Sequence stratigraphic analysis can reveal lithofacies stacking patterns, which are functions of sediment supply and accommodation space. The latter is always associated with relative sea level change, which in turn is affected by eustasy and local tectonism. In geologic time, sea level has risen and fallen in a cyclic manner (Haq and Schutter, 2008). Typically, the sedimentary record produced by a full relative sea level cycle consists of a Falling-Stage Systems Tract (FSST), Lowstand Systems Tract (LST), Transgressive Systems Tract (TST) and Highstand Systems Tract (HST) (Catuneanu et al., 2011). The FSST includes the regressive deposits that accumulate after the onset of a relative sea-level fall and before the start of the next relative sea-level rise. The LST includes deposits that accumulate after the end of regression and before the onset of sea level rise. The TST includes the deposits that accumulate from the onset of transgression until the time of maximum transgression of the coast. The HST includes the progradational deposits that form when sediment accumulation rates exceed the rate of increase in accommodation during the late stages of relative sea-level rise.

Sequence stratigraphy has rarely been applied to deep-water black shales because of

the difficulty of recognizing critical surfaces such as sequence boundaries, maximum flooding surface and system tracts. A small number of recent studies have demonstrated that, despite the apparent homogeneity in visual inspection of gas shales, stratigraphic sequences can be identified in shale formations based on the subtle variations in lithofacies and rock properties, sometimes indicated by geochemical composition and well log response (Loucks, 2007; Hulsy, 2011; Lash and Engelder, 2011; Ver Straeten, et al., 2011; Abouelresh and Slatt, 2012; Hammes and Frébourg, 2012; Hemmesch et al., 2014). A combined sequence stratigraphic methodology from sedimentologic and geochemical analysis can provide improved correlation and understanding of coeval depositional system and lithofacies (Slatt and Rodriguez, 2012).

In conventional petroleum systems, the spatial and temporal distribution of a source rock is a critical factor controlling hydrocarbon occurrence. In shale gas systems, organic matter not only serves as a source rock, but also as reservoir which affects porosity and gas saturation (Loucks et al., 2009; Passey et al., 2010; Chalmers et al., 2012; Curtis et al., 2012; Dong et al., 2015). Total organic carbon (TOC), the most important parameter for evaluating source rock quality, varies vertically and laterally at different scales, controlled by depositional environment. Recent studies indicate that the accumulation of organic-rich rocks is a complex function of three processes- organic production, organic preservation and dilution (Katz, 2005). Organic matter can accumulate in a variety of settings, resulting from an interaction among these three processes (Bohacs et al., 2005). Studying the accumulation of organic matter in the context of sequence stratigraphy can help us predict the best organic-rich interval which is favorable for both gas generation and storage. One aspect of our study is to test if the sea level fluctuation has direct effect on the three factors: productivity, redox conditions, and dilution.

Shales are generally regarded as impermeable intervals because of their low porosity and permeability. Porosity and permeability are two critical reservoir parameters controlling gas storage and production capacity. Investigating the pore structure of gas

shales is critical to estimating original gas in place and flow characteristics of rock matrix. Because of its small particle size present in shale formations, these rocks are typically characterized by very low porosities (3.1-11.7%) (Curtis et al., 2012), pore sizes in the nanometer range (from less than 1.8nm to more than 1000nm) (Curtis et al., 2011), and extremely low permeabilities, typically fall in nano-darcy and micron-darcy range (Kwon et al., 2004; Yang and Aplin, 2007; 2010). In conventional coarser grained reservoirs, hydrocarbons are mainly stored in primary and secondary pores between grains and in inorganic matrix, which can be viewed under the optical microscope. However, it is hard to investigate pore systems within shales using traditional methods like optical microscopy because of their fine-grained nature. Recently, the application of high resolution scanning electron microscopy to samples polished with ion-beam milling technology, has discovered important porosity systems primarily developed within organic matter (Loucks et al, 2009, 2012; Curtis et al., 2012; Chalmers et al., 2012). In some organic-rich shales, organic matter pores may account for as much as 50% of the total porosity (Loucks et al, 2009; Gupta, 2012). Investigation of pore structure and pore size distribution can help understand where the gas is stored and how it flows. In this study, the pore system in shale reservoirs was evaluated by direct methods, scanning electron microscopy images combined with ion-milling techniques, and indirect methods, including mercury injection analysis and nitrogen adsorption analysis. In addition, porosity and permeability were measured and correlated to geochemical composition in order to identify the effects of composition on pore development.

Because of their extremely inherent low permeabilities, gas shales are generally subjected to hydraulic fracturing treatments, as that is the best way to enhance well productivity. Two geomechanical properties, Young's modulus and Poisson's ratio, are considered key parameters in hydraulic fracturing treatments. Formations with high Young's modulus and low Poisson's ratio are defined as brittle rock which is more likely to fail under stress and maintain open fractures after they are created. In contrast, rock

with low Young's modulus and high Poisson's ratio is defined as ductile rock, which is more resistant to fracture initiation (Rickman et al. 2008). These two parameters are strongly related to mineral components (quartz, clay, carbonates, feldspar and pyrite content) and total organic carbon (TOC) (Aoudia et al., 2010; Harris et al., 2011; Sone and Zoback, 2013; Labani and Rezaee, 2015). Characterizing the relationship between geomechanical properties and mineralogy as well as organic matter is essential to predicting brittle intervals, which in turn influences the occurrence and distribution of natural fractures and the rock's response to hydraulic fracture stimulation. Sea level changes directly determine mineralogy and organic matter concentration, and to some extent, may affect geomechanics, however, the relationship is complex and poorly known (Slatt and Abousleiman, 2011). Our purpose here is to rigorously test relationships between stratigraphic sequence and geomechanical properties, because correlating geomechanical properties to stratigraphic sequences will make them more predictable prior to drilling (Slatt and Abousleiman, 2011).

## **1.2 Study area**

The Horn River Basin is located in northeastern British Columbia and extends northward into the Northwest Territories (Fig. 1.1), covering nearly 12,000 km<sup>2</sup>. It is bordered to the east by Slave Point carbonate platform, separating it from Cordova Embayment, south by Presqu'ile Barrier and west by Bovie fault, which separates it from Liard Basin by a great displacement. Horn River Basin, Cordova Embayment and associated carbonates are situated in the northwest of Western Canada Sedimentary Basin (WCSB), a vast wedge-shaped depositional basin, which existed as a passive margin along the western edge of the Canadian craton and mainly deposited carbonates and marine shales during Middle and Upper Devonian (Fig. 1.2) (Oldale and Munday, 1994; Hulsey, 2011).

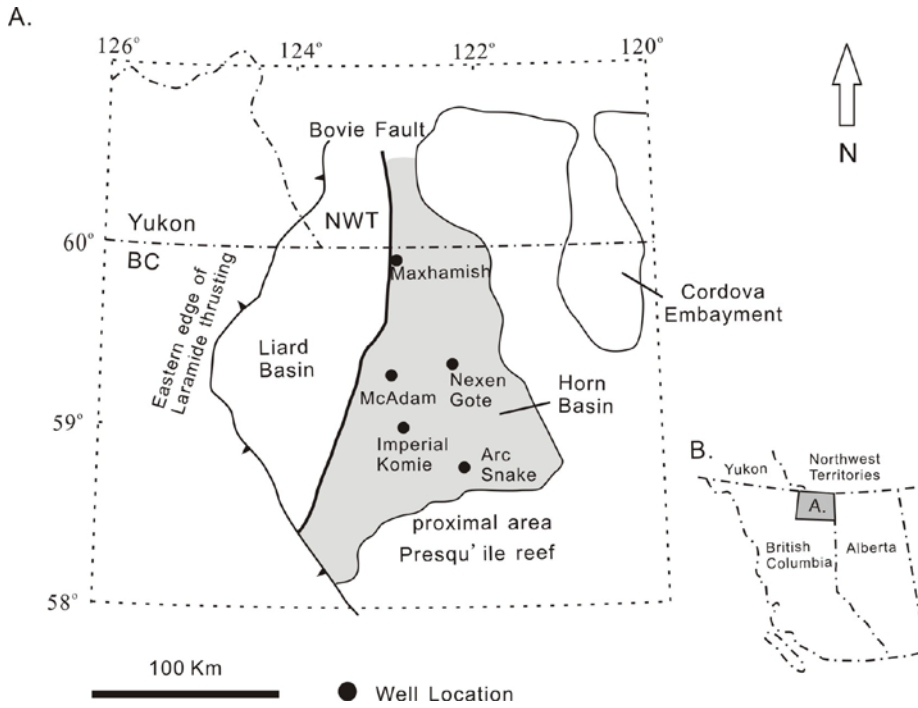


Fig. 1.1. Map of Horn River basin and adjacent areas (modified after Ross and Bustin, 2008).

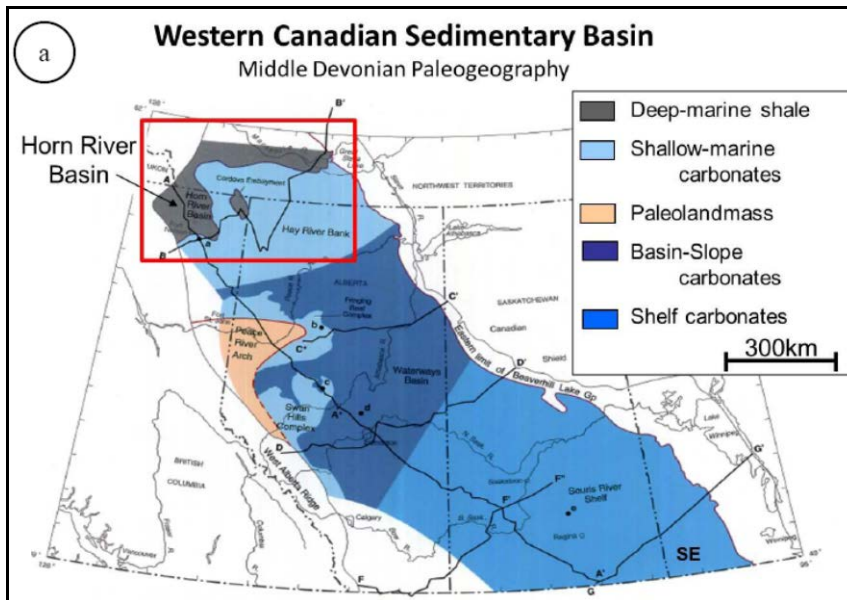


Fig. 1.2. Middle Devonian paleogeography of Horn River Basin and Western Canadian Sedimentary Basin (Oldale and Munday, 1994)

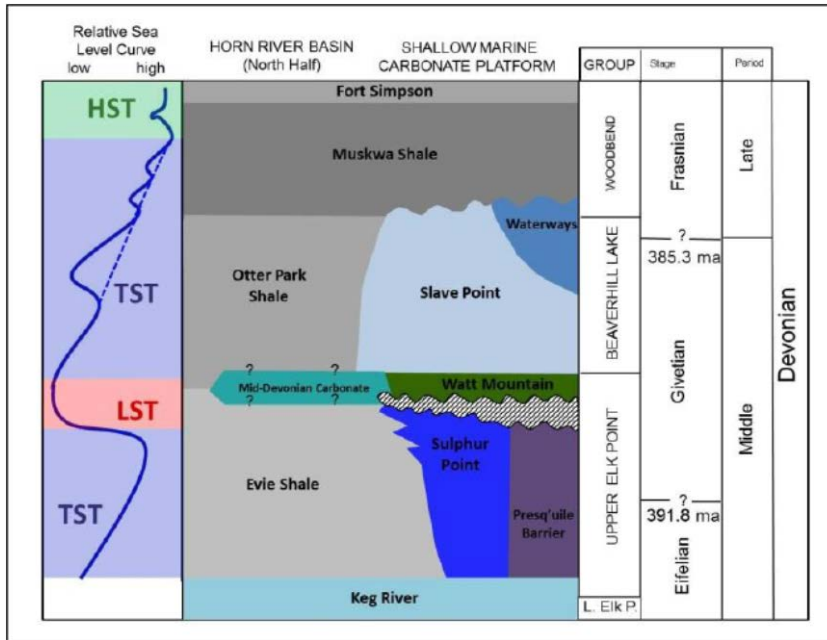


Fig. 1.3. Stratigraphic column, depositional history, and interpreted relative sea level curve (Hulsey, 2011)

The Middle and Upper Devonian Horn River Shale was deposited from late Eifelian (around 392 Ma) to early Frasnian stage (approximately 383 Ma), comprising Evie, Otter Park Members and Muskwa Formation (Fig. 1.3). These shale units are the basinal equivalents of the Elk Point Group, the Beaverhill Lake Group, and the Woodbend Group, which are carbonates facies situated along the southeastern portion of WCSB. The Evie Member is the equivalent of upper Elk Point Group deposited through late Eifelian to early Givetian. The Otter Park Member is the equivalent of the Beaverhill Lake Group deposited during middle and late Givetian stage. The Muskwa Formation is the equivalent of the Lower Woodbend Group deposited during early Frasnian stage.

### Evie Member

The Evie Member unconformably overlies the shallow marine carbonates of the Lower Keg River Formation, consisting of primarily limestones and dolostones. The Evie Member is a dark grey to black, calcareous, siliceous mudstone. It becomes more argillaceous (clay-rich) toward the top of the interval. It is characterized by high and moderate gamma ray readings. The Evie Member contains the highest total organic

content of the Horn River Shale (McPhail et al., 2008; Dong et al., 2015). It reaches a maximum thickness of over 270m in the southeast corner of the Horn River Basin in which it dominantly comprising medium to dark grey calcareous shale (McPhail et al., 2008).

### **Otter Park Member**

The Otter Park Member is generally described as a grey to dark grey, pyritic, non-calcareous to calcareous, siliceous shale that becomes less calcareous and more siliceous upward. This interval is low in total organic content in comparison to the underlying Evie and overlying Muskwa Formation (McPhail et al., 2008; Dong et al., 2015). On well logs, the Otter Park has the lowest gamma ray reading compared with the other two formations. The Otter Park is interpreted to have been deposited during the initial portion of a transgressive phase (Oldale and Munday, 1994), underlying a regionally correlative dolomitic carbonate interval (Hulsey, 2011).

### **Muskwa Formation**

The dark grey to black, organic-rich, generally non-calcareous, siliceous, Muskwa shale, is characterized by high gamma ray values which correlate to high organic content (McPhail et al., 2008; Zahrani, 2011; Dong et al., 2015) and high resistivity, overlying the Otter Park Member. It has a thickness ranging from 50 to 90m (Hulsey, 2011). It is interpreted to be deposited during continued transgression.

## **1.3 Organization of the thesis**

The main objectives of this thesis are to characterize the petrophysical and geomechanical properties in shale formation and tie these properties to the geochemical composition. This is a paper-based thesis, primarily consisting of four chapters. Each chapter has been published/submitted or will be submitted to peer-reviewed journals.

Chapter 2 examines the effect of sea level change on detrital flux, redox conditions, productivity and therefore organic matter accumulation models. High resolution

geochemical datasets including TOC content, major, minor and trace elements on five long continuous cores were applied to provide insights into the mechanisms and controls on the stratigraphic and geographic variation.

Chapter 3 and 4 examines the influence of geochemical composition on porosity, permeability and pore structure, including pore morphology, pore size and pore throat size distribution. Shale samples were examined by core description, porosity and permeability measurement, SEM, and TEM imaging of ion milled samples, nitrogen adsorption and mercury injection analysis in order to develop a better understanding of the controls of organic and inorganic rock constituents on porosity development and pore microstructure.

Chapter 5 examines the impact of geochemical composition on geomechanical properties in the shale formation and their temporal and geographic variation. We evaluate the rock mechanical properties in the Middle and Upper Devonian Horn River Shale using core hardness measurements, Young's modulus, Poisson's ratio, brittleness and relate these to shale composition and texture. The availability of many core samples and modern wire-line log data make the Horn River Shale an unparalleled opportunity for such an analysis.

#### **1.4 References:**

Abouelresh, M. O., Slatt, R.M., 2012. Lithofacies and sequence stratigraphy of the Barnett shale in east-central Fort Worth basin, Texas. AAPG Bulletin 96, 1-22.

Aoudia, K., Miskimins, J.L., Harris, N.B., Mnich, C.A., 2010. Statistical analysis of the effects of mineralogy on rock mechanical properties of the Woodford shale and the associated impacts for hydraulic fracture treatment design. 44th US Rock Mechanics Symposium and 5th U.S.-Canada Rock Mechanics Symposium, Salt Lake, 11p.

B.C. Ministry of Energy and Mines, National Energy Board, 2011. Ultimate potential for

- unconventional natural gas in Northeastern British Columbia's Horn River Basin. Oil and Gas Reports 2011-1.
- B.C. Oil and Gas Commission, 2014. Horn River Basin Unconventional Shale Gas Play Atlas, 15p.
- Bohacs, K., 2005. Production, destruction, and dilution-the many paths to source-rock development. SEPM Special Publication 82, 61-101.
- Catuneanu, O., Galloway, W.E., Kendall, C.G., Miall, A.D., Posamentier, H.W., Strasser, A. and Tucker, M.E., 2011. Sequence stratigraphy: methodology and nomenclature. Newsletters on Stratigraphy 44, 173-245.
- Chalmers, G. R., Bustin, R. M., Power, L. M., 2012. Characterization of gas shale pore systems by porosimetry, pycnometry, surface area, and field emission scanning electron microscopy/transmission electron microscopy image analyses: Examples from the Barnett, Woodford, Haynesville, Marcellus, and Doig units. AAPG Bulletin 96, 1099-1119.
- Curiale, J.A., Curtis, J.B., 2015. Organic geochemical applications to the exploration for source-rock reservoirs - A review. Journal of Unconventional Oil and Gas Resources (in press).
- Curtis, J. B., 2002. Fractured shale-gas systems. AAPG Bulletin 86, 1921-1938.
- Curtis, M. E., Ambrose, R.J., Sondergeld, C.H. and Rai, C.S., 2011. Transmission and scanning electron microscopy investigation of pore connectivity of gas shales on the nanoscale. SPE Paper 144391, SPE North American Unconventional Gas Conference and Exhibition, the Woodlands, 10p.
- Curtis, M. E., Sondergeld, C.H., Ambrose, R.J. and Rai, C.S., 2012. Microstructural investigation of gas shales in two and three dimensions using nanometer-scale resolution imaging. AAPG Bulletin 96, 665-677.
- Dong, T., Harris, N.B., Ayranci, K., Twemlow, C.E., Nassichuk, B.R., 2015. Porosity characteristics of the Devonian Horn River shale, Canada: Insights from lithofacies

- classification and shale composition. *International Journal of Coal Geology* 141-142, 74-90.
- Gupta, N., 2012. Multi-scale characterization of the Woodford shale in west-central Oklahoma: from scanning electron microscope to 3D seismic. PhD thesis, University of Oklahoma, 182p.
- Hammes, U, Frébourg, G., 2012. Haynesville and Bossier mudrocks: A facies and sequence stratigraphic investigation, East Texas and Louisiana, USA. *Marine and Petroleum Geology* 31, 8-26.
- Haq, B. U. and Schutter, S.R., 2008. A Chronology of Paleozoic Sea-Level Changes. *Science* 322, 64-68.
- Harris, N.B., Miskimins, J.L., Mnich, C.A., 2011. Mechanical anisotropy in the Woodford shale, Permian Basin: origin, magnitude, and scale: *The Leading Edge* 30(3), 284-291.
- Hemmesch, N.T., Harris, N.B., Mnich, C.A., Selby, D., 2014. A sequence-stratigraphic framework for the Upper Devonian Woodford Shale, Permian Basin, west Texas. *AAPG Bulletin* 98, 23-47.
- Hulsey, K. M., 2011. Lithofacies characterization and sequence stratigraphic framework for some gas-bearing shales within the Horn River basin, Northeastern British Columbia. Master thesis, University of Oklahoma, 76p.
- Jarvie, D. M., Hill, R. J., Ruble, T. E., Pollastro, R. M., 2007. Unconventional shale-gas systems: the Mississippian Barnett shale of north-central Texas as one model for thermogenic shale-gas assessment. *AAPG Bulletin* 91, 475-499.
- Katz, B. J., 2005. Controlling factors on source rock development – a review of productivity, preservation, and sedimentation rate. *SEPM Special Publication* 82, 7-16.
- Knapp, L.J., McMillan, J.M., Harris, N.B., 2015. Duvernay Formation sequence

- stratigraphy: integrating sedimentology, geochemistry, and petrophysics. Canadian Society of Petroleum Geologists, Annual convention, Calgary.
- Kwon, O., Kronenberg, A.K., Gangi, A.F., Johnson, B., Herbert, B.E., 2004. Permeability of illite-bearing shale: 1. Anisotropy and effects of clay content and loading. *Journal of Geophysical Research* 109, B10205, 19p.
- Labani, M.M., Rezaee, R., 2015. The importance of geochemical parameters and shale composition on rock mechanical properties of gas shale reservoirs: a case study from the Kockatea Shale and Carynginia Formation from the Perth Basin, Western Australia. *Rock Mechanics and Rock Engineering* 48, 1249-1257.
- Lash, G. G. and Engelder, T., 2011. Thickness trends and sequence stratigraphy of the Middle Devonian Marcellus Formation, Appalachian basin: implications for Acadian foreland basin evolution. *AAPG Bulletin* 95, 61-103.
- Loucks, R. G., and Ruppel, S.C., 2007. Mississippian Barnett shale: lithofacies and depositional setting of a deep-water shale-gas succession in the Fort Worth basin, Texas. *AAPG Bulletin* 91, 579-601.
- Loucks, R. G., Reed, R. M., Ruppel, S. C., and Jarvie, D. M., 2009. Morphology, genesis, and distribution of nanometer-scale pores in siliceous mudstones of the Mississippian Barnett shale. *Journal of Sedimentary Research* 79,848-861.
- Loucks, R. G., Reed, R. M., Ruppel, S. C., Hammes, U. 2012. Spectrum of pore types and networks in mudrocks and a descriptive classification for matrix-related mudrock pores. *AAPG Bulletin* 96, 1071-1098.
- McPhail, S., Walsh, W., Lee, C., Monahan, P.A., 2008. Shale units of the Horn River formation, Horn River basin and Cordova Embayment, Northeastern British Columbia: (abs.), Canadian Society of Petroleum Geologists and Canadian Well Logging Society Convention, 14 p.
- National Energy Board, 2013. The ultimate potential for unconventional petroleum from the Montney Formation of British Columbia and Alberta. 17p.

<https://www.nwb-one.gc.ca/nrg/sttstc/ntrlgs/rprt/lmtptntlmntnyfrmtn2013/lmtptntlmntnyfrmtn2013-eng.pdf>.

Oldale, H. S., Munday, R.J., 1994. Devonian Beaver Hill Group of the Western Canada Sedimentary Basin; in Geological Atlas of the Western Canada Sedimentary Basin, Canadian Society of Petroleum Geologists and Alberta Research Council, Special Report 4.

Passey, Q. R., Bohacs, K.M., Esch, W.L., Klimentidis, R. and Sinha, S., 2010. From oil-prone source rock to gas-producing shale reservoir-geological and petrophysical characterization of unconventional shale gas reservoirs. SPE Paper 131350, SPE International Oil and Gas Conference and Exhibition, Beijing, 29p.

Rickman, R., Mullem, m., Petre, E., Grieser, B., Kundert, D., 2008. A practical use of shale petrophysics for stimulation design optimization: all shale plays are not clones of the Barnett shale. SPE Paper 115258, SPE Annual Technical Conference and Exhibition, Colorado, 11p.

Rivard, C., Lavoie, D., Lefebvre, R., Sejourne, S., Lamontagne, C., Duchesne, M., 2014. An overview of Canadian shale gas production and environmental concerns. International Journal of Coal Geology 126, 64-76.

Ross, D. J. K., and R. M. Bustin, 2008, Characterizing the shale gas resource potential of Devonian-Mississippian strata in the western Canada sedimentary basin: Application of an integrated formation evaluation: AAPG Bulletin, v.92, p. 87-125.

Slatt, R., 2011. Important geological properties of unconventional resource shales. Central European Journal of Geosciences 3, 435-448.

Slatt, R. M., Abousleiman, Y., 2011. Merging sequence stratigraphy and geomechanics for unconventional gas shales. The Leading Edge, special section: shales, 274-282.

Slatt, R. and Rodriguez, N.D., 2012. Comparative sequence stratigraphy and organic geochemistry of unconventional gas shale: commonality or coincidence? Journal of Natural Gas Science and Engineering 8, 68-84.

- Sone, H., Zoback, M.D., 2013. Mechanical properties of shale-gas reservoir rocks - Part 1: Static and dynamic elastic properties and anisotropy. *Geophysics* 78, 381-392.
- U.S. EIA, 2012. Annual Energy Outlook 2012, June 2012, p.252.
- Vaisblat, N., Harris, N.B., Euzen, T., 2015. Petrophysics, geomechanics and rock composition in the Montney Formation. Canadian Society of Petroleum Geologists, Annual convention, Calgary.
- Van, W. J. C., Mitchum, R.M., Campion, K.M., Rahmanian, V. D., 1990. Siliciclastic sequence stratigraphy in well logs, cores, and outcrops: concepts for high-resolution correlation of time and facies. AAPG Methods in Exploration Series, No.7, 55p.
- Ver Straeten, C. A., Brett, C. E., Sageman, B. B., 2011. Mudrock sequence stratigraphy: a multi-proxy (sedimentological, paleobiological and geochemical) approach, Devonian Appalachian Basin. *Palaeogeography, Palaeoclimatology, Palaeoecology* 304, 54-73.
- Wood, J.M., Sanei, H., Curtis, M.E., Clarkson, C.R., 2015. Solid bitumen as a determinant of reservoir quality in an unconventional tight gas siltstone play. *International Journal of Coal Geology* 150-151, 287-295.
- Yang, Y.L., Aplin, A.C., 2007. Permeability and petrophysical properties of 30 natural mudstones. *Journal of Geophysical research* 112, B03206.
- Yang, Y.L., Aplin, A.C., 2010. A permeability-porosity relationship for mudstones. *Marine and Petroleum Geology* 27, 1692-1697.
- Zahrani, A. A., 2011. Interpretation of 3D multicomponent seismic data for investigating natural fractures in the Horn River Basin, northeast British Columbia. Master thesis, University of Calgary, 118p.

## **CHAPTER 2 Sea level fluctuation and organic matter accumulation in Horn River Shale, Northeastern British Columbia, Canada: Insights into sediment flux, redox conditions, and productivity from major and trace element geochemistry**

### **Abstract:**

The Middle and Upper Devonian Horn River Shale is a prominent organic-rich shale sequence in northeastern British Columbia, Canada and is host to major natural gas reserves. High resolution geochemical datasets on five long continuous cores provide insights into the effect of sea level changes on redox conditions, productivity, detrital flux and organic matter accumulation and their geographic variation.

Three third-order transgressive-regressive cycles are represented in the Horn River Shale. Organic matter accumulation was controlled by multiple factors, including redox conditions, productivity and dilution by detrital input, all of which were directly affected by sea level fluctuation. Organic carbon content is typically enriched in transgressive system tracts and depleted in regressive system tracts. Detrital sediment flux to the basin, measured by aluminum and titanium concentrations, varied systematically as a function of relative sea level and paleogeographic position, higher during regressions than transgressions and higher in proximal than distal areas of the basin. Redox proxies exhibit a strong correlation to TOC content, suggesting that redox condition were the primary control on the organic carbon deposition, although it was also influenced by bioproductivity and dilution. Key redox-sensitive trace elements ratios and  $C_{org}$ -Fe-S relationships suggest that redox conditions in bottom water, which are typically related to water depth, were more anoxic during transgressions than regressions, and were more anoxic in distal areas than proximal parts of the basin. Variation in biogenic silica concentrations generally demonstrates an enhanced productivity during transgressions, which we suggest was caused by recycling of nutrients under anoxic conditions.

The Evie and Muskwa intervals of the Horn River sequence, deposited during

second-order high sea level stands, were favorable for organic matter accumulation due to anoxic bottom water conditions, high primary productivity and reduced clastic dilution. The Otter Park Member, depositing during a period of falling sea level, has relatively low organic matter concentrations, which may have been due to high clastic dilution and dysoxic to oxic bottom water conditions.

## **2.1. Introduction**

Three fundamental models have been identified for the accumulation of organic matter in organic-rich sediments: enhanced organic productivity (Pedersen and Calvert, 1990; Tribovillard et al., 1994; Sageman et al., 2003; Tyson, 2001, 2005; Wei et al., 2012), enhanced preservation, associated with reducing conditions (Demaison and Moore, 1980; Arthur and Sageman, 1994; Calvert et al., 1996; Mort et al., 2007; Lash and Blood, 2014) and low sedimentation rate (minimal dilution) (Creaney and Passey, 1993; Tyson, 2005).

Recent work suggests that in most instances, the deposition of organic carbon-rich sediments is controlled by complicated, nonlinear interactions between the three main factors: productivity, preservation and sedimentation rate (Tyson and Pearson, 1991; Bohacs et al., 2005; Katz, 2005; Yan et al., 2015). Generally no individual control accounts for organic accumulation in any individual source rock; instead a combination of two or three controls contributes to deposition of organic-rich sediments (Harris et al., 2004; Rimmer et al., 2004). High organic productivity is generally a function of elevated nutrient supply (Hay, 1995), which in turn can result from several mechanisms, including upwelling, river runoff and nutrient cycling (Pedersen and Calvert, 1990; Parrish, 1995; Arthur and Sageman, 2005; Algeo and Ingall, 2007), either alone or in combination. Preservation of organic matter is strongly associated with a deficiency in oxygen in bottom waters, which is favorable for organic matter accumulation because organic matter is destroyed by respiration under oxic conditions (Demaison and Moore, 1980).

Anoxic conditions occur when oxygen consumption exceeds supply. In most cases, shallow water depth and less stratification results in an increase in bottom water oxygen level. It has been shown that both free oxygen and secondary oxidizers like sulfate control organic matter preservation, although the importance of these secondary oxidizers is disputed (Jørgensen, 1982). The effect of sedimentation rate on organic matter accumulation is complex, as it can enhance the organic matter enrichment by isolating organic matter from the oxidizing water column, or deplete organic carbon content by clastic or carbonate dilution (Tyson, 2001; Harris et al., 2004).

Although the interaction between the three primary controls on organic matter accumulation can be complex, sea level fluctuations appear to exert a significant control on all three factors and therefore on the organic matter accumulation (Arthur and Sageman, 2005; Bohacs et al., 2005). Arthur and Sageman (2005) proposed, for example, that in the Holocene Black Sea, the Mid-Cretaceous Western Interior Seaway and the Late Devonian Appalachian Basin, rising sea level was favorable for organic matter accumulation by (1) promoting retention of nutrients in marginal seas, leading to higher production; (2) enhancing water-column stratification, leading to the development of anoxia; (3) trapping terrigenous clastic materials nearshore, creating condensed sections enriched in organic matter. Because the analysis of varying sea level is critical to understanding organic matter accumulation, sequence stratigraphy can be applied to black shales to better understand the influence of sea level fluctuation on organic matter deposition (Schieber, 1998; Sageman et al., 2003; Arthur and Sageman, 2005; Macquaker et al., 2007; Ver Straeten et al., 2011; Hemmesch et al., 2014).

The Middle and Upper Devonian Horn River shale sequence in northeastern British Columbia is a thick succession of organic-rich sediments that has proven in the last ten years to be an important gas resource with ultimate recoverable reserves of 78 TCF gas (Ross and Bustin, 2008; Reynolds and Munn, 2010; B.C. Ministry of Energy and Mines, 2011; Chalmers et al., 2012). The origins of the organic matter accumulation and

conditions during deposition of the Horn River sediments are poorly understood. Although the abundant organic matter enrichment in Horn River Shale has been reported in previous studies (Ross and Bustin, 2008; Dong et al., 2015), a systematic analysis of how stratigraphic variation in organic matter enrichment and controls on this variation is still lacking. In this study, we examine the total organic carbon (TOC) content variation and trace element concentrations on five long, densely sampled cores from Horn River Basin in order to gain insights on paleo-redox conditions, paleo-productivity and clastic sediment flux during the deposition of the Middle and Upper Devonian Horn River Shale. This enables us to characterize the variation of significant geochemical proxies within the context of sequence stratigraphic framework to identify mechanisms for organic matter accumulation in the Horn River Shale. The availability of many long cores and a well-constrained paleogeographic setting make the Horn River Basin an unparalleled opportunity for such an analysis.

## **2.2. Geological Setting**

The Horn River Basin is located in northeastern British Columbia and the southwestern corner of the Northwest Territories (NWT) (Fig. 2.1), covering nearly 12,000 km<sup>2</sup>. It is bordered on the east and south by by Presqu'ile Barrier and to the west by Bovie fault, which separates the Horn River Basin from the Liard Basin by a large down-to-the-west displacement (Ross and Bustin, 2008). The Horn River Basin, Cordova Embayment and associated carbonates are situated in the northwest part of the Western Canada Sedimentary Basin (WCSB). Within the basin, the southern part is proximal to sources of siliciclastic and carbonate sediment, while northern part is relatively distal (Fig. 2.1).

Basinal shales laterally equivalent to shallow water carbonate units comprise the Evie, Otter Park Member and the Muskwa Formation of the Horn River shale sequence (Fig. 2.2) (McPhail et al., 2008; Reynolds et al., 2010). The Evie Member overlies the

shallow marine carbonates of the Lower Keg River Formation. The Evie shale is a dark grey to black, calcareous mudstone, characterized by high gamma ray readings, that becomes more argillaceous toward the top of the interval. The Otter Park shale is generally a grey to dark grey, pyritic shale that is relatively calcareous in the lower part, becoming more siliceous upward. This interval is lower in total organic content than the Evie Member and the Muskwa Formation (McPhail et al., 2008; Dong et al., 2015). The dark grey to black, organic-rich, generally siliceous, Muskwa shale is characterized by high gamma ray values, which correlate with the organic carbon content (McPhail et al., 2008; Zahrani, 2011; Dong and Harris, 2013). The Muskwa is conformably overlain by the Fort Simpson Formation, a lower TOC formation (Ross and Bustin, 2008).

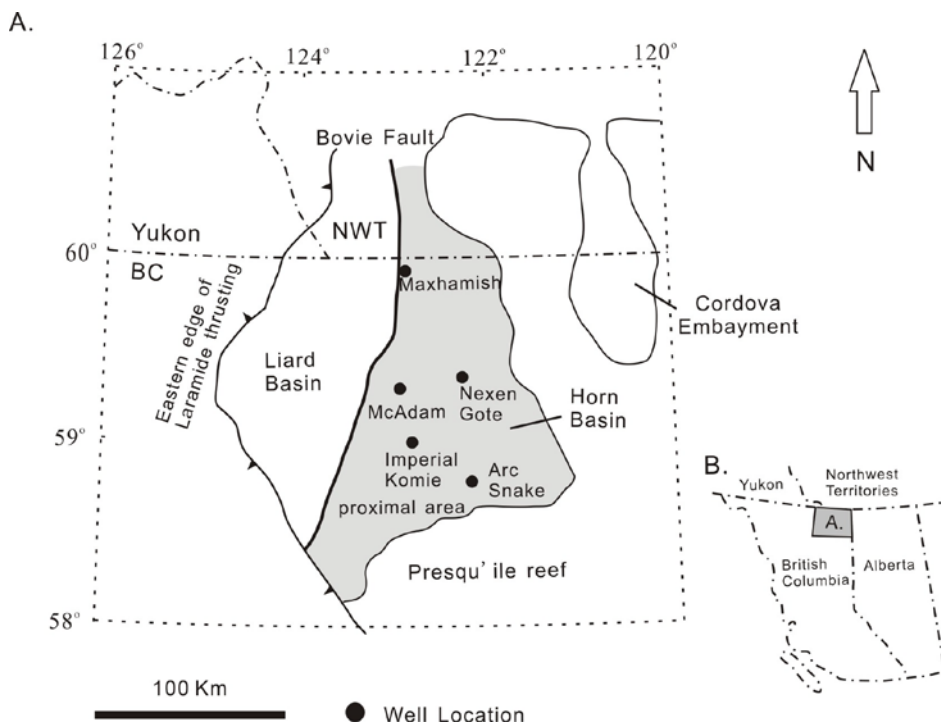


Fig. 2.1. Map of Horn River Basin and adjacent areas (Liard Basin and Cordova Embayment), showing well location (modified after Ross and Bustin, 2008).

			Liard Basin	Horn River Basin	Platform	
Devonian	Upper	Frasnian	Besa River Formation	Fort Simpson Formation	Fort Simpson Formation	
			Muskwa Fm	Muskwa Fm	Muskwa Fm	
	Middle	Givetian	Horn River Fm	Otter Park Mbr	Horn River Fm	Slave Point Fm
						Watt Myn Fm
						Sulphur Point Fm
						Upper Keg River Fm
			Horn River Fm	Evie Mbr		
			Dunedin Fm	Keg River Fm	Lower Keg River Fm	

Fig. 2.2. Middle and Upper Devonian stratigraphy of the Liard Basin, Horn River Basin and Cordova Embayment (modified after Ferri et al., 2011).

The Horn River Shale was deposited within a roughly 8 m.y. time interval spanning the late Givetian to early Frasnian Stages of the Middle to Upper Devonian (~ 392 to 384 Ma) (Mossop and Shetsen, 1994). Moore (1989) proposed that the Middle and Upper Devonian strata in Western Canada Sedimentary Basin comprise the transgressive part of Kaskaskia sequence and can be subdivided into several T-R cycles (transgressive and regressive) of sea level change. Previous studies demonstrate that the Evie shale was deposited during a second-order highstand stage (Hulsey, 2011; Potma et al., 2012). The Otter Park shale was deposited during a second order sea level low stand stage and the Muskwa shale was deposited during the following second-order transgressive stage (Hulsey, 2011; Potma et al., 2012).

## 2.3. Methodology

### 2.3.1 Samples

A total of 789 hand samples were collected from five long cores drilled in the Horn River Basin: EOG Maxhamish D-012-L/094-O-15 (122.89° W, 59.93° N), Nexen Gote A-27-I/094-O-8 (122.08°W, 59.44°N), ConocoPhillips McAdam C-87-K/094-O-7 (122.84°W, 59.49°N), Imperial Komie D-069-K/094-O-02 (122.86°W, 59.22°N), and

Arc Snake D-020-F/094-J-16 (122.37°W, 58.85°N) (Fig. 2.1). The five cores were sampled at approximately 0.5 m intervals for Maxhamish well and 1 m intervals for the other wells; each sample represents approximately a ten centimeter stratigraphic interval.

### **2.3.2 Analytical methods**

Five cores were logged in order to identify the sedimentological and ichnological characteristics, which were then used to define lithofacies. Observations included lithology, grain size, physical sedimentary structures, trace fossil assemblages and bioturbation intensity, the presence of cements, and the frequency of fractures. Twenty-five samples were selected for thin section analysis to support the lithofacies analysis.

Two splits were cut vertically from the side of each hand sample. Identical splits of these samples were analyzed for total organic carbon (TOC) data and whole-rock geochemical data, including major, minor and trace elements. Total organic carbon content of the total 789 samples was determined by LECO combustion in Weatherford Labs. Samples for whole-rock major, minor, and trace element data were analyzed at Acme Analytical Laboratories by ICP- Mass Spectrometry (ICP-MS) analysis and Leco (for Total C and Total S). All the samples were crushed and pulverized until 85% of the material passed through 200 mesh. One split of the powdered samples was then analyzed by ICP-emission spectrometry following a lithium metaborate/tetraborate fusion and dilute nitric acid digestion for the abundance of major oxides and several minor elements. Another split of the powdered samples was analyzed by ICP-MS following a lithium metaborate/tetraborate fusion and nitric acid digestion for rare earth and refractory elements. Oxides and elements analyzed by ICP-MS include SiO<sub>2</sub>, Al<sub>2</sub>O<sub>3</sub>, Fe<sub>2</sub>O<sub>3</sub>, MgO, CaO, Na<sub>2</sub>O, K<sub>2</sub>O, TiO<sub>2</sub>, P<sub>2</sub>O<sub>5</sub>, MnO, Cr<sub>2</sub>O<sub>3</sub>, total C, total S, LOI, Ba, Be, Co, Cs, Ga, Hf, Nb, Rb, Sn, Sr, Ta, Th, U, V, W, Zr, Y, La, Ce, Pr, Nd, Sm, Eu, Gd, Tb, Dy, Ho, Er, Tm, Yb, Lu, Mo, Cu, Pb, Zn, Ni, As, Cd, Sb, Bi, Ag, Au, Hg, Tl, Se and Sc. Analyzed results were calibrated using laboratory internal standards, international standards submitted as

Table 1. Major, trace and minor elements concentration of Cody shale, replicate sample and recommended values (U.S. Geological Survey standards, SCo-1).

Sample type	SiO <sub>2</sub> (%)	Al <sub>2</sub> O <sub>3</sub> (%)	Fe <sub>2</sub> O <sub>3</sub> (%)	MgO(%)	CaO(%)	Na <sub>2</sub> O(%)	K <sub>2</sub> O(%)	TiO <sub>2</sub> (%)	P <sub>2</sub> O <sub>5</sub> (%)	MnO(%)	Cr <sub>2</sub> O <sub>3</sub> (%)
Cody shale sample	63.15	13.54	5.1	2.68	2.59	0.88	2.77	0.57	0.21	0.05	0.01
Replicate sample	61.52	13.7	4.98	2.67	2.59	0.89	2.74	0.58	0.2	0.05	0.01
Recommend values	62.8	13.7	5.13	2.72	2.62	0.9	2.77	0.63	0.21	-	-
Sample type	Ni(ppm)	Sc(ppm)	Ba(ppm)	Be(ppm)	Co(ppm)	Cs(ppm)	Ga(ppm)	Hf(ppm)	Nb(ppm)	Rb(ppm)	Sn(ppm)
Cody shale sample	<20	11	593	2	10.8	7.7	15.2	5.3	10.4	99.5	3
Replicate sample	24	13	590	1	10.8	8	15.5	4.3	10.9	114.3	3
Recommend values	27	11	570	1.8	11	7.8	15	-	11	110	3.7
Sample type	Sr(ppm)	Ta(ppm)	Th(ppm)	U(ppm)	V(ppm)	W(ppm)	Zr(ppm)	Y(ppm)	La(ppm)	Ce(ppm)	Pr(ppm)
Cody shale sample	179.1	0.8	9.2	3.1	138	1.9	156.6	21.2	29.8	58.8	6.79
Replicate sample	169.5	0.7	9.2	2.8	131	1.5	169.9	21.9	28.6	54.8	6.79
Recommend values	170	-	9.7	-	130	1.4	160	26	30	62	6.6
Sample type	Nd(ppm)	Sm(ppm)	Eu(ppm)	Gd(ppm)	Tb(ppm)	Dy(ppm)	Ho(ppm)	Er(ppm)	Tm(ppm)	Yb(ppm)	Lu(ppm)
Cody shale sample	23.5	4.53	0.98	4.33	0.73	4.06	0.77	2.23	0.33	2.24	0.34
Replicate sample	25	4.73	1.03	4.29	0.66	3.84	0.73	2.17	0.34	2.14	0.33
Recommend values	26	-	-	-	-	-	-	-	-	-	-

Sample type	Total C(%)	Total S(%)	Mo(ppm)	Cu(ppm)	Pb(ppm)	Zn(ppm)	Ni(ppm)	As(ppm)	Cd(ppm)	Sb(ppm)	Bi(ppm)
Cody shale sample	1.03	0.11	0.5	24.2	25.5	78	22	9.9	<0.1	0.5	0.3
Replicate sample	1.1	0.04	0.7	24.5	26.9	87	22.6	9.8	0.1	0.6	0.4
Recommend values	-	-	1.4	29	31	100	27	12	-	2.5	-

---

Sample type	Ag(ppm)	Au(ppb)	Hg(ppm)	Tl(ppm)	Se(ppm)
Cody shale sample	<0.1	<0.5	0.05	0.1	<0.5
Replicate sample	<0.1	2.3	0.06	0.2	1.4
Recommend values	-	-	-	-	--

blind samples (U.S. Geological Survey standards, SCo-1), and analysis of replicate samples (Table 2.1).

## **2.4. Results**

### **2.4.1 Core description and Sequence Stratigraphy**

Five major lithofacies have been identified in the Horn River cores based on sedimentological and ichnological characteristics: massive mudstones, massive mudstones with abundant pyrite streaks, laminated mudstones, bioturbated mudstones and carbonates. Representative core photos of the lithofacies are shown in Dong et al., 2015. These lithofacies were formed in different depositional conditions and through differing depositional processes.

The massive mudstone lithofacies is found primarily in the Muskwa Formation and Evie Member. It is grey to light brown and contains siliceous and calcareous fossils, such as radiolaria, tentaculites, sponge spicules and agglutinated foraminifera. It displays very few sedimentary structures; these include horizontal parallel laminae, thin carbonate-rich bands, and starved ripples. The massive mudstones with abundant pyrite streaks (pyritic mudstones) is the most abundant lithofacies in the Horn River Shale, dominating the Muskwa and Evie intervals and present to a lesser extent in the Otter Park Member. It is a grey, massive mudstone that contains pyrite-rich laminae that are discontinuous to continuous at the scale of a core. The massive mudstone and the massive mudstone with abundant pyrite streaks lithofacies are quartz-rich. The laminated mudstones lithofacies is most common in the Otter Park Member and relatively rare in the Muskwa and Evie intervals. It consists of alternating beds of dark grey mudstone laminae and grey limestone layers. The bioturbated mudstones lithofacies is relatively rare in the Horn River Shale and is mainly localized in the lower part of the Otter Park Member. The laminated mudstone and bioturbated mudstone lithofacies are rich in clay. The

carbonates lithofacies is limited to the lower part of the Evie Member and consists of massive to irregularly bedded, well cemented packstone to grainstone lithofacies.

The massive mudstone and pyritic mudstone lithofacies are interpreted to represent a relatively deep-water basin floor setting, and low-energy, anoxic depositional conditions. Laminated to heterolithic bedded mudstones and bioturbated mudstones represent fluctuating depositional energy. Striking features in these lithofacies include the presence of silty current ripples, climbing ripples intervals of relatively thick units of flaser beds, and scattered double mud-drapes and thin-thick laminae set alternation. These features indicate a relatively shallow water depth and oxic conditions. We identified three third-order transgressive-regressive (T-R cycle) in the Horn River Shale based on the spatial and stratigraphic distribution of relatively deep and shallow depositional settings. In this study, regressive system tracts include the falling stage system tract, lowstand system tract and highstand system tract. The first T-R cycle (T-R1) is identified in the Evie Member; the second T-R cycle (T-R2) is primarily in the Otter Park Member and the third T-R cycle (T-R3) is present in the Muskwa Formation (Figs. 2.3, 2.4, 2.5, 2.6 and 2.7). At a second order, the Evie, Otter Park and Muskwa intervals were identified to deposit during high sea level, low sea level and sea level rising stage, respectively.

#### **2.4.2 Organic matter enrichment**

Total organic carbon (TOC) enrichment is clearly differentiated by stratigraphic units. TOC contents range from 0.17 wt% to 9.38 wt.% (Figs. 2.3, 2.4, 2.5, 2.6 and 2.7). In T-R1, TOC increases upward and is relatively high in the TST1 (average TOC =3.2 wt.%), followed by a decrease upward in the RST1 (average TOC = 2.58 wt.%). The T-R2 cycle has lower TOC overall compared to the T-R1. TOC contents are also generally higher in the TST2 than in the RST2 (average TOC of 3.12 wt.% versus 2.06 wt.%). TOC contents are highest in the T-R3, increasing upward in the TST3 (average TOC = 3.55 wt.%) and decreasing upward in the RST3 (averaging TOC = 2.87 wt.%).

From south to north (proximal to distal), the wells show a general increase in TOC, from an average of 1.99% in the Arc Snake core, to 2.47% in the Imperial Komie core, 2.92% in the McAdam core, 3.1% in the Nexen Gote core and 3.09% in Maxhamish core.

### **2.4.3 Terrestrial input proxies**

Aluminum, titanium and zirconium have very low concentrations in sea water and are generally considered immobile during diagenesis (Sageman and Lyons, 2004; Brumsack, 2006; Tribovillard et al., 2006) and have therefore been used as indicators of detrital flux (Caplan and Bustin, 1998). The profiles of aluminum and titanium concentration for each well are plotted vs. depth in Figs. 2.3, 2.4, 2.5, 2.6 and 2.7.

The concentration of  $\text{Al}_2\text{O}_3$  ranges from 0.04 to 26.85%, whereas the concentration of  $\text{TiO}_2$  ranges from 0.005 to 0.79%. It is apparent that the concentrations of aluminum and titanium are generally higher in the RSTs than in the TSTs (Fig. 2.8). In the T-R1, the concentrations of aluminum and titanium are low and constant in the TST1, while in the RST1, the concentrations of aluminum and titanium increase upward (Figs. 2.3, 2.4, 2.5, 2.6, and 2.7). In the T-R2,  $\text{Al}_2\text{O}_3$  and  $\text{TiO}_2$  decreases upward in the TST2, and gradually increase upward in the RST2, although in the Nexen Gote core,  $\text{Al}_2\text{O}_3$  and  $\text{TiO}_2$  are relatively low in the RST2. In the T-R3, the concentrations of  $\text{Al}_2\text{O}_3$  and  $\text{TiO}_2$  are relatively low in the TST3 and gradually decrease upward in the lower part of RST3, followed by a significant increase in the upper part of RST3.

$\text{TiO}_2$  decreases from south to north, from an average of 0.42% in the Arc Snake core, 0.45% in the Imperial Komie core to 0.36% in the McAdam core, 0.35% in the Nexen Gote core and 0.31% in the Maxhamish core (Figs. 2.3, 2.4, 2.5, 2.6 and 2.7). A similar trend was observed in the concentration in  $\text{Al}_2\text{O}_3$ , from an average of 11.33% in the Arc Snake core, 10.92% in the Imperial Komie core to 8.5% in the McAdam core, 8.2% in the Nexen Gote core and 7.53% in the Maxhamish core (Figs. 2.3, 2.4, 2.5, 2.6 and 2.7).

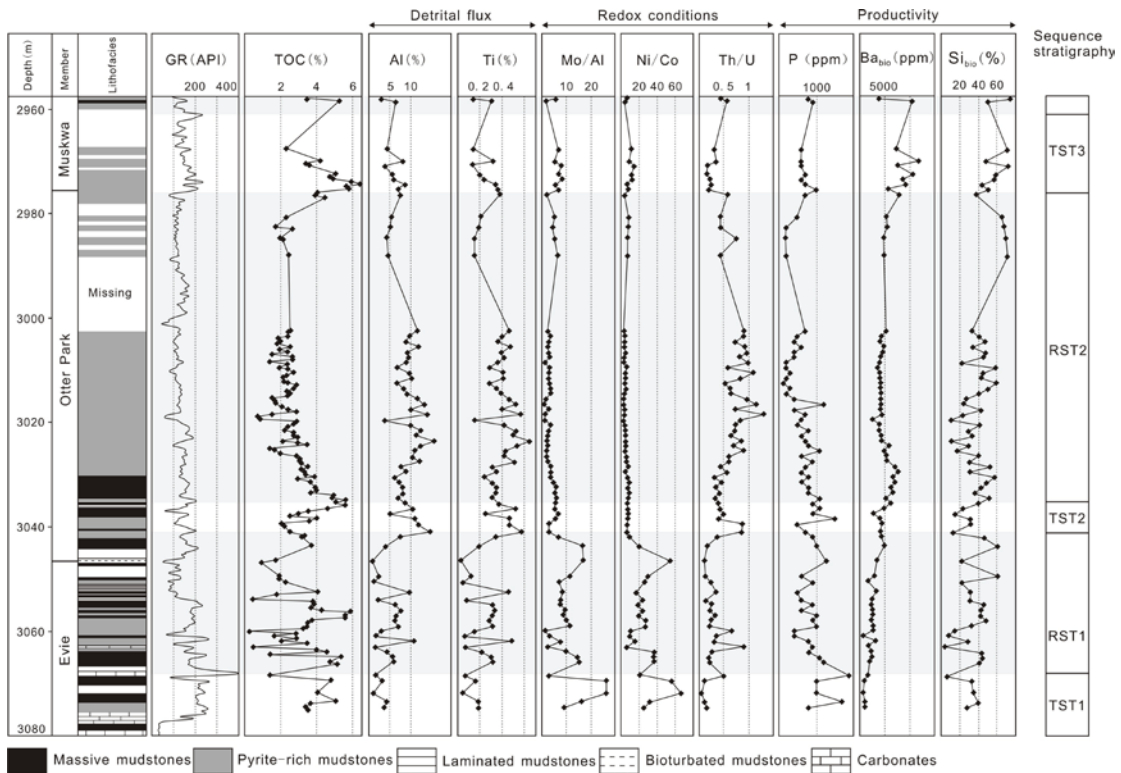


Fig. 2.3. Stratigraphic distribution of lithofacies, gamma-ray log, TOC contents and geochemical indices for detrital flux, redox conditions, productivity and inferred sequence stratigraphy of the EOG Maxhamish D-012-L/094-O-15 core. TST: transgressive system tract, RST: Regressive system tract.

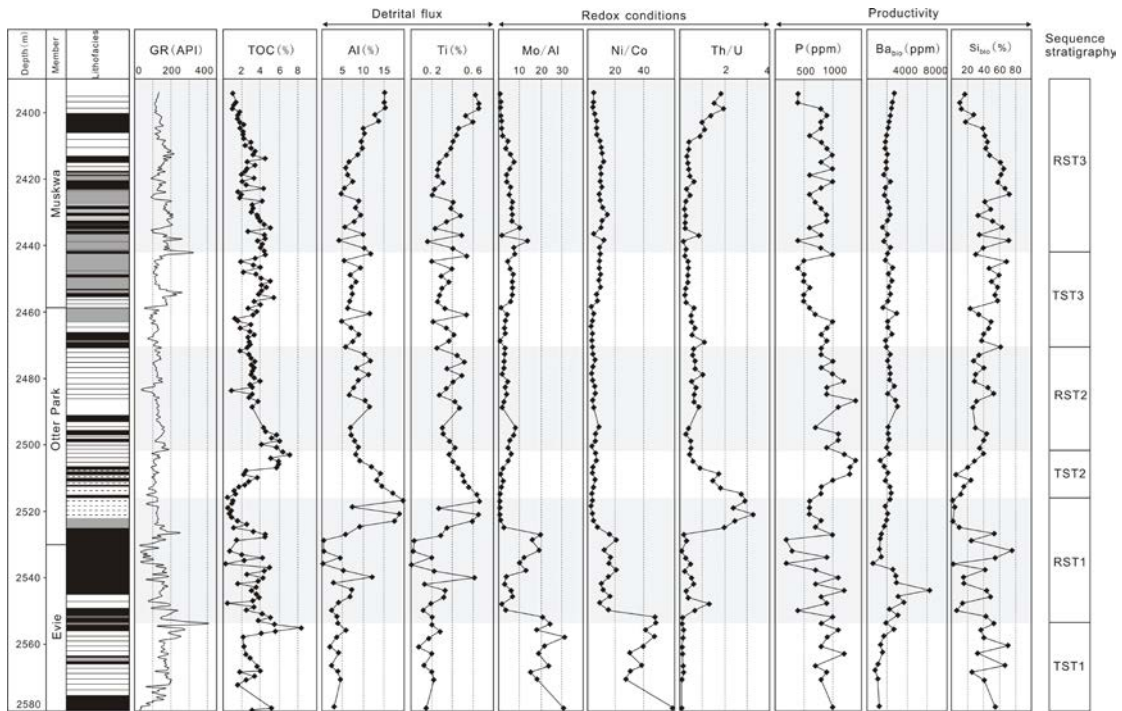


Fig. 2.4. Stratigraphic distribution of lithofacies, gamma-ray log, TOC contents and geochemical indices for detrital flux, redox conditions, productivity and inferred sequence stratigraphy of the Nexen Gote A-27-I/094-O-8 core. TST: transgressive system tract, RST: Regressive system tract.

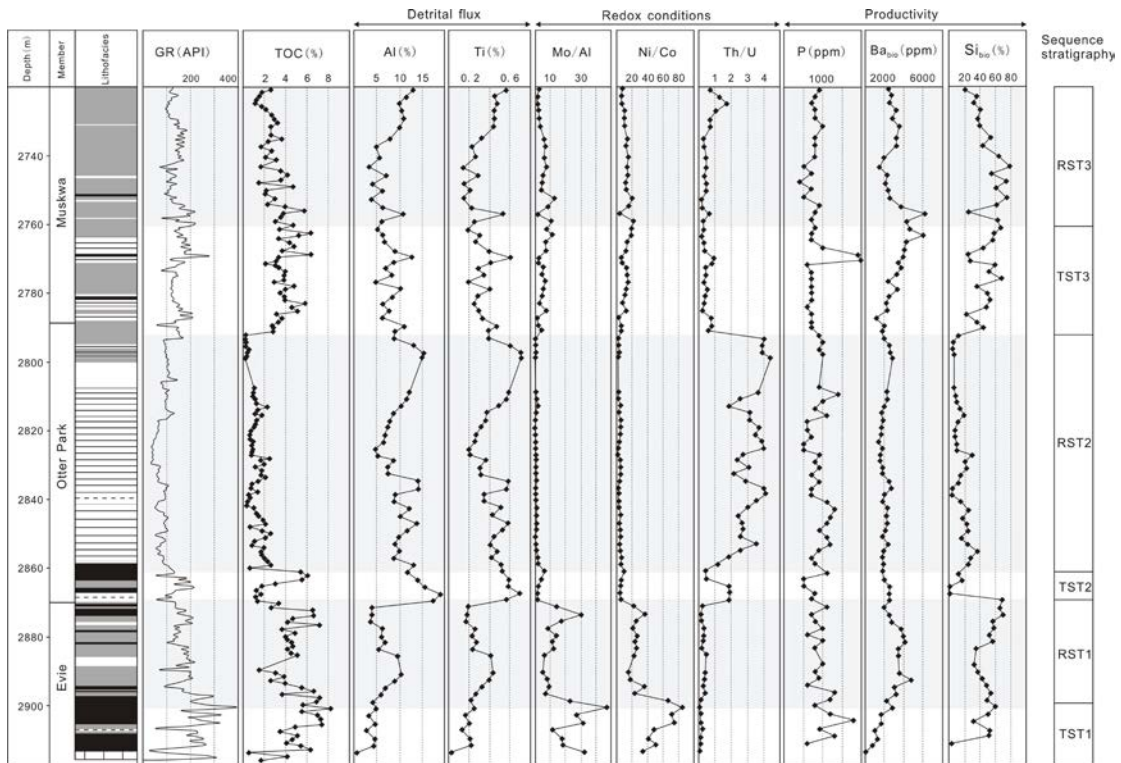


Fig. 2.5. Stratigraphic distribution of lithofacies, gamma-ray log, TOC contents and geochemical indices for detrital flux, redox conditions, productivity and inferred sequence stratigraphy of the ConocoPhillips McAdam C-87-K/094-O-7 core. TST: transgressive system tract, RST: Regressive system tract.

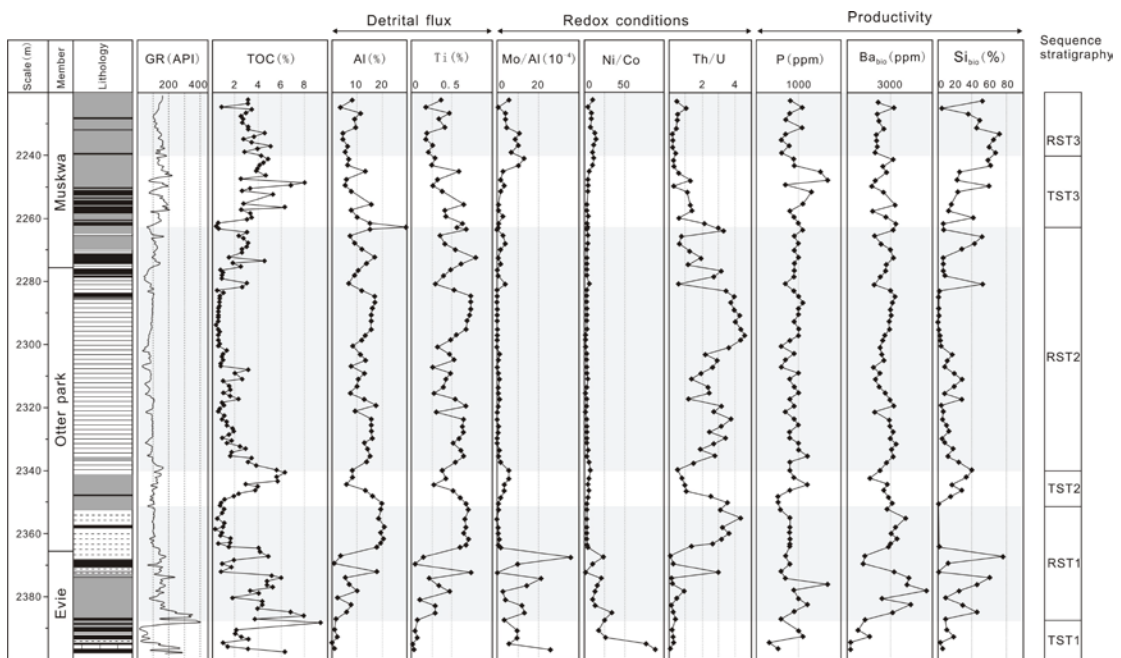


Fig. 2.6. Stratigraphic distribution of lithofacies, gamma-ray log, TOC contents and geochemical indices for detrital flux, redox conditions, productivity and inferred sequence stratigraphy of the Imperial Komie D-069-K/094-O-02 core. TST: transgressive system tract, RST: Regressive system tract.

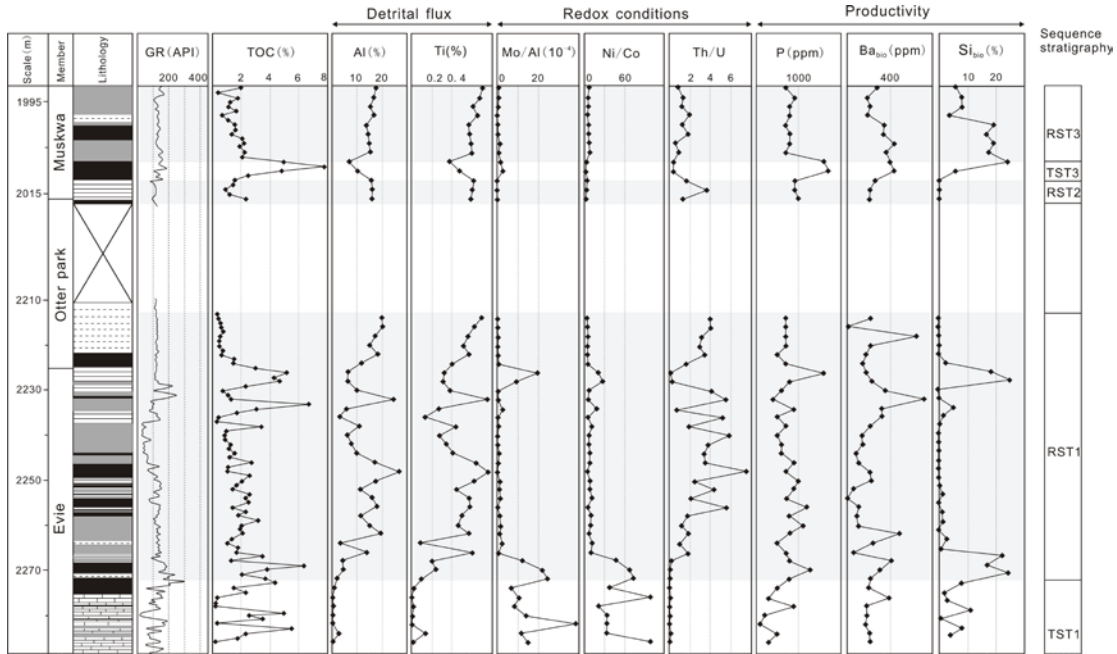


Fig. 2.7. Stratigraphic distribution of lithofacies, gamma-ray log, TOC contents and geochemical indices for detrital flux, redox conditions, productivity and inferred sequence stratigraphy of the Arc Snake D-020-F/094-J-16 core. TST: transgressive system tract, RST: Regressive system tract.

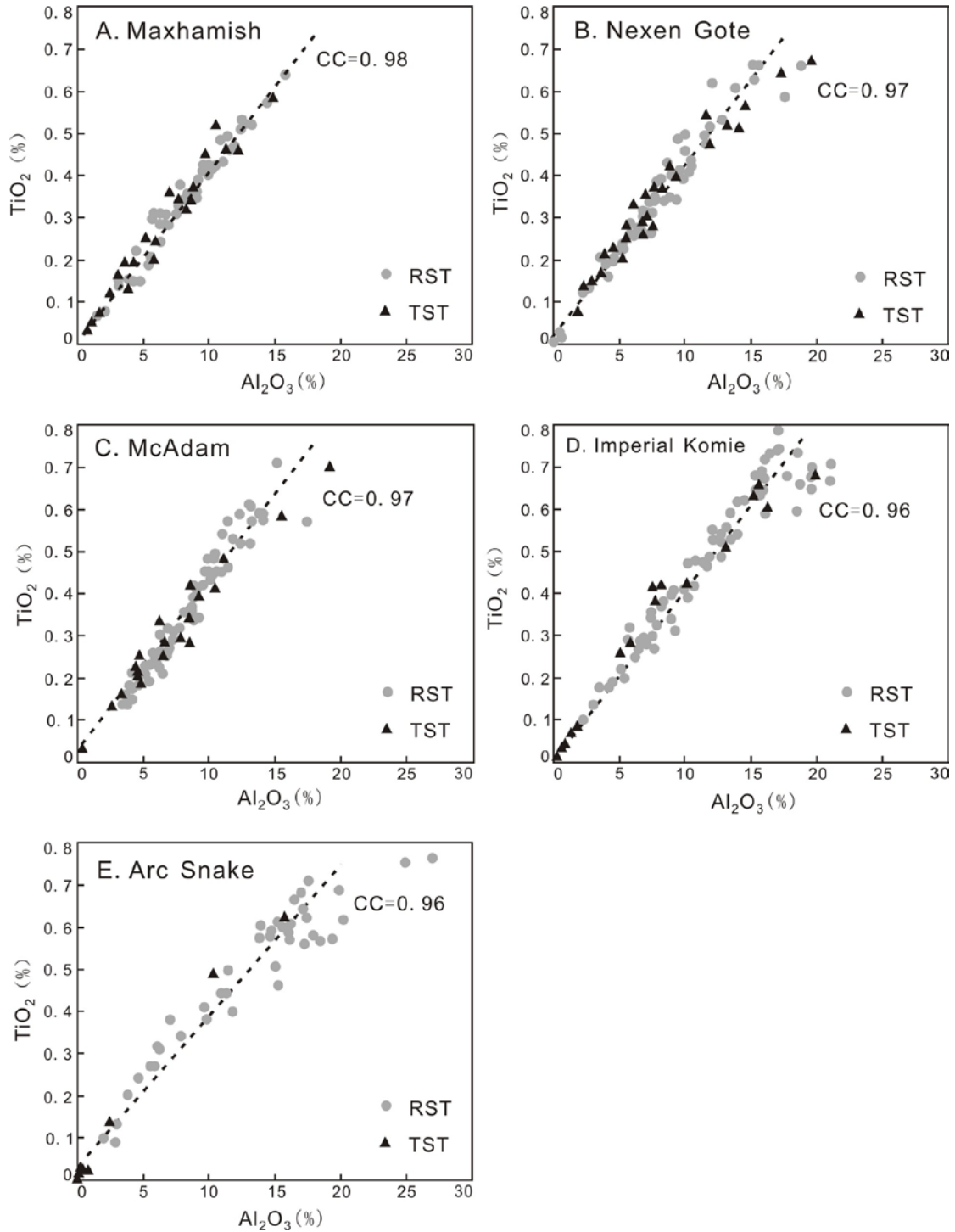


Fig. 2.8. Correlation between  $\text{TiO}_2$  and  $\text{Al}_2\text{O}_3$ . A) Maxhamish, B) Nexen Gote, C) McAdam, D) Imperial Komie, and E) Arc Snake. TST: transgressive system tract, RST: Regressive system tract. cc: correlation coefficient.

## **2.4.4 Redox proxies**

### **2.4.4.1 Redox-sensitive trace elements**

Trace elements, like Mo, U and V are redox-sensitive, where high concentrations are generally thought to indicate more reducing conditions (Calvert and Pedersen, 1993; Algeo and Maynard, 2004; Tribovillard et al., 2006; Algeo and Tribovillard, 2009; Harris et al., 2013). Studies have utilized either Al-normalized elements ratios such as Mo/Al, U/Al (Lyons et al., 2003) or trace element ratios such as U/Th (Wignall and Twitchett, 1996), Ni/Co, and V/Cr (Jones and Manning, 1994; Rimmer et al., 2004) to evaluate paleo-redox conditions. Three inorganic proxies, Mo/Al, Ni/Co and Th/U were examined in this study to elucidate redox conditions during deposition.

It is customary to normalize Mo to aluminum content, which is an important detrital element and a proxy for clay that is not affected by diagenetic processes (Brumsack, 2006); this compensates for the effect of dilution by clastic sedimentation on trace metal concentrations (Calvert and Pedersen, 1993; Tribovillard et al., 2006). Nickel (Ni) is thought to be preserved preferentially under anoxic conditions (Lewan and Maynard, 1982; Rimmer et al., 2004), and the distribution of Co in sediments is strongly tied to the abundance of clastic material (Tribovillard et al., 2006). High Ni/Co ratios are thought to be associated with anoxic conditions (Jones and Manning, 1994). Uranium is present mainly in a highly soluble state  $UO_2^{2+}$  in oxic conditions and is much less soluble and precipitates under reducing conditions (Anderson et al., 1989). Thorium, which occurs in heavy minerals or in the clay fraction in fine-grained sediments, is relatively immobile during diagenesis. Therefore, low Th/U ratios are interpreted to indicate reducing conditions during deposition (Jones and Manning, 1994; Lash and Blood, 2014). Jones and Manning (1994) suggested that suboxic to anoxic conditions are indicated by  $Th/U < 0.8$ .

In the five Horn River cores (Figs. 2.3, 2.4, 2.5, 2.6 and 2.7), Mo/Al and Ni/Co ratios behave similarly. In the T-R1, Mo/Al and Ni/Co ratios are higher in the TST1 than in the

RST1, generally decreasing upward through this cycle. In the T-R2, Mo/Al and Ni/Co ratios maintain constant and low values. In the T-R3, Mo/Al and Ni/Co ratios gradually increase upward in the TST3, then decrease upward in the RST3.

Th/U ratios are relatively low throughout the T-R1 and generally increase upward (Figs. 2.3, 2.4, 2.5, 2.6 and 2.7). In the T-R2 cycle, Th/U ratios are generally higher than in the other two cycles. The Th/U ratio is lower in the TST2 than in the RST2 in all cores except the Nexen Gote core, which shows the opposite trend (Fig. 2.4). In the T-R3 cycle, Th/U ratio is low through the entire cycle followed by an increase in the upper RST3. The same basic trend is evident in all cycles: lower in TST and higher in the RST, with the exception of the Nexen Gote core in T-R2.

Geographically, from south to north, the cores show a decrease in the average Th/U ratio, from 2.04 for Arc Snake core, to 1.82 for the Imperial Komie core, 1.39 for the McAdam core, 0.70 for the Nexen Gote core, and 0.51 for the Maxhamish core (Figs. 2.3, 2.4, 2.5, 2.6 and 2.7). Similar trends were observed in the Mo/Al and Ni/Co ratios. Mo/Al ratios is relatively low in the south, averaging 5.5 and 3.8 for Arc Snake and Imperial Komie cores, relatively high in the north, averaging 6.1, 6.9 and 6.0 for the McAdam, Nexen Gote and Maxhamish core. The average Ni/Co ratios for Arc Snake, Imperial Komie, McAdam, Nexen Gote and Maxhamish cores are 16.5, 8.3, 14.7, 11.4 and 12.8, respectively.

#### **2.4.4.2 Carbon<sub>org</sub>, sulfur and iron relationships**

Dean and Arthur (1989) and Arthur and Sageman (1994) demonstrated that C<sub>org</sub>-S-Fe relationships are useful proxies for evaluating paleoredox conditions at the time of sediment deposition; such plots are also pertinent for thermally mature shale formations (Berner and Raiswell, 1983; Raiswell and Berner, 1987; Rimmer et al., 2004; Ross and Bustin, 2009; Algeo et al., 2011). Fig. 2.9 illustrates the C<sub>org</sub>-S-Fe relationship of Horn River shale samples from Maxhamish well (Fig. 2.9A), Nexen Gote well (Fig. 2.9B), McAdam well (Fig. 2.9C), Imperial Komie well (Fig. 2.9D) and Arc Snake well (Fig.

2.9E).

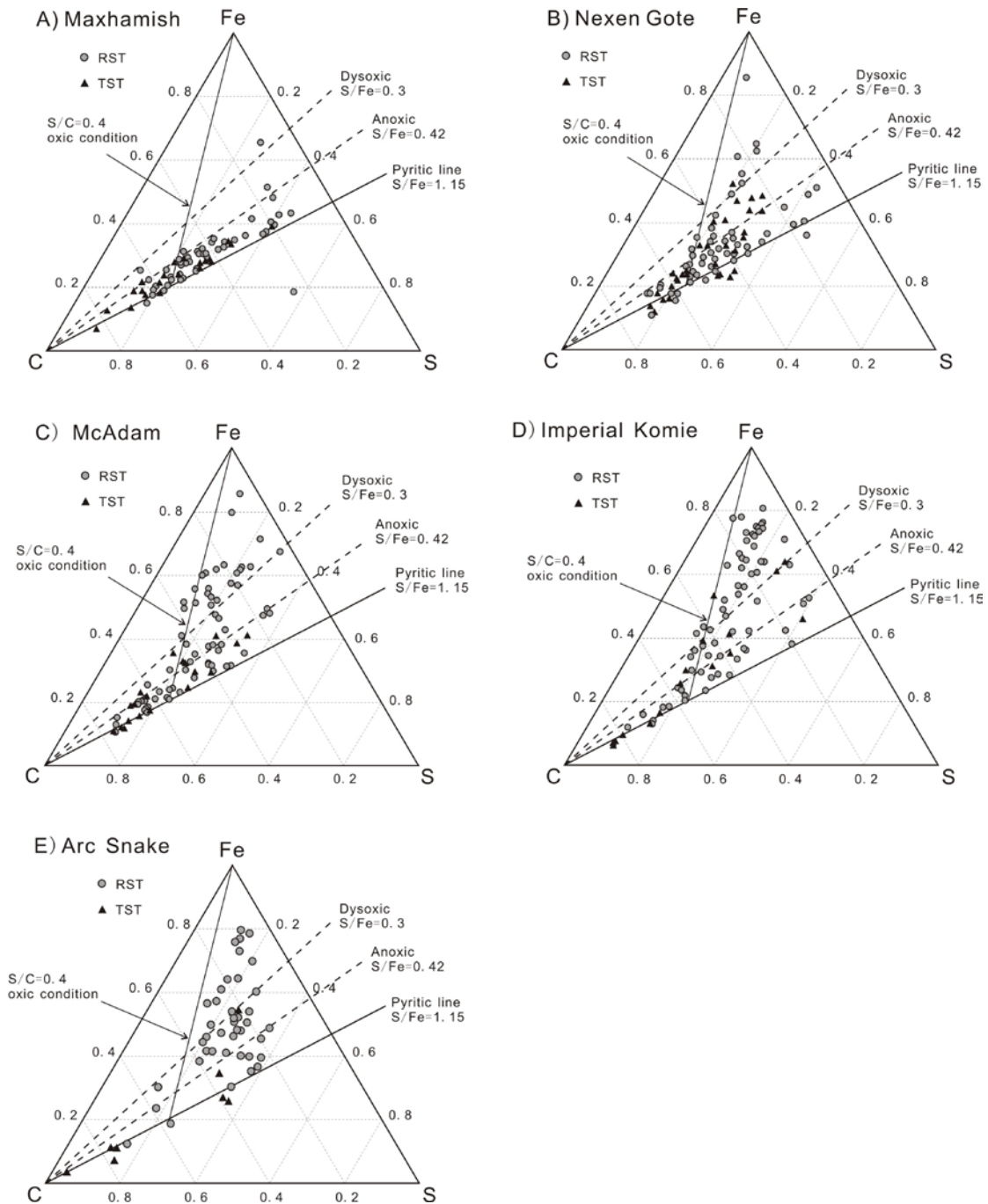


Fig. 2.9.  $C_{org}$ -S-Fe relationship. A) Maxhamish, B) Nexen Gote, C) McAdam, D) Imperial Komie, and E) Arc Snake. TST: transgressive system tract, RST: Regressive system tract.

Differences between transgressive system tracts and regressive system tracts are significant. Most samples from TSTs plot within the anoxic region with a few samples in

the dysoxic region. Many samples from RSTs plot within dysoxic and oxic regions while a smaller fraction plots within the anoxic region. Differences on the  $C_{org}$ -S-Fe relationships between wells were also observed.

From south to north, progressively fewer samples plot within the dysoxic and oxic regions: most samples from the Maxhamish core plot within the anoxic region (Fig. 2.9A), while a significant number of samples from the Imperial Komie core and Arc Snake core plot within the oxic region (Figs. 2.9D and E).

#### **2.4.5 Productivity proxies**

Several geochemical proxies have been used to evaluate the productivity (Brumsack, 2006; Tribovillard et al., 2006; Schoepfer et al., 2015; Shen et al., 2015); however, each proxy is affected by environment factors such as redox conditions, diagenetic alteration and ocean circulation (Schoepfer et al., 2015). Phosphate is an essential nutrient for marine phytoplankton growth (Schoepfer et al., 2015), and has been used as a productivity indicator in ancient sediments (Schenau et al., 2005). However, the application of phosphate concentration as a productivity indicator is limited owing to its subsequent release back to the water column under reducing conditions (Tribovillard et al., 2006; Algeo and Ingall, 2007). The main source of barium (Ba) is river input and a large part of the barium burial is associated with organic matter sinking flux (Schoepfer et al., 2015). Barium has been identified as an effective proxy for productivity (Anderson and Delaney, 2005; Schoepfer et al., 2015; Zhou et al., 2015); however, its utility can be compromised through diagenetic remobilization (McManus et al., 1998; Xiong et al., 2012; Harris et al., 2013). The abundance of biogenic silica has been proven to be a useful productivity proxy in the Late Devonian Chattanooga and New Albany Shales from the eastern USA (Schieber et al., 2000). Since no single proxy is completely reliable for the productivity evaluation, in this study, we will focus on multiple commonly used proxies, phosphorous, biogenic barium and biogenic silica.

In the T-R1, the concentration of phosphorous generally slightly increases upward in

the TST1 and decreases upward in the RST1 (Figs. 2.3, 2.4, 2.5, 2.6 and 2.7). In the T-R2, trends vary between wells: at the Maxhamish and Nexen Gote cores, the concentration of phosphate increases upward in the TSTs and decreases upward in the RSTs, whereas in the McAdam and Imperial Komie cores, the concentration of phosphorous is constant through the entire T-R2 cycle. In the T-R3, no cyclic variation of the phosphorous was observed. A distinct spike at the top of the TST3 was observed in the McAdam, Imperial Komie and Arc Snake cores.

Barium (Ba) is commonly associated with the detrital fraction of the sediment (Shen et al., 2015; Zhou et al., 2015). In this study, Ba concentrations show positive relationship with aluminum (Fig. 2.10), which is generally of detrital origin. Biogenic Ba is widely used as an effective indicator to productivity (Dymond et al., 1992; Weldeab et al., 2003; Algeo et al., 2011; Wei et al., 2012; Yan et al., 2015; Shen et al., 2015). Biogenic Ba ( $Ba_{bio}$ ) or excess Ba is obtained by subtracting detrital Ba fraction from total Ba concentration (Schroeder et al., 1997; Bonn et al., 1998; Algeo et al., 2011; Yan et al., 2015):

$$Ba_{bio} = Ba_{tot} - [Al \times (Ba/Al)_{detrital}] \quad (1)$$

In this equation,  $Ba_{tot}$  and Al are the total amounts of total Ba and  $Al_2O_3$  in samples. The estimation of  $(Ba/Al)_{detrital}$  ratios is critical to the correct estimation of  $Ba_{bio}$ . Previous compilations of  $(Ba/Al)_{detrital}$  ratios suggest a range between 0.005 and 0.01 for the crustal rocks (Taylor and McLennan, 1985; Dymond et al., 1992). Recent studies suggested a new approach to estimating  $(Ba/Al)_{detrital}$  ratios from Al vs. Ba crossplots (Schoepfer et al., 2015; Shen et al., 2015; Zhou et al., 2015), yielding a range between 0.0032 and 0.0046. In this study, a  $(Ba/Al)_{detrital}$  ratio of 0.0039 (average value of the range) is used to calculate the concentrations of biogenic barium. If the true  $(Ba/Al)_{detrital}$  ratio in our samples was slightly from what used here, we would end up calculating a slightly different  $Ba_{bio}$  value.

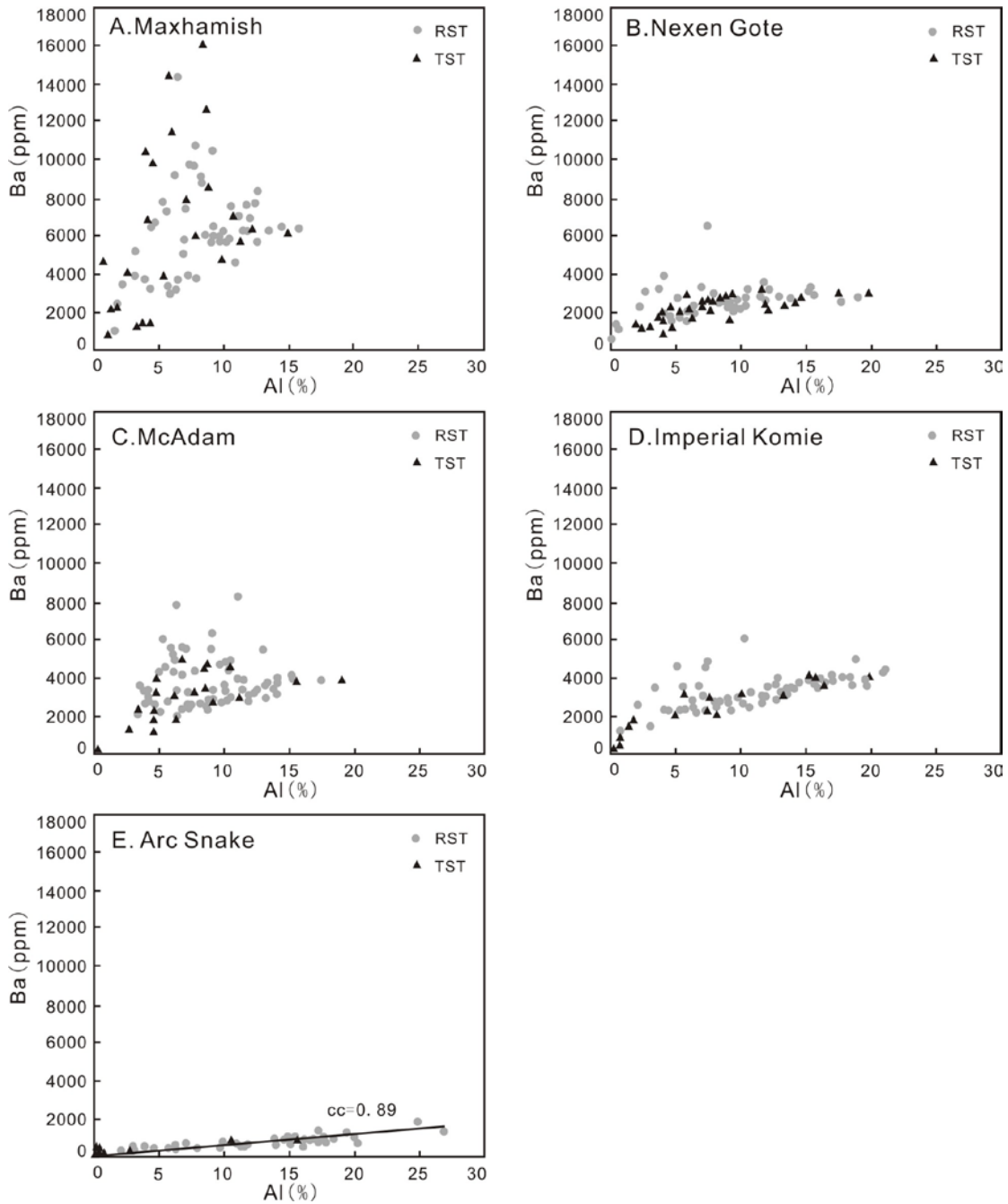


Fig. 2.10. Ba-Al crossplots for the five cores. A) Maxhamish, B) Nexen Gote, C) McAdam, D) Imperial Komie, and E) Arc Snake. TST: transgressive system tract, RST: Regressive system tract. cc: correlation coefficient.

As shown in Figs. 2.3, 2.4, 2.5, 2.6 and 2.7, in the T-R1 cycle, the concentration of biogenic barium generally increases upward in the TST1 to a maximum in the lower part of the overlying RST1, then decreases upward. In the T-R2 cycle, the biogenic barium

concentration is constant through both the TST2 and RST2, with low to moderate values in comparison to the other T-R cycles. In the T-R3 cycle, in Nexen Gote and Imperial Komie cores, the concentration of biogenic barium does not vary systematically with respect to stratigraphic sequences; in the McAdam and Maxhamish cores, biogenic barium concentration core increases upward in the TST3 and decreases upward in the RST3.

The above method can be applied to calculate biogenic silica (excess silica) using the formula (Tribovillard et al., 2006; Ross and Bustin, 2009):

$$Si_{bio} = Si_{sample} - [Al_{sample} \times (Si/Al)_{background}] \quad (2)$$

In this equation,  $Si_{sample}$  and  $Al_{sample}$  are the total amounts of  $SiO_2$  and  $Al_2O_3$  in samples. A Si/Al ratio of 3.1 is used for the background (Wedepohl, 1971).

In T-R1,  $Si_{bio}$  increases upward in the TST1 and then stays constant or decreases upward in the RST1 (Figs. 2.3, 2.4, 2.5, 2.6 and 2.7). In the T-R2,  $Si_{bio}$  shows similar variation to T-R1, increasing in the TST, and staying constant or decreasing upward in the RST. In the T-R3,  $Si_{bio}$  increases upward in the TST3 and keeps constant in the lower RST3, followed by a decreasing upward in the upper RST3 (Figs. 2.4, 2.5, 2.6 and 2.7).

The average concentration of biogenic silica increases from the south to the north, lowest in the Arc Snake core, averaging 8.0%, moderate in the Imperial Komie core (20.0%), McAdam core (35.4%) and Nexen Gote core (37.8%), and highest in the Maxhamish core, averaging 39.9%.

## **2.5. Discussion**

### **2.5.1 Effect of sea level change on detrital flux, redox conditions and productivity**

#### **Detrital flux**

The strong correlation between  $TiO_2$  and  $Al_2O_3$  suggest that Ti is primarily occurs in heavy minerals, whose concentrations vary in parallel with the clay minerals represented by the concentration of aluminum (Fig. 2.8). Concentrations of aluminum and titanium

are systematically higher in RSTs than in TSTs, indicate relatively high detrital flux during regression (Fig. 2.8). Changes in relative sea level can affect detrital flux, forcing sedimentation landward or basinward during transgressions and regressions, respectively (Figs. 2.3, 2.4, 2.5, 2.6 and 2.7).

Regional variation in the detrital flux proxies provides information about the sediment sources. The higher concentrations of titanium in the Arc Snake and Imperial Komie cores than the Nexen Gote and Maxhamish cores (Figs. 2.3, 2.4, 2.5, 2.6 and 2.7) indicate that the Arc Snake and Imperial Komie wells are proximal to the source of clastic sediment, while the Maxhamish well and Nexen Gote wells are located farther from the source.

Wright et al. (2010) proposed that biogenic silica can be distinguished from detrital silica by plotting silica concentration versus Zr concentration, the latter associated with the heavy mineral zircon, representing a proxy for silt-sized detrital input. A positive correlation between silica and Zr concentration indicates a detrital origin for the quartz (Fig. 2.11), whereas a negative correlation between silica and Zr indicates of a biogenic source. Many samples, both from the TSTs and RSTs, plot on the biogenic trend, implying that quartz in these samples is predominantly biogenic in origin. Other samples plot along a trend with positive slope, indicating a detrital origin; and many samples plot between these trends, indicating that both detrital silica and biogenic silica are present in these samples. The presence of abundant biogenic quartz makes the interpretation of silica concentration problematic as an indicator of clastic flux. The proportion of detrital versus biogenic silica varies geographically. The Arc Snake and Imperial Komie samples contain more detrital silica than Maxhamish well (Fig. 2.11), which is consistent with their proximity to sediment source.

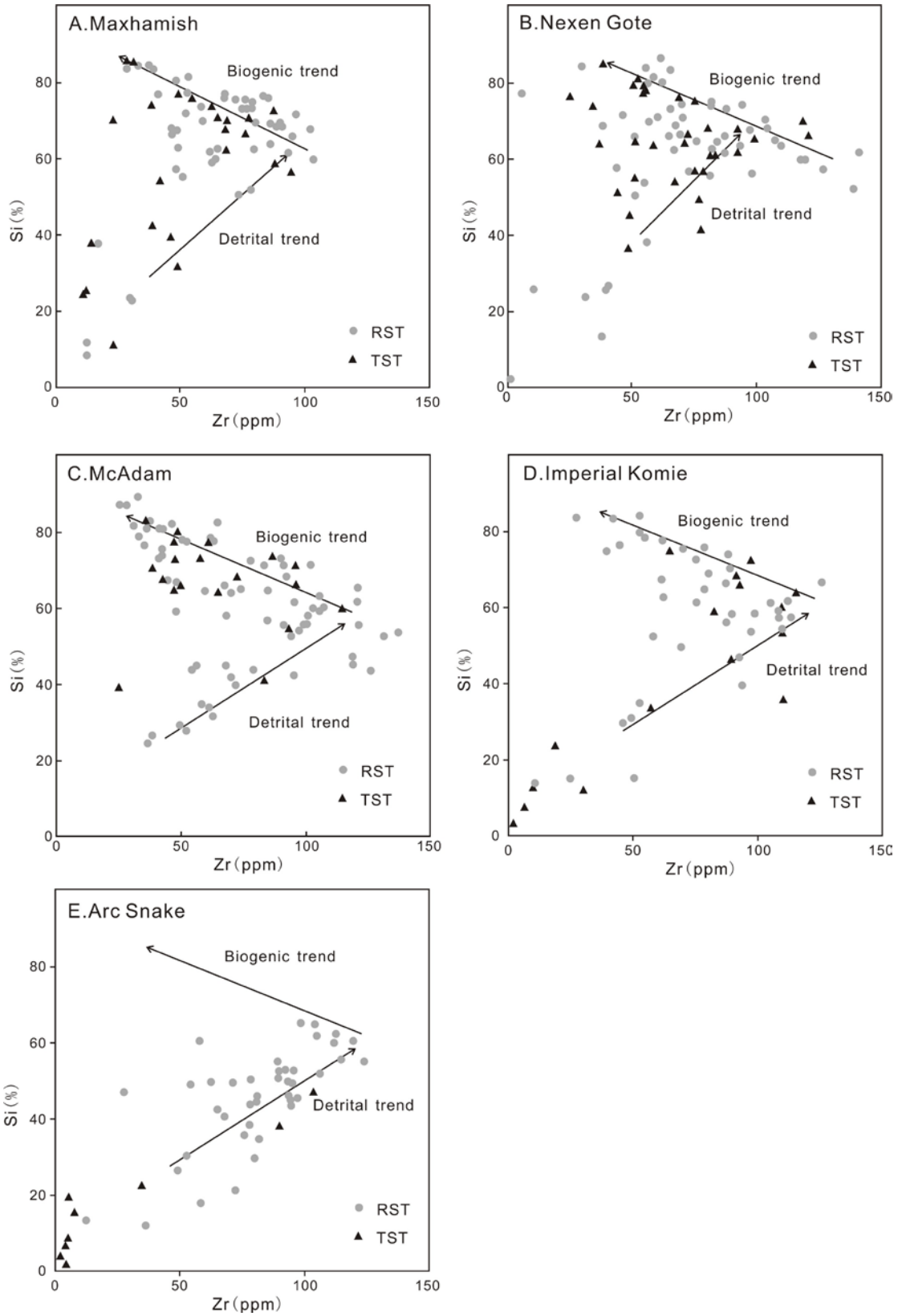


Fig. 2.11. Crossplots of Zr versus SiO<sub>2</sub> for Horn River Shale. Positive relationship refers

to samples where SiO<sub>2</sub> is detrital origin. Negative relationship refers to samples where SiO<sub>2</sub> is mainly biogenic origin. A) Maxhamish, B) Nexen Gote, C) McAdam, D) Imperial Komie, and E) Arc Snake. TST: transgressive system tract, RST: Regressive system tract.

### **Redox conditions**

Redox conditions are commonly classified as oxic, dysoxic and anoxic conditions, based on the dissolved oxygen level in the water column (Tribovillard et al., 2006). Interpretation of redox conditions is complex, and reliance on a single indicator is not recommended (Algeo and Maynard, 2004; Rimmer, 2004). In this study, several proxies are evaluated. Based on the stratigraphic relationships we establish, paleo-redox conditions during the Horn River Shale deposition can be evaluated temporally and spatially by examination of proxies within a core, and between several cores at the same stratigraphic level.

Estimates of redox conditions based on trace element ratios and C<sub>org</sub>-S-Fe relationships are consistent; they collectively illustrate temporal and spatial variation in the paleo-redox conditions during the Horn River Shale deposition. Although specific thresholds that delineate redox zones have not been identified for Mo/Al and Ni/Co ratios, these ratios can provide information on the relative changes in redox conditions. Relatively high Mo/Al and Ni/Co ratios and low Th/U ratio in TSTs indicate more reducing water bottom conditions during transgressions than regressions (Figs. 2.3, 2.4, 2.5, 2.6 and 2.7). This is consistent with redox conditions inferred from C<sub>org</sub>-S-Fe ternary diagram (Fig. 2.9), where samples from TSTs generally plot in the anoxic region and most samples from RSTs plot in the dysoxic and oxic regions. The three T-R cycles differ significantly: Mo/Al and Ni/Co ratios are notably higher in the T-R1, lower in T-R2 and intermediate in T-R3 (Figs. 2.3, 2.4, 2.5, 2.6 and 2.7). As expected, Th/U ratios show opposite trends to the Mo/Al and Ni/Co ratios, with highest values in the T-R2 cycle, lowest values in the T-R1 cycle and intermeddiate values in the T-R3 cycle. This pattern

suggests that higher-order sea level change influenced redox conditions, yielding more oxic conditions during deposition of the T-R2 cycle and more anoxic conditions for the T-R1 and T-R3 cycles. The more oxic conditions indicated for T-R2 coincide with a higher detrital flux during a second-order low sea level stage.

Redox proxies also show systematic spatial patterns. Th/U ratios are highest in Arc Snake core (average Th/U = 2.04) and lowest in Maxhamish core (average Th/U = 0.5), indicating that the distal areas were more reducing than proximal areas (Figs. 2.3, 2.4, 2.5, 2.6 and 2.7). The  $C_{org}$ -S-Fe relationships are consistent with this interpretation. In proximal areas such as the Arc Snake and Imperial Komie wells, a large proportion of samples were plotted in the dysoxic to oxic regions (Fig. 2.9). Most samples from distal areas, represented by the Maxhamish core, whether from a transgressive system tract or a regressive system tract, were deposited under anoxic conditions (Fig. 2.3). We infer that the geographic variation in redox conditions is associated with the water depth. In proximal areas, oxygenated surface water could be mixed to the sediment-water interface as the water column is relatively shallow. Conversely, water depths were sufficiently deep in distal areas that benthic conditions were rarely oxygenated, even during sea level lowstands.

Molybdenum-uranium covariation in the Horn River Shale samples was examined in order to provide more information regarding bottom water euxinia (Algeo and Tribovillard, 2009; Tribovillard et al., 2012). Three patterns of Mo-U covariation were identified in modern marine setting, and each pattern was assigned to a different depositional environment: particulate shuttle, suboxic to anoxic conditions and euxinic conditions. The enrichment factors of Mo and U for Horn River Shale samples are plotted in Fig. 2.12. Most of the samples from TSTs are plotted in the fields for anoxic and euxinic conditions, while most of the samples from RSTs are plotted in the suboxic to anoxic condition regions. Samples plotting in the euxinic fields are primarily from lower Evie Member, which is also characterized by relatively low concentration of  $Al_2O_3$

and  $\text{TiO}_2$  (Figs. 2.3, 2.4, 2.5, 2.6 and 2.7). Since reactive iron is typically associated with clay minerals, little reactive iron would have been available during deposition of the lower Evie Member, limiting the reaction of iron with  $\text{H}_2\text{S}$  to form pyrite and resulting in a build-up of  $\text{H}_2\text{S}$  in the water column.

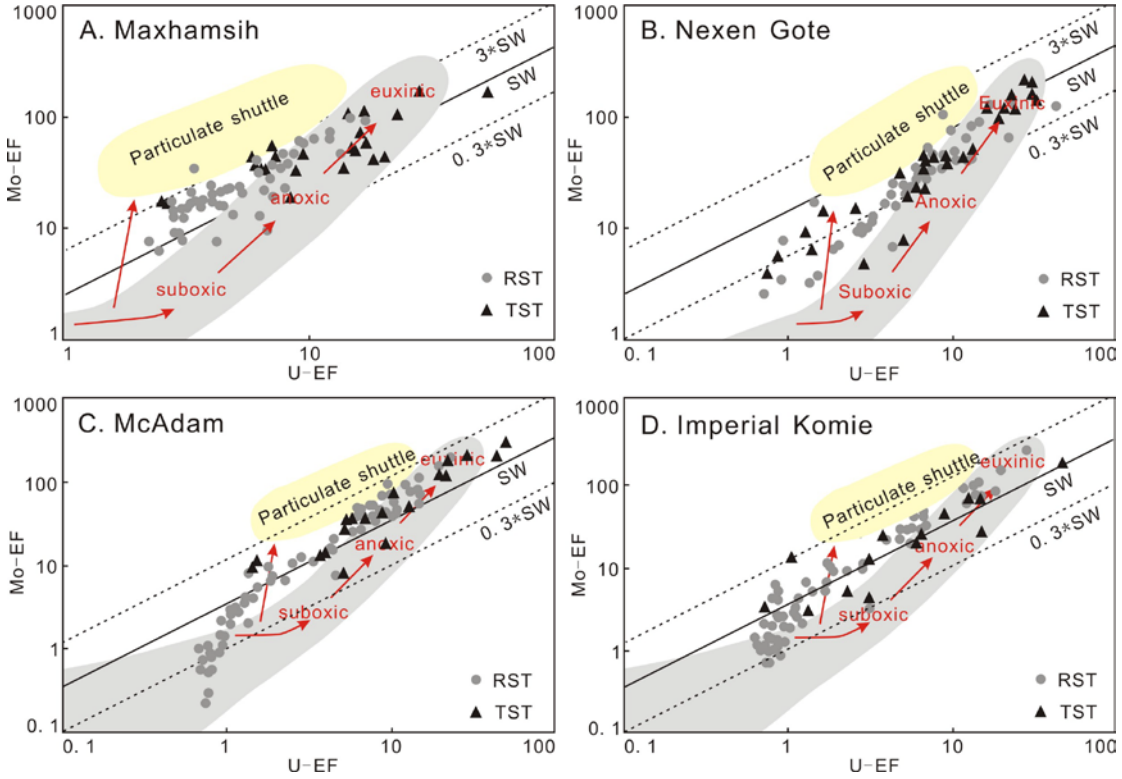


Fig. 2.12. U-EF versus Mo-EF for Horn River Shale samples (Tribovillard et al., 2012). A) Maxhamish, B) Nexen Gote, C) McAdam, and D) Imperial Komie. TST: transgressive system tract, RST: Regressive system tract. The Mo particulate shuttle is discussed in Algeo and Tribovillard, 2009.

### Productivity

We evaluate productivity by highlighting biogenic barium, phosphate, and biogenic silica, which are widely used productivity proxies (Tribovillard et al., 2006; Schoepfer et al., 2015).

Stratigraphic profiles of phosphate and biogenic barium display very different characteristics, and no systematic variation was observed. The obvious lack of correlation between biogenic Ba and TOC peaks (Figs. 2.3, 2.4, 2.5, 2.6 and 2.7) may

imply that the preservation of biogenic Ba were influenced by other environmental factors other than primary productivity, like barite dissolution due to bacterial sulfate reduction (Brumsack and Gieskes, 1983). The lack of correlation between phosphate and TOC variation suggest the remobilization of phosphate.

Ross and Bustin (2009) suggested that in the Devonian-Mississippian shales of the Western Canadian Sedimentary Basin, biogenic silica may be a useful proxy for productivity when other proxies, such as P and Ba, are solubilized and mobile. As shown in Fig. 2.11, TSTs have relatively high proportion of samples plotted along the biogenic trend than samples from RSTs, indicating higher productivity in TSTs than RSTs.

Our data suggest productivity varied across the Horn River Basin. Among the five cores, biogenic Si concentrations in Maxhamish and McAdam cores are much higher than in the Imperial Komie and Arc Snake cores, indicating the higher productivity in distal areas. This is also supported by the crossplot of Si versus Zr (Fig. 2.11). In the Arc Snake core, all samples plot along a detrital trend (Fig. 2.11E), indicating that quartz content in the proximal areas was largely influenced by detrital sedimentation. In distal parts of the basin (Figs. 2.11A, B and C), a large proportion of the samples are plotted along the biogenic trend, indicating relatively high productivity. Two models may explain this geographic variation. First, the recycling of phosphate in reducing conditions may have promoted productivity (Tribovillard et al., 2006), which would have been more pronounced in distal areas. Second, the distal Maxhamish core is closer to open ocean, which could have been a nutrient source, given the basin's position on the western margin of the North American continent during the late Devonian.

Cadmium (Cd) is considered to be delivered to marine sediment mainly in association with organic matter and is commonly regarded as an effective proxy for productivity (Morford and Emerson, 1999; Piper and Perkins, 2004, Tribovillard et al., 2006). However, the preferential accumulation of Cd in reducing conditions may limit its use as a productivity proxy (Tribovillard et al., 2006). In the Horn River data set, a close

correlation is observed between Cd and Mo, the latter controlled by redox conditions (Fig. 2.13). This indicates that Cd is more sensitive to redox conditions rather than to productivity (Russell and Morford, 2001).

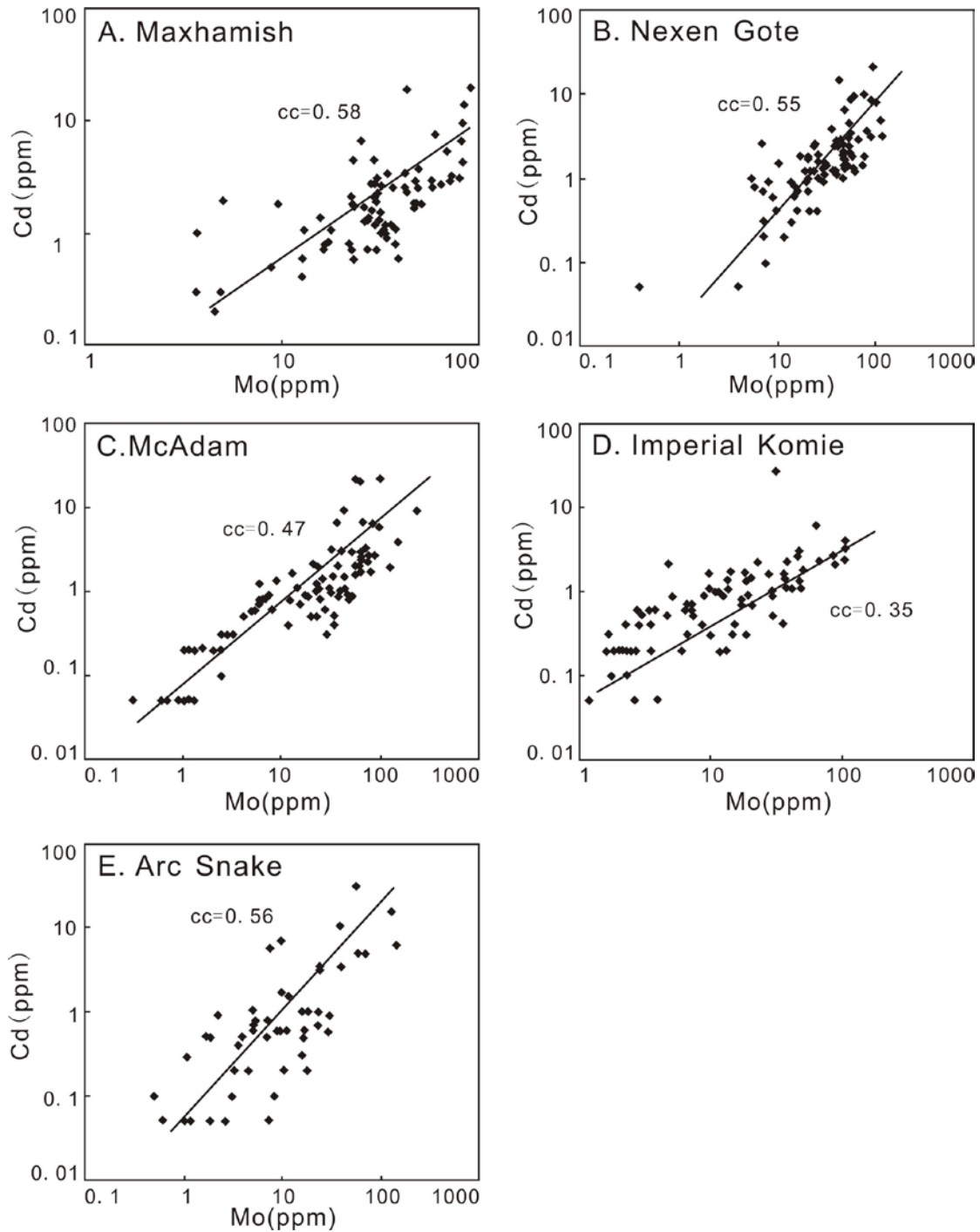


Fig. 2.13. Correlation between concentrations of Cd and Mo. A) Maxhamish, B) Nexen Gote, C) McAdam, D) Imperial Komie, and E) Arc Snake. cc: correlation coefficient.

### **2.5.2 Models for organic carbon deposition**

Primary productivity depends primarily on the availability of nutrients such as phosphate and nitrate, which can be supplied to sedimentary basins by processes such as exchange with the open marine system or upwelling, phosphate recycling in reducing conditions and fluvial input (Arthur and Sageman, 2005; Algeo and Ingall, 2007). Preservation of organic matter is largely determined by the oxygen level in the water column, which is mixed into the water column by exchange with oxygenated surface water and may be depleted through oxidation reactions with organic carbon. The effects of sedimentation rate on organic matter accumulation are complex, as neither very high nor very low rates are beneficial to organic matter deposition (Tyson, 2001; Katz, 2005). Rapid burial enhances organic matter preservation by minimizing the exposure time of organic matter to oxidation, but also dilutes the organic matter. Moderate sedimentation rate may effectively enhance the organic carbon content by minimizing oxidation without substantial dilution. In order to identify the critical triggers for organic enrichment in the Horn River Shale, the relationships between TOC contents and representative geochemical proxies for the three main factors, detrital flux, redox conditions and productivity were evaluated.

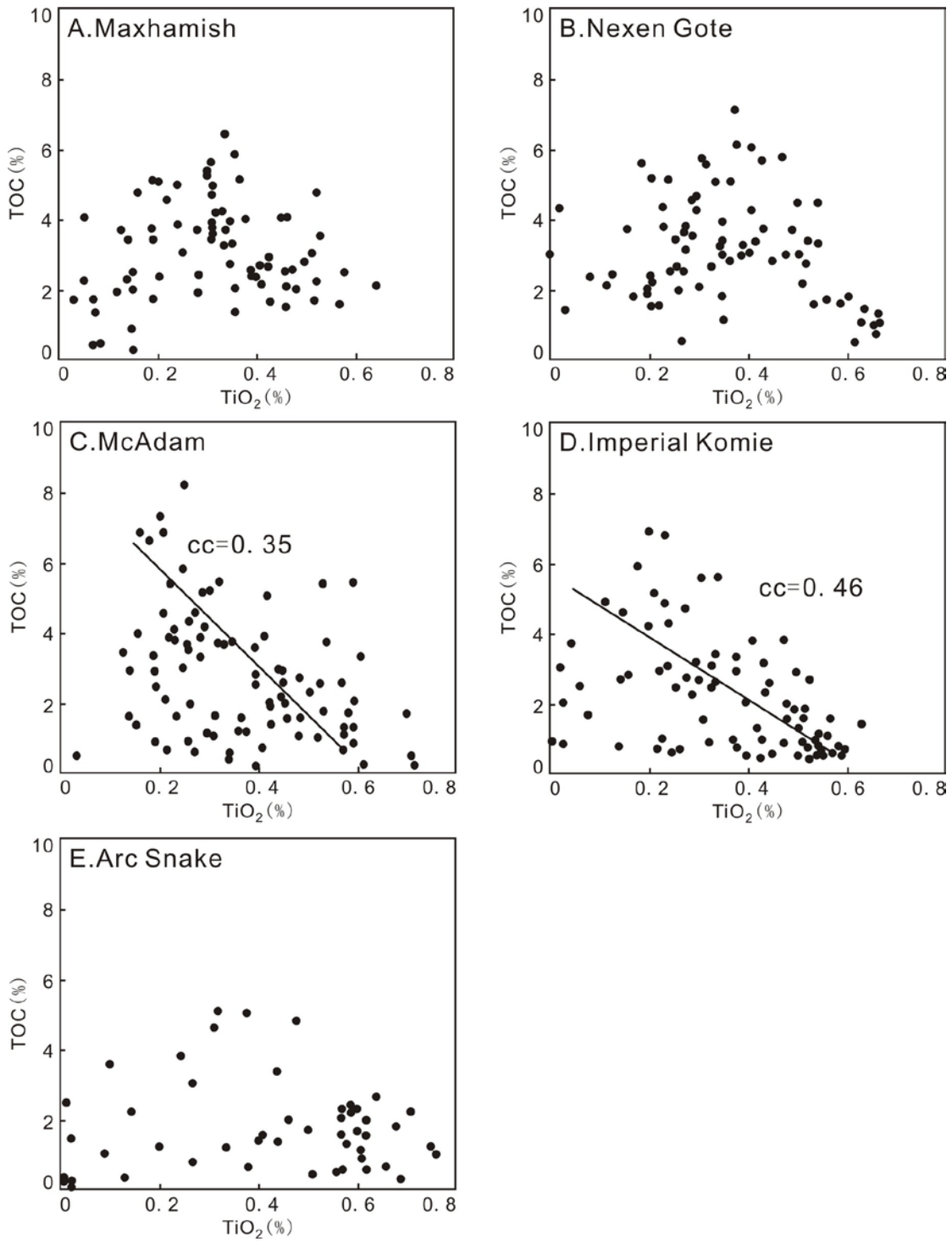


Fig. 2.14. Relationship between TOC content and proxies for detrital fluxes, TiO<sub>2</sub>. A) Maxhamish, B) Nexen Gote, C) McAdam, D) Imperial Komie, and E) Arc Snake. cc: correlation coefficient.

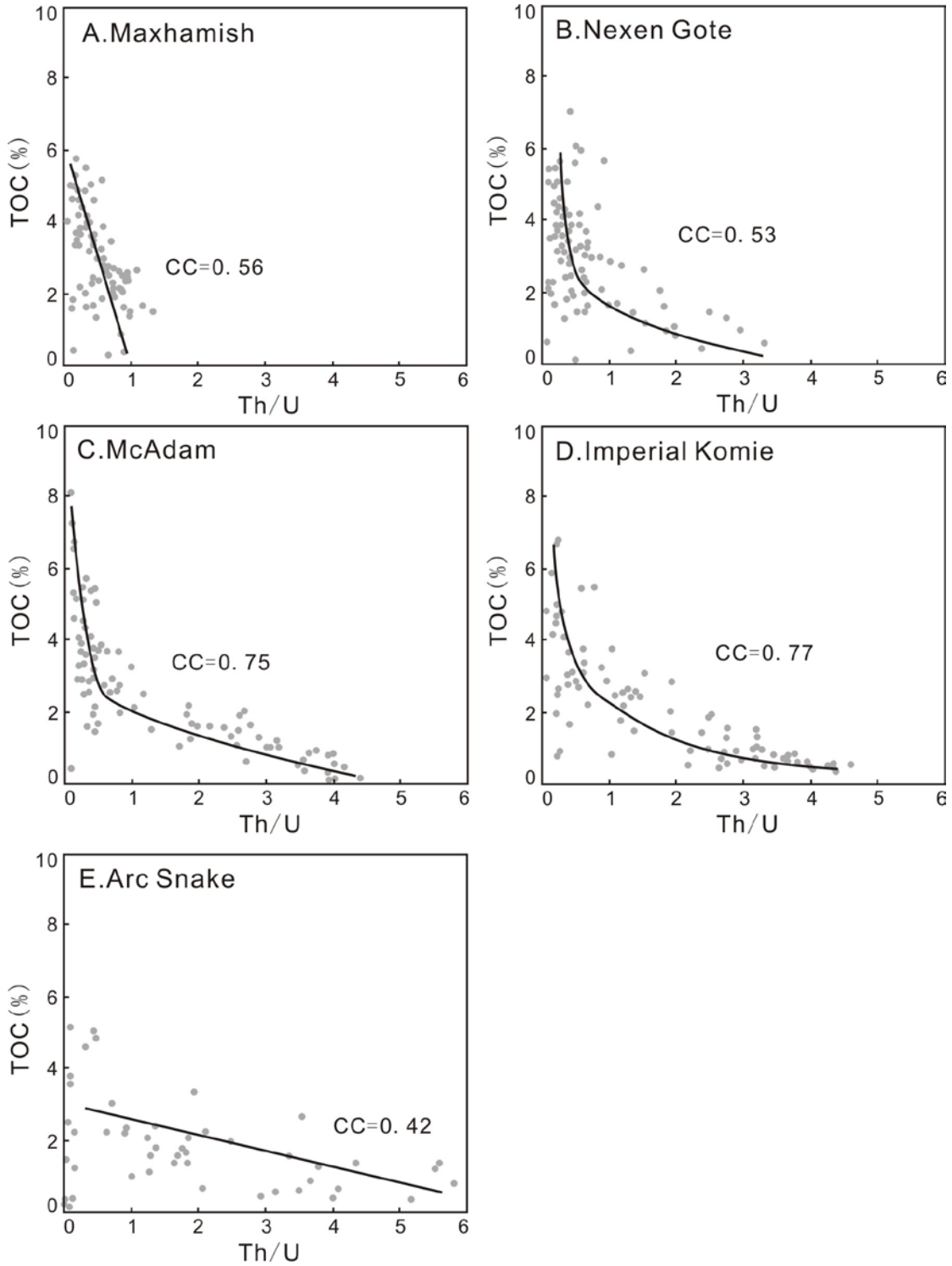


Fig. 2.15. Relationship between TOC content and proxies for redox conditions, Th/U. A) Maxhamish, B) Nexen Gote, C) McAdam, D) Imperial Komie and E) Arc Snake. CC: correlation coefficient.

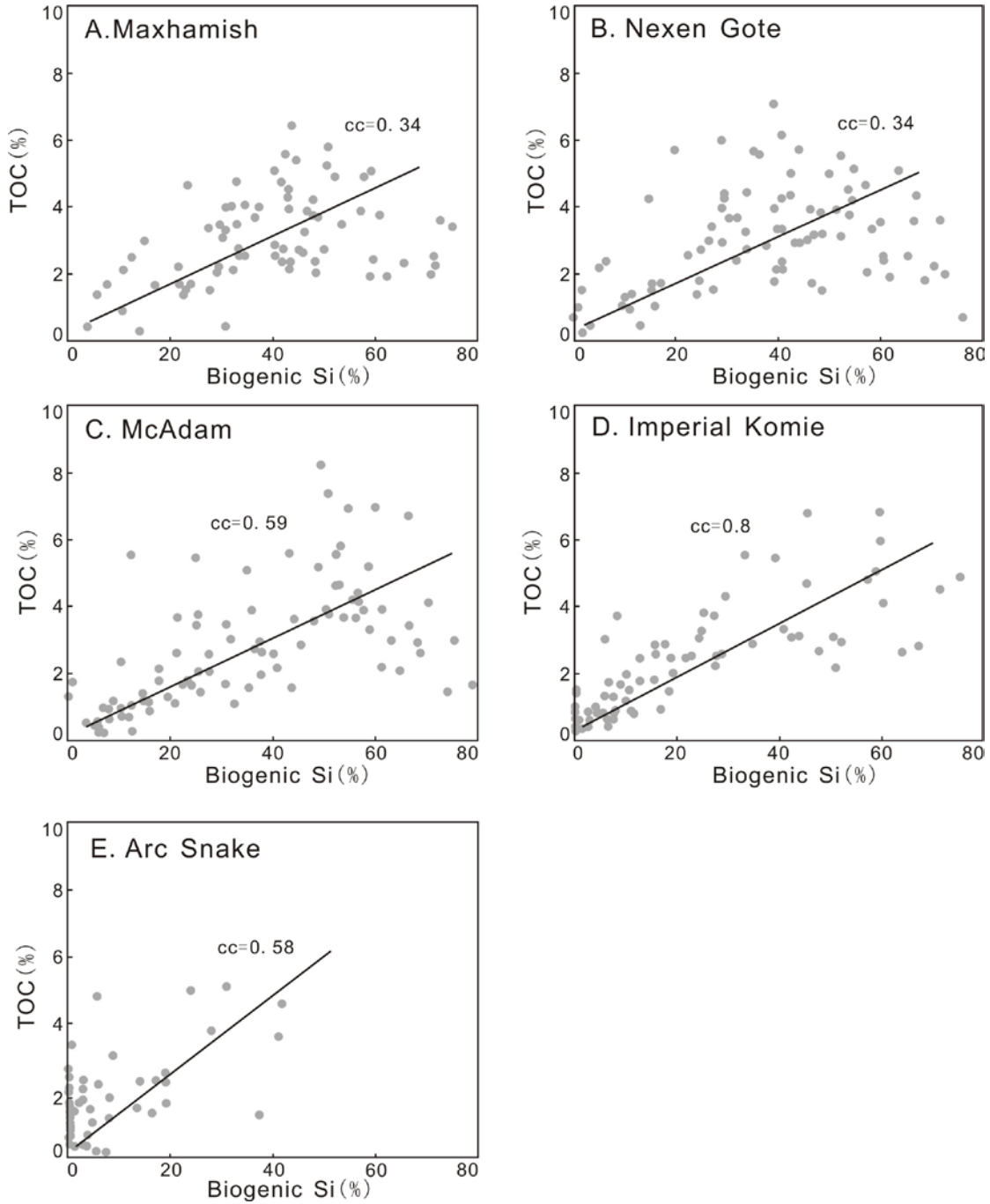


Fig. 2.16. Relationship between TOC content and proxies for productivity, biogenic silica. A) Maxhamish, B) Nexen Gote, C) McAdam, D) Imperial Komie and E) Arc Snake. cc: correlation coefficient.

TOC content shows a weak negative relationship with  $\text{TiO}_2$  (Fig. 2.14), a strong negative relationship with Th/U (Fig. 2.15), and a moderate positive relationship with

biogenic silica concentrations (Fig. 2.16). The most robust relationship is with the redox proxies (Fig. 2.15), indicating that dissolved oxygen levels were the primary control on organic matter accumulation. TOC content decreases with increasing Th/U ratios; and a distinct change in slope occurs at a Th/U ratio of 0.8, which is the cutoff between anoxic conditions and dysoxic conditions. This trend suggests moderate organic enrichment under dysoxic conditions and much stronger enrichment under anoxic conditions.

Reducing conditions were probably not the sole factor responsible for organic matter accumulation. The positive correlation between TOC and biogenic silica indicates enhancement of organic carbon content by increased productivity (Fig. 2.16). The negative correlation between TOC and titanium concentration in McAdam and Imperial Komie cores, both in a proximal location, indicate that detrital flux has negative effect on the organic carbon deposition, presumably due to dilution (Fig. 2.14).

### **2.5.3 Effect of sea level change on organic matter deposition**

A relationship between organic matter accumulation and sea level has been observed in many black shales (for example, Wignall, 1994; Algeo et al., 2004; Arthur and Sageman, 2005). Our data show stratigraphic cyclicity in TOC content, Al, Ti concentration, Th/U ratios and biogenic silica concentrations that demonstrate that the organic matter accumulation, detrital flux, redox conditions and productivity responded to eustasy in the Horn River Shale sequence.

The Evie Member is interpreted to have been deposited during a second-order high sea level stage and consists of a third-order transgressive system tract (TST1) and overlying regressive system tract (RST1). During the deposition of TST1, both TOC contents and  $Si_{bio}$  concentrations increased upward. Low  $TiO_2$  concentrations and Th/U ratios pointed to a low flux of clastic sediment and anoxic bottom water conditions during this time. Our explanation here is that a sea level rise resulted in expanded anoxic conditions by shifting chemocline upward as sea level rose and decreasing the mixing of oxygenated surface water down to the sediment-water interface. Distal areas with greater

water depth were more anoxic than proximal areas with shallow water depth. Phosphate released in reducing conditions further increased the nutrient load in the water column, as more than 90% phosphate diffuses back into the overlying water column in reducing conditions (Benitez-Nelson, 2000; Tribovillard et al., 2006). This would have promoted productivity, indicated by increased biogenic silica. Thus during deposition of T-R1, the integrated response of enhanced productivity and anoxic conditions resulting from sea level rise was favorable for enhanced organic matter accumulation. In the first regressive system tract (RST1), increased  $\text{TiO}_2$  indicates increased detrital flux. Increasing Th/U ratios recorded a gradual change from anoxic conditions in the underlying TST sediments to dysoxic or oxic bottom water conditions during RST deposition. Decreasing TOC contents during this period are attributed to the increased clastic dilution and more oxygenated conditions.

The Otter Park Member is interpreted to be deposited during the second-order sea level low stand, consisting of a third order T-R2 cycle. Variation in detrital flux and redox conditions were more complex in the T-R2 cycle than during the T-R1 cycle. Detrital flux decreased and the bottom water conditions become more anoxic during deposition of TST2. RST2 in the Nexen Gote core was characterized by relatively low detrital flux and more anoxic conditions, while the other three cores were characterized by relatively high detrital flux and more oxic conditions. This suggests that the Nexen Gote location was a bypass zone during deposition of RST2. This is supported by two lines of evidence. Firstly, the RST2 in Nexen Gote core is much thinner than the other three cores. Secondly, an interval with relatively high  $\text{TiO}_2$  and high Th/U ratio in the upper RST2 was present in the Imperial Komie and McAdam cores, but is missing in the Nexen Gote core.

At the second-order scale, Otter Park was deposited during a sea level lowstand, and the basinward shift of facies brought more detrital sediments into the basin, indicated by higher Ti concentrations in T-R2 than in T-R1. The shallow water depth resulted in more

oxygenated water column in the T-R2 cycle than the T-R1 cycle, which is suggested by the relatively high Th/U ratios in the Otter Park samples. Under oxic conditions, iron-oxyhydroxides and clays have been identified as significant factors in trapping phosphate in sediments (Tribovillard et al., 2006). If fluvial phosphate supply was the primary nutrient source in the Horn River Shale, we would expect to see relatively high phosphate concentrations in the T-R2 cycle, as we have demonstrated higher clastic influx that we assume to be fluvial in origin and oxic conditions has been documented during this period. The constant phosphate concentrations indicate that clastic input did not provide a significant nutrient supply. Increased dilution resulting from detrital flux and relatively oxidizing conditions account for the reduced TOC values in the T-R2 cycle.

The Muskwa Formation was deposited during the second-order rise in sea level and is represented by a third-order transgressive system tract (TST3) and overlying regressive system tract (RST3). The decrease upward in Al<sub>2</sub>O<sub>3</sub> and TiO<sub>2</sub> concentration indicates reduced clastic flux. Increasing Mo/Al and Ni/Co and decreasing Th/U ratios suggest that bottom water conditions evolved from oxic to anoxic. Elevated productivity was recorded in the TST3 by increasing biogenic silica concentrations (Figs. 2.3, 2.4, 2.5, 2.6 and 2.7). Remobilization of nutrients from buried organic matter, such as phosphate may lead to the enhanced productivity through nutrient recycling to overlying water column during anoxic bottom water conditions (Wallmann, 2003). This is supported by the low burial efficiency of phosphate as there is no significant increase in the phosphate concentrations with increasing TOC content (Arthur and Sageman, 2005). The opposite trend in TOC is observed in the overlying RST3 (Figs. 2.4 and 2.5), with TOC decreasing upward. In the upper part of RST3, a rapid increase in the TiO<sub>2</sub> and Th/U ratio was observed in the Nexen Gote and McAdam cores (Figs. 2.4 and 2.5), indicating a sharp transition to oxic conditions with high detrital flux.

The Middle and Upper Devonian was a time of extensive black shales deposition

(Rimmer et al., 2004). Our examination of the major and trace elements and organic matter enrichment patterns in the Horn River Shale shows both similarities and differences to other black shales. Several early studies documented relationships between stratigraphic sequences and organic carbon enrichment pattern based on studies of single cores (Algeo et al., 2004; Rimmer et al., 2004; Lash and Blood, 2014). This study of the Horn River Shale, based on detailed chemical profiles of five cores, demonstrates that the patterns of organic carbon enrichment are significantly affected by both third-order and second-order sea level fluctuations, but also that the signature of sea level cycles changes from distal to proximal parts of the basin. Generally, rising sea level favors organic matter deposition by creating sediment starvation, anoxic conditions and elevated productivity resulting from nutrient recycling under reducing conditions. Sea level change has a much stronger effect on the redox conditions variation in proximal areas than in the distal areas by comparing the Imperial Komie core and Maxhamish core, which is located in proximal and distal areas, respectively. In the Marcellus Shale in the Appalachian Basin, nutrient delivery from river input exerted a major control on organic matter accumulation and anoxia developed as a result of enhanced productivity (Arthur and Sageman, 2005; Lash and Blood, 2014). In contrast, in the Horn River Shale, organic enrichment resulted from anoxic conditions due to upward movement of the chemocline and trapping of clastic sediments in the nearshore environments during transgressions.

## **2.6. Conclusions**

Detailed examination of high resolution geochemical data of the Middle and Upper Devonian Horn River shale provides new insights into the effects of sea level change on detrital flux, redox conditions, paleoproductivity and organic matter accumulation.

(1) The Horn River Shale records three third-order transgressive and regressive cycles, which are expressed in patterns of organic carbon enrichment, major oxides and trace elements concentrations. Organic carbon is preferentially accumulated during

transgressions and is depleted during regressions, as sea level fluctuation influences key triggers, including redox conditions, detrital flux, and productivity.

(2) Detrital flux is strongly affected by sea level change, relatively low in the transgressive system tract comparing to regressive system tract. Fluxes vary geographically and are significantly higher in proximal areas, so the geographic variation in detrital flux could provide insights into sediment source. Both detrital silica and biogenic silica are present in Horn River Shale, shown by Zr and Si concentrations.

(3) Redox conditions significantly vary during T-R cycles, more reducing during transgressions than regressions. The concentrations of redox-sensitive elements in the five long cores indicate that redox conditions also vary geographically, more reducing conditions in distal areas than in proximal areas. Redox events, expressed by trace element ratios, may be a tool for chronostratigraphic correlation in other black shales.

(4) The application of barium and phosphate concentrations as productivity proxies may be problematic due to the remobilization and remineralization processes. However biogenic silica concentrations may be useful as proxies for productivity.

(5) Although organic matter accumulation in Horn River Shale was the combined product of detrital flux, redox conditions and productivity, we conclude that redox conditions were the primary control on the organic carbon deposition and preservation, because redox proxies are more strongly correlated to TOC than proxies for detrital flux or bioproductivity.

## **Acknowledgements**

We thank the British Columbia Ministry of Energy and Mines in Victoria for the access to core data and well files. We also thank the BC Oil and Gas Commission for access to cores. We are grateful for the funding support from NSERC (grant CRDPJ 445064 – 12) and co-funders ConocoPhillips Canada, Devon Canada, Husky Energy, Imperial, Nexen-CNOOC, and Shell Canada.

## 2.7 References:

- Algeo, T.J., Ingall, E., 2007. Sedimentary C<sub>org</sub>:P ratios, paleovean ventilation, and Phanerozoic atmospheric pO<sub>2</sub>. *Palaeogeography, Palaeoclimatology, Palaeoecology* 256, 130-155.
- Algeo, T.J., Kuwahara, K., Sano, H., Bates, S., Lyons, T., Elswick, E., Hinnov, L., Ellwood, B., Moser, J., Maynard, J.B., 2011. Spatial variation in sediment fluxes, redox conditions, and productivity in the Permian-Triassic Panthalassic Ocean. *Palaeogeography, Palaeoclimatology, Palaeoecology* 308, 65-83.
- Algeo, T.J., Maynard, J.B., 2004. Trace element behavior and redox facies analysis of core shales of Upper Pennsylvanian Kansas-type cyclotherms. *Chemical Geology* 206, 289-318.
- Algeo, T.J., Schwark, L., Hower, J.C., 2004. High-resolution geochemistry and sequence stratigraphy of the Hushpuckney Shale (Swope Formation, eastern Kansas): implications for climato-environmental dynamics of the Late Pennsylvanian Midcontinent Seaway. *Chemical Geology* 206, 259-288.
- Algeo, T.J., Tribovillard, N., 2009. Environmental analysis of paleoceanographic systems based on molybdenum-uranium covariation. *Chemical Geology* 268, 211-225.
- Anderson, L.D., Delaney, M.L., 2005. Use of multiproxy records on the Agulhas Ridge, Southern Ocean (Ocean Drilling Project Leg 177, Site 1090) to investigate sub-Antarctic hydrography from the Oligocene to the early Miocene. *Paleoceanography* 20, PA3011, 16p.
- Anderson, R.F., Fleisher, M.Q., LeHuray, A.P., 1989. Concentration, oxidation state, and particular flux of uranium in the Black Sea. *Geochimica et Cosmochimica Acta* 53, 2215-2224.
- Arthur, M.A., Sageman, B.B., 1994. Marine black shales: Depositional mechanisms and environments of ancient deposits. *Annual Review of Earth and Planetary Sciences* 22, 499-551.

- Arthur, M.A. and Sageman, B.B., 2005. Sea-level control on source-rock development: perspectives from the Holocene Black Sea, the mid-Cretaceous Western Interior Basin of North America, and the late Devonian Appalachian Basin, in Harris, N.B., ed., *The deposition of Organic-Carbon-Rich Sediments: Models, Mechanisms, and Consequences*. SEPM Special Publication 82, 35-59.
- B.C. Ministry of Energy and Mines, 2011. Ultimate potential for unconventional natural gas in northeastern British Columbia's Horn River Basin. *Oil and Gas Reports*, May 2011 (50 pp).
- Benitez-Nelson, C.R., 2000. The biogeochemical cycling of phosphorus in marine systems. *Earth Science Review* 51, 109-135.
- Berner, R.A., Raiswell, R., 1983. Burial of organic carbon and pyrite sulfur in sediments over Phanerozoic time: a new theory. *Geochimica et Cosmochimica Acta* 47, 855-862.
- Bohacs, K.M., Grabowski, G.J., Carroll, A.R., Mankiewicz, P.J., Gerhardt, K.J., Schwalbach, J.R., Wegner, M.B., Simo, J.A., 2005. Production, destruction, and dilution – the many paths to source rock development, in Harris, N.B., ed., *The deposition of Organic-Carbon-Rich Sediments: Models, Mechanisms, and Consequences*. SEPM Special Publication 82, 61-101.
- Bonn, W.J., Gingle, F.X., Grobe, H., Mackensen, A., Fütterer, D.K., 1998. Palaeoproductivity at the Antarctic continental margin: opal and barium records for the last 400 ka. *Paleogeography, Paleoclimatology, Paleoecology* 139, 195-211.
- Brumsack, H.J., 2006. The trace metal content of recent organic carbon-rich sediments: Implications for Cretaceous black shale formation. *Paleogeography, Paleoclimatology, Paleoecology* 232, 344-361.
- Brumsack, H.J., Gieskes, J.M., 1983. Interstitial water trace-metal chemistry of laminated sediments from the Gulf of California, Mexico. *Marine Chemistry* 14, 89-106.

- Calvert, S.E., Bustin, R.M., Ingall, E.D., 1996. Influence of water column anoxia and sediment supply on the burial and preservation of organic carbon in marine shales. *Geochimica et Cosmochimica Acta* 60, 1577-1593.
- Calvert, S.E., Pedersen, T.F., 1993. Geochemistry of recent oxic and anoxic marine sediments: implications for the geological record. *Marine Geology* 113, 67-88.
- Caplan, M.L., Bustin, R.M., 1998. Paleooceanographic controls on geochemical characteristics of organic-rich Exshaw mudrocks: role of enhanced primary productivity. *Organic Geochemistry* 30, 161-188.
- Chalmers, G.R.L., Ross, D.J.K., Bustin, R.M., 2012. Geological controls on matrix permeability of Devonian gas shales in the Horn River and Liard basins, northeast British Columbia, Canada. *International Journal of Coal Geology* 103, 120-131.
- Creaney, S., Passey, Q.R., 1993. Recurring patterns of total organic carbon and source rock quality within a sequence stratigraphic framework. *AAPG Bulletin* 77, 386-401.
- Dean, W.E., Arthur, M.A., 1989. Iron-sulfur-carbon relationships in organic-carbon-rich sequences: I . Cretaceous W  
708-743.
- Demaison, G.J., Moore, G.T., 1980. Anoxic environments and oil source bed genesis. *AAPG Bulletin* 64, 1179-1209.
- Dong, T., Harris, N. B., 2013. Pore size distribution and morphology in the Horn River shale, Middle and Upper Devonian, northeastern British Columbia, Canada, in W. Camp, E. Diaz and B. Wawak, eds., *Electron microscopy of shale hydrocarbon reservoirs*. *AAPG Memoir* 102, 67-79.
- Dong, T., N.B., Harris, K., Ayranci, C.E., Twemlow, B.R., Nassichuk, 2015. Porosity characteristics of the Devonian Horn River shale, Canada: Insights from lithofacies classification and shale composition. *International Journal of Coal Geology* 141-142, 74-90.
- Dymond, J., Suess, E., Lyle, M., 1992. Barium in deep-sea sediment: a geochemical

- proxy for paleoproductivity. *Paleoceanography* 7, 163-181.
- Ferri, F., Hickin, A.S., Huntley, D.H., 2011. Besa River formation, western Liard Basin, British Columbia (NTS 094N): geochemistry and regional correlations; in *Geoscience Reports 2011*, British Columbia Ministry of Energy, Mines and Natural Gas, 1-18.
- Harris, N.B., Freeman, K.H., Pancost, R.D., White, T.S., Mitchell, G.D., 2004. The character and origin of lacustrine source rocks in the Lower Cretaceous synrift section, Congo Basin, west Africa. *AAPG Bulletin* 88, 1163-1184.
- Harris, N.B., Mnich, C.A., Selby, D., Korn, D., 2013. Minor and trace element and Re-Os chemistry of the Upper Devonian Woodford Shale, Permian Basin, west Texas: insights into metal abundance and basin processes. *Chemical Geology* 356, 76-93.
- Hay, W.W., 1995. Paleooceanography of marine organic-carbon-rich sediments, in Huc, A.Y., ed., *Paleogeography, Paleoclimate, and Source rocks*. American Association of Petroleum Geologists, *Studies in Geology* 40, 21-59.
- Hemmesch, N.T., Harris, N.B., Mnich, C.A., Selby, D., 2014. A sequence-stratigraphic framework for the Upper Devonian Woodford Shale, Permian Basin, west Texas. *AAPG Bulletin* 98, 23-47.
- Hulsey, K.M., 2011. Lithofacies characterization and sequence stratigraphic framework for some gas-bearing shale within the Horn River Basin, northeastern British Columbia. Master thesis, University of Oklahoma, 76p.
- Jones, B., Manning, D.A.C., 1994. Comparison of geochemical indices used for the interpretation of palaeoredox conditions in ancient mudstones. *Chemical Geology* 111, 111-129.
- Jørgensen, B.B., 1982. Mineralization of organic matter in the sea bed—the role of sulphate reduction. *Nature* 296, 643-645.
- Katz, B., 2005. Controlling factors on source rock development – a review of productivity, preservation, and sedimentation rate, in Harris, N.B., ed., *The*

- Deposition of Organic-Carbon-Rich Sediments: Models, Mechanisms, and Consequences. SEPM Special Publication 82, 35-59.
- Lash, G.G., Blood, D.R., 2014. Organic matter accumulation, redox, and diagenetic history of the Marcellus Formation, southwestern Pennsylvania, Appalachian Basin. *Marine and Petroleum Geology* 57, 244-263.
- Lewan, M.D., Maynard, J.B., 1982. Factors controlling enrichment of vanadium and nickel in the bitumen of organic sedimentary rocks. *Geochim. Cosmochim. Acta* 46, 2547-2560.
- Lyons, T.W., Werne, J.P., Hollander, D.J., Murray, R.W., 2003. Contrasting sulfur geochemistry and Fe/Al and Mo/Al ratios across the last oxic-anoxic transition in the Cariaco Basin, Venezuela. *Chemical Geology* 195, 131-157.
- Macquaker, J.H.S., Taylor, K.G., Gawthorpe, R.L., 2007. High-resolution facies analyses of mudstones: implications for paleoenvironmental and sequence stratigraphic interpretations of offshore ancient mud-dominated successions. *Journal of Sedimentary Research* 77, 324-339.
- McManus, J., Berelson, W.M., Klinkhammer, G.P., Johnson, K.S., Coale, K.H., Anderson, R.F., Kumar, N., Burdige, D.J., Hammond, D.E., Brumsack, H.J., McCorkle, D.C., Rushdi, A., 1998. Geochemistry of barium in marine sediments: implications for its use as a paleoproxy. *Geochimica et Cosmochimica Acta* 62, 3453-3473.
- Moore, P.E., 1989. The Kaskaskia Sequence: reefs, platforms, and foredeeps The lower Kaskaskia sequence- Devonian, Western Canada Sedimentary Basin, a case history: Canadian Society of Petroleum Geologist, Special Publication 30, 139-164.
- Mort, H., Jacquat, O., Adatte, T., Steinmann, P., Föllmi, K., Matera, V., Berner, Z., Stüben, D., 2007. The Cenomanian/Turonian anoxic event at the Bonarelli Level in Italy and Spain: enhanced productivity and/or better preservation? *Cretaceous Research* 28, 597-612.
- McPhail, S., W. Walsh, C. Lee and P. A. Monahan, 2008. Shale units of the Horn River

- formation, Horn River basin and Cordova Embayment, Northeastern British Columbia: (abs.), Canadian Society of Petroleum Geologists and Canadian Well Logging Society Convention, 14 p.
- Moore, P.F., 1989. The Kaskaskia Sequence: Reefs, Platforms, and Foredeeps, *in* Ricketts, B.D., eds., The Lower Kaskaskia Sequence-Devonian, Western Canada Sedimentary Basin, a Case History. Canadian Society of Petroleum Geologist, Special Publication 30, 139-164.
- Morford, J.L., Emerson, S., 1999. The geochemistry of redox sensitive trace metals in sediments. *Geochim. Cosmochim. Acta* 63, 1735-1750.
- Mossop, G.D., Shetsen, I., 1994. Geological atlas of the Western Canada Sedimentary Basin, Canadian Society of Petroleum Geologists and Alberta Research Council, Special Report 4.
- Parrish, J. T., 1995. Paleogeography of C<sub>org</sub>-rich rocks and the preservation versus production controversy, in Huc, A.Y., ed., Paleogeography, Paleoclimate, and Source rocks. American Association of Petroleum Geologists, Studies in Geology 40, 1-20.
- Pedersen, T.F., Calvert, S.E., 1990. Anoxia VS. Productivity: What controls the formation of organic-carbon-rich sediments and sedimentary rocks? American Association of Petroleum Geology Bulletin 74, 454-466.
- Piper, D.Z., Perkins, R.B., 2004. A modern vs. Permian black shale- the hydrography, primary productivity, and water-column chemistry of deposition. *Chemical Geology* 206, 177-197.
- Potma, K., Jonk, R., Davie, M., Austin, N., 2012. A mudstone lithofacies classification of the Horn River Group: integrated stratigraphic analysis and inversion from wireline log and seismic data. 6<sup>th</sup> BC Unconventional Gas Technical Forum, Vancouver, Canada, 26p.
- Raiswell, R., Berner, R. A., 1987. Organic carbon losses during burial and thermal maturation of normal marine shales. *Geology* 15, 853-856.

- Reynolds, M.M., Munn, D.L., 2010. Development update for an emerging shale gas giant field-Horn River Basin, British Columbia, Canada. SPE Unconventional Gas Conference, Pittsburgh, USA, Feb 23-25. SPE Paper 130103, 17p.
- Rimmer, S. M., Thompson, J. A., Goodnight, S. A., Robl, 2004. Multiple controls on the preservation of organic matter in Devonian-Mississippian marine black shales: geochemical and petrographic evidence. *Palaeogeography, Palaeoclimatology, Palaeoecology* 215, 125-154.
- Ross, D. J. K., and R. M. Bustin, 2008. Characterizing the shale gas resource potential of Devonian-Mississippian strata in the western Canada sedimentary basin: Application of an integrated formation evaluation. *AAPG Bulletin*, v.92, p. 87-125.
- Ross, D. J. K., and Bustin, R. M., 2009. Investigating the use of sedimentary geochemical proxies for paleoenvironment interpretation of thermally mature organic-rich strata: examples from the Devonian-Mississippian shales, Western Canadian Sedimentary Basin. *Chemical Geology* 260, p. 1-19.
- Russell, A.D., Morford, J.L., 2001. The behaviour of redox-sensitive metals across a laminated-massive-laminated transition in Saanich Inlet, British Columbia. *Marine Geology* 174, 341-354.
- Sageman, B.B., Lyons, T.W., 2004. Geochemistry of fine-grained sediments and sedimentary rocks, In: Mackenzie, F. eds, *Treatise on Geochemistry* 7, 115-158.
- Sageman, B.B., Murphy, A.E., Werne, J.P., Ver Straeten, C.A., Hollander, D.J., Lyons, T.W., 2003. A tale of shales: the relative roles of production, decomposition, and dilution in the accumulation of organic-rich strata, Middle-Upper Devonian, Appalachian basin. *Chemical Geology* 195, 229-273.
- Schenau, S.J., Reichart, G.J., De Lange, G.J., 2005. Phosphorus burial as a function of paleoproductivity and redox conditions in Arabian Sea sediments. *Geochim. Cosmochim. Acta* 69, 919-931.
- Schieber, J., 1998. Developing a sequence stratigraphic framework for the Late Devonian

- Chattanooga Shale of the southeastern US: relevance for the Bakken Shales, in Christopher, J. E., Gilboy, C. F., Paterson, D. F., Bend, S. L., ed. Eighth International Williston Basin Symposium. Saskatchewan Geological Society, Special Publication 13, 58–68.
- Schieber, J., Krinsley, D., Riciputi, L., 2000. Diagenetic origin of quartz silt in mudstones and implications for silica cycling. *Nature* 406, 981-985.
- Schoepfer, S.D., Shen, J., Weil, H.Y., Tyson, R.V., Ingall, E., Algeo, T.J., 2015. Total organic carbon, organic phosphorus, and biogenic barium fluxes as proxies for paleomarine productivity. *Earth-Science Reviews* 149, 23-52.
- Schroeder, J.O., Murray, R.W., Leinen, M., Pflaum., R.C., Janecek, T.R., 1997. Barium in equatorial Pacific carbonate sediments: terrigenous, oxide, and biogenic associations. *Paleoceanography* 12, 125-146.
- Shen, J., Schoepfer, S.D., Feng, Q.L., Zhou, L., Yu, J.X., Song, H.Y., Wei, H.Y., Algeo, T.J., 2015. Marine productivity changes during the end-Permian crisis and Early Triassic recovery. *Earth-Science Reviews* 149, 136-162.
- Taylor, S.R., McLennan, S.M., 1985. *The Continental Crust: Its Composition and Evolution*. Blackwell, Oxford, 312 p.
- Tribovillard, N. P., Desprairies, A., Lallier-Verges, E., Bertrand, P., Moureau, N., Ramdani, A., Ramanampisoa, L., 1994. Geochemical study of organic-matter rich cycles from the Kimmeridge Clay Formation of Yorkshire (UK): productivity versus anoxia. *Palaeogeography, Palaeoclimatology, Palaeoecology* 108, 165-181.
- Tribovillard, N., Algeo, T. J., Lyons, T., Riboulleau, A., 2006. Trace metals as paleoredox and paleoproductivity proxies: an update. *Chemical Geology* 232, 12-32.
- Tribovillard, N., Algeo, T. J., Riboulleau, A., 2012. Analysis of marine environmental conditions based on molybdenum-uranium covariation-Applications to Mesozoic paleoceanography. *Chemical Geology* 324-325, 46-58.
- Tyson, R.V., 2001. Sedimentation rate, dilution, preservation, and total organic carbon:

- some results of a modelling study. *Organic Geochemistry* 32, 333-339.
- Tyson, R. V., 2005. The “productivity versus preservation” controversy: cause, flaws, and resolution. *SEPM Special Publication* 82, 17-33.
- Tyson, R.V., Pearson, T.H., 1991. Modern and ancient continental shelf anoxia: an overview, *in* Tyson, R.V., and Pearson, T.H., eds., *Modern and Ancient Continental Shelf Anoxia*. Geological Society of London, Special Publications 58, 1-24.
- Ver Straeten, C. A., Brett, C. E., Sageman, B. B., 2011. Mudrock sequence stratigraphy: a multi-proxy (sedimentological, paleobiological and geochemical) approach, Devonian Appalachian Basin. *Palaeogeography, Palaeoclimatology, Palaeoecology* 304, 54-73.
- Wallmann, K., 2003. Feedbacks between oceanic redox states and marine productivity: A model perspective focused on benthic phosphorus cycling. *Global Biogeochemical Cycles* 17, 1084, <http://dx.doi.org/10.1029/2002GB001968>.
- Wei, H.Y., Chen, D.Z., Wang, J.G., Yu, H., Tucker, M.E., 2012. Organic accumulation in the lower Chihhsia Formation (Middle Permian) of South China: Constraints from pyrite morphology and multiple geochemical proxies. *Palaeogeography, Palaeoclimatology, Palaeoecology* 353, 73-86.
- Wedephol, K. H., 1971. Environmental influences on the chemical composition of shales and clays. In: Ahrens, L. H., Press, F., Runcorn, S. K., Urey, H. C. (Eds.), *Physics and Chemistry of the Earth*. Pergamon, Oxford, pp. 305-333.
- Weldeab, S., Emeis, K.C., Hemleben, C., Schmiedl, G., Schulz, H., 2003. Spatial productivity variations during formation of sapropels S5 and S6 in the Mediterranean Sea: evidence from Ba contents. *Palaeogeography, Palaeoclimatology, Palaeoecology* 191, 169-190.
- Wignall, P.B., 1994. *Black Shales*: Oxford, U.K., Clarendon, 127p.
- Wignall, P. B., Twitchett, R. J., 1996. Oceanic anoxia and the end Permian mass extinction. *Science* 272, 1155-1158.

- Wright, A. M., Spain, D., Ratcliffe, K. T., 2010, Application of inorganic whole rock geochemistry to shale resource plays: SPE Paper 137946, SPE Canadian Unconventional Resources and International Petroleum Conference, Calgary, 18p.
- Xiong, Z.F., Li, T.G., Algeo, T., Nan, Q.Y., Zhai, B., Lu, B., 2012. Paleoproductivity and paleoredox conditions during late Pleistocene accumulation of laminated diatom mats in the tropical West Pacific. *Chemical Geology* 334, 77-91.
- Yan, D.T., Wang, H., Fu, Q.L., Chen, Z.H., He, J., Gao, Z., 2015. Organic matter accumulation of Late Ordovician sediments in North Guizhou Province, China: Sulfur isotope and trace element evidences. *Marine and Petroleum Geology* 59, 348-358.
- Zahrani, A. A., 2011, Interpretation of 3D multicomponent seismic data for investigating natural fractures in the Horn River Basin, northeast British Columbia: Master thesis, University of Calgary, 118p.
- Zhou, L., Algeo, T.J., Shen, J., Hu, Z.F., Gong, H.M., Xie, S.C., Huang, J.H., Gao, S., 2015. Changes in marine productivity and redox conditions during the Late Ordovician Hirnantian glaciation. *Palaeogeography, Palaeoclimatology, Palaeoecology* 420, 223-234.

## **CHAPTER 3 Porosity characteristics of the Devonian Horn River shale, Canada: Insights from lithofacies classification and shale composition to porosity and pore structure**

### **Abstract:**

This study evaluates pore systems of the Horn River Shale in Western Canada Sedimentary Basin from lithofacies classification of core samples to micro-scale pore structure investigation. Samples from the Middle and Upper Devonian Horn River shale sequence were examined by core description, porosity measurement, SEM, and TEM imaging of ion milled samples, and nitrogen adsorption analysis in order to develop a better understanding of the controls of organic and inorganic rock constituents on porosity development and pore microstructure.

Five primary shale lithofacies were identified by hand-core and thin section analyses: massive mudstones, massive mudstones with pyrite streaks, laminated mudstones, bioturbated mudstones and carbonates. Measured porosity ranges from 0.62% to 12.04% and shows wide variation between different lithofacies. Massive mudstones and pyritic mudstones with high total organic carbon (TOC) content have the highest porosity, whereas bioturbated mudstones and carbonates with low TOC content have the lowest porosity. SEM and TEM images suggest that several kinds of sites for porosity development are present, including organic matter, pyrite framboids, clay platelets, quartz rims, carbonate grains and microfractures. A general positive relationship between TOC and porosity indicates that a large proportion of pores are developed in organic matter. Results from the nitrogen adsorption analysis suggest that samples with more organic matter tend to develop smaller pores. Thus while porosity development is a combined function of organic matter, mineral components, fabric and fractures, it is most affected by organic matter concentration.

The Muskwa Formation and the Evie Member have more gas storage capacity as

they primarily consists of massive mudstones and pyrite-rich mudstones, showing the best porosity. The Otter Park Member has lower porosity, which may relate to the fact that its lithofacies mainly consists of laminated mudstones and bioturbated mudstones.

### **3.1. Introduction**

Shales or mudstones are fine-grained sedimentary rocks with a dominant grain size less than 63 microns (Schieber, 1998). Due to recent advances in horizontal drilling and hydraulic fracturing techniques, oil and gas are now economically produced from shale reservoirs (Curtis, 2002; Jarvie et al., 2007; Hao et al., 2013) that were previously considered only as source rock and seals for conventional oil and gas reservoirs. Shale reservoirs are typically characterized by low porosities ranging from 3.1 to 11.7%, and unlike conventional reservoirs, which usually have micron scale pores (Nelson, 2009; Curtis et al., 2012), pore sizes in the nanometer range (Loucks et al., 2009; Curtis et al., 2010, 2012) and extremely low permeabilities ranging from  $2.4 \times 10^{-1}$  nanodarcies to  $1.6 \times 10^2$  nanodarcies (Yang and Aplin, 2007). Natural gas is stored in three forms: free gas in pores and fractures, gas adsorbed to the surface of organic matter and inorganic composition, and dissolved gas in water, oil and bitumen (Curtis, 2002). Porosity and pore structure are the most significant factors controlling gas storage capacity and deliverability. Understanding factors controlling shale storage capacity and investigating the pore structure are of great significance for successful evaluation and exploitation of shale oil and gas reservoirs.

Two fundamentally different approaches have been applied to elucidate the complex pore systems of shales. Direct imaging methods, including scanning electron microscopy (SEM) and transmission electron microscopy (TEM) imaging methods, combined with focused ion milling techniques, provide information on pore size, pore morphology, sites for pore development and connectivity between pore networks. Indirect methods, such as helium porosimetry, mercury injection capillary pressure, nuclear magnetic resonance

spectroscopy and nitrogen adsorption, provide an estimation of bulk properties of a sample, including porosity, pore size and morphology (Wang and Reed, 2009; Sondergeld et al., 2010; Milner et al., 2010; Curtis et al., 2011; Curtis et al., 2012; Dong and Harris, 2013).

Early investigations of pore systems in shale samples from Mississippian Barnett Shale that applied scanning electron microscopy to Ar-ion-beam milled samples showed that pore size are dominantly nanometer in scale (Loucks et al., 2009). Several modes of porosity development have been identified in both Barnett and Woodford Shales: associated with organic matter, floccules, porous fecal pellets, preserved fossil fragments and various minerals such as pyrite framboids, microchannels, and microfractures (Schieber, 2010; Slatt and O'Brien, 2011). Although a variety of pore shapes and origins have been described in mudrocks (Loucks et al., 2009; Passey et al., 2010), three primary classes of pores within shales are proposed: interparticle mineral pores, intraparticle mineral pores and intra-organic matter pores (Loucks et al., 2012). Porosity in shale successions is thought to be a direct outcome of depositional and diagenetic processes (Schieber, 2010, Jennings and Antia, 2013), depending on organic matter concentration, mineralogy, fabric, texture and microfractures and burial diagenesis (Loucks et al., 2012). Depositional environments significantly control shale fabric and mineralogical composition such as lamination, organic matter concentration, clay, quartz, and carbonate content, while diagenetic processes alter that fabric and composition. Although the geochemical controls on shale microstructure have been discussed (Valenza II et al., 2013), there has been little research on how to combine mudstone lithofacies analysis with petrophysical properties, a major focus of our research. Two significant exceptions are Slatt and O'Brien, 2013 and Dong and Harris, 2013.

The Horn River shale sequence is now an important shale gas resource in the Western Canada Sedimentary Basin (Ross and Bustin, 2008; Reynolds and Munn, 2010). It is reported that the Horn River Basin has very large gas reserves, with a medium case

estimate for marketable natural gas of 78 TCF (B.C. Ministry of Energy and Mines, 2011). The recoverable gas is sweet and dry, averaging 89% methane, 10% CO<sub>2</sub> and trace amounts of ethane and heavier hydrocarbon components (B.C. Oil and Gas Commission, 2014). Production in the Horn River Basin has steadily increased since 2007, due to the application of horizontal drilling combined with multi-stage hydraulic fracturing. Little has been published on the reservoir properties of this gas shale. The major objectives of this article are to (1) identify classes of mudstone that generally have different composition and reservoir properties; (2) examine the relationship between mudstone composition and porosity; (3) investigate the pore microstructures such as pore morphology, pore size distribution and sites for pore development; and (4) identify units within the Horn River shale with the highest porosity.

### **3.2. Geological Setting**

The Horn River basin occupies nearly 12,000 km<sup>2</sup> in northeastern British Columbia, Canada (Fig. 3.1). It is bounded on the east by Slave Point carbonate platform, separating it from Cordova Embayment, on the south by Presqu'île Barrier and on the west by Bovie Fault zone, a fault with displacement reaching a maximum of 1200 m, separating it from Liard Basin (Ross and Bustin, 2008).

Our study focuses on the Horn River shale sequence, which comprises the Evie and Otter Park Members of the Horn River Formation and the Muskwa Formation (Fig. 3.2) (Ferri et al., 2011). These formations are considered to range in age from late Eifelian (approximately 393 Ma) to early Frasnian stage (approximately 383 Ma) (Oldale, 1994). The Evie Member, which is a dark grey to black, calcareous mudstone, overlies the shallow marine carbonates of the Lower Keg River Formation (McPhail et al., 2008). It is characterized by moderate to high gamma ray readings and high resistivity on well logs. This unit is at its thickest in the eastern part of the basin and generally thins westward towards the Bovie Fault structure (B.C. Oil and Gas Commission, 2014). The

Otter Park Member is generally described as a grey to dark grey, pyritic, non-calcareous to calcareous, siliceous shale that becomes less calcareous and more siliceous upward. This interval is low in total organic content in comparison to the Evie Member and the Muskwa Formation (McPhail et al., 2008). The Muskwa Formation is generally dark grey to black, organic-rich, siliceous and non-calcareous and is characterized by high gamma ray values and high organic carbon content (McPhail et al., 2008; Zahrani, 2011). Generally, the Muskwa Formation thickens westward to the Bovie Fault structure and thins eastward into Alberta, stratigraphically equivalent to the Duvernay Shale (B.C. Oil and Gas Commission, 2014).

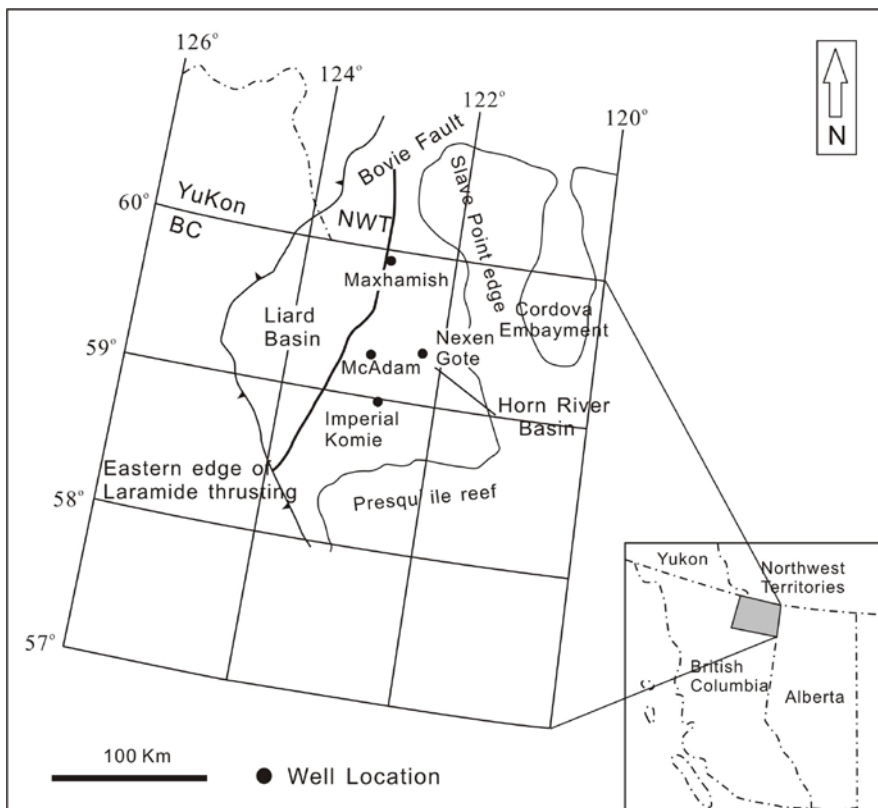


Fig. 3.1. Map of Horn River Basin and adjacent areas (Liard Basin and Cordova Embayment), showing well locations (modified after Ross and Bustin, 2008).

			Liard Basin	Horn River Basin	Platform		
Devonian	Upper	Frasnian	Besa River Formation	Fort Simpson Formation	Fort Simpson Formation	Fort Simpson Formation	
			Muskwa Fm	Muskwa Fm	Muskwa Fm		
	Middle	Givetian	Horn River Fm	Otter Park Mbr	Horn River Fm	Otter Park Mbr	Slave Point Fm
				Evie Mbr		Evie Mbr	Watt Myn Fm
			Dunedin Fm	Keg River Fm	Lower Keg River Fm		
						Sulphur Point Fm	
	Upper Keg River Fm						

Fig. 3.2. Middle and Upper Devonian stratigraphy of the Liard Basin, Horn River Basin and Cordova Embayment (modified after Ferri et al., 2011).

### 3.3. Methodology

#### 3.3.1 Samples and datasets

The 100 samples analyzed in this study are mainly from the four cores in the Horn River Basin, EOG Maxhamish D-012-L/094-O-15, Imperial Komie D-069-K/094-O-02, Nexen Gote A-27-I/094-O-8 and ConocoPhillips McAdam C-87-K/094-O-7 (Fig. 3.1). Core description, thin section, geochemical composition, porosity, nitrogen adsorption, mercury injection, SEM (Scanning Electron Microscopy), and TEM (Transmission Electron Microscopy) images are analyzed. Samples for porosity measurement and pore structure investigation were selected to represent a range of organic matter enrichment and shale composition (Table 3.1). The samples represent a similar thermal maturity level, approximate 1.6 - 2.5%  $R_o$  (Ross and Bustin, 2008; Ross and Bustin, 2009), eliminating maturation as a variable in porosity development.

#### 3.3.2 Methods

Four cores (overall 680 m, excluding ~300 m of missing section) were logged in order to develop a comparison between depositional facies, textural properties of the rocks and geochemical composition. Sedimentological and ichnological characteristics

were determined by visual observations, including: (1) lithology, (2) grain size, (3) physical sedimentary structures, (4) trace fossil assemblages and bioturbation intensity, (5) bioclasts, (6) presence and relative abundance of fractures, and (7) presence of cements (i.e., pyrite and calcite). Additionally, analysis of 25 thin sections was conducted to identify micro-scale sedimentary structures and their internal features, as well as trace fossils. Although preserved individual trace fossils are present (e.g., *Phycosiphon*), ichnological characteristics (i.e., bioturbation intensity) were predominantly represented by laminae disruption and bio-deformation structures.

One hundred 10 cm-long core samples were split lengthwise for multiple analyses. One split was analyzed for total organic carbon (TOC) contents, and approximately 20% of these samples were analyzed for hydrogen index (HI) and oxygen index (OI). Total organic carbon (TOC) was analyzed by Weatherford Laboratories using LECO combustion; Rockeval parameters (S1, S2, S3, Tmax, HI, OI) were analyzed with the Weatherford Source Rock Analyzer. A second sample split was analyzed using Inductively Coupled Plasma Mass Spectrometry (ICP-MS) at Acme Analytical Laboratories for SiO<sub>2</sub>, Al<sub>2</sub>O<sub>3</sub>, Fe<sub>2</sub>O<sub>3</sub>, MgO, CaO, Na<sub>2</sub>O, K<sub>2</sub>O, TiO<sub>2</sub>, P<sub>2</sub>O<sub>5</sub>, MnO, and Cr<sub>2</sub>O<sub>3</sub>. Samples were crushed and pulverized until 85% of the material passed through 200 mesh. The powdered samples were combined with lithium borate and digested by nitric acid digestion. Analytical results were calibrated with laboratory internal standards, international standards (U.S. Geological Survey standards, SCO-1), and analysis of replicate samples. All the major oxides are expressed in weight percent.

A third split from the same sample was analyzed for porosity at Trican Well Service Ltd., Calgary, Alberta. The samples were crushed, sieved with a 10 mesh screen and dried in an oven at 105 degrees Celsius to remove any existing fluids. Porosity measurements were conducted on crushed and dried samples of approximately 30-45 grams using a Quantachrome Pentapyc 5200e helium pycnometer. Bulk densities were calculated from the sample weight and volume, measured on a dried 5-10 gram

uncrushed split of the sample. Sample volume was determined by measuring the weight of displaced mercury and the density of mercury at lab temperature. Helium pycnometry was used to measure the skeletal density of crushed samples. Ultra-high purity helium was used to maximize penetration of pore space and minimize potential reactions with the samples (Cui et al., 2009). The helium pycnometer contained five sample cells, one reference cell of known volume and a precise pressure transducer. The crushed sample was loaded into a sample cell and sealed. The reference cell was filled with helium and the pressure was recorded after the pressure within the reference cell had equilibrated. The reference cell and sample cell were then opened to each other, allowing the helium from the reference cell to enter the sample cell. The volume of the system was calculated using Boyle's gas law and the pressure recorded after the system had reached a new equilibrium. The difference between the known volume of the sample cell and the measured volume of gas is equal to the skeletal volume of the sample. Skeletal density was then calculated from the weight of the sample.

Nitrogen adsorption and desorption experiments were conducted on a Quantachrome Autosorb-1 instrument at the NanoFab Facility at the University of Alberta. Thirty three samples were selected from Maxhamish, Imperial Komie and Nexen Gote well for nitrogen adsorption analysis, representing a wide range of mineral composition and organic matter enrichment (Table 3.2). Samples were crushed and sieved to 0.5-1 mm, dried in an oven for 12 h and degassed under high vacuum, typically 10 h at 150°. Both adsorption and desorption isotherms were obtained to document the hysteresis loop and calculate surface area and pore size distribution based on BET and BJH models. The BET method (Brunauer et al., 1938; Schettler et al., 1989) provides a direct measure of the surface area of sample materials. Barrett, Joyner, Halenda (BJH) theory (Barret et al., 1951; Gregg and Sing, 1982) can be used in combination with Kelvin equation to obtain mesopore size distributions (pore diameter 2-50 nm) from the desorption isotherm, assuming cylindrical geometry (Dong and Harris, 2013).

Five samples were prepared using argon ion-milling techniques (Fischione Model 1060 SEM Mill at University of Alberta) to create smooth surface (Loucks et al., 2009; Loucks et al., 2012). Ion-milled samples were imaged using a JEOL 6301F field emission scanning electron microscope (FE-SEM) to document matrix components, organic matter, and pore size, shape and host at the Scanning Electron Microscope Facility at the University of Alberta. The FE-SEM was performed using an accelerating voltage of 5.0 kV and working distances range from 10-15 mm.

Transmission electron microscopy (TEM) is an imaging technique in which a beam of electrons is transmitted through an ultra-thin specimen, and an image is formed from the interaction between electrons and the specimen as they move through the specimen. TEM requires the sample to be thin enough that it can transmit electrons, typically less than 100 nm. The specimen was milled by focused ion beam milling technique to obtain sufficiently thin samples, typically less than 100 nm; the analysis was performed on the JEOL 2200 FS Soft Materials TEM instrument at the National Institute for Nanotechnology at the University of Alberta, using an accelerating voltage of 200 kV to image the shale porosity.

### **3.4. Results**

#### **3.4.1 Lithofacies classification**

Five predominant lithofacies were identified, based on sedimentological and ichnological characteristics of four cores. These are massive mudstones, massive mudstones with abundant pyrite streaks, laminated to heterolithic bedded mudstones, bioturbated mudstones, and carbonates (Fig. 3.3).

#### **Massive Mudstones Lithofacies**

The massive mudstone lithofacies is a major component of the Muskwa Formation and the Evie Member (Figs. 3.4 and 3.5). This lithofacies is represented by grey to light brown, massive mudstone (Fig. 3.3A), containing siliceous and calcareous fossils, such

as radiolaria, tentaculites and sponge spicules. It displays very few sedimentary structures, which include horizontal parallel laminae, thin carbonate-rich bands, and starved ripples. Fossil forms are commonly dispersed but rarely form laminae or beds, particularly within the Evie Member. There are also calcite cemented zones, commonly found at the lithofacies boundaries. Bioturbation is generally very sparse and is dominated by simple trace fossils, such as *Planolites*.

### **Massive Mudstones Lithofacies with abundant pyrite streaks**

Massive mudstone with abundant pyrite streaks (pyritic mudstone) is the most abundant lithofacies in the Horn River shale, dominating the Muskwa Formation and the Evie Member, and to a lesser extent, the Otter Park Member (Figs. 3.4 and 3.5). It is a grey, massive mudstone containing discontinuous to continuous pyrite laminae (Fig. 3.3B). Sedimentary structures are rare; these include organic-rich beds, siliciclastic fossil-rich laminae and micro-scale starved ripples. Fossil-rich laminae locally display normal grading and low to moderate bioturbation. Trace fossil assemblages include *Thalassinoides*, *Planolites*, rare *Teichichnus*, as well as bio-deformation and mantle-swirl structures.

Table 3.1. Porosity, TOC content, inorganic geochemical composition and Rock-Eval data for selected samples.

Well	Depth (m)	Formation	Lithofacies	Porosity (%)	TOC (%)	SiO <sub>2</sub> (%)	Al <sub>2</sub> O <sub>3</sub> (%)	MgO (%)	CaO (%)	HI (mg/g)	OI (mg/g)
Maxhamish	2958.50	Muskwa	Massive mudstones	6.15	5.24	70.73	6.44	1.16	1.51	11	8
Maxhamish	2970.84	Muskwa	Pyrite-rich mudstones	6.03	3.60	85.04	3.95	0.50	0.73	7	7
Maxhamish	2974.45	Muskwa	Pyrite-rich mudstones	5.02	6.44	70.69	8.64	0.54	0.36	3	5
Maxhamish	2988.16	Otter Park	Pyrite-rich mudstones	4.87	2.46	86.06	4.68	0.30	0.19	20	8
Maxhamish	3004.56	Otter Park	Pyrite-rich mudstones	5.46	2.03	76.21	9.03	0.92	0.85	12	11
Maxhamish	3008.55	Otter Park	Pyrite-rich mudstones	3.08	1.39	50.77	9.07	5.12	8.41	15	19
Maxhamish	3011.55	Otter Park	Pyrite-rich mudstones	6.48	2.15	75.31	10.34	0.73	0.41	12	8
Maxhamish	3015.56	Otter Park	Pyrite-rich mudstones	6.73	1.53	64.10	11.72	1.95	2.25	14	10
Maxhamish	3023.65	Otter Park	Pyrite-rich mudstones	5.78	2.12	60.17	15.82	1.12	0.50	4	8
Maxhamish	3031.55	Otter Park	Massive mudstones	7.39	3.67	72.18	7.44	0.53	3.92	5	8
Maxhamish	3033.55	Otter Park	Massive mudstones	8.54	3.66	62.19	8.16	0.71	3.96	7	6
Maxhamish	3035.55	Otter Park	Massive mudstones	8.74	5.09	68.06	8.85	0.77	4.32	5	5
Maxhamish	3038.55	Otter Park	Pyrite-rich mudstones	8.26	4.02	66.54	11.31	0.80	2.07	4	5
Maxhamish	3039.55	Otter Park	Pyrite-rich mudstones	6.09	2.08	70.00	12.15	0.80	1.32	10	10
Maxhamish	3050.65	Evie	Pyrite-rich mudstones	5.40	2.24	25.48	1.24	0.88	37.69	7	15

Maxhamish	3057.05	Evie	Massive mudstones	8.89	5.57	62.81	6.51	1.47	9.17	9	6
Maxhamish	3060.01	Evie	Pyrite-rich mudstones	6.61	0.30	23.62	3.12	11.88	24.84	28	115
Maxhamish	3060.95	Evie	Massive mudstones	3.67	1.70	12.29	1.52	2.18	43.80	19	25
Maxhamish	3064.04	Evie	Massive mudstones	6.43	4.51	56.80	4.32	0.89	15.54	11	6
Maxhamish	3065.04	Evie	Massive mudstones	6.39	5.37	62.68	5.71	0.81	9.88	13	7
Maxhamish	3065.95	Evie	Massive mudstones	8.24	4.71	60.20	5.93	0.75	11.01	8	8
Maxhamish	3073.55	Evie	Massive mudstones	4.20	5.09	54.20	4.36	1.18	16.74	7	7
Maxhamish	3077.55	Evie	Carbonates	4.26	0.32	3.54	0.52	0.49	52.57	38	91
Maxhamish	3078.55	Evie	Massive mudstones	3.80	1.90	9.88	2.63	1.00	45.48	17	17
Maxhamish	3088.50	Evie	Carbonates	3.71	0.04	9.18	2.78	1.00	46.26	n.m.	n.m.
Imperial Komie	2226.56	Muskwa	Massive mudstones	2.45	0.82	15.51	3.41	13.32	24.43	n.m.	n.m.
Imperial Komie	2228.54	Muskwa	Pyrite-rich mudstones	2.99	2.88	70.78	11.61	0.95	0.60	n.m.	n.m.
Imperial Komie	2238.97	Muskwa	Pyrite-rich mudstones	5.09	5.07	78.92	6.38	0.64	0.63	n.m.	n.m.
Imperial Komie	2240.96	Muskwa	Pyrite-rich mudstones	4.54	2.79	83.69	5.30	0.53	0.60	n.m.	n.m.
Imperial Komie	2245.04	Muskwa	Pyrite-rich mudstones	7.57	4.12	80.10	6.22	0.45	0.34	n.m.	n.m.
Imperial Komie	2251.55	Muskwa	Massive mudstones	9.81	6.85	75.43	5.01	0.85	2.14	n.m.	n.m.
Imperial Komie	2259.53	Muskwa	Massive mudstones	4.20	2.45	35.67	7.50	5.37	10.81	n.m.	n.m.

Imperial Komie	2261.55	Muskwa	Pyrite-rich mudstones	5.59	3.38	72.64	10.11	0.91	0.96	n.m.	n.m.
Imperial Komie	2278.05	Otter Park	Laminated mudstones	2.58	0.68	39.41	10.70	2.93	18.39	n.m.	n.m.
Imperial Komie	2288.55	Otter Park	Laminated mudstones	7.36	0.61	51.77	17.02	2.34	6.24	n.m.	n.m.
Imperial Komie	2294.55	Otter Park	Laminated mudstones	3.98	0.46	48.95	15.87	2.33	9.14	11	39
Imperial Komie	2312.51	Otter Park	Laminated mudstones	8.59	2.57	61.48	10.64	1.16	8.31	n.m.	n.m.
Imperial Komie	2315.06	Otter Park	Laminated mudstones	4.31	1.49	49.72	10.19	1.40	15.82	31	12
Imperial Komie	2317.05	Otter Park	Laminated mudstones	5.30	0.96	29.69	7.02	6.47	20.25	n.m.	n.m.
Imperial Komie	2333.00	Otter Park	Laminated mudstones	5.55	1.28	47.26	12.86	3.60	10.41	n.m.	n.m.
Imperial Komie	2341.56	Otter Park	Pyrite-rich mudstones	2.43	5.52	65.08	8.31	1.48	4.49	n.m.	n.m.
Imperial Komie	2346.08	Otter Park	Massive mudstones	7.81	2.93	33.54	5.71	8.05	16.51	n.m.	n.m.
Imperial Komie	2354.02	Otter Park	Bioturbated mudstones	4.91	0.99	59.27	19.65	1.69	1.09	n.m.	n.m.
Imperial Komie	2365.06	Evie	Bioturbated mudstones	10.76	0.47	56.58	19.58	1.86	1.81	88	45
Imperial Komie	2375.07	Evie	Pyrite-rich mudstones	6.79	5.97	75.60	5.05	0.56	2.72	30	2
Imperial Komie	2383.05	Evie	Pyrite-rich mudstones	3.90	4.28	52.47	7.51	1.80	14.14	n.m.	n.m.
Imperial Komie	2385.41	Evie	Pyrite-rich mudstones	5.70	6.81	62.91	5.65	0.99	8.58	6	2
Imperial Komie	2387.55	Evie	Pyrite-rich mudstones	7.55	3.75	12.29	1.32	2.30	42.78	n.m.	n.m.
Imperial Komie	2390.05	Evie	Massive mudstones	5.86	2.02	12.53	0.74	0.95	46.12	n.m.	n.m.

Imperial Komie	2396.05	Evie	Massive mudstones	4.03	3.05	7.58	0.61	0.85	48.54	n.m.	n.m.
Nexen Gote	2395.20	Muskwa	Laminated mudstones	3.13	1.28	57.37	15.23	2.97	3.48	42	14
Nexen Gote	2397.00	Muskwa	Laminated mudstones	5.75	0.97	59.40	15.52	2.63	2.55	n.m.	n.m.
Nexen Gote	2408.96	Muskwa	Laminated mudstones	4.66	2.93	73.75	9.84	1.03	0.51	n.m.	n.m.
Nexen Gote	2423.00	Muskwa	Laminated mudstones	5.49	2.00	86.36	4.44	0.35	0.34	n.m.	n.m.
Nexen Gote	2432.96	Muskwa	Massive mudstones	7.77	5.10	80.05	5.29	0.84	1.01	n.m.	n.m.
Nexen Gote	2441.00	Muskwa	Laminated mudstones	1.63	4.46	66.33	11.87	0.81	0.30	n.m.	n.m.
Nexen Gote	2457.00	Muskwa	Laminated mudstones	4.54	2.59	41.51	6.15	7.50	14.61	n.m.	n.m.
Nexen Gote	2473.02	Otter Park	Laminated mudstones	4.16	3.43	63.69	11.81	1.24	3.79	n.m.	n.m.
Nexen Gote	2485.00	Otter Park	Laminated mudstones	4.66	3.73	62.94	10.46	1.51	5.50	35	6
Nexen Gote	2496.97	Otter Park	Massive mudstones	3.97	6.09	64.96	7.85	1.33	4.62	n.m.	n.m.
Nexen Gote	2500.98	Otter Park	Laminated mudstones	6.12	7.09	64.11	8.12	1.45	4.39	n.m.	n.m.
Nexen Gote	2521.00	Otter Park	Bioturbated mudstones	4.35	1.52	56.22	17.61	1.92	2.32	n.m.	n.m.
Nexen Gote	2523.02	Otter Park	Pyrite-rich mudstones	5.48	1.10	38.73	9.35	5.46	10.97	n.m.	n.m.
Nexen Gote	2525.26	Otter Park	Massive mudstones	6.29	4.50	71.45	5.80	1.35	3.50	n.m.	n.m.
Nexen Gote	2526.88	Otter Park	Massive mudstones	2.32	1.39	25.62	0.46	0.88	39.80	n.m.	n.m.
Nexen Gote	2535.87	MDC	Massive mudstones	7.17	4.36	57.91	5.07	1.01	13.81	42	6

Nexen Gote	2542.02	Evie	Massive mudstones	6.29	2.98	66.19	7.34	0.87	7.18	n.m.	n.m.
Nexen Gote	2544.04	Evie	Massive mudstones	6.11	3.80	69.31	6.84	0.77	5.35	n.m.	n.m.
Nexen Gote	2545.88	Evie	Laminated mudstones	4.95	0.46	25.84	4.06	2.01	33.83	n.m.	n.m.
Nexen Gote	2548.00	Evie	Laminated mudstones	7.69	2.40	13.42	2.27	8.20	35.33	n.m.	n.m.
Nexen Gote	2550.00	Evie	Massive mudstones	4.45	5.04	54.12	3.74	0.96	17.39	n.m.	n.m.
Nexen Gote	2554.02	Evie	Massive mudstones	6.82	5.57	54.25	5.73	0.95	14.71	n.m.	n.m.
Nexen Gote	2558.87	Evie	Massive mudstones	1.80	2.21	76.57	1.96	0.50	8.53	n.m.	n.m.
Nexen Gote	2566.53	Evie	Laminated mudstones	4.69	1.80	36.81	3.95	0.86	28.90	n.m.	n.m.
Nexen Gote	2577.17	Evie	Massive mudstones	1.76	5.16	64.15	3.02	0.71	12.19	n.m.	n.m.
Mcadam	2723.66	Muskwa	Massive mudstones	2.84	1.10	63.19	9.92	3.10	4.54	n.m.	n.m.
Mcadam	2742.3	Muskwa	Pyrite-rich mudstones	3.24	1.68	89.38	3.37	0.28	0.26	n.m.	n.m.
Mcadam	2751.35	Muskwa	Pyrite-rich mudstones	4.19	2.97	87.22	3.79	0.23	0.20	n.m.	n.m.
Mcadam	2755.8	Muskwa	Pyrite-rich mudstones	2.87	3.78	59.51	11.00	1.95	2.34	20	12
Mcadam	2762.08	Muskwa	Pyrite-rich mudstones	12.04	5.24	78.17	6.29	0.33	0.20	n.m.	n.m.
Mcadam	2768.53	Muskwa	Laminated mudstones	4.87	3.38	65.39	12.99	1.24	1.11	n.m.	n.m.
Mcadam	2779.79	Muskwa	Massive mudstones	2.80	3.90	77.55	8.63	0.58	0.29	n.m.	n.m.
Mcadam	2786.13	Muskwa	Laminated mudstones	8.46	3.69	41.08	6.32	5.65	15.76	14	7

Mcadam	2792.15	Otter Park	Laminated mudstones	4.94	0.24	39.95	8.85	2.74	19.91	n.m.	n.m.
Mcadam	2807.76	Otter Park	Laminated mudstones	2.59	0.91	45.54	12.39	1.96	13.49	n.m.	n.m.
Mcadam	2815.93	Otter Park	Laminated mudstones	2.08	1.30	44.78	8.07	2.13	18.45	n.m.	n.m.
Mcadam	2824.25	Otter Park	Laminated mudstones	1.95	0.95	24.86	4.64	1.83	33.09	45	36
Mcadam	2826.02	Otter Park	Laminated mudstones	3.22	0.73	26.77	5.15	2.23	30.98	n.m.	n.m.
Mcadam	2837.49	Otter Park	Bioturbated mudstones	0.62	0.56	33.59	9.09	2.04	24.19	n.m.	n.m.
Mcadam	2849.8	Otter Park	Laminated mudstones	3.01	2.05	55.53	9.73	1.41	11.71	n.m.	n.m.
Mcadam	2862.35	Otter Park	Massive mudstones	4.13	5.49	55.89	13.97	1.60	2.86	n.m.	n.m.
Mcadam	2866.25	Otter Park	Bioturbated mudstones	2.65	1.70	59.99	19.12	1.31	0.38	n.m.	n.m.
Mcadam	2868.25	Otter Park	Bioturbated mudstones	3.31	1.32	52.86	17.45	2.78	3.69	n.m.	n.m.
Mcadam	2870.25	Evie	Pyrite-rich mudstones	3.86	2.58	81.07	3.96	1.15	2.17	n.m.	n.m.
Mcadam	2872.5	Evie	Pyrite-rich mudstones	5.71	6.72	78.90	4.02	0.84	1.93	n.m.	n.m.
Mcadam	2882.45	Evie	Pyrite-rich mudstones	4.51	4.13	73.22	5.35	0.99	5.02	n.m.	n.m.
Mcadam	2897.59	Evie	Massive mudstones	4.01	6.91	67.12	4.11	0.57	7.86	32	8
Mcadam	2899.6	Evie	Massive mudstones	4.49	8.25	64.14	4.80	0.64	7.11	n.m.	n.m.
Mcadam	2904.1	Evie	Massive mudstones	2.89	7.38	64.87	4.61	0.61	8.83	n.m.	n.m.
Mcadam	2912.5	Evie	Carbonates	2.61	0.56	5.27	0.45	4.45	47.07	n.m.	n.m.

Table 3.2. TOC content, major mineralogical components, and pore size at half pore volume from nitrogen adsorption.

Sample No.	Well name	Depth(m)	TOC (%)	SiO <sub>2</sub> (%)	Al <sub>2</sub> O <sub>3</sub> (%)	MgO (%)	CaO (%)	Pore size at half pore volume (nm)
Sample 1	Maxhamish	2958.50	5.241	84.6	3.11	0.81	1.29	3.4
Sample 2	Maxhamish	2967.70	2.302	85.74	4.42	0.25	0.22	16.8
Sample 3	Maxhamish	2974.41	6.437	70.69	8.64	0.54	0.36	8.2
Sample 4	Maxhamish	3003.50	2.379	72.85	9.94	1.02	0.98	11.7
Sample 5	Maxhamish	3018.50	1.547	67.65	14.38	1.01	0.4	8.4
Sample 6	Maxhamish	3037.50	3.007	31.42	5.26	7.5	21.17	11.3
Sample 7	Maxhamish	3057.00	5.572	62.81	6.51	1.47	9.17	11.3
Sample 8	Maxhamish	3062.00	2.067	63.01	10.86	1.14	4.42	6.1
Sample 9	Maxhamish	3069.50	4.783	42.8	3.18	0.88	24.68	6.9
Sample 10	Maxhamish	3085.47	0.027	8.88	2.39	1	46.99	34.6
Sample 11	Maxhamish	2959.41	2.33	82.29	5.32	0.36	0.35	6.3
Sample 12	Maxhamish	2974.99	4.95	75.21	6.76	0.62	0.62	15.9
Sample 13	Maxhamish	2977.89	2.5	80.04	4.94	1.18	1.77	16.2
Sample 14	Maxhamish	3027.37	2.59	37.06	7.04	7.65	14.77	12.4

Sample 15	Maxhamish	3033.73	3.06	70.06	7.6	0.74	4.61	13
Sample 16	Maxhamish	3041.67	2.88	60.74	14.16	1.36	2.81	6.1
Sample 17	Maxhamish	3050.65	2.45	27.92	1.47	0.92	36.09	25.4
Sample 18	Maxhamish	3069.01	6.98	60.51	5.95	0.69	9.39	6.8
Sample 19	Maxhamish	3072.28	4.46	51.83	4.02	1.04	18.42	9.4
Sample 20	Imperial Komie	2233.13	4.54	84.46	4.33	0.50	0.59	4.6
Sample 21	Imperial Komie	2249.60	6.85	75.43	5.01	0.85	2.14	10.2
Sample 22	Imperial Komie	2272.50	1.40	58.65	17.10	1.91	2.57	11.4
Sample 23	Imperial Komie	2339.91	5.52	65.08	8.31	1.48	4.49	5.2
Sample 24	Imperial Komie	2344.43	2.93	33.54	5.71	8.05	16.51	13.3
Sample 25	Imperial Komie	2361.84	1.53	59.12	21.12	1.39	0.61	7.2
Sample 26	Imperial Komie	2385.09	6.81	62.91	5.65	0.99	8.58	5.8
Sample 27	Imperial Komie	2394.77	0.93	3.05	0.20	0.57	53.11	22.8
Sample 28	Nexen Gote	2442.75	4.46	66.33	11.87	0.81	0.30	14.3
Sample 29	Nexen Gote	2486.75	3.73	62.94	10.46	1.51	5.50	11.4
Sample 30	Nexen Gote	2502.73	7.09	64.11	8.12	1.45	4.39	6.6
Sample 31	Nexen Gote	2522.75	1.52	56.22	17.61	1.92	2.32	8.8

Sample 32	Nexen Gote	2545.79	3.80	69.31	6.84	0.77	5.35	11.9
Sample 33	Nexen Gote	2555.76	5.57	54.25	5.73	0.95	14.71	12.1

Table 3.3. Statistics on porosity, TOC content, major oxides for selected samples.

Lithofacies	Porosity (%)	TOC(%)	SiO <sub>2</sub> (%)	Al <sub>2</sub> O <sub>3</sub> (%)	CaO+MgO(%)
Massive mudstones	<u>1.76-9.81</u>	<u>0.82-8.25</u>	<u>7.58-80.05</u>	<u>0.46-13.97</u>	<u>0.87-49.39</u>
	5.37(34)	4.23(34)	54.4(34)	5.41(34)	15.63(34)
Pyrite-rich mudstones	<u>2.43-12.04</u>	<u>0.3-6.81</u>	<u>12.29-89.38</u>	<u>1.24-15.82</u>	<u>0.43-45.08</u>
	5.46(30)	3.44(30)	66.5(30)	7.19(30)	7.53(30)
Laminated mudstones	<u>1.63-8.59</u>	<u>0.24-7.09</u>	<u>13.42-86.36</u>	<u>2.27-17.02</u>	<u>0.69-43.53</u>
	4.68(27)	2.02(27)	49(27)	9.49(27)	16.17(27)
Bioturbated mudstones	<u>0.62-10.76</u>	<u>0.47-1.7</u>	<u>33.59-59.99</u>	<u>9.09-19.65</u>	<u>1.69-26.23</u>
	4.43(6)	1.09(6)	53.1(6)	17.08(6)	7.51(6)
Carbonates	<u>2.61-4.26</u>	<u>0.04-0.56</u>	<u>3.54-9.18</u>	<u>0.45-2.78</u>	<u>47.26-53.06</u>
	3.53(3)	0.31(3)	6(3)	1.25(3)	50.61(3)

Note: minimum – maximum

average (sample numbers)

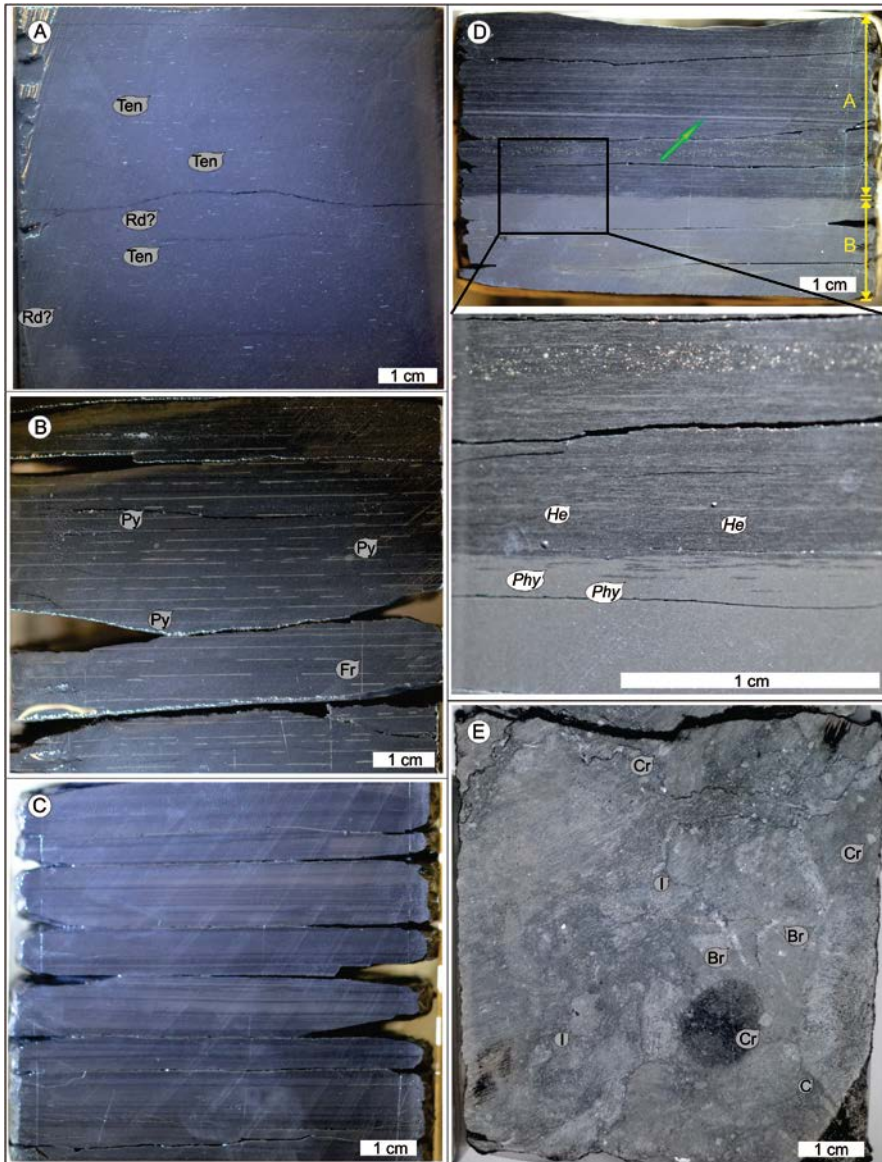


Fig. 3.3. Representative core photographs of Horn River Group lithofacies. **A.** Massive mudstone lithofacies showing calcareous *tentaculites* and possible radiolarians. Ten; Tentaculites, Rd; Radiolarian. **B.** Massive mudstone lithofacies displaying pyrite-rich laminae sets and pyrite lenses. Vertical to oblique fractures are also present. Py; pyrite, Fr; Fracture. **C.** Light to dark grey mudstone interlamination. **D.** Intensely bioturbated mudstone (upper part) and unbioturbated massive mudstone bed (lower part). In upper part, remnant of a horizontal parallel lamination (green arrow) is visible, but majority of the unit is disturbed by high biogenic activity. Top portion of the lower part is partially bioturbated and represents opportunist trace-maker behavior. Trace fossils are very

diminutive, and can be seen in the close-up picture. **E.** Well-cemented carbonate lithofacies. A variety of allochems are present, including a large coral, brachiopods, crinoids, and intraclasts. C; coral, Cr; Crinoid, Br; Brachiopod, I; intraclast.

### **Laminated to heterolithic bedded Mudstones Lithofacies**

The laminated mudstones lithofacies is common in the Otter Park Member and is relatively rare in the Muskwa Formation and the Evie Member (Figs. 3.4 and 3.5). It consists of light to dark grey mudstone laminae or heterolithic siltstone-claystone alternations (Fig. 3.3C). It displays current ripples, normal graded beds, transported shell debris, soft-sediment deformation, double mud-drapes as well as wavy, horizontal and low-angle parallel laminations. Bioturbation is low to moderate, and is dominated by *Planolites*, *Cylindrichnus*, *Thalassinoides*, *Phycosiphon* and disrupted lamina.

### **Bioturbated Mudstones Lithofacies**

The bioturbated mudstones lithofacies is relatively rare and is mainly restricted to the lower part of the Otter Park Member (Figs. 3.4 and 3.5). It consists of moderately to intensely bioturbated, dark to light grey mudstones (Fig. 3.3D). Rare unbioturbated massive light grey mudstone beds (Fig. 3.3D), parallel to irregular horizontal laminations and cemented zones are also present. In some sections, only remnants of physical sedimentary structures are present, due to the high biogenic activity (see the green arrow; Fig. 3.3D). Trace fossil assemblages include *Thalassinoides*, *Planolites*, diminutive *Helminthopsis*, and *Phycosiphon* (Fig. 3.3D).

### **Carbonate Lithofacies**

The carbonate lithofacies is limited to the lower part of the Evie Member (Figs. 3.4 and 3.5). It represents massive to irregularly bedded, well cemented packstone to grainstone lithofacies (Fig. 3.3E). The allochem fraction can reach up to about 80% in this lithofacies. Bioturbation intensity shows varies significantly throughout this lithofacies. Trace fossil assemblages include *Thalassinoides*, *Planolites*, *Arenicolites*, *Asterosoma*, and bio-deformation structures.

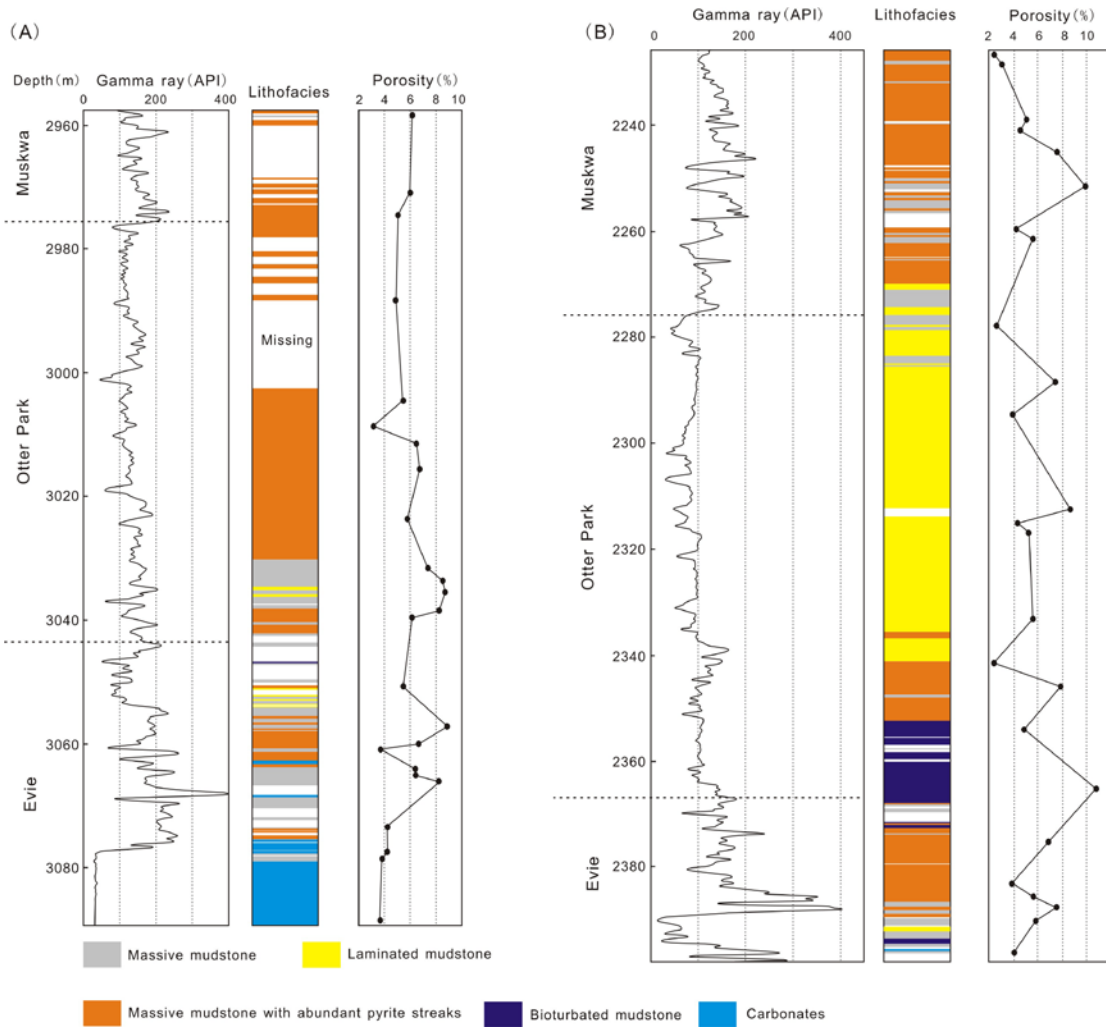


Fig. 3.4. Gamma ray log, core description and porosity data for Maxhamish well (A) and Imperial Komie well (B).

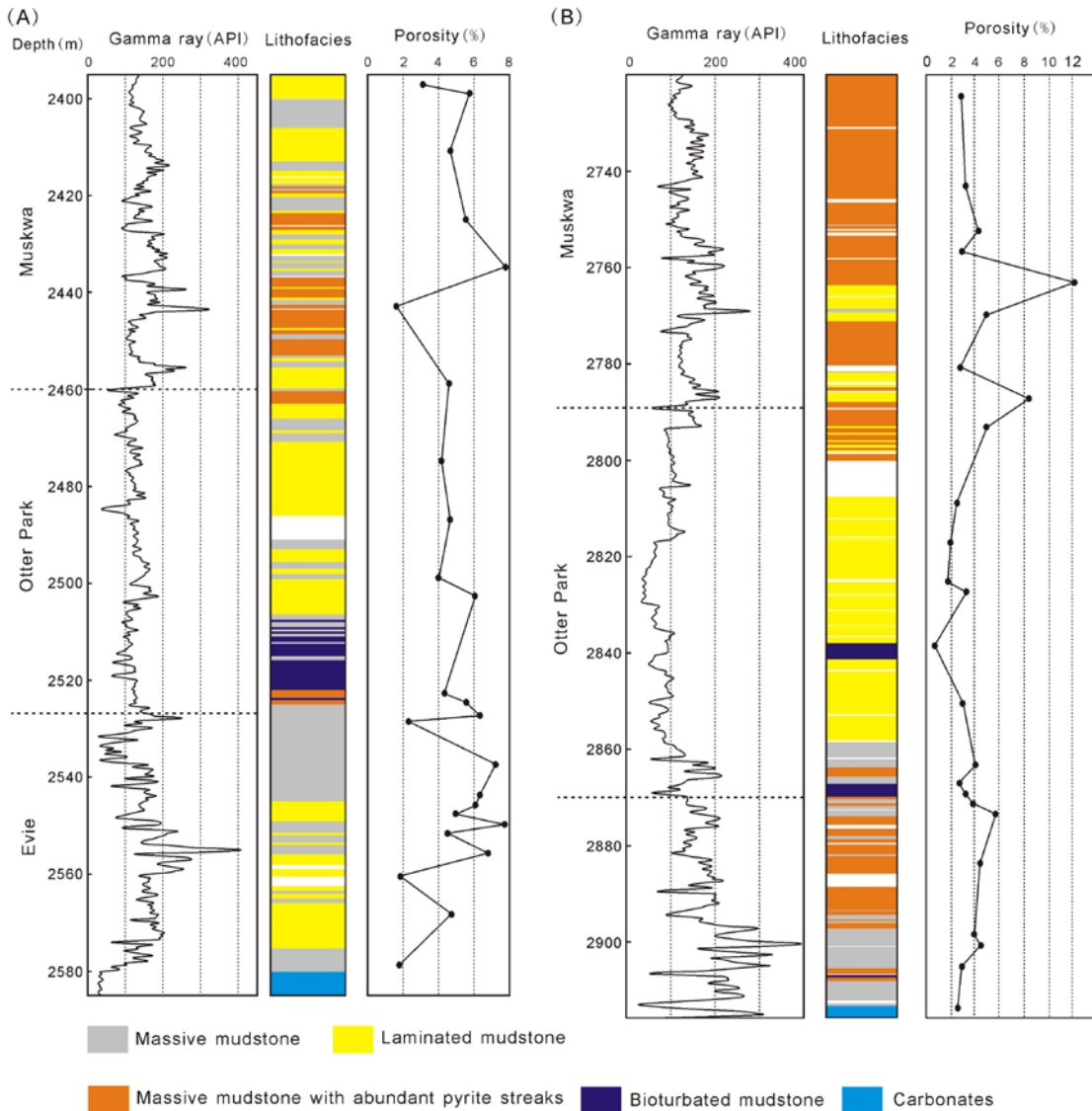


Fig. 3.5. Gamma ray log, core description and porosity data for Nexen Gote well (A) and McAdam well (B).

### 3.4.2 Geochemical composition

Mineralogy, organic matter concentration and thermal maturity are the three critical parameters in evaluation of shale reservoir properties (Curtis, 2002). Wright et al. (2010) demonstrated that in shale reservoirs, selected major elements can provide a reasonable indication of bulk mineralogy, as there is a close relationship between the major element composition and the minerals present in the mudstone. The oxides,  $\text{SiO}_2$ ,  $\text{Al}_2\text{O}_3$  and  $\text{CaO}+\text{MgO}$  can be used as proxies for the quartz, clay and carbonate contents,

respectively.

The variation of geochemical composition of samples from different lithofacies is shown in Fig. 3.6. Pyritic mudstones are most enriched in SiO<sub>2</sub>, showing a range from 12.29% to 89.38%, averaging 66.5% (Fig. 3.6 and 3.7; Table 3.1). Bioturbated mudstones are most enriched in Al<sub>2</sub>O<sub>3</sub>, in the range of 9.09%-19.65%, averaging 17.08%. The carbonate lithofacies is most enriched in CaO + MgO, in the range of 47.26%-53.06%, averaging 50.61%.

The TOC content of the samples averages 3.09 wt.%, ranging from 0.04 to 8.25 wt.% (Fig. 3.7 and Table 3.1), which is generally consistent with data published by Ross and Bustin (2008). Massive mudstones have the highest TOC content, ranging from 0.82 to 8.25 wt.% with an average TOC of 4.23 wt.%. Pyritic mudstones also have relatively high TOC content, ranging from 0.3 to 6.81 wt.% with an average TOC of 3.44 wt.%. Laminated mudstones have moderate TOC content, ranging from 0.24 to 7.09 wt.%, with an average TOC of 2.02 wt.%. The TOC content of the bioturbated mudstones are relatively low, in the range of 0.47-1.7 wt.%, averaging 1.09 wt.%. Carbonates have the lowest TOC content, in the range of 0.04-0.56 wt.%, averaging 0.31 wt.%. The hydrogen index (HI) and oxygen index (OI) values are extremely low, with HI and OI values of most of the samples less than 100, which makes determination of organic matter type by pyrolysis techniques unreliable (Table 3.1).

A moderately positive relationship between TOC content and quartz content is observed (Fig. 3.7), suggesting quartz is at least partially of biogenic origin. Other studies (Chalmers et al., 2012a) also suggest that high silica content of Horn River shale samples is largely associated with biogenic quartz, consistent with the presence of siliceous radiolarian assemblages (Fig. 3.3).

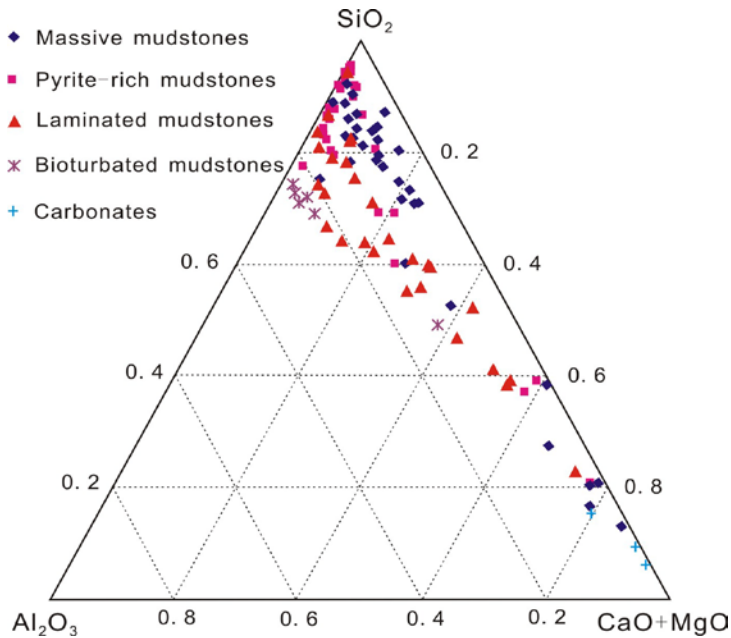


Fig. 3.6. Ternary diagram showing the variation of major oxides among different lithofacies.

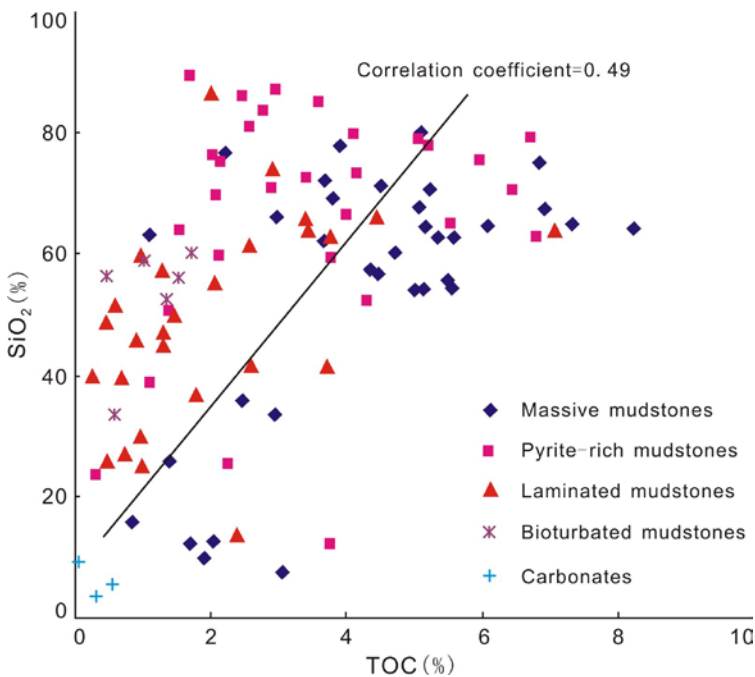


Fig. 3.7. The relationship between TOC content and quartz content.

### 3.4.3 Porosity

Porosities measured in samples from the 4 cores (Figs. 3.4 and 3.5), show a wide range of values. Sedimentary facies vary in porosity, with the massive mudstones and

pyritic massive mudstones displaying relatively high porosity, in the ranges of 1.76-9.81% and 2.43-12.04%, averaging 5.37% and 5.46%, respectively (Table 3.1, Fig. 3.8). Laminated mudstones display moderate porosity values of 1.63-8.59%, averaging 4.68%. Bioturbated mudstones and carbonates display relatively low porosity values of 0.62-10.76% and 2.61-4.26%, averaging 4.43% and 3.53%, respectively (Fig. 3.8).

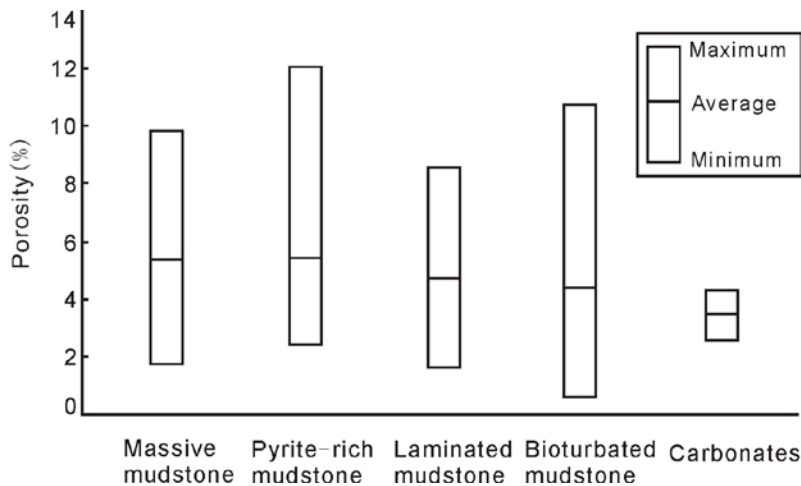


Fig. 3.8. Histogram showing differences in porosity among different lithofacies.

A positive relationship exists between porosity and TOC content, although the correlation coefficient is relatively low (Fig. 3.9A). SiO<sub>2</sub> concentration and porosity also correlate positively (Fig. 3.9B), although this may be due to the positive relationship between the TOC content and SiO<sub>2</sub> concentration, shown in Fig. 3.7. No clear relationship between the TOC content and SiO<sub>2</sub> concentration, shown in Fig. 3.7. No clear relationship between Al<sub>2</sub>O<sub>3</sub> concentration and porosity is evident (Fig. 3.9C). A negative correlation exists between carbonates content (CaO+MgO) and porosity ( Fig. 3.9D). This may result from the antithetic relationships between carbonate and SiO<sub>2</sub>.

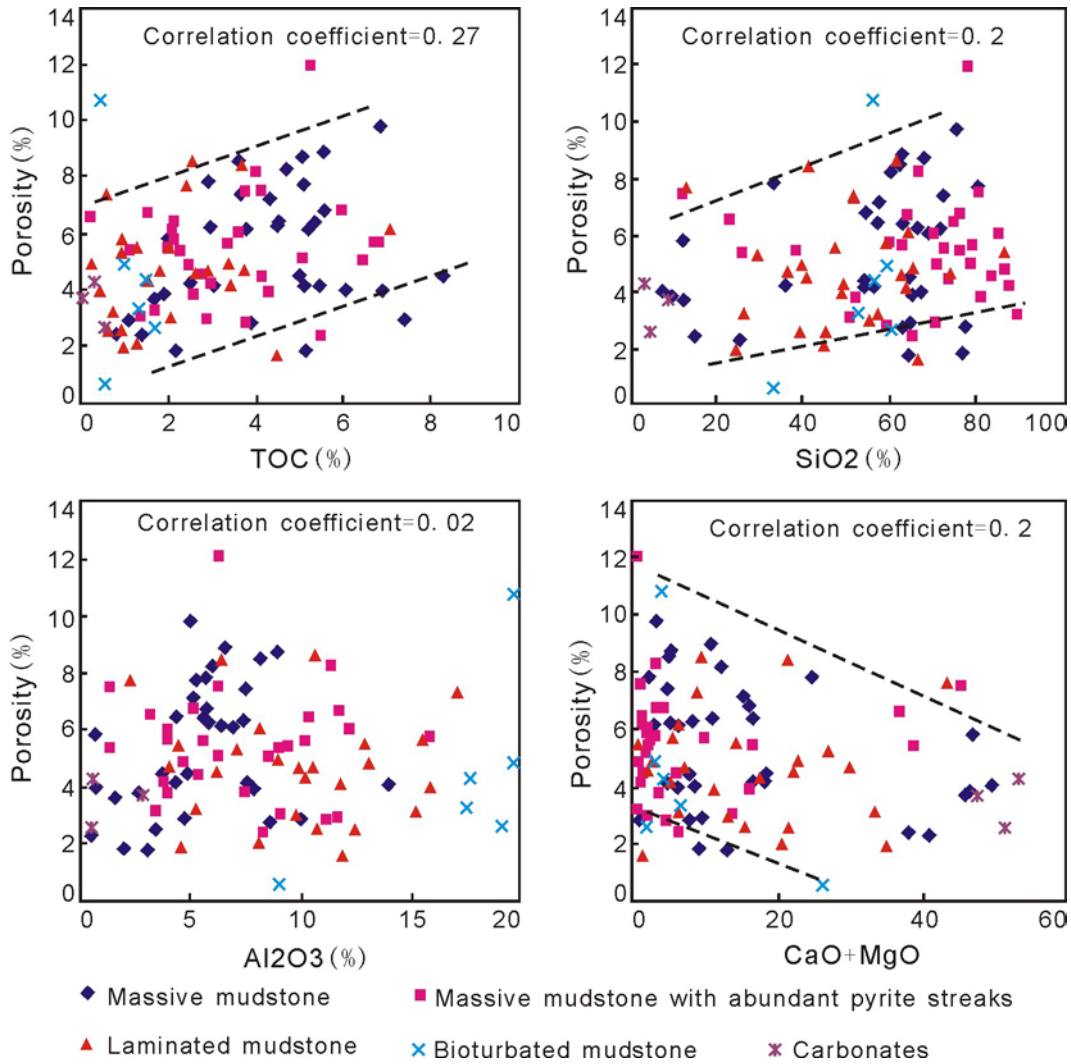


Fig. 3.9. The relationship between porosity and TOC content, concentration of SiO<sub>2</sub>, Al<sub>2</sub>O<sub>3</sub> and CaO+MgO, representing quartz, clay and carbonate content, respectively.

### 3.4.4 Pore microstructure

#### 3.4.4.1 Nitrogen adsorption and desorption

Nitrogen adsorption analyses were performed on 33 samples that varied widely in terms of organic matter concentration and major oxide concentrations (Table 3.2). In this data set, TOC content varies between 0.03 and 7.09 wt.%, SiO<sub>2</sub> varies between 3.05 and 85.74 wt.%, Al<sub>2</sub>O<sub>3</sub> varies between 0.2 and 21.12 wt.% and CaO+MgO varies between 0.47 and 53.68 wt.%. Nitrogen adsorption and desorption isotherms of 4 representative samples, which have TOC contents of 6.44, 1.55, 3.01 and 0.03 wt.%, are presented in

Fig. 3.10. Sample 10, which has an extremely low TOC content of 0.03 wt.%, yields the lowest adsorption amount of approximately 2.7 cm<sup>3</sup>/g. Sample 3 with the relatively high TOC content of 6.44 wt.% has a moderate adsorption amount of 6 cm<sup>3</sup>/g (Fig. 3.10).

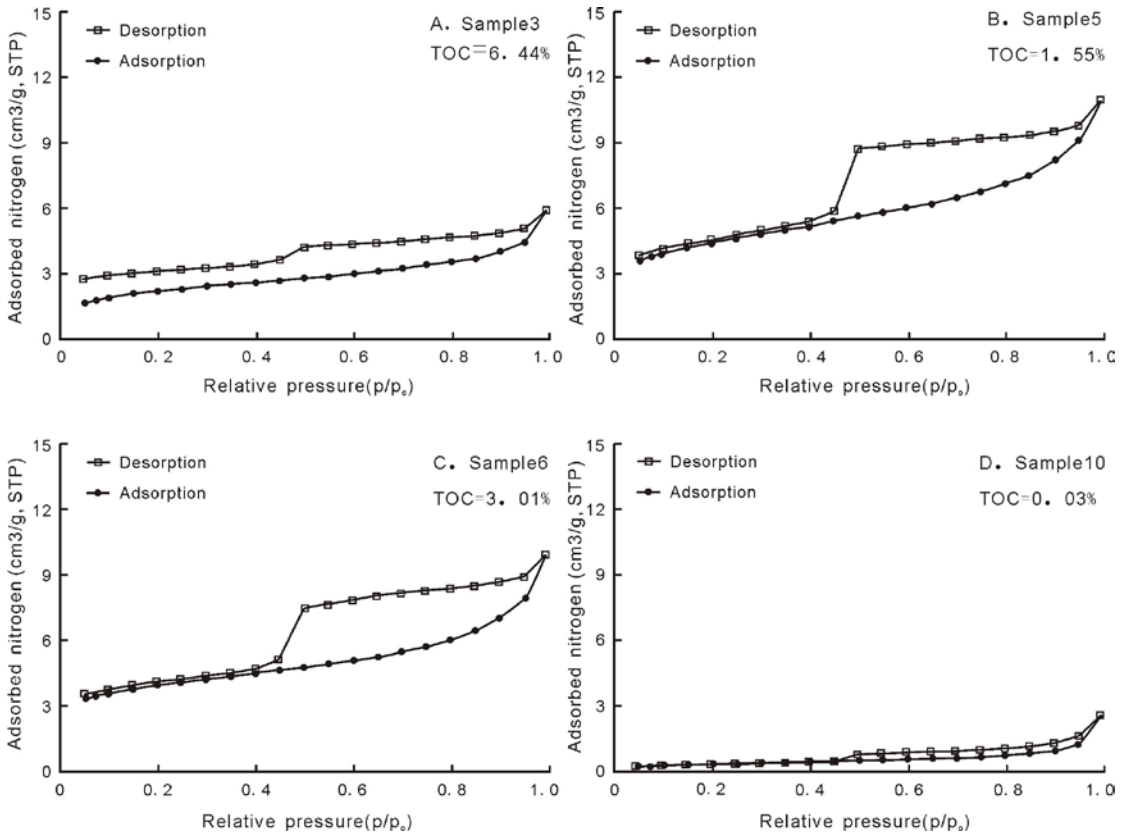


Fig. 3.10. Nitrogen adsorption and desorption isotherms for four representative core samples.

Pores in mudrocks are generally classified by size into three categories: micropore (smaller than 2 nm diameter), mesopore (between 2 and 50 nm) and macropore (larger than 50 nm). The nitrogen adsorption branch of a hysteresis loop is preferred for calculation of pore size distribution over the desorption branch using BJH model (Groen et al., 2003; Tian et al., 2013). Their studies reported that pore size distribution derived from the desorption branch of the isotherm shows a strong artificial peak in pore size at approximately 4 nm (Groen et al., 2003; Tian et al., 2013). Pore size distributions calculated from nitrogen adsorption isotherm are presented in Fig. 3.11. Pore size distributions suggest that the majority of pores have diameters less than 10 nm,

especially less than 2 nm (micropores). Sample 1 with a high TOC content of 5.24 wt.% has the highest proportion of micropores. Sample 10 with the lowest TOC content of 0.03 wt.% exhibits the lowest proportion of micropores. Plots of pore volume with respect to pore diameter derived from nitrogen adsorption isotherm are documented in Fig. 3.12. While the number of small pores greatly exceeds the number of large pores, the largest fraction of pore volume resides in large pores. This effect is particularly strong in the sample with the lowest TOC content (sample 10). The N<sub>2</sub> adsorption isotherms show hysteresis loop patterns indicative of mixtures of mesopores and micropores in the samples (Sing et al., 1985; Mastalerz et al., 2013; Tian et al., 2013).

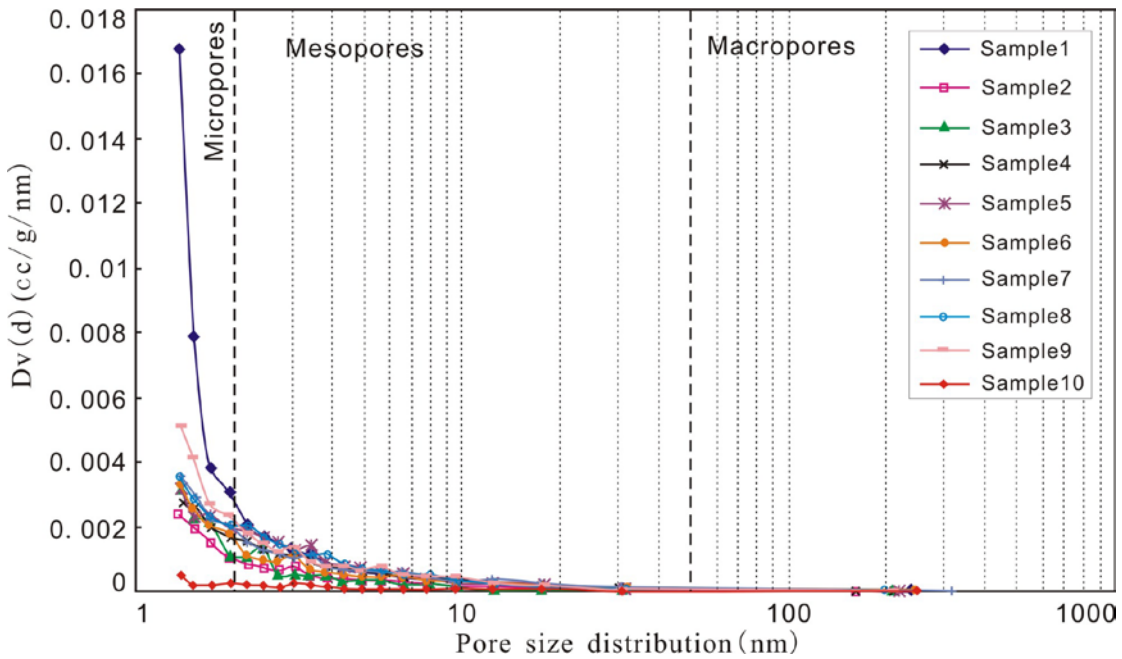


Fig. 3.11. Pore size distribution of representative shale samples determined from nitrogen adsorption using BJH model.

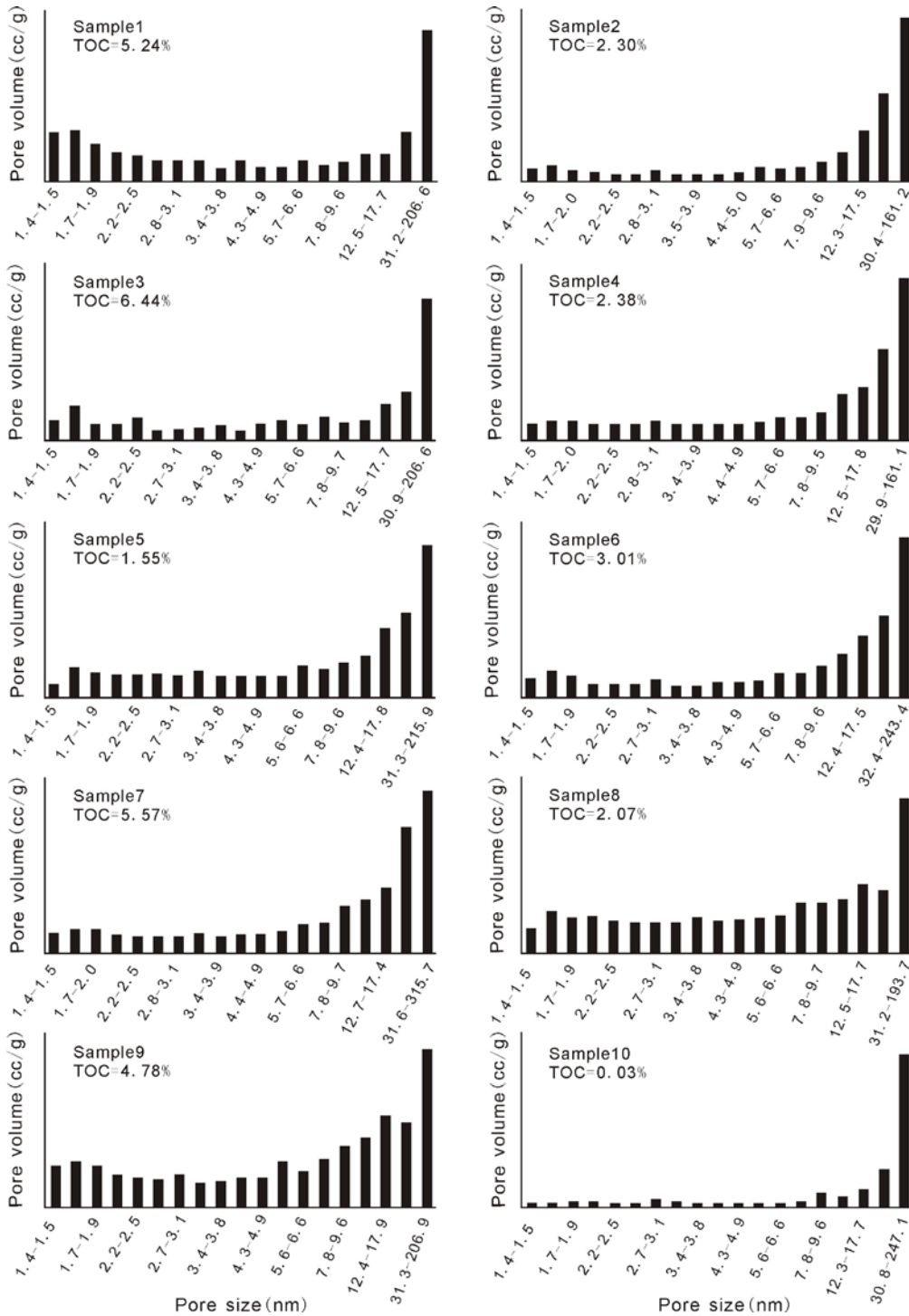


Fig. 3.12. Plot of pore volume versus pore size derived from nitrogen adsorption isotherm for representative shale samples.

In order to investigate the effect of shale composition on pore size distribution, we define a new variable "pore size at half pore volume" as the pore size at which nitrogen

fills half of the pore spaces during nitrogen adsorption process; this is effectively the median pore size in a specific sample. The relationship between pore size at half pore volume versus shale composition shows a negative relationship between pore size at half pore volume and TOC content, yielding a correlation coefficient of 0.49 (Fig. 3.13A). Pore size at half pore volume displays a negative correlation with SiO<sub>2</sub> content (Fig. 3.13B) no correlation with Al<sub>2</sub>O<sub>3</sub> content (Fig. 3.13C) and a good positive correlation with the concentration of CaO+MgO (Fig. 3.13 D).

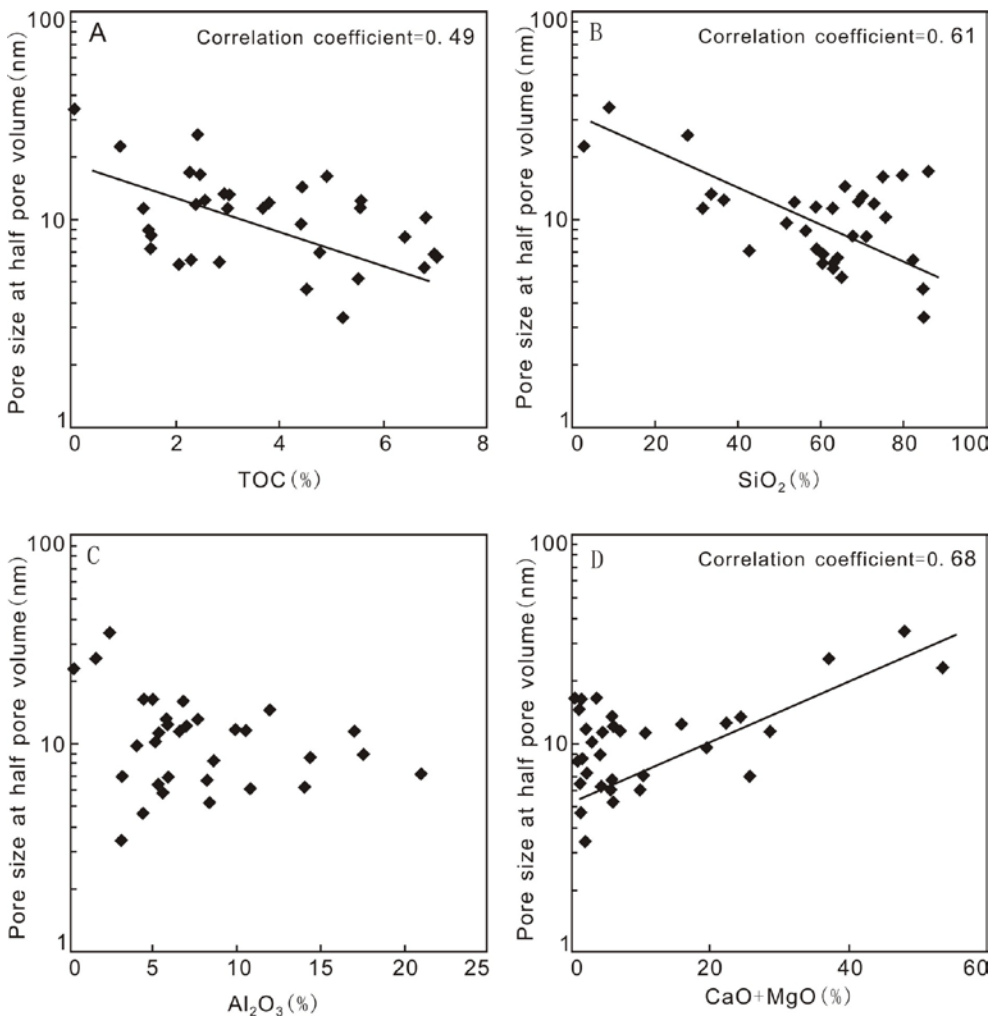


Fig. 3.13. Pore size at half pore volume versus shale composition.

#### 3.4.4.2 Scanning electron microscopy and transmission electron microscopy

While nitrogen adsorption and mercury injection techniques demonstrate a predominance of pores in nanometer scale in the Horn River shale samples, these

methods do not directly image individual pores or provide information on their mode (Curtis, 2011). FE-SEM analysis, which provides visual observation of pore spaces, was performed on two samples from the Maxhamish well (Fig. 3.14) and two samples from the Imperial Komie well (Fig. 3.15), chosen to represent a range of mineralogical composition and TOC content. Various types and sizes of pores are observed in the Horn River shale, including organic matter-hosted pores, interparticle pores and intraparticle pores, developed within detrital grains or authigenic dolomite or calcite crystals. The quartz-rich sample from Maxhamish well shows limited porosity with isolated pores developed within quartz cements (Fig. 3.14A). Micro-fractures occur along the margin of dolomite grains (Fig. 3.14B), which may have resulted from the process of carbonate dissolution. Kerogen may be solid (Fig. 3.14C), or contain numerous small pores (probably mesopores) (Fig. 3.14D). This type of porous organic matter is rare, and its occurrences are small in size, usually in several microns range. The organic matter-rich sample from Maxhamish well shows a large volume of mesopores and macropores developed within kerogen (Fig. 3.14E). These pores are round to oval, and have relatively well-defined boundaries. Porosity can be distributed very heterogeneously within single occurrences of kerogen (Fig. 3.14F); in this example, numerous pores developed in the upper part and no porosity in the lower part. Visual observations suggest that in organic matter-rich samples, organic matter-hosted pores are the most ubiquitous pore type.

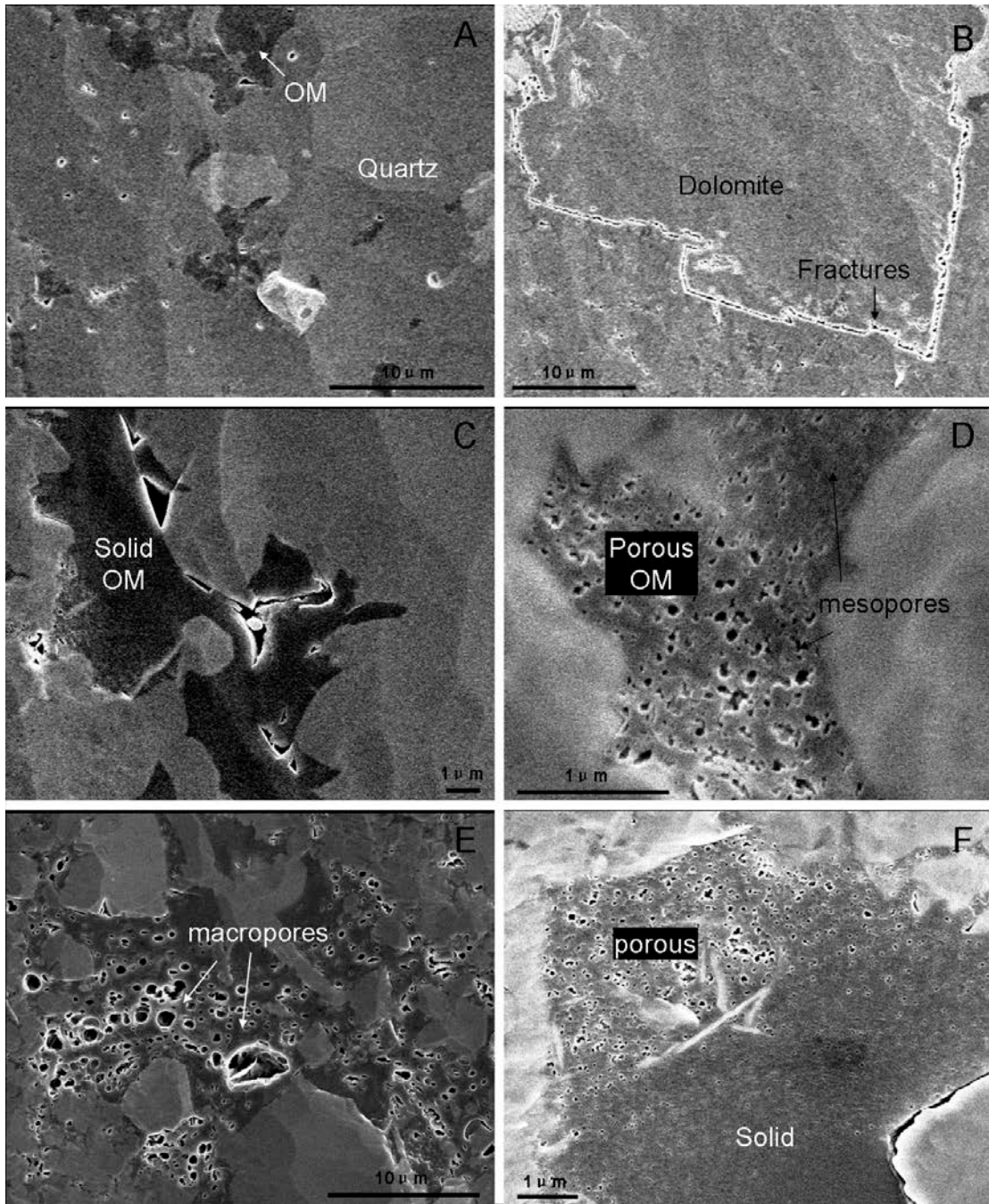


Fig. 3.14. Field emission scanning electron microscope (FE-SEM) images of shale samples from Maxhamish well.

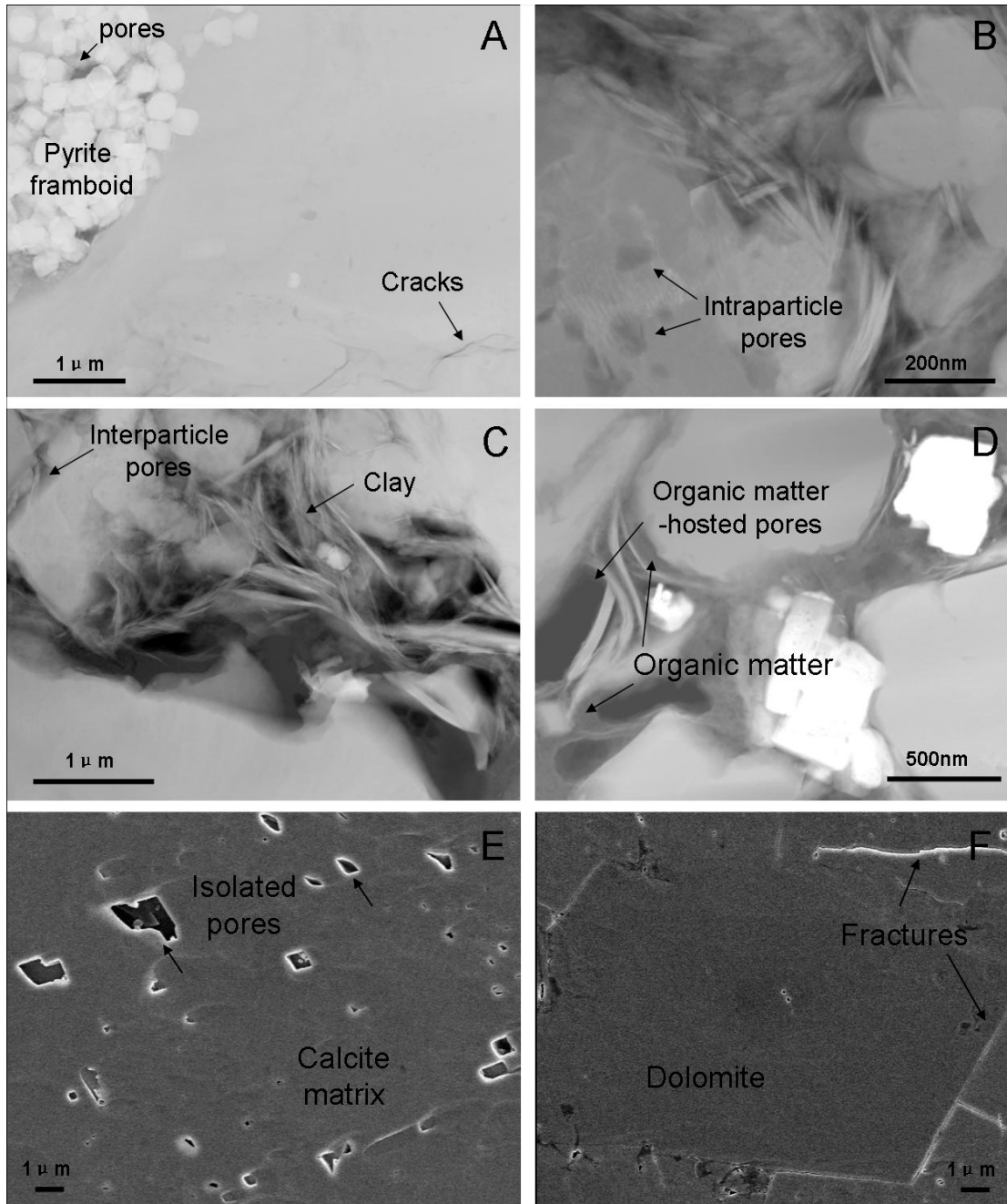


Fig. 3.15. Field emission scanning electron microscope (FE-SEM) images of shale samples from Imperial Komie well. A. Intraparticle pores exist between the pyrite crystalites within a pyrite framboid. B. Intraparticle pores developed within matrix grains. C. Interparticle pores between matrix grains and clay assemblage. D. Organic matter-hosted pores developed. E and F. Intraparticle pores develop within single calcite or dolomite grains.

In samples that are rich in clay, intraparticle pores, interparticle pores, organic matter-hosted pores and cracks are observed within pyrite framboids (Fig. 3.15A), within mineral grains (Fig. 3.15B), between clay flakes (Fig. 3.15B and C), and within organic matter (Fig. 3.15D). Inclined micro-cracks around matrix components are observed (Fig. 3.15A). Pores associated with clay mineral platelets appear to be the dominant pore type in this sample and organic matter appears to fill part of those pores (Fig. 3.15C and D). Those pores are relatively large and mostly have triangular and linear outlines (Fig. 3.15C). FE-SEM images were also obtained from a carbonate-rich sample from the Imperial Komie well (Fig. 3.15E and F). In this sample, isolated pores that may have resulted from carbonates dissolution were observed within calcite matrix (Fig. 3.15E), and partial dissolution was observed along margins of dolomite grains and within the carbonate matrix (Fig. 3.15F).

Because the FE-SEM has a lower resolution limit of 5 nm (Dong and Harris, 2013) and cannot resolve the smallest pores and pore throats, a higher resolution technique, TEM, can be employed in order to better document the complicated pore system within shales (Curtis, 2011). The TEM technique relies on material density differences or thickness changes, with darker areas being denser or thicker than brighter areas which represent lighter material or lesser thickness in bright field and vice versa in dark field (Chalmers et al., 2012b). Fig. 3.16 shows dark field TEM images of one sample from the Muskwa Formation from the Imperial Komie well, which is rich in organic matter (TOC = 6.85 wt.%) and quartz. Macropores are present in clay aggregates, and some pores are concentrated around the quartz grains (Fig. 3.16A). Pores are elongated and show little to no preferential orientation. Some have triangular outlines and are interpreted to be the remaining space between rigid particles after compaction (Fig. 3.16B). Intergranular space between clay and quartz grains locally contains mixtures of kerogen and pore space (Fig. 3.16C). Fig. 3.16D shows an internal structure of kerogen at a higher resolution than SEM images. Numerous small pores in the kerogen can be seen and pores

as small as 2 nm in diameter, or even sub-nanometer scale pores, can be observed in the image. These pores are irregular in shape and size, commonly isolated or connected with each other by smaller pore throats.

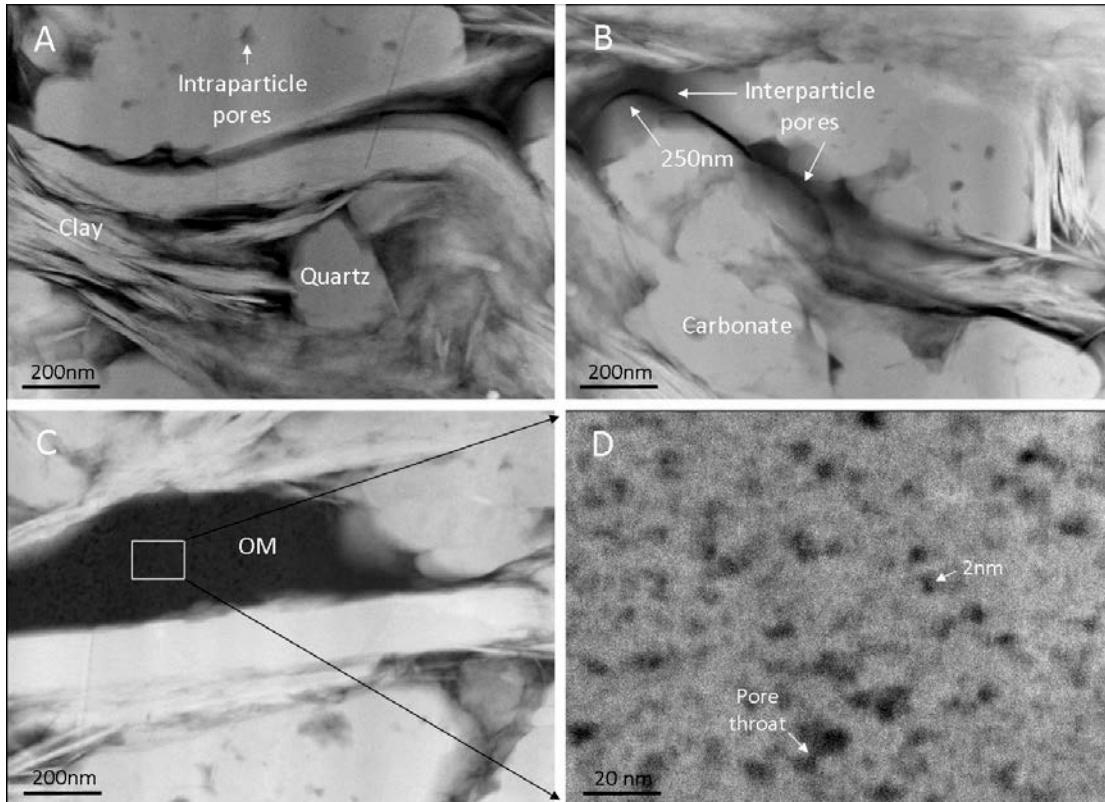


Fig. 3.16. Transmission electron microscope (TEM) images of focused ion beam-milled sample from the Muskwa Formation, Imperial Komie well (see Fig.1 for well locations). A. Dark field TEM image of clay aggregates. B. Two macropores are observed between mineral components. C and D. TEM images showing internal structure within organic matter (OM); a 2 nm pore is labeled.

### 3.5. Discussion

#### 3.5.1 Contributors to pore development

Although considerable effort has been devoted to characterize the complex pore systems within shales (Loucks et al., 2009; Sondergeld et al., 2010; Curtis et al., 2012; Chalmers et al., 2012a, b), less attention has been paid to the factors that control pore

development. Porosity in shale reservoirs is a product of initial (depositional) porosity, compaction and chemical diagenesis (mineralogical transformation, cementation and dissolution) and decreases dramatically during burial (Fishman et al., 2012; Milliken and Day-Stirrat, 2013). Processes that preserve primary porosity or produce secondary porosity are both beneficial in enhancing storage capacity in shale reservoirs (Fishman et al., 2012). Several diagenetic processes that create secondary porosity have been identified. These include the formation of organic matter-hosted pores, which results from volume loss associated with organic matter conversion during maturation and can contribute significantly to the total porosity in shales (Jarvie et al., 2007; Loucks et al., 2009; Milliken et al., 2013). Carbonate dissolution porosity, documented for example in the Upper Devonian to Lower Mississippian New Albany shale, is generally interpreted to result from organic acids in pore waters that are associated with thermal maturation of kerogen (Schieber, 2010).

In this study of the Horn River shale, all the samples have similar high thermal maturity, so the effects of differences in maturity on porosity development are excluded. Our results demonstrate that shale lithofacies and shale composition influence petrophysical properties. Only TOC and quartz content show positive associations with porosity (Fig. 3.8). Multivariate stepwise linear regression analysis was carried out on porosity and major oxide data in order to determine the best predictors of porosity and identify additional relationships. Across all the samples, TOC content is the best and only single predictor of porosity. Although the correlation coefficient is low (correlation coefficient=0.27), this suggests that organic matter provides significant sites for pore development. This is also supported by the evidence in images of numerous pores within organic matter (Fig. 3.14D, E and F). Our results are consistent with observations by Milliken et al. (2013) on Marcellus Shale, in which TOC content is a relatively strong control on the development of organic matter-hosted pore systems, because there are few pores if the samples have low or no TOC.

There are at least two possible explanations for the positive correlation between SiO<sub>2</sub> and porosity: 1) Quartz is primarily biogenic in origin (Fig. 3.7), and SiO<sub>2</sub> correlates positively with TOC, perhaps reflecting organic productivity in the water column during deposition. In this case, the fundamental or causal relationship is between TOC and porosity. The second explanation is that primary porosity preservation is enhanced by quartz cements, which provides a rigid framework that prevents clay platelets (clay floccules) from collapsing (Fig. 3.16A). The negative relationship between porosity and CaO+MgO, which represents the fraction of carbonate minerals, may be due to the antithetic relationship between carbonate mineral content and quartz (Fig. 3.9D).

Pores also develop in association with the dissolution of carbonate minerals (Fig. 3.15E); however, the overall volume of pore spaces in carbonate minerals is low, as indicated by the low nitrogen adsorption in the carbonate-rich sample (Fig. 3.10D and Table 3.2). Thus neither carbonate content nor carbonate dissolution are significant controls on porosity development in Horn River shales.

No significant association between clay content (Al<sub>2</sub>O<sub>3</sub>) and porosity is present in our datasets (Fig. 3.9C); however, we observed that pores may be preserved between clay platelets (Fig. 3.15B, C and Fig. 3.16A). Fishman et al. (2012) proposed that increasing clay content would promote the collapse of organic pores and pores developed between clay platelets if there were insufficient rigid grains to preserve these pores. This appears to be a second-order effect in our Horn River data.

Interparticle pores were observed in pyrite framboids (Fig. 3.16A), suggesting that pyrite content is another contributor to porosity, although this is a minor effect largely owing to its relatively low pyrite content. Fractures are probably additional but minor contributors to porosity (Fig. 3.14B and Fig. 3.15F).

### **3.5.2 Pore structure and models for pore system**

Pore size distributions calculated from nitrogen adsorption analysis suggest that

pores with diameter less than 10 nm, especially pores with diameter less than 2 nm (micropores), are the dominant pore type in terms of frequency (Fig. 3.11). However mesopores and macropores are more significant contributors to total pore volume (Fig. 3.12). Our data also suggest that samples with high TOC content have a greater proportion of micropores and mesopores than macropores. The relationship between pore size at half pore volume (Fig. 3.13A) indicate that in organic-rich samples, pores of smaller size scales contribute more to the porosity. In samples with TOC content greater than 4%, more than half pore volume is contributed by pores with size less than 10 nm (Fig. 3.13A). BET results are consistent with SEM images that show pores developed in association with organic matter are much smaller in diameter than intraparticle pores and interparticle pores (Fig. 3.14). Organic matter-associated pores also include a large fraction of pores below the detection limit of SEM imaging technique, which can be imaged by TEM imaging technique. These results indicate that the high porosity in organic-rich shales is primarily due to the development of micropores and mesopores within organic matter.

Intraparticle pores observed in this study primarily result from the partial dissolution of carbonates (Fig. 3.15E) and possibly silicate grains or cement (Fig. 3.14A). These pores are generally bigger than organic matter-hosted pores. The positive relationship between pore size at half pore volume and concentration of CaO+MgO (Fig. 3.13D), and the plot of pore volume versus pore size (Fig. 3.12) suggest that in organic-lean shales (for example, carbonate-rich shales), pores are large and generally developed within mineral matrix.

In Horn River shale samples, interparticle pores are present in several forms, occurring within pyrite framboids, between clay platelets, between or around rigid grains like quartz and carbonates. Pores occurring within pyrite framboids are much smaller, typically as mesopores or micropores, and are usually isolated (Fig. 3.15A). Pores formed between clay platelets and rigid grains are much larger (Fig. 3.15B and C).

Clear differences between depositional facies in total porosity are demonstrated by our data. Massive mudstones and pyritic mudstones have relatively high porosity (Table 3.3 and Fig. 3.8), probably because they have the highest TOC content and quartz content. Laminated mudstones with moderate TOC content exhibit intermediate porosity. Bioturbated mudstones and carbonates have relatively low porosity, because they have the lowest TOC content as well as the highest clay content and carbonate content. The Muskwa Formation and the Evie Member which are dominated by massive mudstones and pyritic mudstones lithofacies have the highest porosity, while the Otter Park Member, which primarily comprises laminated mudstones and bioturbated mudstones, has lower porosity.

### **3.6. Conclusions**

This detailed study of shale samples from Horn River shale included lithofacies classification, organic matter enrichment, inorganic rock composition analysis, porosity measurements, nitrogen adsorption, FE-SEM, and TEM observation. Our results provide critical new insights on porosity development and pore system:

(1) Five shale lithofacies are identified, including massive mudstones, pyritic mudstones, laminated mudstones, bioturbated mudstones and carbonates. Massive mudstones and pyritic mudstones have the highest porosity; laminated mudstones have moderate porosity; bioturbated mudstones and carbonates have the lowest porosity.

(2) Organic matter-hosted pores, intraparticle pores and interparticle pores are present in Horn River shale reservoirs. The former appear to have developed by cracking of kerogen to hydrocarbon, while the latter two types result from carbonate dissolution and rearrangement of phyllosilicate platelets during mechanical compaction, respectively. Organic matter provides the main site for pore space development, while quartz, carbonate, clay and pyrite framboids also contribute to pore development.

(3) Organic matter-hosted pores are much smaller than intraparticle pores and

interparticle pores. Micropores dominate in frequency, while mesopores and macropores contribute more to total pore volume.

(4) Our results indicate that the Muskwa Formation and the Evie Member have higher porosity for shale gas storage, as they mainly consist of massive mudstones and pyritic mudstones with relatively high TOC. The Otter Park is a poorer reservoir, as it primarily comprises laminated mudstones and bioturbated mudstones with lower TOC.

### **Acknowledgements**

We thank all the colleagues who have significantly contributed to this work. We thank the British Columbia Ministry of Energy and Mines in Victoria for the access to core data and well files. We are grateful for the funding support from NSERC (grant CRDPJ 445064 – 12) and co-funders ConocoPhillips Canada, Devon Canada, Husky Energy, Imperial, Nexen-CNOOC, and Shell Canada. A grant-in-aid from the AAPG Foundation provided additional funding for the TEM analysis. The authors also thank Drs. Nancy Zhang of the Integrated Nanosystems Research Facility at the University of Alberta for training and guidance in the use of the Autosorb-1 instrument, Randy Kofman for carrying out high-pressure MICP measurements in Physical department at the University of Alberta, and Peng Li for training and carrying out TEM analysis in the National Institute for Nanotechnology at University of Alberta. We sincerely thank Dr. Ozgen Karacan and the two anonymous reviewers for their detailed and constructive reviews.

### **3.7 References:**

- Barret, E.P., Joyner, L.G., Halenda, P.P., 1951. The determination of pore volume and area distribution in porous substances. I. Computation from nitrogen isotherms: The Bureau of Chemistry and Soils and George Washington University 73, 373–380.
- B.C. Ministry of Energy and Mines, 2011. Ultimate potential for unconventional natural

- gas in northeastern British Columbia's Horn River Basin. Oil and Gas Reports, May 2011, 50p.
- B.C. Oil and Gas Commission, 2014. Horn River Basin Unconventional Shale Gas Play Atlas, 15p.
- Brunauer, B.S., Emmett, P.H., Teller, E., 1938. Adsorption of gases in multimolecular layers: The Bureau of Chemistry and Soils and George Washington University 60, 309–319.
- Chalmers, G. R. L., Ross, D. J. K., Bustin, R. M., 2012a. Geological controls on matrix permeability of Devonian gas shales in the Horn River and Liard basins, northeast British Columbia, Canada. International Journal of Coal Geology 103, 120-131.
- Chalmers, G. R., Bustin, R. M., Power, L. M., 2012b. Characterization of gas shale pore systems by porosimetry, pycnometry, surface area, and field emission scanning electron microscopy/transmission electron microscopy image analyses: Examples from the Barnett, Woodford, Haynesville, Marcellus, and Doig units. AAPG Bulletin 96, 1099-1119.
- Cui, X., Bustin, A.M.M., Bustin, R.M., 2009. Measurements of gas permeability and diffusivity of tight reservoir rocks: different approaches and their application. Geofluids 9, 208-223.
- Curtis, J. B., 2002. Fractured shale-gas systems. AAPG Bulletin 86, 1921-1938.
- Curtis, M. E., Ambrose, R. J., Sondergeld, C. H., Rai, C. S., 2010. Structural characterization of gas shales on the micro- and nano-scales. Canadian Unconventional Resources and International Petroleum Conference, Calgary, Alberta, Canada, October 19-21, 2010, SPE Paper 137693, 15p.
- Curtis, M. E., Ambrose, R. J., Sondergeld, C. H., Rai, C. S., 2011. Transmission and scanning electron microscopy investigation of pore connectivity of gas shales on the nanoscale. Society of Petroleum Engineers Unconventional Gas Conference, Woodlands, Texas, June 14-16, 2011, SPE Paper 144391, 10p.

- Curtis, M. E., Sondergeld, C. H., Ambrose, R. J., Rai, C. S., 2012. Microstructural investigation of gas shales in two and three dimensions using nanometer-scale resolution imaging. *AAPG Bulletin* 96, 665-677.
- Dong, T., Harris, N. B., 2013. Pore size distribution and morphology in the Horn River shale, Middle and Upper Devonian, northeastern British Columbia, Canada, in W. Camp, E. Diaz and B. Wawak, eds., *Electron microscopy of shale hydrocarbon reservoirs*. *AAPG Memoir* 102, 67-79.
- Ferri, F., Hickin, A. S., Huntley, D. H., 2011. Besa River formation, western Liard Basin, British Columbia (NTS 094N): geochemistry and regional correlations; in *Geoscience Reports 2011*, British Columbia Ministry of Energy, Mines and Natural Gas, 1-18.
- Fishman, N. S., Hackley, P. C., Lowers, H. A., Hill, R. J., Egenhoff, S. O., Eberl, D. D., Blum, A. E., 2012. The nature of porosity in organic-rich mudstones of the Upper Jurassic Kimmeridge clay formation, North Sea, offshore United Kingdom. *International Journal of Coal Geology* 103, 32-50.
- Gregg, S. J., and K. S. W. Sing, 1982, *Adsorption, surface area and porosity*, 2d: London, Academic Press, 303 p.
- Groen, J. C., Peffer, L. A. A., Pérez-Ramírez, J., 2003. Pore size determination in modified micro- and mesoporous materials. Pitfalls and limitations in gas adsorption data analysis. *Microporous and Mesoporous Materials* 60, 1-17.
- Hao, F., Zou, H. Y., Lu, Y. C., 2013. Mechanisms of shale gas storage: implications for shale gas exploration in China. *AAPG Bulletin* 97, 1325-1346.
- Jarvie, D. M., Hill, R. J., Ruble, T. E., Pollastro, R. M., 2007. Unconventional shale-gas systems: the Mississippian Barnett shale of north-central Texas as one model for thermogenic shale-gas assessment. *AAPG Bulletin* 91, 475-499.
- Jennings, D. S., Antia, J., 2013. Petrographic characterization of the Eagle Ford shale, south Texas: mineralogy, common constituents, and distribution of nanometer-scale

- pore types, in W. Camp, E. Diaz, and B. Wawak, eds., *Electron microscopy of shale hydrocarbon reservoirs*. AAPG Memoir 102, 101-113.
- Loucks, R. G., Reed, R. M., Ruppel, S. C., Jarvie, D. M., 2009. Morphology, genesis, and distribution of nanometer-scale pores in siliceous mudstones of the Mississippian Barnett shale. *Journal of Sedimentary Research* 79, 848-861.
- Loucks, R. G., Reed, R. M., Ruppel, S. C., Hammes, U. 2012. Spectrum of pore types and networks in mudrocks and a descriptive classification for matrix-related mudrock pores. *AAPG Bulletin* 96, 1071-1098.
- Mastalerz, M., Schimmelmann, A., Drobniak, A., Chen, Y. Y., 2013. Porosity of Devonian and Mississippian New Albany shale across a maturation gradient: insights from organic petrology, gas adsorption, and mercury intrusion. *AAPG Bulletin* 93, 1621-1643.
- McPhail, S., Walsh, W., Lee, C., Monahan, P. A., 2008. Shale units of the Horn River formation, Horn River basin and Cordova Embayment, Northeastern British Columbia: (abs.), Canadian Society of Petroleum Geologists and Canadian Well Logging Society Convention, 14 p.
- Milliken, K., Day-Stirrat, R., 2013. Cementation in mudrocks: brief review with examples from cratonic basin mudrocks: Critical Assessment of Shale Resource Plays. *AAPG Memoir* 203, 133-150.
- Milliken, K.L., Rudnicki, M., Awwiller, D.N., Zhang, T.W., 2013. Organic matter-hosted pore system, Marcellus Formation (Devonian), Pennsylvania. *AAPG Bulletin* 97, 177-200.
- Milner, M., Mclin, R., Petriello, J., 2010. Imaging texture and porosity in mudstones and shales: comparison of secondary and ion-milled backscatter SEM methods. *Canadian Unconventional Resources & International Petroleum Conference*, Calgary, Alberta, June 19-21, 2010, CSUG/SPE Paper 138975, 10p.
- Nelson, P. H., 2009. Pore-throat sizes in sandstones, tight sandstones, and shales. *AAPG*

Bulletin 93, 329-340.

Oldale, H. S., Munday, R. J. 1994. Devonian Beaver Hill Group of the Western Canada Sedimentary Basin; in Geological Atlas of the Western Canada Sedimentary Basin, Canadian Society of Petroleum Geologists and Alberta Research Council, Special Report 4.

Passey, Q. R., Bohacs, K. M., Esch, W. L., Klimentidis, R. Sinha, S. 2010. From oil-prone source rock to gas-producing shale reservoir: geological and petrophysical characterization of unconventional shale-gas reservoirs. International Oil and Gas Conference and Exhibition, Beijing, China, June 8-10, 2010, SPE Paper 131350, 29 p.

Reynolds, M.M., Munn, D.L., 2010. Development update for an emerging shale gas giant field-Horn River Basin, British Columbia, Canada. SPE Unconventional Gas Conference, Pittsburgh, USA, Feb 23-25. SPE Paper 130103, 17p.

Ross, D. J. K., Bustin, R. M., 2008. Characterizing the shale gas resource potential of Devonian-Mississippian strata in the western Canada sedimentary basin: Application of an integrated formation evaluation. AAPG Bulletin 92, 87-125.

Ross, D. J. K., Bustin, R. M., 2009. The importance of shale composition and pore structure upon gas storage potential of shale gas reservoirs. Marine and Petroleum Geology 26, 916-927.

Schettler, P. D., Parmely, C. R., W. J. Lee, 1989. Gas storage and transport in Devonian shales, SPE Formation Evaluation, p. 371–376.

Schieber, J., 1998. Deposition of mudstones and shales: overview, problems, and challenges. In: J. Schieber, W. Zimmerle, and P. Sethi, eds. Shales and Mudstones: Basin Studies, Sedimentology and Paleontology, Schweizerbart'sche Verlagsbuchhandlung, Stuttgart, 131-146.

Schieber, J., 2010. Common themes in the formation and preservation of porosity in shales and mudstones: Illustrated with examples across the Phanerozoic. Society of

- Petroleum Engineers Unconventional Gas Conference, Pittsburgh, Pennsylvania, February 23-25, 2010, SPE Paper 132370, 12 p.
- Sing, K. S., Everett, D. H., Haul, R.A.W., Moscou, L., Pierotti, R. A., Rouquerol, J., Siemieniewska, T., 1985. Reporting physisorption data for gas/solid systems with special reference to the determination of surface area and porosity. *Pure and Applied Chemistry* 57, 603-619.
- Slatt, R. M., O'Brien, N. R., 2011. Pore types in the Barnett and Woodford gas shales: contribution to understanding gas storage and migration pathways in fine-grained rocks. *AAPG Bulletin* 95, 2017-2030.
- Slatt, R.M., O'Brien, N.R., 2013. Microfabrics related to porosity development, sedimentary and diagenetic processes, and composition of unconventional resource shale reservoirs as determined by conventional scanning electron microscopy, in W. Camp, E. Diaz and B. Wawak, eds., *Electron microscopy of shale hydrocarbon reservoirs*. AAPG Memoir 102, 37-44.
- Sondergeld, C. H., Ambrose, R. J., Rai, C. S., Moncrieff, J., 2010. Microstructural studies of gas shales. Society of Petroleum Engineers Unconventional Gas Conference, Pittsburgh, Pennsylvania, February 23-25, 2010, SPE Paper 131771, 17p.
- Tian, H., Pan, L., Xiao, X. M., Wilkins, R. W. T., Meng, Z. P., Huang, B. J., 2013. A preliminary study on the pore characterization of lower Silurian black shales in the Chuandong thrust fold belt, southwestern China using low pressure N<sub>2</sub> adsorption and FE-SEM methods. *Marine and Petroleum Geology* 48, 8-19.
- Valenza II, J. J., Drenzek, N., Marques, F. Pagels, M., Mastalerz, M., 2013. Geochemical controls on shale microstructure. *Geology* 41, 611-614.
- Wang, F. P., Reed, R. M., 2009. Pore networks and fluid flow in gas shales. Society of Petroleum Engineers Annual Technical Conference and Exhibition, New Orleans, Louisiana, October 4-7, 2009, SPE Paper 124253, 8p.

- Wright, A.M., Spain, D., Ratcliffe, K.T., 2010. Application of inorganic whole rock geochemistry to shale resource plays. Canadian Unconventional Resources & International Petroleum Conference, Calgary, Alberta, October 19-21, 2010, SPE Paper 137946, 18p.
- Yang, Y., Aplin, A. C. 2007. Permeability and petrophysical properties of 30 natural mudstones. Journal of Geophysical Research 112, 1-14.
- Zahrani, A. A., 2011, Interpretation of 3D multicomponent seismic data for investigating natural fractures in the Horn River Basin, northeast British Columbia: Master thesis, University of Calgary, 118p.

## **CHAPTER 4 Shale composition, pore throat size and permeability in a high maturity shale: an example in Middle and Upper Devonian Horn River Shale, northeastern British Columbia, Canada**

### **Abstract**

The Middle and Upper Devonian Horn River Shale provides an outstanding opportunity to study the influence of geochemical composition on permeability and pore throat size distribution in a high maturity shale reservoir. Sedimentological, geochemical and petrophysical analyses were applied to samples from several long cores in order to investigate relationships between rock composition, pore throat size and matrix permeability.

In our sample set, measured matrix permeability values range between 1.7 and 42.8 nanodarcies and increase with increasing porosity. Total organic carbon (TOC) content is positively correlated to permeability and exerts a stronger control on permeability than inorganic composition. A positive correlation between silica content and permeability and the abundant presence of interparticle pores between quartz crystals identified by SEM images suggest that quartz content may be another factor enhancing the permeability. Pore throat size distributions are strongly related to TOC content. In organic-rich samples, the dominant pore throat size are less than 10 nm, whereas in organic-lean samples, pore throat size distribution was characterized by a dominant range of greater than 20 nm. SEM images suggest that in organic-rich samples, organic matter-hosted pores are the dominant pore type, while, in quartz-rich samples, the dominant pore type was interparticle pores existing between quartz grains. In clay-rich and carbonate-rich samples, the dominant pore type is intraparticle pores which are fewer in abundance and smaller in size.

Relatively high permeability shales are associated with specific depositional facies. Massive and pyritic mudstones, rich in TOC and quartz, have relatively high

permeability. Laminated mudstone, bioturbated mudstone and carbonate facies, which are rich in clay and carbonate content, have relatively low permeability.

#### **4.1. Introduction**

Matrix permeability is a fundamental property in conventional reservoirs that controls hydrocarbon production rate. It is presumably also important in shale reservoirs for long term flow rates, although initial production rates are influenced by natural and artificial fracture systems. Permeabilities in fine-grained mudstones are several orders of magnitude lower than in coarser grained lithologies, such as siltstones and sandstones (Dewhurst et al., 1999; Yang and Aplin, 2010). Published absolute permeabilities, measured on a variety of shales and by different analytical methods, typically fall in the nano-darcy range (Kwon et al., 2004). Largely because of the extremely low permeability of shale, accurate measurements of permeability in shale samples are challenging (Sakhaee-Pour and Bryant, 2011; Moghadam and Chalaturnyk, 2015). Steady-state flow techniques are impractical because it is difficult to achieve flow through shale and mudstone plugs in a reasonable amount of time (Mallon and Swarbrick, 2008; Sakhaee-Pour and Bryant, 2011). Consequently transient pulse decay methods, which require much less time, are generally employed to measure shale permeability on both plugs and crushed particles (Cui et al., 2009). One potential problem in using core plugs for pulse-decay measurements is that the induced fractures may influence the measurements (Ghanizadeh et al., 2015); therefore a crushed-rock technique (the GRI method) may be a favorable technique to measure the matrix permeability. On the other hand, where microfractures exist naturally in a shale, the GRI method might not be appropriate.

In mudstone samples, permeability primarily depends on the abundance and size of pores and pore throats (Yang and Aplin, 1998; Dewhurst et al., 1999). Permeability under *in-situ* conditions is difficult to measure, but it can be estimated from more easily

determined petrophysical properties such as pore size and pore throat size distribution as well as specific surface area (Yang and Aplin, 1998). Mercury injection capillary pressure measurements provide a qualitative understanding of permeability by giving useful information about the pore throat size and connectivity. Mercury injection data suggest that pore throat size distributions in mudstones are influenced by both porosity and grain size, or clay content (Dewhurst et al., 1999; Yang and Aplin, 2007). Previously published data indicate that pore throat sizes in shales range from 5 nm to more than 100 nm (Nelson, 2009).

Reported permeabilities in mudstones vary by several orders of magnitude, primarily controlled by the presence of clay minerals which decreases permeability by clogging mineral-associated pores (Neuzil, 1994; Yang and Aplin, 1998, 2007, 2010; Dewhurst et al., 1998; Dewhurst et al., 1999). Most of the samples in their studies are either organic-lean mudstones or in the low maturity, and the dominant pores in their samples existed between particles. Recently, the application of high resolution scanning electron microscopy combined with ion-milling techniques applied to mudstone samples documented another important set of pores developed within organic matter (Loucks et al., 2009; Loucks et al., 2012; Nelson, 2009; Slatt and O'Brien, 2011; Chalmers et al., 2012a; Curtis et al., 2012a; Curtis et al., 2012b; Dong and Harris, 2013; Dong et al., 2015a; Mastalerz et al., 2013; Klaver et al., 2015; Tian et al., 2015). Benefiting from technological advances, we can now study more complex pore systems, including pores developed within organic matter. However, little work has been done on the relationship between organic matter concentration and other compositional variables and permeability, so it is necessary to document the control of organic matter on pore throat size distribution and permeability.

Although some studies describing pore features and factors controlling the matrix permeability in Horn River Shale have been carried out (Ross and Bustin, 2009; Chalmers et al., 2012b), none have been sufficiently detailed to determine the

compositional factors influencing pore throat size distribution and permeability. In this study, we present a large dataset of permeability measurements on crushed samples. By integrating geochemical data and petrophysical data for the Horn River Shale, we aim to investigate the potential effects of shale composition and organic matter on pore networks geometry, pore throat size distribution and permeability, and then link the permeability to lithofacies, which can be used to predict spatial variation in permeability.

#### **4.2. Geological setting**

The Horn River Basin, an area of nearly 12000 km<sup>2</sup>, is situated in the deep northwest portion of the Western Canada Sedimentary Basin in the northeastern British Columbia, Canada (Fig. 4.1). It is bounded to the south and east by carbonate barrier reefs (Presqu'île barrier) and to the west by the Bovie Fault, a Cretaceous structure associated with Laramide tectonism (Ross and Bustin, 2008). The southern part of the Horn River Basin is considered to be proximal to the paleo-shoreline, while the northern part is relatively distal (Fig. 4.1). The Middle and Upper Devonian Horn River shale comprises the Evie and Otter Park Members and the Muskwa Formation (Fig. 4.2), all deposited within a roughly 8 m.y. interval spanning the Givetian to early Frasnian Stages (~ 392 to 384 Ma) (Mossop and Shetsen, 1994). Most of the Upper Devonian Horn River Shale is within dry gas window with vitrinite reflectance ( $R_o$ ) ranging between 1.6 and 2.5% (Ross and Bustin, 2008, 2009; Rivard et al., 2014).

The Evie Member is a dark grey, organic-rich, variably calcareous mudstone that overlies the shallow marine carbonates of the Lower Keg River Formation (McPhail et al., 2008; Hulsy, 2011). It is up to 75 meters thick near the Presqu'île barrier, thinning to less than 40 meters to the west (McPhail et al., 2008). Its well log response is characterized by high gamma ray and high resistivity. The average TOC content for Evie Member is 3.7 wt.% (Dong et al., 2015a). The Otter Park Member is generally grey, pyritic, non-calcareous to calcareous mudstone. It is much thicker than the underlying

Evie Member and the overlying Muskwa Formation, as much as 270 meters in the southeast Horn River Basin (McPhail et al., 2008). The Otter Park shale generally has lower organic content than either the Evie or the Muskwa, averaging 2.4 wt.% TOC (Dong et al., 2015a). The Otter Park shale varies geographically in composition, becoming less calcareous to distal parts of the basin to the north and west. The Muskwa shale is gray to black siliceous, pyritic, organic-rich shale that overlies the Otter Park Member. It varies in thickness from 50 to 90 meters (Oldale and Munday, 1994). Organic carbon enrichment in the Muskwa Formation is higher than in the Otter Park Member but lower than in the Evie Member, averaging 3.41wt.% TOC (Dong et al., 2015a). The Horn River Shale is overlain by the Fort Simpson Formation which is poor in organic matter.

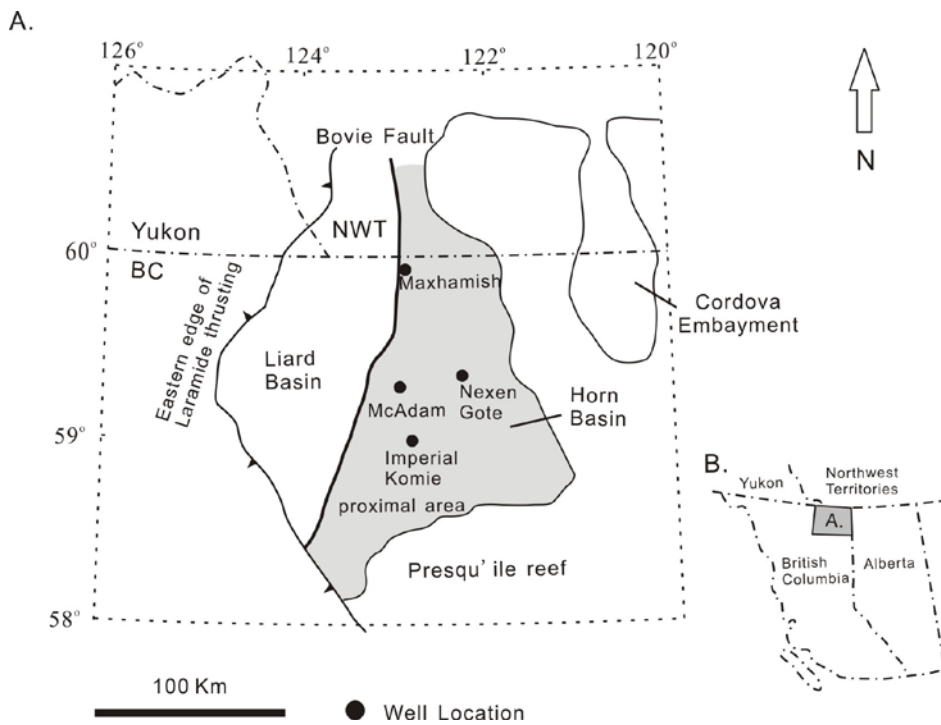


Fig. 4.1. Map of Horn River Basin and adjacent areas, showing well locations (modified after Ross and Bustin, 2008).

			Liard Basin	Horn River Basin	Platform	
Devonian	Upper	Frasnian	Fort Simpson Formation		Fort Simpson Formation	
			Muskwa Fm		Muskwa Fm	
	Middle	Givetian	Besa River Formation	Horn River Fm	Otter Park Mbr	Slave Point Fm
						Horn River Fm
			Horn River Fm	Keg River Fm	Sulphur Point Fm	
					Dunedin Fm	Lower Keg River Fm

Fig. 4.2. Middle and Upper Devonian stratigraphy of Horn River Basin and adjacent areas (modified after Ferri et al., 2011).

### 4.3. Methodology

Samples were obtained from four wells drilled in the Horn River Basin: EOG Maxhamish D-012-L/094-O-15, Imperial Komie D-069-K/094-O-02, Nexen Gote A-27-I/094-O-8 and ConocoPhillips McAdam C-87-K/094-O-7 (Fig. 4.1). All samples were slabs cut from a 10 cm diameter core and were, on average, 10 cm long and 6 cm wide. Splits were cut vertically along the sides of the core samples for geochemical analysis, permeability measurements, mercury injection capillary pressure analysis and SEM image analysis, so that the different analyses were performed on the same interval of rock. Before sampling, these four cores were logged in order to identify the sedimentological and ichnological characteristics and define lithofacies (see Dong et al., 2015a for methods on sedimentological analysis).

Total organic carbon (TOC) content was analyzed by Weatherford Laboratories using LECO combustion. Major element concentrations, including SiO<sub>2</sub>, Al<sub>2</sub>O<sub>3</sub>, Fe<sub>2</sub>O<sub>3</sub>, MgO, CaO, Na<sub>2</sub>O, K<sub>2</sub>O, TiO<sub>2</sub>, P<sub>2</sub>O<sub>5</sub>, MnO and Cr<sub>2</sub>O<sub>3</sub> were determined using Inductively Coupled Plasma Mass Spectrometry (ICP-MS) at Acme Analytical Laboratories. Detailed information on analytical procedures for TOC and major oxides was provided

in Dong et al. (2015a). Four samples were selected for bulk mineralogical analysis and <2 microns clay fraction analysis using X-Ray Diffraction (XRD) method by James Hutton Limited. Received samples were wet ground (in ethanol) in a McCrone mill and then dried to produce random powder. Quantitative analysis was carried out based on the full X-ray powder diffraction patterns recorded from 4-70° 2θ using Copper Kα radiation. Clay fraction (< 2 microns) were separated by using filter peel transfer technique and scanned using Copper Kα radiation in the air-dried state, after glycolation, and after heating to 300 °C for one hour. Detailed methodology on the bulk mineralogy and clay fraction analysis was documented in Hillier (2003) and Omotoso et al. (2006).

Five samples representing different lithofacies were selected to do QEMSCAN analysis, carried out in the Whiting Petroleum Corporation, Denver. QEMSCAN is an automated SEM-based mineralogical analysis tool, and can be used for quantitative determination of mineral abundance and identification of micro-texture on shale samples.

Permeability and porosity were measured on one hundred splits from the same samples at Trican Well Service Ltd., Calgary, Alberta. Samples were crushed, sieved with a 10 mesh screen and dried in an oven at 105°C to remove any existing fluids. Matrix permeability was measured on the crushed and sieved samples using the GRI method. Helium pycnometry was used to measure the skeletal densities of each crushed sample. Ultra-high purity helium was used to maximize penetration of pore space and minimize potential reactions with the samples (Cui et al., 2009). Permeability was calculated at ambient conditions based on a method refined from ResTech (1996) and Luffel et al. (1993), and was not calibrated to *in-situ* conditions.

Pore throat size distributions were measured by mercury porosimeter on shale chips. Thirty-six samples from the four wells representing a wide range of TOC values were selected to be analyzed by mercury injection experiments. Mercury injection capillary pressure (MICP) experiments force mercury into pores and pore throats space under increasing applied pressure. Pore throat diameters, not pore diameters, were determined

by MICP measurements in this study. Thirty-six samples were dried in a vacuum oven over 12 hours and then intruded with mercury from 2 to 60000 psi using Micromeritics AutoPore IV 9500 V1.09 apparatus at the Department of Physics, University of Alberta.

Visualization of pores in this study was accomplished by SEM analysis on samples polished with ion-milling techniques, which produce extremely smooth surfaces (Loucks et al., 2009). Thirteen shale samples from core plugs were first mechanically polished and then further polished using ion-milling techniques (Fischione Model 1060 SEM Mill at the Department of Earth and Atmospheric Sciences, University of Alberta). Detailed information, including geochemical composition of the 13 samples, is provided in Table 4.1. Ion milled samples were mounted to SEM stubs using carbon paste and coated with carbon or chromium (Cr) to provide conductive surfaces. The prepared samples were imaged with two different field-emission SEMs. One was a JEOL 6301 F field-emission scanning electron microscope host at the Scanning Electron Microscope Facility at the University of Alberta. The FE-SEM analysis was performed using an accelerating voltage of 5.0 kV and working distance range from 10-15 mm. The other was a Zeiss Sigma field-emission scanning electron microscope coupled with an EDX & EBSD host at the nanoFAB facility, University of Alberta. The FE-SEM was performed using an accelerating voltage of 10.0 kV and working distances of around 8.5 mm. Secondary electron (SE) images were acquired to document the pore systems and topographic variation. Backscatter Electron Detector (BSE) and Oxford Instruments 150mm X-Max Energy Dispersive X-Ray Detector (EDX) were used to determine the compositional and mineralogical variation.

Table 4.1. Geochemical composition for the thirteen samples selected for SEM imaging analysis.

Group	Sample No.	Well	Buried depth (m)	Formation	Lithofacies	TOC(%)	SiO <sub>2</sub> (%)	Al <sub>2</sub> O <sub>3</sub> (%)	CaO(%)
Organic-rich samples	IK4	Imperial Komie	2385	Evie	Pyritic mudstone	6.81	62.91	5.65	8.58
	IK2	Imperial Komie	2251.55	Muskwa	Massive mudstone	6.85	75.43	5.01	2.14
	Mc1	ConocoPhillips McAdam	2872.5	Otter Park	Massive mudstone	6.715	78.9	4.02	1.93
	M2	EOG Maxhamish	2971.91	Muskwa	Pyritic mudstone	6.44	70.69	8.64	0.36
Quartz-rich samples	IK1	Imperial Komie	2235	Muskwa	Pyritic mudstone	4.54	84.46	4.33	0.59
	M1	EOG Maxhamish	2968.3	Muskwa	Pyritic mudstone	3.60	85.04	3.95	0.73
	NG1	Nexen Gote	2485.03	Otter Park	laminated mudstone	3.7	62.94	10.46	5.5
Clay-rich samples	M3	EOG Maxhamish	3021.1	Otter Park	Pyritic mudstone	2.12	60.17	15.82	0.5
	IK3	Imperial Komie	2363.53	Otter Park	Bioturbated mudstone	1.53	59.12	21.12	0.61
	NG3	Nexen Gote	2521.03	Otter Park	Bioturbated mudstone	1.52	56.22	17.61	2.32
Carbonate-rich samples	IK5	Imperial Komie	2393.97	Evie	carbonate	0.93	3.05	0.2	53.11
	NG4	Nexen Gote	2548	Evie	laminated mudstone	2.4	13.42	2.27	35.33
	Mc2	ConocoPhillips McAdam	2912.5	Evie	carbonate	0.558	5.27	0.45	47.07

Table 4.2. X-Ray Diffraction (XRD) analyzed mineralogy of the four samples from EOG Maxhamish and Imperial Komie well.

Sample ID	Quartz(%)	K-feldspar(%)	Plagioclase(%)	Calcite(%)	Dolomite(%)	Anatase(%)	Pyrite(%)	Chlorite(%)	Muscovite(%)	I+I/S-ML(%)
IK2228.49	49.8	1.2	3.7	0.1	1.1	0.3	3.3	0.1	8.6	31.9
IK2240.91	69.6	1.6	3.9	0.3	1.2	0.1	1.6	0.2	6.3	15.2
M3016	43	2.8	4.3	0.3	0.4	0.1	3.1	0	6.3	39.6
M3060.5	4.8	0	4.7	86.7	0.5	0	0.6	0.5	0	2

Note: I+I/S-ML = mixed layer illite+illite/smectite

## 4.4. Results

### 4.4.1 Lithofacies classification

Five lithofacies were identified, based on the thin section analysis and core observation from the four cores within Horn River Basin: massive mudstone lithofacies; massive mudstone with abundant pyrite lenses and pyrite laminae (pyritic mudstones); laminated to heterolithic bedded mudstone lithofacies (laminated mudstone); bioturbated mudstone; and carbonate lithofacies. More detailed descriptions and photographs of the lithofacies are presented in Dong et al. (2015a).

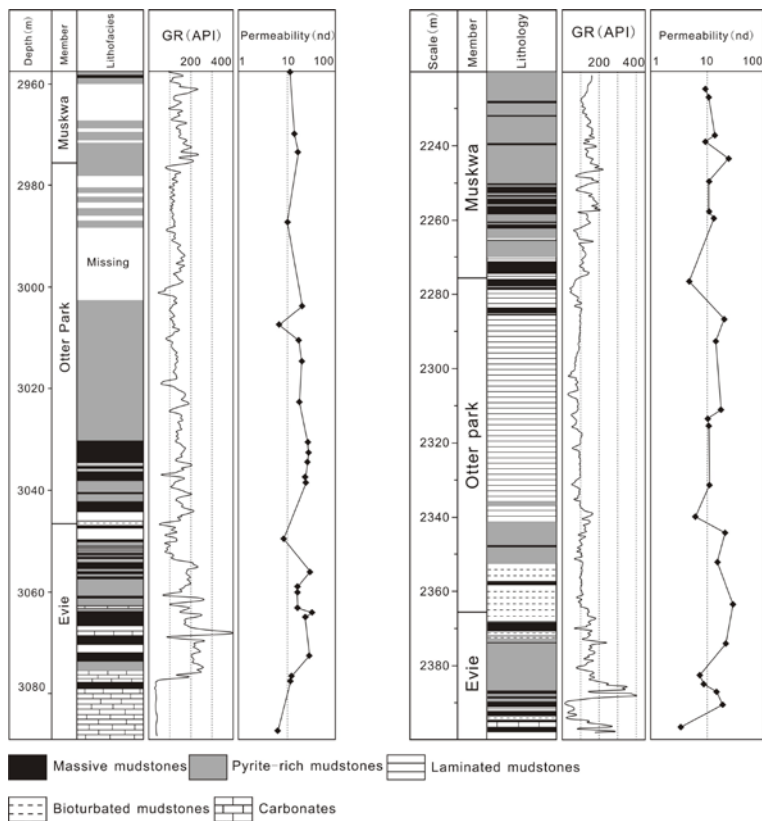


Fig. 4.3. Core description, gamma ray and permeability profile for EOG Maxhamish well (left) and Imperial Komie well (right).

The massive mudstone lithofacies dominates in the Muskwa Formation and the Evie Member (Figs. 4.3 and 4.4). This lithofacies is primarily composed of quartz and minor amounts of clay minerals (Fig. 4.5A). The pyritic mudstone dominates the Muskwa Formation in ConocoPhillips McAdam, Nexen Gote, Imperial Komie and EOG

Maxhamish cores, and also dominates the Otter Park Member in the EOG Maxhamish core (Figs. 4.3 and 4.4). This lithofacies is characterized by ubiquitous pyrite-rich laminae and pyrite nodules (Fig. 4.5B). Comparing to massive mudstone, this lithofacies has less quartz content but more clay content. The laminated mudstone is commonly observed in the Otter Park Member (Figs. 4.3 and 4.4). This lithofacies consists of millimeter-scale interlaminated clay rich mudstone with quartz silt and calcite silt laminations (Fig. 4.5C). The bioturbated mudstone lithofacies primarily occurs in the lower part of the Otter Park Member (Figs. 4.3 and 4.4). It consists of moderately to intensely bioturbated mudstone, showing weak lamination (Fig. 4.5D). Compared to the massive and pyritic mudstones, the laminated and bioturbated mudstones are relatively rich in clay (Figs. 4.5C and D). The carbonate lithofacies, rich in calcite (Figs. 4.5E), is restricted to the lower part of the Evie Member (Figs. 4.3 and 4.4).

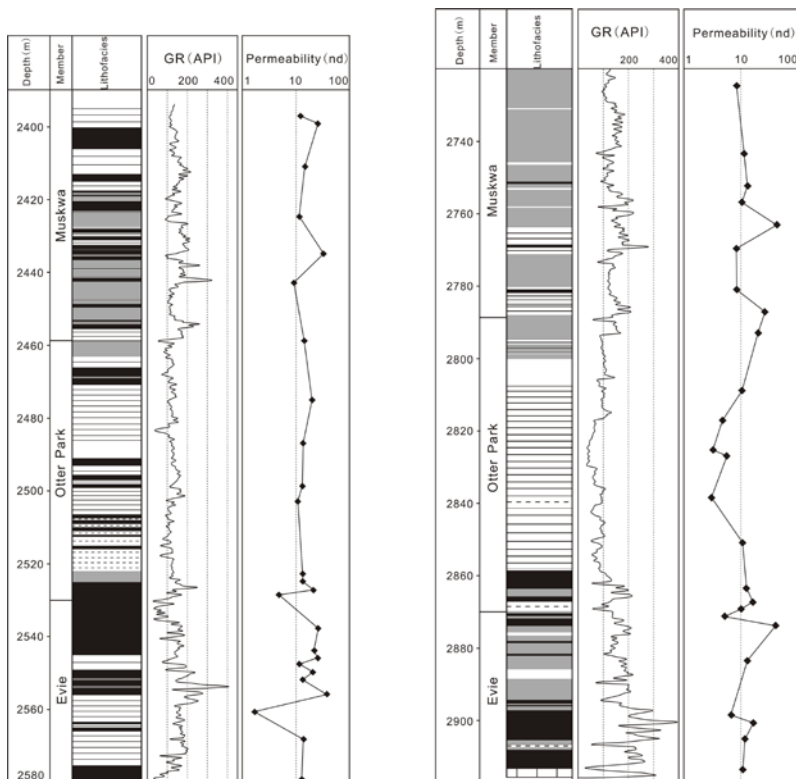


Fig. 4.4. Core description, gamma ray and permeability profile for Nexen Gote well (left) and ConocoPhillips McAdam well (right).

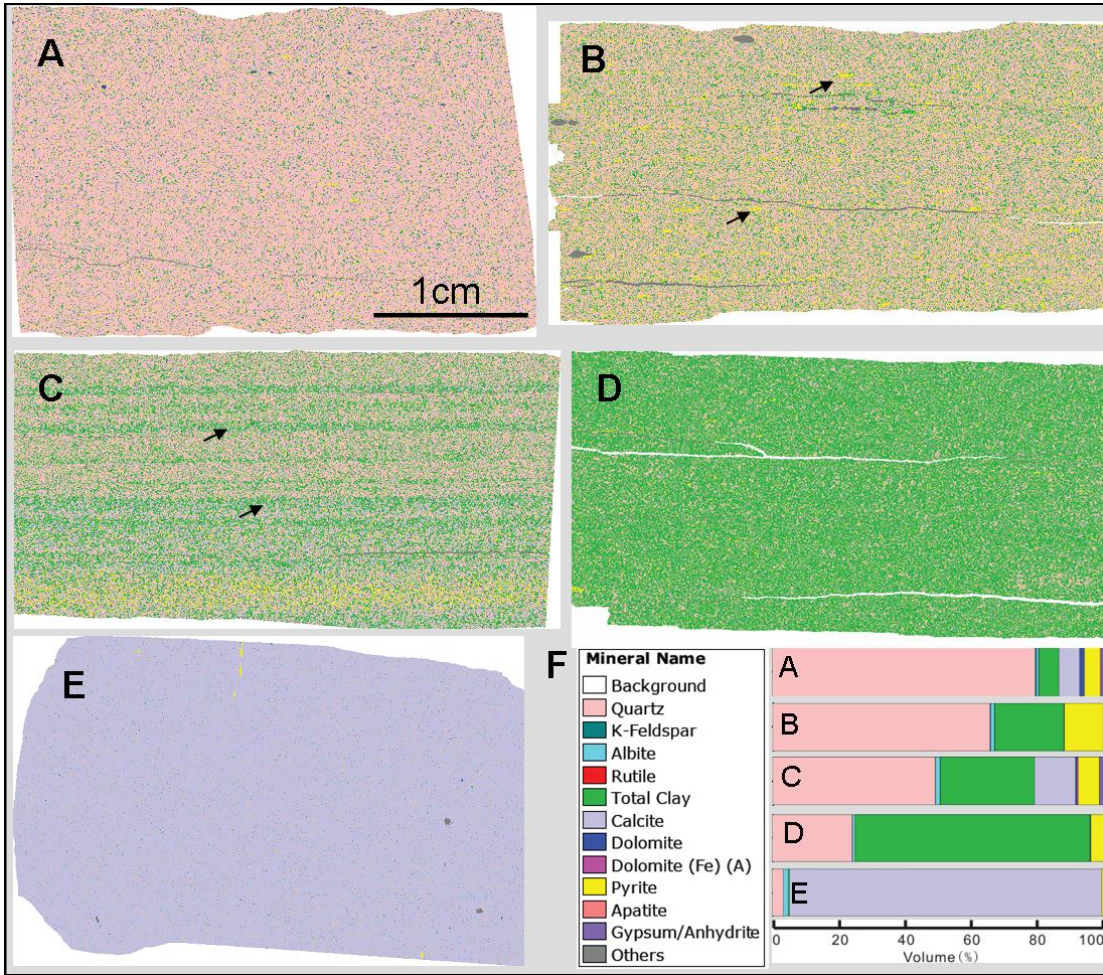


Fig. 4.5. QEMSCAN images showing the mineral distribution and fabric of representative samples from the five lithofacies. A) Massive mudstone; B) Pyritic mudstone, arrows referring to the pyrite nodules and laminae; C) Laminated mudstone, arrows referring to the lamination structure; D) Bioturbated mudstone; E) Carbonate; F) Legend for mineralogy and volume percentage of mineral composition for the five samples.

#### 4.4.2 TOC content, major oxides concentration and mineralogy

TOC content for all samples in our data set ranges from 0.04 to 8.25 wt.%, with a mean value of 3.09% (Dong et al., 2015a). Lithofacies vary systematically in TOC content (Fig. 4.7A). Massive mudstone samples are richest in TOC, ranging from 0.82 to 8.25%, averaging 4.23 wt.%. Pyritic mudstone samples have TOC values ranging from

0.3 to 6.81 %, averaging 3.44 wt.%. Laminated mudstone samples have relatively low TOC, between 0.24 and 7.09 % (mean TOC = 2.02 wt.%). Bioturbated mudstone and carbonate mudstone samples have the lowest TOC values, between 0.04 and 3.05 % (mean TOC = 1.11 wt.%).

The oxides SiO<sub>2</sub>, Al<sub>2</sub>O<sub>3</sub> and CaO represent the major components of quartz, clay and carbonate minerals, indicated by the strong correlation coefficient between major oxides and quantitative mineralogy from XRD analysis (Fig. 4.6), so their concentrations can be used to represent the concentration of quartz, clay and carbonate minerals, respectively. Oxide compositions differ greatly among lithofacies (Fig. 4.7). The massive mudstone and pyritic mudstone lithofacies are relatively rich in SiO<sub>2</sub>, ranging from 9.9-80.1% and 12.3-89.4% with average values of 56.3 and 66.5%, respectively. The laminated mudstone and bioturbated mudstone lithofacies are richer in Al<sub>2</sub>O<sub>3</sub>, with concentrations of Al<sub>2</sub>O<sub>3</sub> ranging from 2.0-17.0% and 9.1-19.7% with average values of 9.2 and 17.1%, respectively. The carbonate lithofacies is richest in CaO, ranging from 43.8-52.6% with an average of 47.6%.

The mineral components identified by X-Ray Diffraction (XRD) are shown in Table 4.2 and include quartz, K-feldspar, plagioclase, calcite, dolomite, pyrite and clay minerals (Dong et al., 2015b). The clay fraction is dominated by illite and mixed layer illite/smectite, plus a trace of chlorite in some samples.

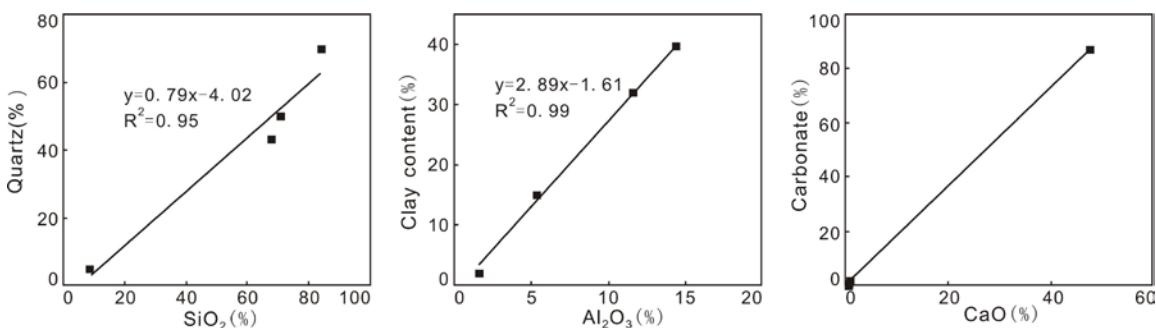


Fig. 4.6. Correlation between the concentrations of selected major oxides (SiO<sub>2</sub>, Al<sub>2</sub>O<sub>3</sub> and CaO) and mineralogy from XRD analysis (quartz, clay and carbonate) (Dong et al., 2015b).

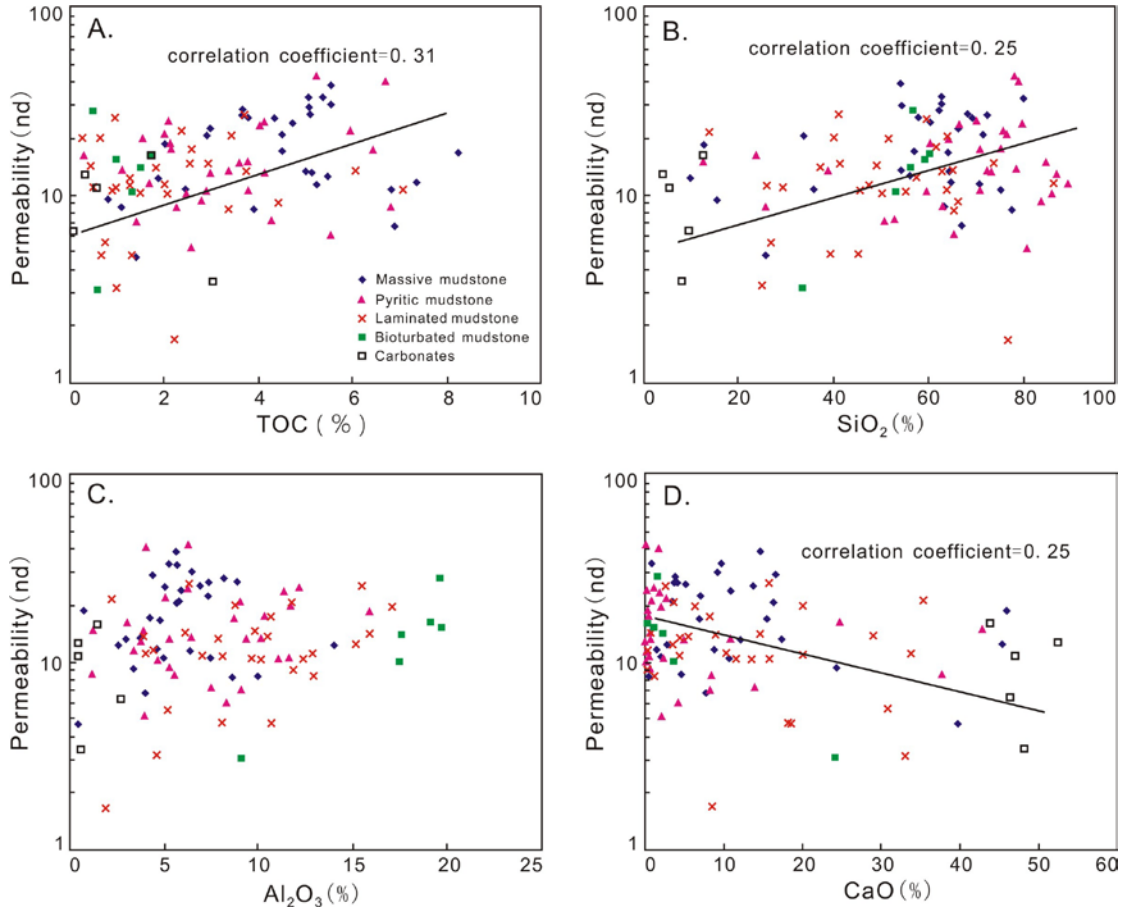


Fig. 4.7. The relationship between permeability and TOC content, concentrations of major oxides, SiO<sub>2</sub>, Al<sub>2</sub>O<sub>3</sub>, CaO, representing quartz, clay and carbonate, respectively.

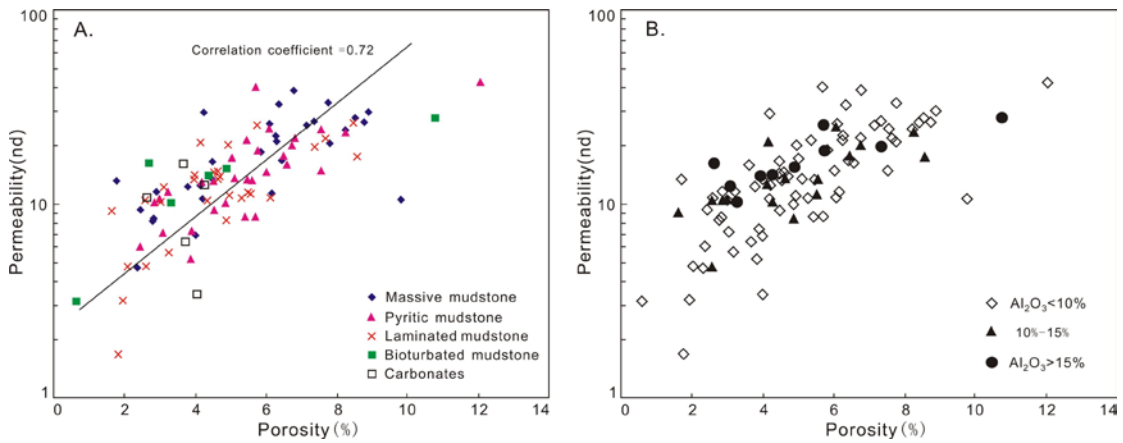


Fig. 4.8. Correlation between porosity and permeability for Horn River Shale samples. Legend shows the lithofacies (A) and the concentration of Al<sub>2</sub>O<sub>3</sub>(B).

#### **4.4.3 Permeability**

Matrix permeability profiles from the EOG Maxhamish, Imperial Komie, Nexen Gote and ConocoPhillips McAdam cores are shown in Figs. 4.3 and 4.4. The average permeability for all the samples is 15.6 nD, ranging from 1.7 to 42.8 nD (Fig. 4.8A). In general, permeability is highest in the massive mudstone samples, with an average permeability of 19 nD (Fig. 4.8A). Pyritic mudstone samples are characterized by permeability ranging from 5.2-42.8 nD with an average of 16 nD. Permeabilities are relatively low in laminated mudstone, bioturbated mudstone and carbonate samples with average values of 12.8, 14.5 and 9.8 nD, respectively.

#### **4.4.4 Pore system**

Porosity measured on core samples ranges from 0.62% to 12.04%, averaging 5.1% (Dong et al., 2015a). Pores are categorized as micropores (pore diameter < 2 nm), mesopores (2-50 nm) and macropores (pore diameter > 50 nm) by the International Union of Pure and Applied Chemistry (Sing, 1985). Loucks et al. (2012) recognized three general types of pores in organic-rich shale formation: organic matter-hosted pores, interparticle pores developed between grains and crystals, intraparticle pores contained within a particle boundary, and fractures. In our Horn River Shale samples, mesopores and macropores were observed in the high resolution SEM images (Figs. 4.9, 4.10 and 4.11), while micropores are smaller, below the limit of the SEM images resolution (Dong and Harris, 2013). All three fundamental pore types were observed in the Horn River Shale samples (Figs. 4.9, 4.10 and 4.11).

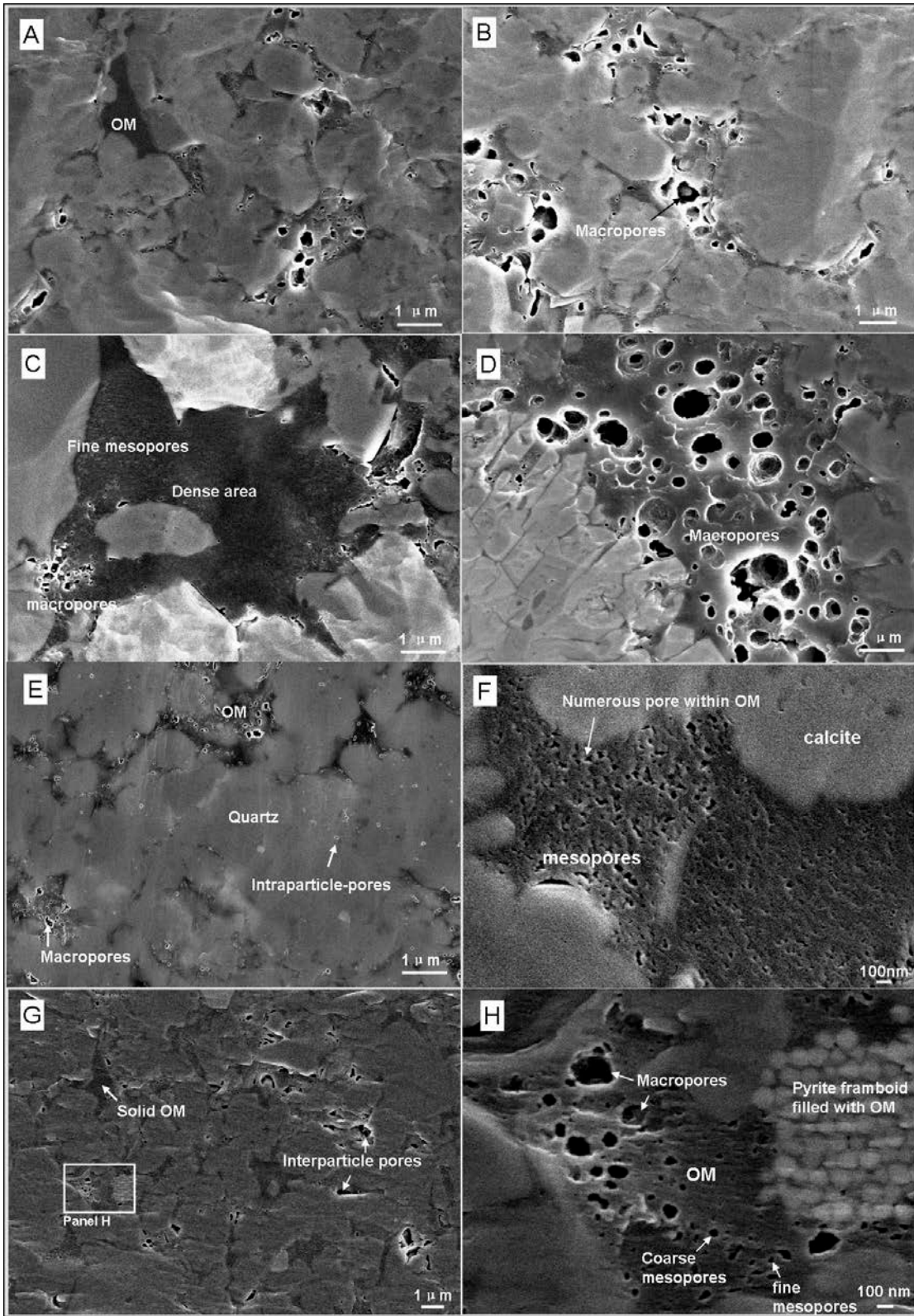


Fig. 4.9. SEM images showing pore structure of organic-rich shale samples, OM: organic

matter. (A, B, C, D) Samples M2, organic matter in this sample develops bubble-like macropores. (E) Samples McA, organic matter-hosted pores in dispersed organic matter. (F) Sample IK4, porous organic matter, where most of the pores are mesopores. (G, H) Sample IK2, organic matter shows heterogeneity in pore development.

Pores are common in the organic matter and are predominately round or ellipsoidal in cross-section with a wide range of pore diameters, ranging from a few nanometers (Figs. 4.9C, E, F and H) to greater than 1 micron (Fig. 4.9D). Pore networks within organic matter are strongly heterogeneous, with both non-porous solid organic matter and porous organic matter commonly observed within the same SEM image (Figs. 4.9C and G). The pore size of organic matter-hosted pores is also highly variable; for example, sample IK4 is dominated by mesopores (Fig. 4.9F), whereas sample M2 dominated by macropores (Figs. 4.9A, B and D).

Interparticle pores are observed between quartz crystals, calcite crystals and other detrital particles, such as feldspar (Figs. 4.10A, B, C, G and H). These pores display triangular and elongated shapes that are substantially different in morphology and size from organic matter-hosted pores. The pore size and morphology of interparticle pores depends on the surrounding minerals, geometry and arrangement of adjacent particles. Most interparticle pores are much larger than organic matter-hosted pores, typically greater than 100nm. Interparticle pores are also present between fine-grained phyllosilicate particles that occupy primary pores between carbonate particles (Fig. 4.11G). These pores are dissolution-modified primary pores and shows variable sizes and shapes.

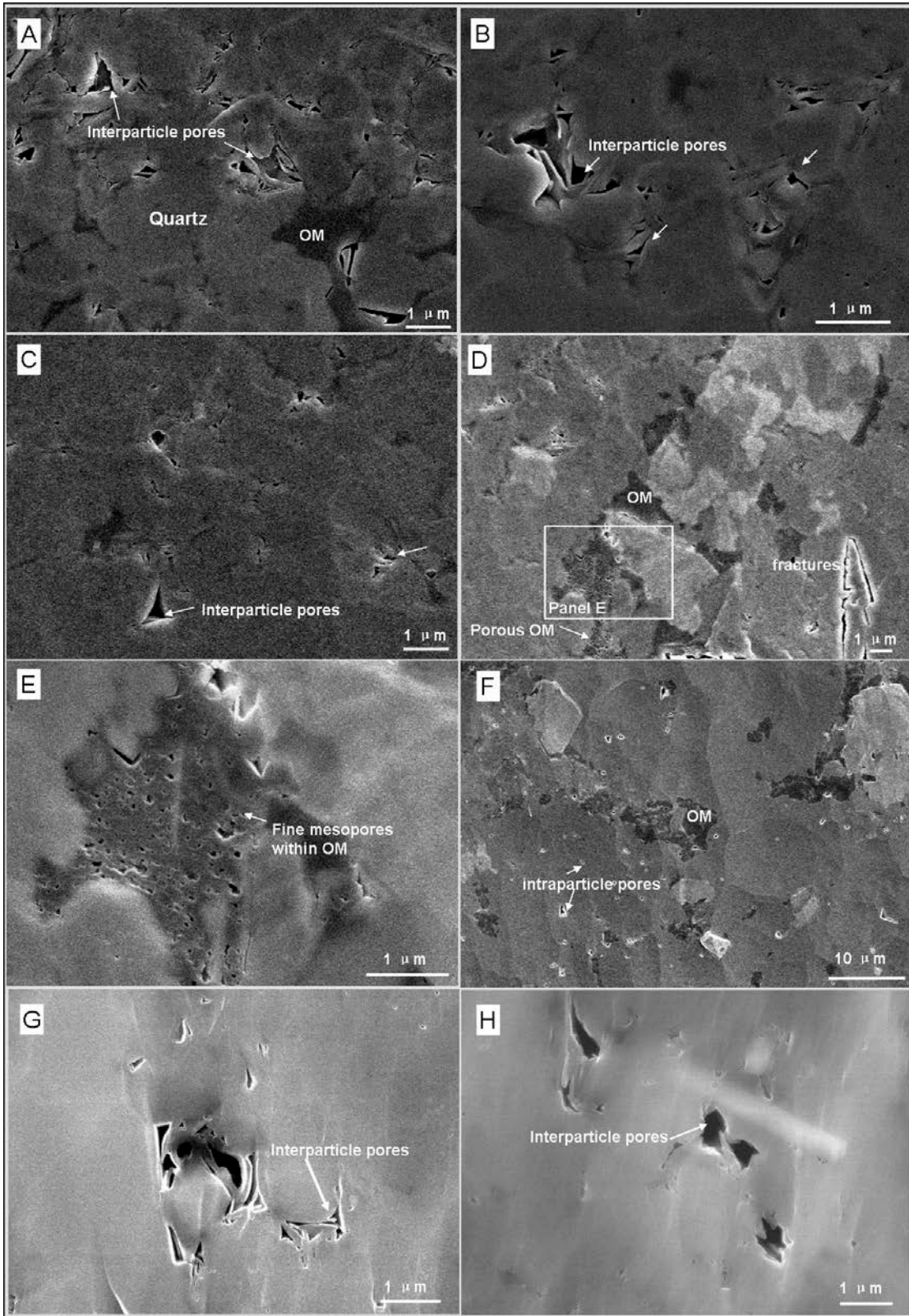


Fig. 4.10. SEM images showing pore structure of quartz-rich shale samples. (A, B, C)

Sample IK1, large-sized interparticle pores are present between quartz crystals indicated by white arrows. (D, E, F) Sample M1, mesopores developed within organic matter and intraparticle pores. (G, H) Sample NG1, interparticle pores with irregular shape.

Intraparticle pores are found within particles or mineral grains, such as clay minerals, carbonate grains, pyrite framboids, apatite and fossil fragments. They include primary pores preserved during burial and diagenetic processes or secondary pores generated by dissolution. Pore spaces within clay aggregates are common in clay-rich samples (Figs. 4.11B and C). Pyrite framboids, aggregates of submicron pyrite crystals, are relatively common in Horn River Shale (Fig. 4.9H and Fig. 4.11C). Both residual organic matter (Fig. 4.9H) and fine mesopores (Fig. 4.11C) occur between the submicron pyrite crystals. These pores may be secondary bubble pores in organic matter or primary pores that resulted from incomplete filling of framboids by organic matter. Fossil fragments such as spicules with hollow chambers are sites for primary intraparticle pores (Fig. 4.11A). Apatite is also found to provide another space for porosity development (Fig. 4.11F). Numerous intraparticle pores are present within carbonate grains due to carbonate dissolution which are clearly of diagenetic origins (Figs. 4.11F and H).

All microfractures observed in the Horn River Shale are completely open and lack cements filling (Figs. 4.11D and E). In clay-rich samples, the microfractures are probably artificial shrinkage cracks as clays dehydrate (Fig. 4.11D). In the carbonate-rich samples, the observed micro-fractures surrounding calcite grains are probably natural fractures (Fig. 4.11E).

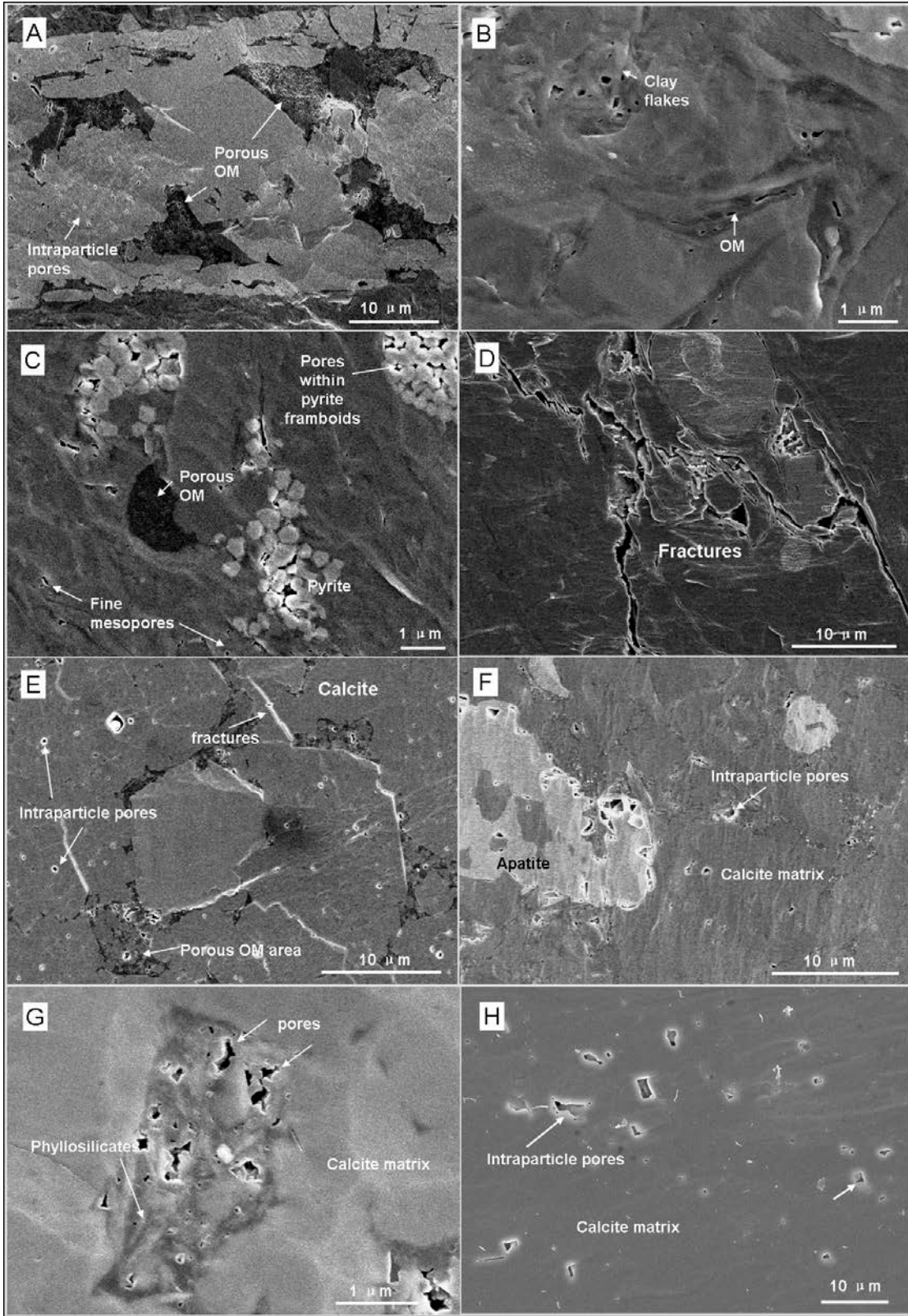


Fig. 4.11. SEM images showing pore structure of clay-rich shale samples (A, B, C, D)

and carbonate-rich samples (E, F, G, H). (A) Sample M3, porous organic matter within fossil fragments. (B) Sample IK3, mesopores are associated with twisted clay flakes. (C, D) Sample NG3, pores developed within pyrite framboids and the presence of microfractures. (E) Sample IK5, intraparticle pores and fractures developed within carbonate minerals. (F, G) Sample NG4, intraparticle pores occurred in calcite matrix and apatite minerals (F); mixture of pores, organic matter and phyllosilicates filled in primary pores between carbonate grains (G). (H) Sample Mc2, intraparticle pores developed within carbonate grains.

#### **4.4.5 Pore throat size distributions**

Porosity and pore size distributions, calculated from nitrogen adsorption experiments, were presented by Dong et al. (2015a). These data showed that the Horn River Shale samples contain mixtures of macropores, mesopores and micropores. Pore throat size distributions are more critical than pore size distributions to estimations of permeability and in our study were calculated from mercury injection data (Fig. 4.12). These are grouped into six histograms according to their TOC contents. Group A, B and C samples, defined as organic-lean groups, have TOC contents ranging from 0.24-1.53wt.%, 1.55-2.2wt.%, 2.24-2.93 wt.%, respectively. Group D, E and F samples, defined as organic-rich groups, have TOC contents ranging from 3.01-4.46 wt.%, 4.54-6.72wt.% and 6.81-8.25wt.%, respectively.

Pore throat diameter distributions are increasingly skewed towards smaller values with increasing TOC content. Organic-lean groups (TOC from 0.24-2.93%) are characterized by asymmetric distributions with dominant pore throat radii greater than 20 nm. Organic-rich groups (TOC ranges from 3.01 to 8.25%) are dominated by pore throat diameter less than 10nm. Median pore throat diameter is negatively correlated to TOC content (Fig. 4.13A), but no association with major inorganic components is evident (Figs. 4.13B, C and D).

Mercury intrusion porosimetry measures the volume of mercury injected into the

connected pore space of the rock, so the mercury injection data can be used to calculate effective porosity. The porosity calculated from mercury injection ranges from 0.6% to 2.9%, averaging 1.5%, which is much lower than total porosity measured by helium pycnometer. There is a moderate positive correlation between TOC content and effective porosity, yielding a correlation coefficient of 0.44 (Fig. 4.14).

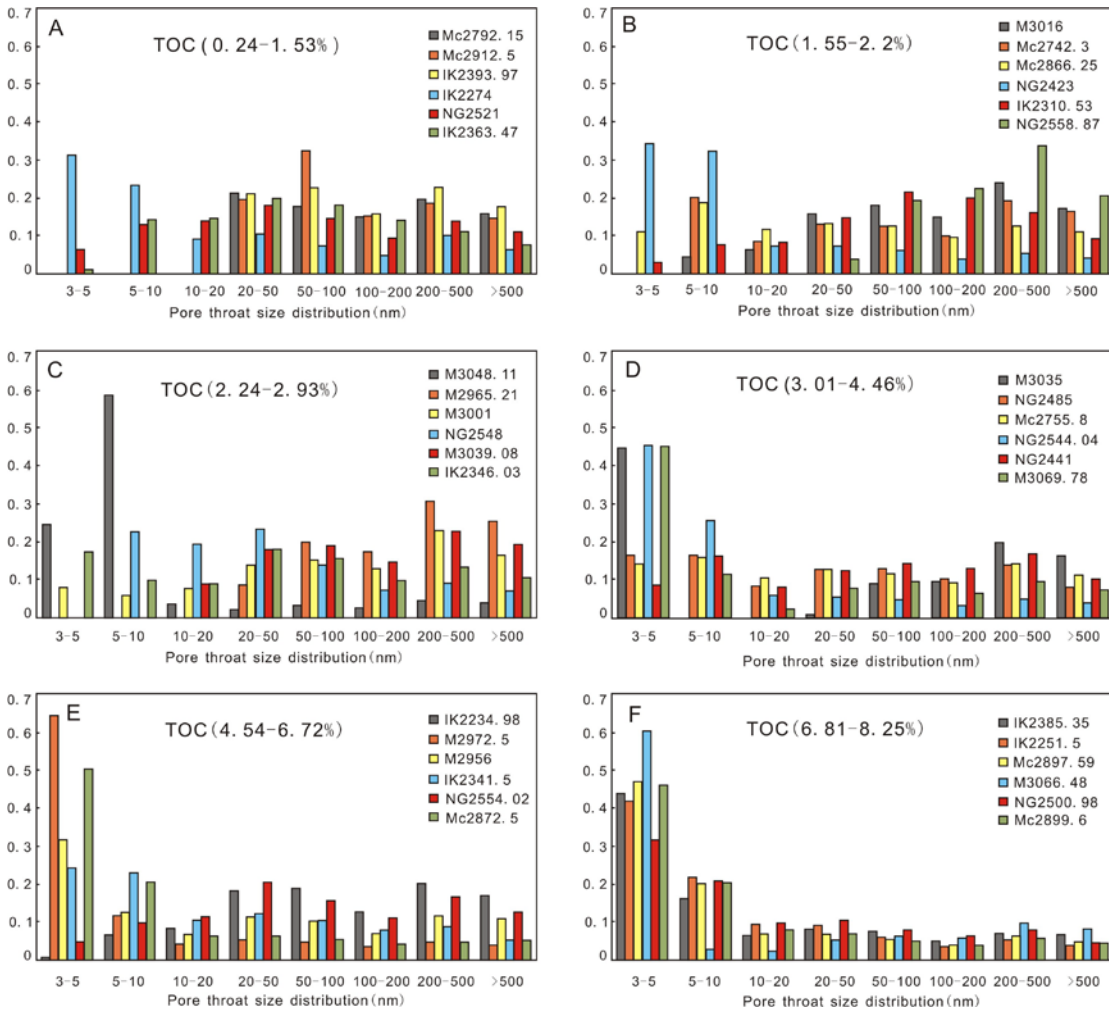


Fig. 4.12. Histogram of pore throat size distribution calculated from mercury injection data. (A, B, C) organic lean group; (D, E, F) organic-rich group. The legends in the upper right of each histogram represents different samples.

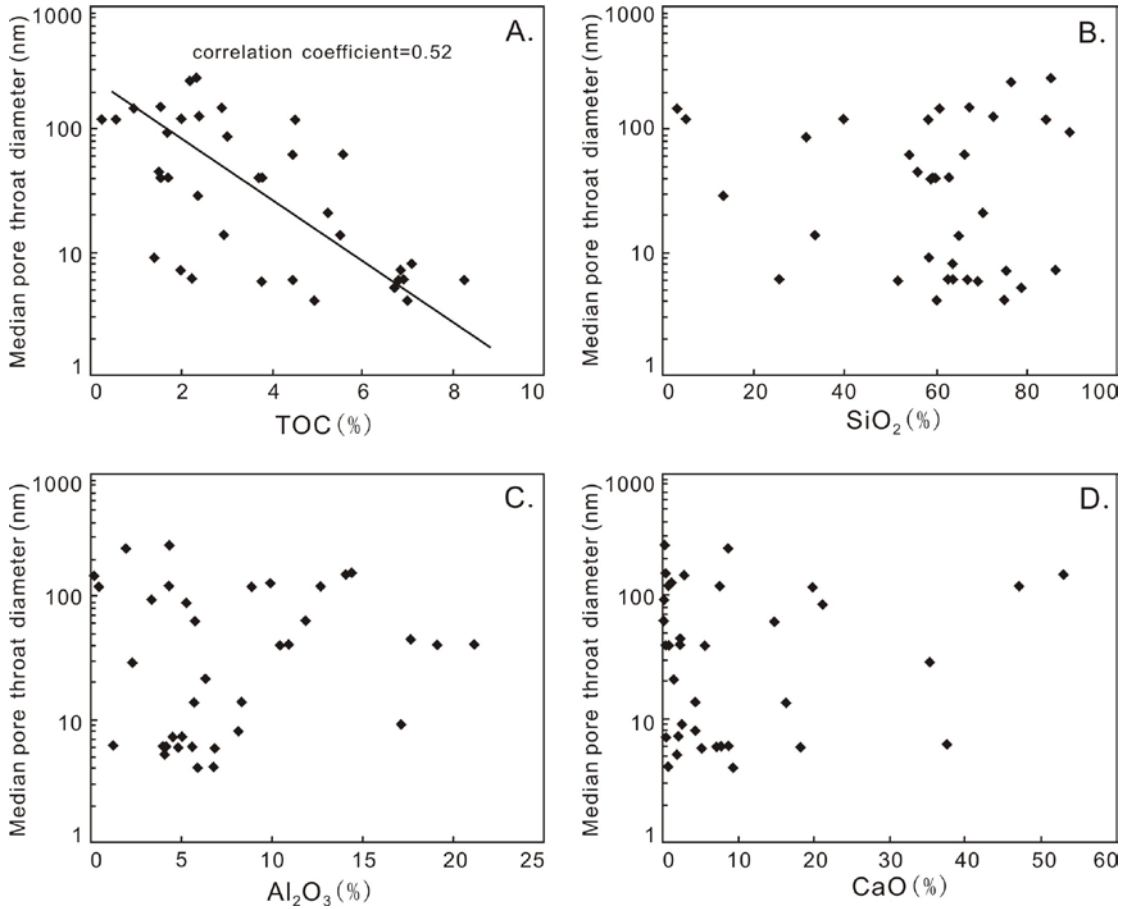


Fig. 4.13. The relationship between median pore throat diameter calculated from mercury injection data and shale composition.

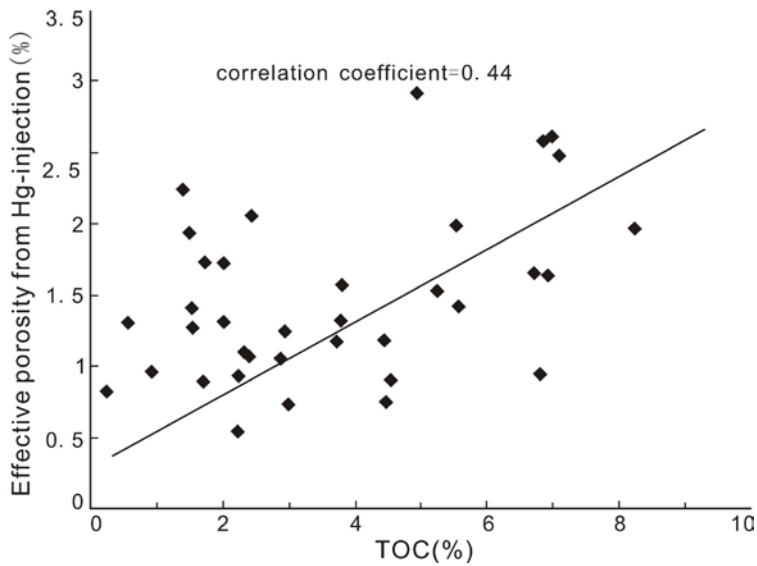


Fig. 4.14. Effective porosity calculated from mercury injection data versus organic

matter concentration (TOC content).

## **4.5. Discussion**

### **4.5.1 Relationship between porosity and permeability**

Previous studies demonstrated that the relationship between porosity and permeability is primarily controlled by the clay content (Yang and Aplin, 2007; 2010). At a given porosity, clay-poor mudstones are much more permeable than clay-rich mudstones (Dewhurst et al., 1998, 1999). The samples in the Dewhurst et al. (1998, 1999) studies are shallowly buried London clay, with a TOC content between 0.2 and 0.9 wt.%. The samples in the study of Yang and Aplin (2007) are core samples from the North Sea and Gulf of Mexico, with a range of TOC from 0.1 to 2.4 wt.%. Samples in those studies are organic-lean mudstones and no organic matter-hosted pores were reported in their studies. In organic-lean mudstones, clay fraction is regarded as the most significant parameter affecting the relationship between porosity and permeability (Yang and Aplin, 2010). The wide range of permeability variation can be explained by the differences in grain size, which is in turn affected by the clay content (Dewhurst et al., 1998, 1999; Yang and Aplin, 2007).

In the Horn River Shale dataset, the relationship between porosity and permeability does not correlate with the concentration of  $Al_2O_3$ , which is an approximation for clay content (Fig. 4.8B). The primary reasons for the contrast between our results and those of Dewhurst et al. (1998, 1999) and Yang and Aplin (2007) are the high organic content and the high maturity of the shale samples in our study. The samples in this study have a TOC content range of 0.04-8.25 wt.%, with a mean value of 3.09%, and are within the dry gas window. Pores developed within organic matter, which are of secondary origin, contribute significantly to porosity and permeability.

Porosity-permeability relationships are shown in Fig. 4.8A. Our permeability data shows a logarithmically positive correlation with porosity, yielding a correlation coefficient of

0.72 for all the samples (Fig. 4.8). Porosity is the strongest predictor of matrix permeability, stronger than any correlation between any compositional parameter and permeability (Fig. 4.7). Wang et al. (2009) reported that permeability measurements in crushed samples are significantly lower than that in core plugs, probably because the effects of microfractures on permeability were incorporated into the latter but not the former. The matrix permeabilities measured on crushed samples in this study, which should include only a minor effect from microfractures, range between 1.7 and 42.8 nanodarcy.

#### **4.5.2 Relationship between shale composition and pore throat size distribution**

The negative correlation between median pore throat size calculated from mercury injection data and TOC content (Fig. 4.13) suggests that organic matter concentration strongly influences median pore throat size, reflecting much smaller median pore throat size in organic-rich samples than organic-lean samples. The smaller pore throat size in organic carbon rich samples (predominantly less than 10 nm) is also evident in histograms of pore throat size distribution (Fig. 4.12). This is consistent with observations from the SEM images (Fig. 4.9), where most of the organic matter-hosted pores are less than 100 nm. Similar phenomenon was observed in the Devonian shales, Appalachian Basin, where pore throat size is much smaller in organic-rich samples (averaging 8 nm) than in organic-poor samples (averaging 22 nm) (Nelson, 2009).

Bernard et al. (2012) suggest that in the Barnett Shale, pores formed not in kerogen, but rather in bitumen probably derived from thermally degraded kerogen in oil window samples and in pyrobitumen resulting from secondary cracking of bitumen in gas window maturity samples. Although it is operationally challenging to distinguish geochemically-defined bitumen or pyrobitumen from kerogen from the SEM images, organic matter in the Horn River Shale probably consists of mixtures of kerogen, bitumen and pyrobitumen (Figs. 4.9C, D and E), as the formation is currently in the dry gas window ( $R_o > 1.6\%$ ). In this study, we define bitumen, solid bitumen and pyrobitumen

as secondary organic matter (Pommer and Milliken, 2015). A certain fraction of the buried detrital and marine kerogen has been converted to hydrocarbon and secondary organic matter, generating numerous bubble-like pores (Fig. 4.9). Pommer and Milliken (2015) identified similar processes in the Eagle Ford Shale, where, over a range of thermal maturities from oil window to gas window, original primary mineral-associated pores are largely infilled by secondary organic matter, in which much smaller organic matter-hosted pores (median size 13.2 nm) later develop.

Clay content, regarded as the most significant parameter in controlling pore throat size in some previous studies (Yang and Aplin, 2007; 2010) does not appear to be a significant control in the Horn River Shale (Fig. 4.13C). At deposition, pore throat size and connectivity is a function of the shape, size and packing pattern of the constituent clasts. Large primary pores may have been present in the Horn River Shale at low maturities and relatively shallow burial depths. Under those conditions, the presence of clay minerals damages matrix permeability by clogging pore bodies and throats (Yang and Aplin, 2007, 2010). But by the time Horn River Shale has reached its present-day high thermal maturity (gas window), primary pores were largely lost due to compaction, suggested by the twisted clay flakes (Figs. 4.11B and C). In clay-rich samples, most of the primary pores have disappeared through compaction, and only a minor amount of secondary organic matter-hosted pores are present (Fig. 4.11A and C). The correlation between clay content and pore throat size that probably existed at low maturity was effectively erased by diagenetic processes.

#### **4.5.3 Shale composition and permeability**

Organic matter-hosted pores, which are generally interpreted to have been generated during burial and maturation of organic materials (Jarvie et al., 2007; Zargari et al., 2015), have been well documented in organic-rich shales such as Barnett Shale, Woodford Shale, Marcellus Shale and the Kimmeridge Clay Formation (Loucks et al., 2009; Passey et al., 2010; Curtis et al., 2012b; Fishman et al., 2012; Milliken et al., 2013).

Previous studies demonstrate that in the Horn River Shale, secondary organic matter contains significant amount of porosity and that porosity is positively correlated with TOC content (Ross and Bustin, 2009; Chalmers et al., 2012a; Dong et al., 2015a). In the Horn River Shale, organic matter enhances permeability (Fig. 4.7A) because of its significant contribution to both total porosity and effective porosity measured by mercury injection (Fig. 4.14). TOC content is positively correlated to permeability and negatively correlated to pore throat size, indicating that higher porosity in organic carbon-rich samples overcomes the effect of smaller pore-throat size.

It is noteworthy that the control of organic carbon content on permeability is stronger in the distal areas than in the proximal areas, indicated by the correlation coefficients between TOC content and permeability (Fig. 4.16). The correlation coefficient between TOC and permeability in samples from the EOG Maxhamish well, drilled in the distal (northern) part of the basin, is 0.58, whereas the correlation coefficient for samples from the Imperial Komie well, drilled in a proximal area (southern), was -0.06. SEM images indicate that samples from the Imperial Komie core have more interparticle pores (Fig. 4.9G) than samples from the EOG Maxhamish core in which the dominant pore type is organic matter-hosted porosity (Figs. 4.9A, B, C and D). This suggests that, at the same level of TOC content, organic matter-hosted pores are the dominant pore type in samples from distal areas, whereas interparticle pores are more abundant in samples from the proximal areas.

A positive correlation between  $\text{SiO}_2$  and permeability was observed in our dataset (Fig. 4.7B). In part, this results from a positive correlation between  $\text{SiO}_2$  and TOC content (Dong et al., 2015a), and TOC content positively correlates with permeability. Abundant quartz may also be favorable for the preservation of primary pores. As shown in SEM images, interparticle pores are more evident in quartz-rich (Figs. 4.10A, B and C) and rare in clay-rich (Figs. 4.11A, B, C and D) or carbonate-rich samples (Figs. 4.11E, F, G and H). The characteristic triangular shape suggests that these pores were primary

pores rather than secondary pores that, typical of dissolution pores, display sawtooth shapes (Lei et al., 2015). Biogenic quartz, or authigenic quartz cement, has been reported in the Horn River Shale (Dong et al., 2015a). We suggest that a rigid framework formed by detrital quartz and recrystallized authigenic quartz cement limited pore collapse during burial, preserving primary interparticle pores that contribute to the matrix permeability.

No correlation between  $\text{Al}_2\text{O}_3$  and permeability was observed (Fig. 4.7C), indicating that clay content is not a significant factor controlling permeability. As porosity is the primary control on permeability, the lack of correlation between  $\text{Al}_2\text{O}_3$  and permeability may simply result from the fact that  $\text{Al}_2\text{O}_3$  is unrelated to porosity (Dong et al., 2015a).

As shown in the SEM images (Figs. 4.11A, B, C and D), fewer pores are visible in clay-rich samples than in the either organic-rich or quartz-rich samples. Although organic matter-hosted pores (Figs. 4.11A and C) and intraparticle pores (Figs. 4.11B and C) are present in the clay-rich samples, these two pore types are dispersed and small in size, less than 50 nanometers.

Several types of pores are present in carbonate-rich samples, including intraparticle pores in carbonate grains (Figs. 4.11E, F and H), organic matter-hosted pores (Fig. 4.11E) and fractures (Fig. 4.11E). Compared to organic-rich and quartz-rich samples (Figs. 4.9 and 4.10), pores within carbonate-rich samples are less abundant and more dispersed (Fig. 4.11), which limits their contribution to matrix permeability. No large-sized interparticle pores between calcite or dolomite grains were observed, indicating that most of the primary pores were filled by carbonate cements or other materials (Figs. 4.11E, F and G). Secondary pores were developed within carbonate minerals due to dissolution, probably by reaction with formation water enriched in organic acids (Fig. 4.11H).

Lithofacies exert a strong control on mineral composition and organic richness, which in turn are closely related to reservoir properties such as porosity, pore size, pore throat size, and permeability. The five lithofacies present in the Horn River Shale,

massive mudstone, pyritic mudstone, laminated mudstone, bioturbated mudstone and carbonate have variable compositions (Fig. 4.7). Massive mudstone has the highest permeability (Fig. 4.15), probably because of its highest TOC content. Pyritic mudstone has higher permeability than laminated mudstone, bioturbated mudstone and carbonate, probably because of its higher silica and TOC content. Laminated and bioturbated mudstones have moderate permeability and carbonate has the lowest permeability as they have much less TOC content and silica concentration than massive mudstone and pyritic mudstones (Fig. 4.15).

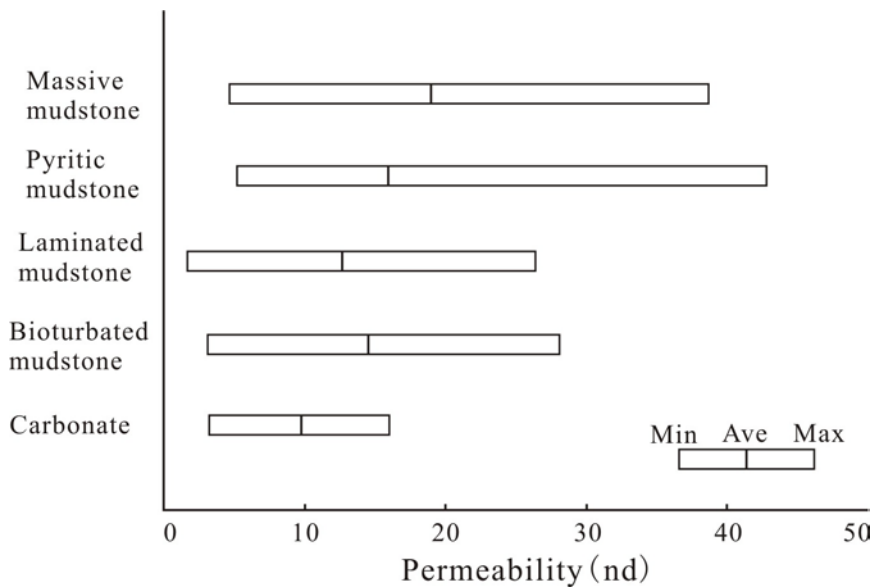


Fig. 4.15. Statistics on the permeability data among the five lithofacies.

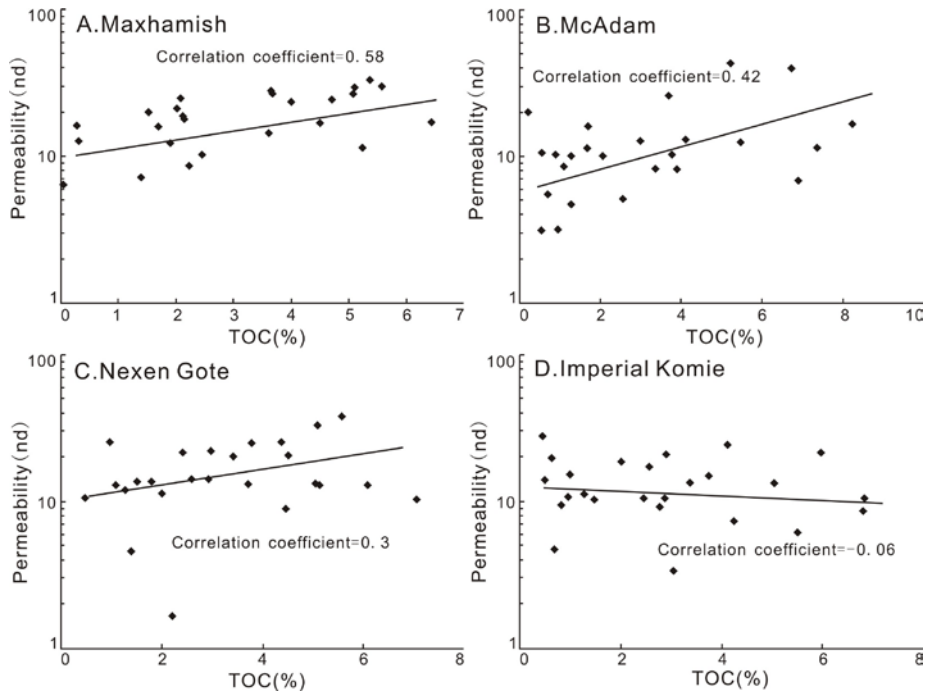


Fig. 4.16. Correlation between TOC content and permeability among different wells. A) EOG Maxhamish well, B) ConocoPhillips McAdam well, C) Nexen Gote well, and D) Imperial Komie well.

#### 4.6. Conclusion

A detailed examination of factors controlling pore throat size and permeability in high maturity Horn River Shale has been carried out. Several conclusions drawn from this study are:

(1) Permeability in the high maturity Horn River Shale is largely controlled by the porosity. Of the major geochemical components, organic matter abundance has the strongest influence on permeability.

(2) Pore throat size distribution from mercury injection data indicate that in Horn River Shale, organic carbon content rather than clay content exert a major control on the pore throat size. The samples with high TOC content have pore throat radii less than 10 nm, while the samples with low TOC content have pore throat radii greater than 20 nm. Relatively high effective porosity in organic carbon-rich samples overcomes the effect of

smaller pore-throat size on matrix permeability.

(3) SEM images confirm that pores with diameter less than 100 nm are pervasive within the organic matter, while pores with diameter greater than 100 nm typically occur between rigid quartz grains. Interparticle pores are more pervasive in quartz-rich samples, while intraparticle pores and fractures are more pervasive in clay-rich and carbonate-rich samples.

(4) Permeability, which is a combined function of organic and inorganic composition, varies among shale lithofacies. Massive mudstone and pyritic mudstone lithofacies have much higher permeability than laminated mudstone, bioturbated mudstone and carbonate, probably because of relatively high concentrations of organic carbon and silica.

#### **Acknowledgements:**

We thank the British Columbia Ministry of Energy and Mines in Victoria for the access to core data and well files, and the British Columbia Oil and Gas Commission for access to cores. We are grateful for the funding support from NSERC (grant CRDPJ 445064 – 12) and co-funders ConocoPhillips Canada, Devon Canada, Husky Energy, Imperial, Nexen-CNOOC, and Shell Canada. The authors also thank Randy Kofman for carrying out high-pressure MICP measurements in Department of Physics at the University of Alberta, Peng Li for training and carrying out SEM analysis in the National Institute for Nanotechnology at University of Alberta, Nathan Gerein for carrying out the SEM analysis in Department of Earth and Atmospheric Science at University of Alberta, and Stephen Hillier at the Hutton Institute for performing XRD analyses.

#### **4.7 References:**

Bernard, S., Wirth, R., Schreiber, A., Schulz, H.M., Horsfield, B., 2012. Formation of nanoporous pyrobitumen residues during maturation of the Barnett Shale (Fort Worth Basin). *International Journal of Coal Geology* 103, 3-11.

- Chalmers, G. R., Bustin, R. M., Power, L. M., 2012a. Characterization of gas shale pore systems by porosimetry, pycnometry, surface area, and field emission scanning electron microscopy/transmission electron microscopy image analyses: Examples from the Barnett, Woodford, Haynesville, Marcellus, and Doig units. *AAPG Bulletin* 96, 1099-1119.
- Chalmers, G.R., Ross, D.J.K., Bustin, R.M., 2012b. Geological controls on matrix permeability of Devonian gas shales in the Horn River and Liard basins, northeastern British Columbia, Canada. *International Journal of Coal Geology* 103, 120-131.
- Cui, X., Bustin, A.M.M., Bustin, R.M., 2009. Measurements of gas permeability and diffusivity of tight reservoir rocks: different approaches and their applications. *Geofluids* 9, 208-223.
- Curtis, M.E., Sondergeld, C.H., Ambrose, R.J., Rai, C.S., 2012a. Microstructural investigation of gas shales in two and three dimensions using nanometer-scale resolution imaging. *AAPG Bulletin* 96, 665-677.
- Curtis, M.E., Cardott, B.J., Sondergeld, C.H., Rai, C.S., 2012b. Development of organic porosity in the Woodford Shale with increasing thermal maturity. *International Journal of Coal Geology* 103, 26-31.
- Dewhurst, D.N., Aplin, A.C., Sarda, J.P., Yang, Y.L., 1998. Compaction-driven evolution of porosity and permeability in natural mudstones: An experimental study. *Journal of Geophysical Research* 103, 651-661.
- Dewhurst, D.N., Yang, Y.L., Aplin, A.C., 1999. Permeability and fluid flow in natural mudstones, in A.C. Aplin et al., *Muds and mudstones: Physical and fluid flow properties*, Geological Society Special Publication 158, 23-43.
- Dong, T., Harris, N. B., 2013. Pore size distribution and morphology in the Horn River shale, Middle and Upper Devonian, northeastern British Columbia, Canada, in W. Camp, E. Diaz and B. Wawak, eds., *Electron microscopy of shale hydrocarbon*

reservoirs. AAPG Memoir 102, 67-79.

Dong, T., Harris, N.B., Ayranci, K., Twemlow, C.E., Nassichuk, B.R., 2015a. Porosity characteristics of the Devonian Horn River shale, Canada: Insights from lithofacies classification and shale composition. *International Journal of Coal Geology* 141-142, 74-90.

Dong, T., Harris, N.B., Ayranci, K., Yang, S., 2015b. The impact of rock composition on geomechanical properties in a shale formation: Middle and Upper Devonian Horn River Shale, Northeast British Columbia. submitted to AAPG Bulletin.

Ferri, F., Hickin, A.S., Huntley, D.H., 2011. Besa River formation, western Liard Basin, British Columbia (NTS 094N): geochemistry and regional correlations; in *Geoscience Reports 2011*, British Columbia Ministry of Energy, Mines and Natural Gas, 1-18.

Fishman, N.S., Hackley, P.C., Lowers, H.A., Hill, R.J., Egenhoff, S.O., 2012. The nature of porosity in organic-rich mudstones of the Upper Jurassic Kimmeridge Clay Formation, North Sea, offshore United Kingdom. *International Journal of Coal Geology* 103, 32-50.

Ghanizadeh, A., Clarkson, C.R., Aquino, S., Ardakani, O.H., Sanei, H., 2015. Petrophysical and geomechanical characteristics of Canadian tight oil and liquid-rich gas reservoirs: I. Pore network and permeability characterization. *Fuel* 153, 664-681.

Hillier, S., 2003. Quantitative analysis of clay and other minerals in sandstones by X-ray powder diffraction (XRPD). *Int. Assoc. Sedimentol. Special Publication* 34, 213-251.

Hulsey, K.M., 2011. Lithofacies characterization and sequence stratigraphic framework for some gas-bearing shales within the Horn River Basin, northeastern British Columbia. University of Oklahoma, MSc. thesis, 76p.

Jarvie, D. M., Hill, R. J., Ruble, T. E., Pollastro, R. M., 2007. Unconventional shale-gas

- systems: the Mississippian Barnett shale of north-central Texas as one model for thermogenic shale-gas assessment. *AAPG Bulletin* 91, 475-499.
- Klaver, J., Hemes, S., Houben, M., Desbois, G., Radi, Z., Urai, J.L., 2015. The connectivity of pore space in mudstones: insights from high-pressure Wood's metal injection, BIB-SEM imaging, and mercury intrusion porosimetry. *Geofluids*. doi: 10.1111/gfl.12128.
- Kwon, O., Kronenberg, A.K., Gangi, A.F., Johnson, B., Herbert, B.E., 2004. Permeability of illite-bearing shale: 1. Anisotropy and effects of clay content and loading. *Journal of Geophysical Research* 109, B10205, 19p.
- Lei, Y.H., Luo, X.R., Wang, X.Z., Zhang, L.X., Jiang, C.F., Yang, W., Yu, Y.X., Cheng, M., Zhang, L.K., 2015. Characteristics of silty laminae in Zhangjiatan Shale of southeastern Ordos Basin, China: Implications for shale gas formation. *AAPG Bulletin* 99, 661-687.
- Loucks, R. G., Reed, R. M., Ruppel, S. C., Jarvie, D. M., 2009. Morphology, genesis, and distribution of nanometer-scale pores in siliceous mudstones of the Mississippian Barnett shale. *Journal of Sedimentary Research* 79, 848-861.
- Loucks, R. G., Reed, R. M., Ruppel, S. C., Hammes, U. 2012. Spectrum of pore types and networks in mudrocks and a descriptive classification for matrix-related mudrock pores. *AAPG Bulletin* 96, 1071-1098.
- Luffel, D.L., Hopkins, C.W., Shettler, P.D., 1993. Matrix Permeability measurements of gas productive shales. *SPE Paper*, 1993 SPE Annual Technical Conference and exhibition, Houston, Texas, US, 10p.
- Mallon, A.J., Swarbrick, R.E., 2008. How should permeability be measured in fine-grained lithologies? Evidence from the chalk. *Geofluids* 8, 35-45.
- Mastalerz, M., Schimmelmann, A., Drobniak, A., Chen, Y. Y., 2013. Porosity of Devonian and Mississippian New Albany shale across a maturation gradient: insights from organic petrology, gas adsorption, and mercury intrusion. *AAPG*

Bulletin 93, 1621-1643.

- McPhail, S., Walsh, W., Lee, C., Monahan, P. A., 2008. Shale units of the Horn River formation, Horn River basin and Cordova Embayment, Northeastern British Columbia: (abs.), Canadian Society of Petroleum Geologists and Canadian Well Logging Society Convention, 14 p.
- Milliken, K.L., Rudnicki, M., Awwiller, D.N., Zhang, T.W., 2013. Organic matter-hosted pore system, Marcellus Formation (Devonian), Pennsylvania. AAPG Bulletin 97, 177-200.
- Moghadam, A.A., Chalaturnyk, R., 2015. Laboratory investigation of shale permeability. SPE Paper 175919-MS, 2015 SPE/CSUP Unconventional Resources Conference, Calgary, Alberta, Canada, 30p.
- Mossop, G.D., Shetsen, I., 1994. Geological atlas of the Western Canada Sedimentary Basin, Canadian Society of Petroleum Geologists and Alberta Research Council, Special Report 4.
- Nelson, P.H., 2009. Pore-throat sizes in sandstones, tight sandstones, and shales. AAPG Bulletin 93, 329-340.
- Neuzil, C.E., 1994. How permeable are clays and shales? Water Resources Research 30, 145-150.
- Oldale, H.S., Munday, R.J., 1994. Devonian Beaver Hill Group of the Western Canada Sedimentary Basin. Geological Atlas of the Western Canada Sedimentary Basin, Canadian Society of Petroleum Geologists and Alberta Research Council, Special Report, 4p.
- Omotoso, O., McCarty, D.K., Hillier, S., Kleeberg, R., 2006. Some successful approaches to quantitative mineral analysis as revealed by the 3rd Reynolds cup contest. Clay and Clay Minerals 54, 748-760.
- Passey, Q.R., Bohacs, K.M., Esch, W.L., Klimentidis, R., Sinha, S., 2010. From oil-prone source rock to gas-producing shale reservoir-geologic and petrophysical

- characterization of unconventional shale-gas reservoirs. SPE Paper 131350, 2010 CPS/SPE International Oil & Gas Conference and Exhibition, Beijing, China, 29p.
- Pommer, M., Milliken, K., 2015. Pore types and pore-size distributions across thermal maturity, Eagle Ford Formation, Southern Texas. AAPG Bulletin 99, 1713-1744.
- ResTech, 1996. Development of Laboratory and Petrophysical Techniques for Evaluating Shale Reservoirs. GRI-95/ 0496, Gas Research Institute, Chicago, Illinois, 279.
- Rivard, C., Lavoie, D., Lefebvre, R., Séjourné, S., Lamonagne, C., Duchesne, M., 2014. An overview of Canadian shale gas production and environmental concerns. International Journal of Coal Geology 126, 64-76.
- Ross, D. J. K., Bustin, R. M., 2008. Characterizing the shale gas resource potential of Devonian-Mississippian strata in the western Canada sedimentary basin: Application of an integrated formation evaluation. AAPG Bulletin 92, 87-125.
- Ross, D. J. K., Bustin, R.M., 2009. The importance of shale composition and pore structure upon gas storage potential of shale gas reservoirs: Marine and Petroleum Geology 26, 916-927.
- Sakhaee-Pour, A., Bryant, S.L., 2011. Gas permeability of shale. SPE Paper 146944, 2011 SPE Annual Technical Conference and Exhibition, Denver, Colorado, USA, 14p.
- Sing, K.S., 1985. Reporting physisorption data for gas/solid systems with special reference to the determination of surface area and porosity. Pure and Applied Chemistry 57, 603-619.
- Slatt, R.M., O'Brien, N.R., 2011. Pore types in the Barnett and Woodford gas shales: Contribution to understanding gas storage and migration pathways in fine-grained rocks. AAPG Bulletin 95, 2017-2030.
- Tian, H., Pan, L., Zhang, T.W., Xiao, X.M., Meng, Z.P., Huang, B.J., 2015. Pore characterization of organic-rich Lower Cambrian shales in Qiannan Depression of

- Guizhou Province, Southwestern China. *Marine and Petroleum Geology* 62, 28-43.
- Wang, F.P., Reed, R.M., Jackson, J.A., Jackson, K.G., 2009. Pore networks and fluid flow in gas shales. SPE Paper 124253, 2009 SPE Annual Technical Conference and Exhibition, New Orleans, LA, USA, 8p.
- Yang, Y.L., Aplin, A.C., 1998. Influence of lithology and effective stress on the pore size distribution and modelled permeability of some mudstones from the Norwegian margin. *Marine and Petroleum Geology* 15, 163-175.
- Yang, Y.L., Aplin, A.C., 2007. Permeability and petrophysical properties of 30 natural mudstones. *Journal of Geophysical research* 112, B03206.
- Yang, Y.L., Aplin, A.C., 2010. A permeability-porosity relationship for mudstones. *Marine and Petroleum Geology* 27, 1692-1697.
- Zargari, S. Canter, K.L., Prasad, M., 2015. Porosity evolution in oil-prone source rocks. *Fuel* 153, 110-117.

**CHAPTER 5 The impact of rock composition on geomechanical properties in a shale formation: Middle and Upper Devonian Horn River Shale, Northeast British Columbia, Canada.**

**Abstract**

The geomechanical properties of a shale reservoir are essential both to the development of natural fractures and to the formation's response to hydraulic fracture stimulation. We evaluate the rock mechanical properties in the Middle and Upper Devonian Horn River Shale, including the Evie, Otter Park Members and the Muskwa Formation, using core hardness measurements, Young's modulus, Poisson's ratio, brittleness and relate these to shale composition and texture. Clay content is the most significant factor controlling the brittleness of shale rocks. The effect of quartz content on rock mechanical properties depends on the type of the quartz present in the rock: authigenic quartz is positively correlated with brittleness, but detrital quartz has little or no effect. Factor analysis indicates that carbonate increases brittleness, while no obvious correlation between TOC content and brittleness was observed in this study.

Depositional facies are related to geomechanical properties because each facies has a distinctive composition. Massive mudstone and pyritic mudstone are relatively brittle because of abundant authigenic quartz cement. Laminated mudstone and bioturbated mudstone are relatively ductile because most detrital carbonate and quartz grains are set in a matrix of clay minerals. Brittleness in Horn River Shale shows both geographic and stratigraphic variability. Increasing brittleness in the northwest part of the basin largely results from greater distance from the sediment source. The Otter Park member represents a period of major relative sea level fall and is more ductile than the underlying Evie Member and the overlying Muskwa Formation because of its high clay content.

## 5.1 Introduction

The extremely low inherent permeability of shale reservoirs necessitates hydraulic fracturing treatment to improve production rates (Bowker, 2007; Bustin and Bustin, 2012; Sone and Zoback, 2013). Variation in composition and fabric causes shale intervals to respond differently to hydraulic fracturing (Passey et al., 2010). Geomechanical properties are one of the most significant factors controlling the response of a shale formation to hydraulic fracture stimulation, and it is therefore important to identify and understand the factors affecting these properties.

Two geomechanical parameters, Young's modulus and Poisson's ratio, are considered key in the evaluation of hydraulic fracturing treatments (Rickman et al., 2008; Labani and Rezaee, 2015). Rocks with high Young's modulus and low Poisson's ratio are generally interpreted as brittle and are more likely to fracture under stress and to maintain open fractures. In contrast, rocks with low Young's modulus and high Poisson's ratio are interpreted as ductile and are more resistant to fracture initiation (Rickman et al., 2008). In some studies, these parameters have been related to mineral composition (e.g., quartz, clay, carbonates, feldspar and pyrite content) and total organic carbon (TOC) (Jarvie et al., 2007; Rickman et al., 2008; Aoudia et al., 2010; Harris et al., 2011). Quartz and carbonate are considered as relatively brittle materials, while clay and organic matter are regarded as ductile (Sondergeld, et al., 2010). Harris et al. (2011) demonstrated that the Upper Devonian Woodford Shale in the Permian Basin, Texas, displays significant stratigraphic variation in mechanical properties because of variation in rock mineralogy, which is related to varying sea level. Similarly, Slatt and Abousleiman (2011) demonstrate that geomechanical properties of shales are strongly related to stratigraphic cycles in Barnett Shale.

Gas production from Canadian shale formations started in 2005 and has significantly increased since 2007 (B.C. Oil and Gas Commission, 2014). The Middle and Upper Devonian Horn River Shale, which comprises Evie, Otter Park and Muskwa

intervals, is a major gas resource in western Canada (McPhail et al., 2008). As with other shale reservoirs, an understanding of the geomechanical properties of Horn River Shale is beneficial to optimizing hydraulic fracturing stimulation. However, neither the factors affecting mechanical properties nor the stratigraphic and geographic variations in mechanical properties have received substantial attention to date in the Horn River Shale. This study identifies key factors controlling geomechanical properties and documents regional and stratigraphic variation of these properties in the Horn River Shale.

## **5.2 Geological Setting**

The Horn River Basin (HRB), covering nearly 12,000 km<sup>2</sup>, is located in northeastern British Columbia, Canada, extending a short distance northward into the Northwest Territories, (Fig. 5.1). The Horn River Basin is situated in the northwest of Western Canada Sedimentary Basin (WCSB), a vast wedge-shaped depositional basin that existed as a passive margin along the western edge of the Canadian craton during the Middle and Late Devonian and was mainly the site of carbonate and marine shale deposition (Oldale and Munday, 1994; Hulsey, 2011). The Horn River Basin is bounded by carbonate platform on the east and south. On the west, the basin is separated from the Liard Basin by the Bovie Fault zone (Fig. 5.1). During Middle and Upper Devonian, siliciclastic sediments were thought to come from a paleotopographic high, the Peace River Arch, which was located southeast of the basin (O'Connell, 1994). Within the basin, the southern part is considered to have been proximal to sources of siliciclastic and carbonate sediment, while the northern part is relatively distal (Fig. 5.1).

The Horn River Shale sequence comprises the Evie and Otter Park Members of the Horn River Formation and the Muskwa Formation (Fig. 5.2) and ranges in age from late Givetian (approximately 393 Ma) to early Frasnian stage (approximately 383 Ma) (Oldale and Munday, 1994). The Evie Member overlies the shallow marine carbonates of the Lower Keg River Formation, which consists primarily of limestones and dolostones.

The Evie Member is a dark grey to black, calcareous mudstone, characterized by moderate to high gamma ray readings that becomes more argillaceous toward the top. It contains the highest total organic carbon (TOC) content of the Horn River Shale, averaging 3.65 wt. % (McPhail et al., 2008; Dong et al., 2015). The overlying Otter Park Member is a dark gray, pyritic, non-calcareous to calcareous or siliceous mudstone, reaching a maximum thickness of 270 meters in the southeast (McPhail et al., 2008). The Otter Park typically contains less organic matter than the Evie Member and the Muskwa Formation, averaging 2.35 wt. % TOC (Dong et al., 2015) and exhibits a low gamma ray signature in well logs. The Muskwa Formation overlies the Otter Park Member and is composed of gray to black siliceous, pyritic, radioactive, organic-rich mudstone. It varies in thickness from 30 to 60 meters and thickens to the west. Organic carbon enrichment in the Muskwa Formation is high, averaging 3.41 wt. % TOC (Dong et al., 2015). The top of the Muskwa Formation has a depth ranging between 2175 and approximately 3000m (Al-Zahrani, 2011) and is conformably overlain by the overlying Fort Simpson Formation. The Horn River Shale is currently in dry gas window, with reported thermal maturities ranging from 1.6 to 2.5%  $R_o$  (Ross and Bustin, 2008; 2009a).

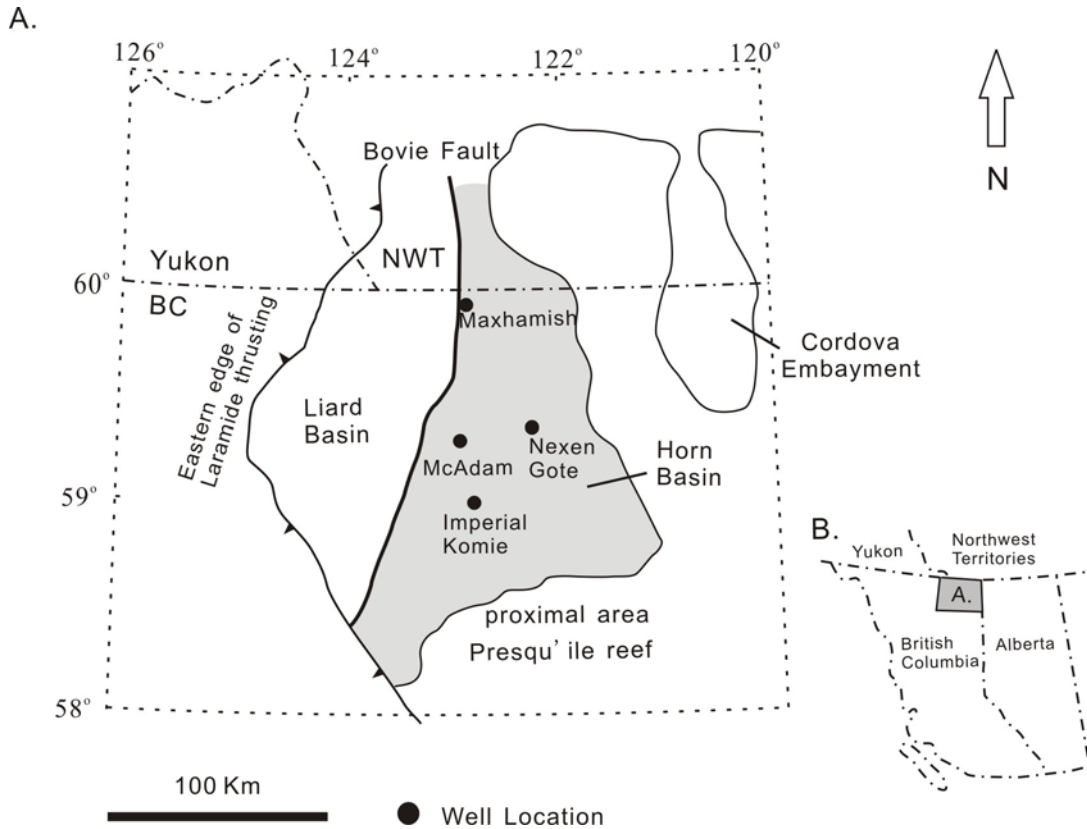


Fig. 5.1. A. Map of Horn River Basin and adjacent areas, Liard Basin and Cordova Embayment, showing well locations; B. Map of Western Canada, showing the location of the Horn River Basin (modified after Ross and Bustin, 2008).

			Liard Basin	Horn River Basin	Platform
Devonian	Upper	Frasnian	Fort Simpson Formation		Fort Simpson Formation
			Muskwa Fm	Muskwa Fm	Muskwa Fm
	Middle	Givetian	Horn River Fm	Otter Park Mbr	Slave Point Fm
					Watt Myn Fm
			Evie Mbr	Evie Mbr	Upper Keg River Fm
			Dunedin Fm	Keg River Fm	Lower Keg River Fm

Fig. 5.2. Middle and Upper Devonian stratigraphy of the Liard Basin, Horn River Basin and Cordova Embayment (modified after Ferri et al., 2011)

## **5.3 Methodology**

### **5.3.1 Materials**

This study is primarily based on four long cores drilled in the Horn River Basin. The locations of these wells (EOG Maxhamish D-012-L/094-O-15, Imperial Komie D-069-K/094-O-02, Nexen Gote A-27-I/094-O-8 and ConocoPhillips McAdam C-87-K/094-O-7) are shown in Figure 5.1. Detailed core descriptions and hardness measurements were obtained on the four cores. The four cores were sampled at approximately a 1 m interval and each sample was approximately 10 cm long.

### **5.3.2 Methods**

#### **Core description**

In order to develop a comparison between lithofacies, rock texture and composition, four cores (overall 680 m, excluding ~300 m of missing section) were logged at centimeter scale (1:100). Sedimentological and ichnological characteristics determined during core descriptions included (1) lithology, (2) grain size, (3) physical sedimentary structures, (4) trace fossil assemblages and bioturbation intensity, (5) bioclasts, and (6) presence of cements (i.e., pyrite and calcite) (Dong et al., 2015). Twenty five thin sections, including at least one thin section from each lithofacies, were analyzed to identify microscale sedimentary structures (Dong et al., 2015).

#### **Geochemical analysis**

All the core samples were split lengthwise for organic and inorganic geochemical analyses. One split was analyzed for total organic carbon (TOC) contents in Weatherford Laboratories by LECO combustion. A second sample split was analyzed at Acme Analytical Laboratories using Inductively Coupled Plasma and Inductively Coupled Plasma-Mass Spectrometry (ICP and ICP-MS) to determine the concentration of major oxides, including SiO<sub>2</sub>, Al<sub>2</sub>O<sub>3</sub>, Fe<sub>2</sub>O<sub>3</sub>, MgO, CaO, Na<sub>2</sub>O, K<sub>2</sub>O, TiO<sub>2</sub>, P<sub>2</sub>O<sub>5</sub>, and MnO (Dong et al., 2015). All the major oxide concentrations (see appendix data) are expressed in weight percent. Samples were crushed and pulverized until 85% of the material passed

through 200 mesh. Powdered samples were combined with lithium borate and digested by nitric acid. Analytical results were calibrated with laboratory internal standards, an international standard (U.S. Geological Survey standards, SCo-1, Cody Shale), and analysis of replicate samples, reported in Table 5.1.

Four samples were selected for bulk mineralogical analysis and <2 microns clay fraction analysis by x-ray diffraction performed at the James Hutton Limited laboratory in order to identify mineral components, including quartz, albite, calcite, dolomite, siderite, pyrite, apatite, smectite and illite. Received samples were wet ground (in ethanol) in a McCrone mill and then dried to produce random powder. Quantitative analysis was carried out based on the full x-ray powder diffraction patterns recorded from 4-70° 2θ using Copper Kα radiation. The clay fraction (< 2 microns) was separated from the sample by using filter peel transfer technique and scanned using Copper Kα radiation in the air-dried state, after glycolation, and after heating to 300 °C for one hour. Qualitative and quantitative analysis on clay minerals were carried out on the peak positions, shapes and intensities based on the X-ray powder diffraction patterns. Details on the bulk mineralogical analysis, clay mineralogy analysis and their standards were reported in Hillier (2003) and Omotoso et al. (2006).

### **Methods for rock mechanical properties**

Multiple parameters were utilized to evaluate geomechanical properties of the Horn River Shale, including hardness measured on slabbed core samples and Young's modulus, Poisson's ratio and brittleness calculated from dipole sonic and density logs.

An Equotip Bambino 2 hardness tester was used to perform hardness test measurements on the four long Horn River cores. In this measurement, a hard metal ball is launched at a target core sample and then rebounds, recording the rebound velocity and impact velocity. The ratio of the rebound velocity to the impact velocity is multiplied by 1000 to yield the hardness value (Leeb hardness). We measured the hardness on in the center of core slabs at a spacing of approximately 20 cm for the entire length of the cores,

avoiding fractures and rough surfaces. We obtained three measurements at each point, in order to calculate average values.

Young's modulus and Poisson's ratio can be determined through static and dynamic analysis (Labani and Rezaee, 2015). In this study, we developed dynamic Young's modulus and Poisson's ratio profiles, calculated from compressional velocity, shear velocity and density logs.

$$\text{Young's modulus} = \frac{\rho V_s^2 (3V_p^2 - 4V_s^2)}{V_p^2 - V_s^2} \quad (1)$$

$$\text{Poisson's ratio} = \frac{V_p^2 - 2V_s^2}{2(V_p^2 - V_s^2)} \quad (2)$$

where  $\rho$  is the bulk density and  $V_p$  and  $V_s$  are P-sonic wave and S-sonic wave velocities, respectively (Rickman et al., 2008).

Rickman et al. (2008) defined the brittleness as a combined function of both Young's modulus and Poisson's ratio.

$$\text{YM}_{\text{Brit}} = \frac{100(YMS - 1)}{(8 - 1)} \quad (3)$$

$$\text{PR}_{\text{Brit}} = \frac{100(PR - 0.4)}{(0.15 - 0.4)} \quad (4)$$

$$\text{Brit} = \frac{(\text{YM}_{\text{Brit}} + \text{PR}_{\text{Brit}})}{2} \quad (5)$$

where YMS and PR are the Young's Modulus (E) and Poisson's ratio ( $\nu$ ), respectively, calculated from P-wave sonic, S-wave sonic and density logs, and Brit is brittleness.

Although shale rocks have long been known to be mechanically anisotropic, a function of the anisotropic microstructure and composition, such as bedding layers, preferential alignment of clay plates, clay and organic matter content, and thermal maturity (Sone and Zoback, 2013; Melendez-Martinez and Schmitt, 2016), they are usually assumed to be transversely isotropic. All the hardness data in this study were measured parallel to the bedding plane, so we don't expect anisotropy for the hardness data.

### Scanning Electron Microscopy-Cathodoluminescence (SEM-CL)

SEM-CL imaging requires a flat, well-polished plug or thin section, as polish is critical in producing high quality SEM-CL images (Frelinger et al., 2015). Five samples (Table 5.2) representing the five major lithofacies were prepared using argon ion-milling techniques (Fischione Model 1060 SEM Mill at University of Alberta) to create smooth surface for SEM-CL analysis. SEM, SEM-CL and EDS analyses were carried out at the IFFAEM (Instrumentation Facility for Analytical Electron Microscopy) Facility at the University of Calgary. Ion-milled samples were imaged with a FEI Quanta 250 FEG field emission scanning electron microscope (FE-SEM) coupled with a Bruker Quantax EDS system to document the texture and mineral distribution. A Gatan MonoCL4Elite cathodoluminescence detector was set up with the SEM instrument to provide high sensitivity CL-SEM images. The CL-SEM system was performed using an accelerating voltage of 10 kV and a working distance of approximately 13.5 mm.

Table 5.1. Major elements concentration of Cody Shale (USGS, SCo-1), replicate sample and the recommended values.

Sample	SiO <sub>2</sub> (%)	Al <sub>2</sub> O <sub>3</sub> (%)	Fe <sub>2</sub> O <sub>3</sub> (%)	MgO(%)	CaO(%)	Na <sub>2</sub> O(%)	K <sub>2</sub> O(%)	TiO <sub>2</sub> (%)	P <sub>2</sub> O <sub>5</sub> (%)
Cody Shale, SCo-1	63.15	13.54	5.1	2.68	2.59	0.88	2.77	0.57	0.21
Replicate sample of Cody Shale, SCo-1	63.26	13.54	5	2.66	2.6	0.88	2.76	0.58	0.2
USGS recommended values of Cody Shale, SCo-1	62.8	13.7	5.13	2.72	2.62	0.9	2.77	0.63	0.21

Note: USGS refers to United States Geological Survey

Table 5.2. Five shale samples and their geochemical composition data

Well name	Depth (m)	Lithofacies	TOC (%)	SiO <sub>2</sub> (%)	Al <sub>2</sub> O <sub>3</sub> (%)	CaO (%)	Hardness
McAdam	2742.3	Massive mudstone	1.7	89.4	3.4	0.3	766
Imperial Komie	2346.08	Pyritic mudstone	2.9	33.5	5.7	16.5	543
Nexen Gote	2501.03	Laminated mudstone	7.1	64.1	8.1	4.4	565
McAdam	2866.25	Bioturbated mudstone	1.7	60	19.1	0.4	409
McAdam	2912.5	Carbonate	0.6	5.3	0.5	47.1	625

## 5.4 Results

### 5.4.1 Lithofacies

The sedimentological and ichnological characteristics of four cores were used to define major lithofacies.

#### Massive mudstone lithofacies

This lithofacies comprises silicic to calcareous, dark grey massive mudstones (Fig. 5.3A). It occurs predominantly in the Muskwa Formation and the Evie Member and to a lesser extent in the Otter Park Member, particularly in the northern part of the basin (i.e. the Maxhamish core). It typically lacks physical sedimentary structures, but rare parallel laminae, thin carbonate-rich layers, and micro-scale starved ripples are locally present. Fossil forms include dominantly silicic, calcareous or pyritic *radiolaria*, sponge spicules, and *tentaculites*, as well as rare *conodonts*. *Tentaculites* and *radiolarians* are commonly dispersed but rarely form laminae or beds. The massive mudstone lithofacies displays sparse bioturbation and is dominated by low diversity of simple trace fossils, such as *Planolites*.

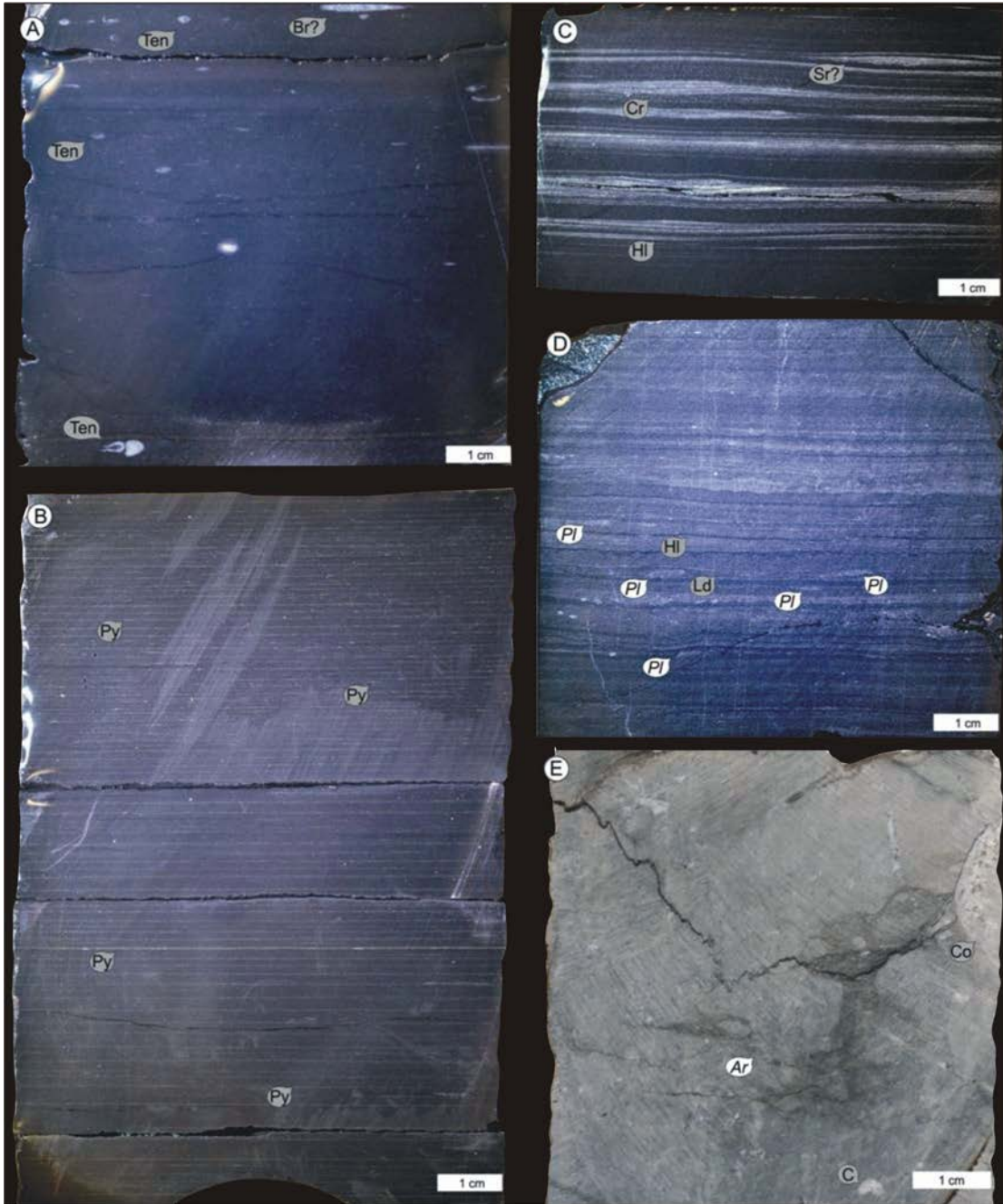


Fig. 5.3. Representative core photographs of Horn River Group lithofacies. **A.** Massive mudstone lithofacies, showing calcareous tentaculites and possible brachiopod. Ten: Tentaculites, Br: Brachiopod. **B.** Massive mudstone lithofacies displaying pyrite-rich laminae sets and pyrite lenses. Py: Pyrite. **C.** Laminated to heterolithic bedded mudstone. Cr: Climbing ripple, Hl: Horizontal lamination, Sr: Starved ripple. **D.** Intensely bioturbated mudstone. Ld: Lamina disruption, Pl: *Planolites*. **E.** Well-cemented

carbonate lithofacies. Ar: *Arenicolites*, C: Crinoid, Co: Coral.

### **Pyritic mudstone lithofacies**

The pyritic mudstone lithofacies is represented by dark grey massive mudstones with common pyrite-rich laminae and lenses and rare pyritized grains (Fig. 5.3B). Similar to the massive mudstone lithofacies, pyritic mudstones are common in the Muskwa Formation and the Evie Member. Preserved sedimentary structures include rare siliciclastic, fossil-rich laminae and micro-scale (~ 400 $\mu$ ) starved ripples. Fossil forms are also similar to the massive mudstone lithofacies. This lithofacies is sparsely bioturbated; where present, burrow types include low diversity trace assemblages of *Thalassinoides*, *Planolites*, rare *Teichichnus*, as well as bio-deformation and mantle-swirl structures.

### **Laminated to heterolithic bedded mudstone lithofacies**

This lithofacies represents interlaminated light to dark grey mudstones (Fig. 5.3C) and is commonly observed in the Otter Park Member. Preserved physical sedimentary structures include silty current ripples, climbing ripples, normal graded beds, soft-sediment deformation, double mud-drapes, thin–thick laminae sets, as well as wavy, horizontal and low-angle parallel laminae. Observed fossil forms include *radiolaria*, transported shell debris, *gastropods*, *brachiopods*, rare sponge spicules, plant material, *tentaculites*, and conodonts. This lithofacies is low to moderately bioturbated, and is dominated by lamina disruptions; burrow types include *Planolites*, *Cylindrichnus*, *Thalassinoides*, and *Phycosiphon*.

### **Bioturbated mudstone lithofacies**

Bioturbated mudstones (Fig. 5.3D) are rare in comparison to the other mudstone lithofacies and typically occur in lower intervals of the Otter Park Member. This lithofacies includes moderately to intensely bioturbated, interlaminated dark to light grey color mudstone. Intensely bioturbated units display homogeneous fabric, but remnant trace fossils are visible. Trace fossil assemblages include *Thalassinoides*, *Planolites*,

diminutive *Helminthopsis*, and *Phycosiphon*, and disrupted laminae are also a common biogenic structure. Preserved sedimentary structures include parallel to irregular horizontal laminations.

### **Carbonate lithofacies**

The carbonate lithofacies (Fig. 5.3E) is restricted to the lower part of the Evie Member. It represents massive to irregularly bedded, well-cemented assemblages of packstone and grainstone. Allochems are present in abundances reaching about 80% and include crinoids, brachiopods, intraclast, extraclasts, and bryozoans. This lithofacies displays a wide range of bioturbation intensities. Ichnological characteristics of this lithofacies vary throughout this lithofacies. Trace fossil assemblages include *Thalassinoides*, *Planolites*, *Arenicolites*, *Asterosoma*, and bio-deformation structures.

### **5.4.2 Abundance of organic matter and major oxides**

The profiles of TOC values and major geochemical oxides (Figs. 5.4, 5.5, 5.6 and 5.7) demonstrate systematic variations in the mineralogy and organic matter enrichment. TOC values fluctuate between 0.21 - 9.38 wt.% with an average of 2.89 wt.% for all the samples. TOC is highest in the Evie Member, averaging 3.86 wt.%, lowest in the Otter Park Member, averaging 2.21%, and intermediate in the Muskwa Formation, averaging 3.28 wt.%.

Three TOC cycles are present, peaking in the Evie Member, the lower Otter Park Member and the Muskwa Formation, respectively (Figs. 5.4, 5.5, 5.6 and 5.7). TOC values are typically higher in distal areas than proximal area. The average TOC values for samples from Maxhamish, Nexen Gote and McAdam cores are 3.09 wt.%, 3.1 wt.% and 2.92 wt.%, respectively, while samples from the more proximal Imperial Komie core have relatively low TOC values, averaging 2.47 wt.%.

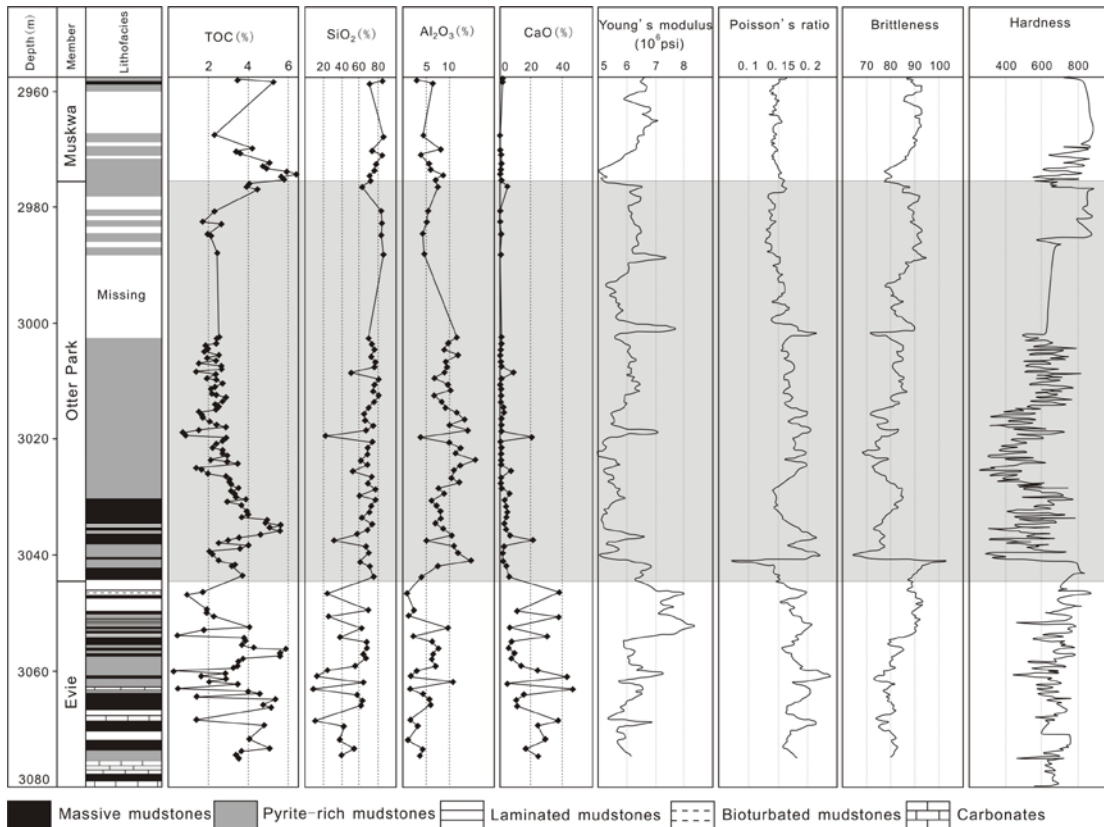


Fig. 5.4. Core description, profiles of TOC content, major oxides ( $\text{SiO}_2$ ,  $\text{Al}_2\text{O}_3$ ,  $\text{CaO}$ ), Young's modulus (psi), Poisson's ratio, brittleness and hardness for EOG Maxhamish D-012-L/094-O-15.

In shale reservoirs, selected major elements can provide a reasonable indication of bulk mineralogy, as there is a close relationship between the major element composition and the minerals present in the mudstone (Wright et al., 2010). Fig. 5.8 demonstrates that the oxides  $\text{SiO}_2$ ,  $\text{Al}_2\text{O}_3$  and  $\text{CaO}$  can be used as proxies for the quartz, clay and carbonate contents, as there is a close relationship between the selected major oxides and minerals.  $\text{SiO}_2$  concentration is highest in the Muskwa Formation, averaging 71.7%, lowest in the Evie Member, averaging 51.7%, and intermediate in the Otter Park Member, averaging 57.9% (oxide profiles for the four wells are presented in Figs. 5.4, 5.5, 5.6 and 5.7).  $\text{Al}_2\text{O}_3$  concentration is highest in the Otter Park Member, averaging 11.1%, lowest in the Evie Member, averaging 4.6%, and intermediate in the Muskwa Formation, averaging 8.4%.  $\text{CaO}$  concentration is highest in the Evie Member, averaging 17.3%, lowest in the

Muskwa Formation, averaging 2.1%, and intermediate in the Otter Park Member, averaging 7.5%. Thus, the Muskwa Formation is relatively rich in quartz, while the Otter Park and Evie Members are relatively rich in clay and carbonate. There are significant geographic differences: the concentrations of CaO and Al<sub>2</sub>O<sub>3</sub> are relatively high in proximal areas (eg. Imperial Komie well; Fig. 5.5), while the concentration of SiO<sub>2</sub> is relatively high in distal areas (Maxhamish well; Fig. 5.4).

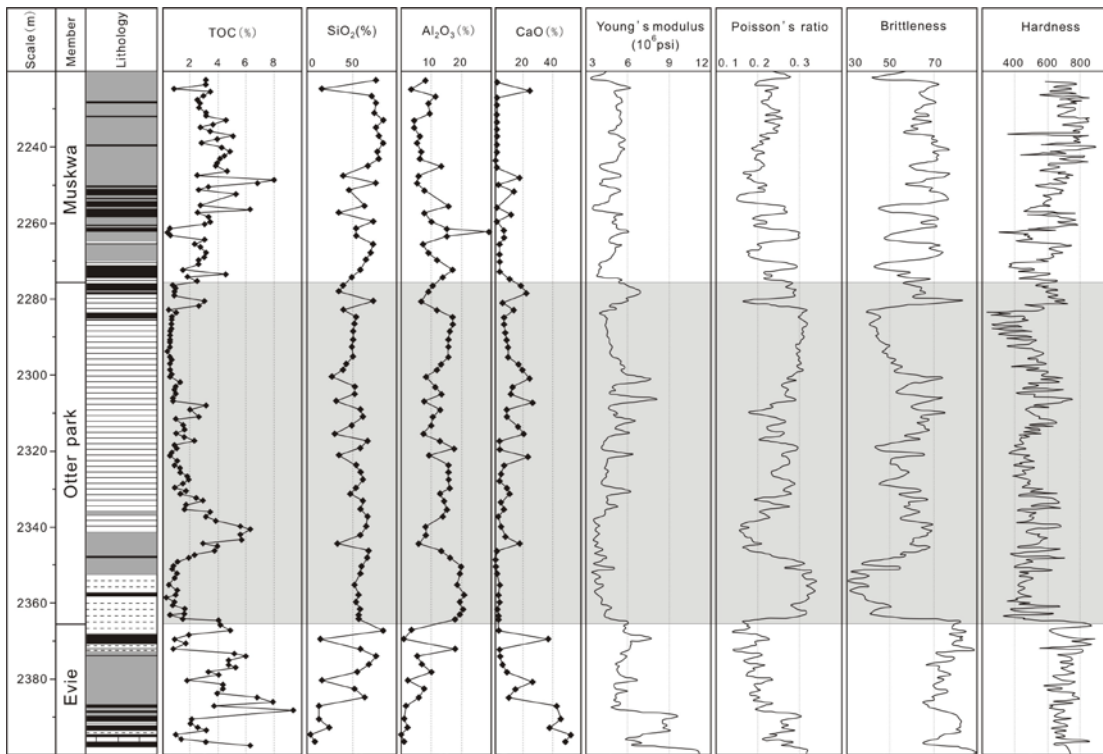


Fig. 5.5. Core description, profiles of TOC content, major oxides (SiO<sub>2</sub>, Al<sub>2</sub>O<sub>3</sub>, CaO), Young's modulus (psi), Poisson's ratio, brittleness and hardness for Imperial Komie D-069-K/094-O-02.

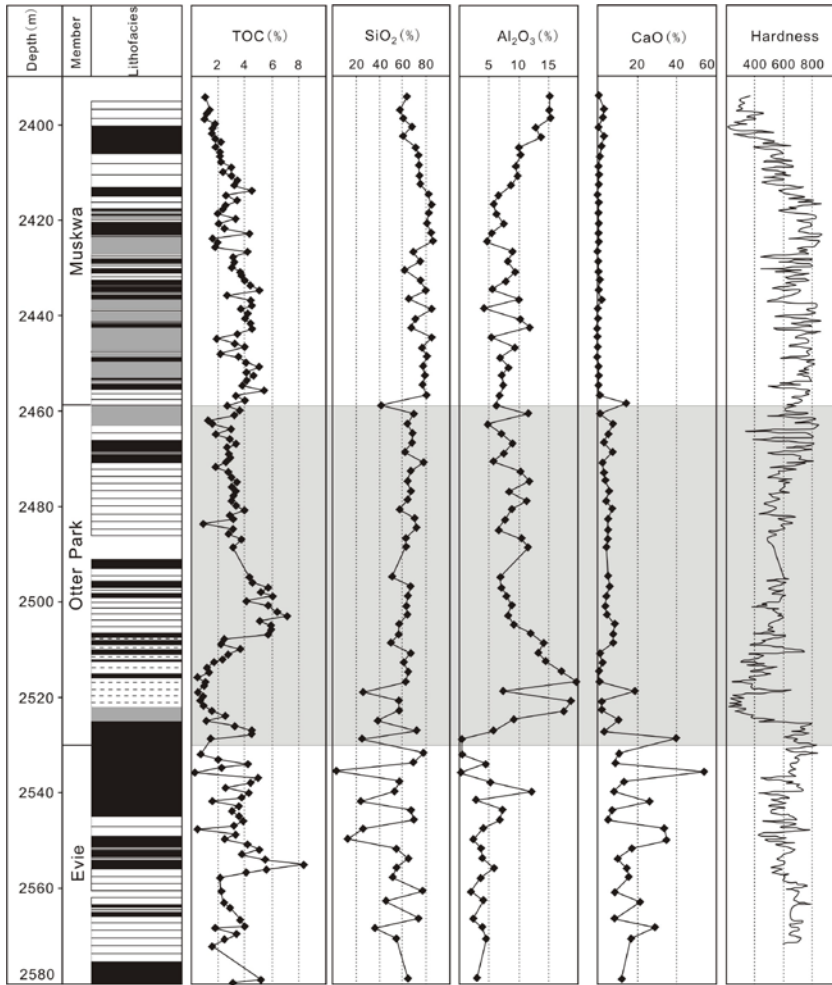


Fig. 5.6. Core description, profiles of TOC content, major oxides (SiO<sub>2</sub>, Al<sub>2</sub>O<sub>3</sub>, CaO) hardness for Nexen Gote A-27-I/094-O-8.

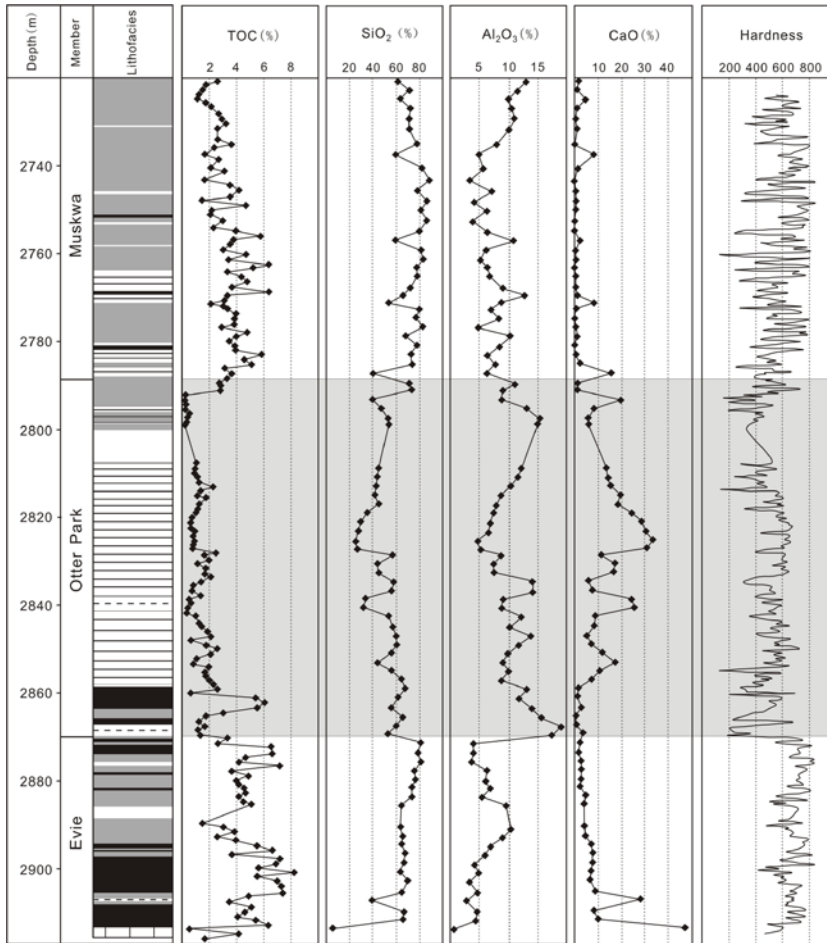


Fig. 5.7. Core description, profiles of TOC content, major oxides ( $\text{SiO}_2$ ,  $\text{Al}_2\text{O}_3$ ,  $\text{CaO}$ ) hardness for ConocoPhillips McAdam C-87-K/094-O-7.

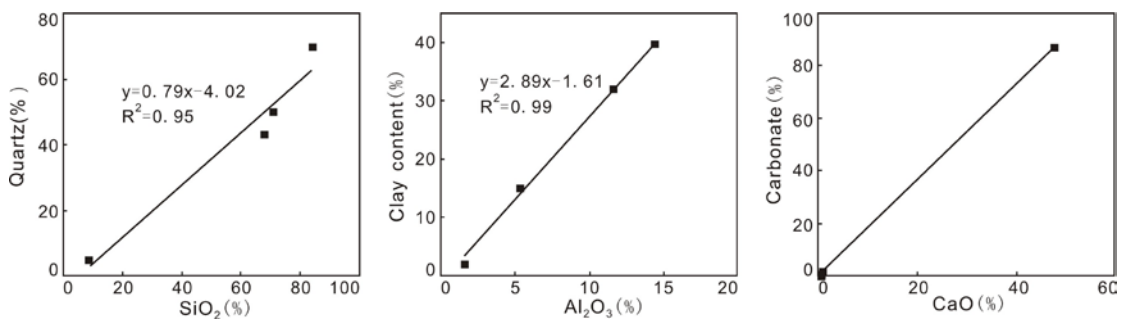


Fig. 5.8. Crossplots of selected major oxide ( $\text{SiO}_2$ ,  $\text{Al}_2\text{O}_3$  and  $\text{CaO}$ ) and mineral (quartz, clay and carbonate determined by XRD analysis) contents.

#### 5.4.3 Scanning Electron Microscopy - Cathodoluminescence (SEM-CL)

Scanning electron microscopy combined with cathodoluminescence was applied to investigate the texture of shale samples and to study petrologic features of quartz

(Schieber et al., 2000; Bernet and Basset, 2005; Milliken et al., 2012; Frelinger et al., 2015). Figs. 5.9, 5.10 and 5.11 show the scanning electron microscopy (SEM) images, EDS maps and scanning electron microscopy- cathodoluminescence (SEM-CL) images of five shale samples representing the five different lithofacies: massive mudstone (Figs. 5.9A, B and C), pyritic mudstone (Figs. 5.9D, E and F), laminated mudstone (Fig. 5.10), bioturbated mudstone (Figs. 5.11A, B and C), and carbonate (Figs. 5.11 D, E and F). Energy dispersive spectroscopy (EDS) was used to identify the mineralogy of the shale samples and SEM-CL images were used to reveal the textures of quartz minerals.

The massive mudstone sample examined here is rich in silica ( $\text{SiO}_2=89.4\%$ ). The SEM image (Fig. 5.9A) and EDS map (Fig. 5.9B) demonstrate that this sample is primarily composed of quartz minerals. The SEM-CL image (Fig. 5.9C) reveals subtle variability and fine structure in the quartz minerals. Most of the quartz crystals are less than 4 microns and display multiple generations of growth. The fine-grained detrital quartz grains are connected by authigenic quartz, forming rigid networks. The pyritic mudstone sample displayed distinct differences in texture and mineral distribution from the massive mudstone sample (Figs. 5.9D, E, F). Na-feldspar, K-feldspar, quartz, pyrite and dolomite minerals were identified in the SEM image and EDS map. Detrital quartz grains are dispersed throughout the sample (Figs. 5.9D, E), although quartz cements were observed to surround the original detrital quartz crystals (Fig. 5.9F). The laminated mudstone sample is rich in organic matter ( $\text{TOC}=7.1\%$ ) and displays lamination in the SE-SEM images and EDS maps (Fig. 5.10). This sample is dominated by detrital and massive authigenic quartz which cements individual detrital grains; minor amounts of feldspar, pyrite, calcite, dolomite and clay minerals are also present (Fig. 5.10C). In the bioturbated mudstone sample, quartz and dolomite grains are isolated within clay (Figs. 5.11A and B), and only minor quartz cements were observed surround the detrital quartz grains (Fig. 5.11C). The carbonate sample is primarily composed of calcite and dolomite minerals, as shown in the EDS map (Fig. 5.11D), with minor amounts of quartz.

Although multiple generation of authigenic quartz surround detrital quartz grains in this sample (Fig. 5.11F), the grains are dispersed in the carbonate matrix (Fig. 5.11E). EDS map shows that the calcite minerals form an interconnected matrix (Figs. 5.11D and E).

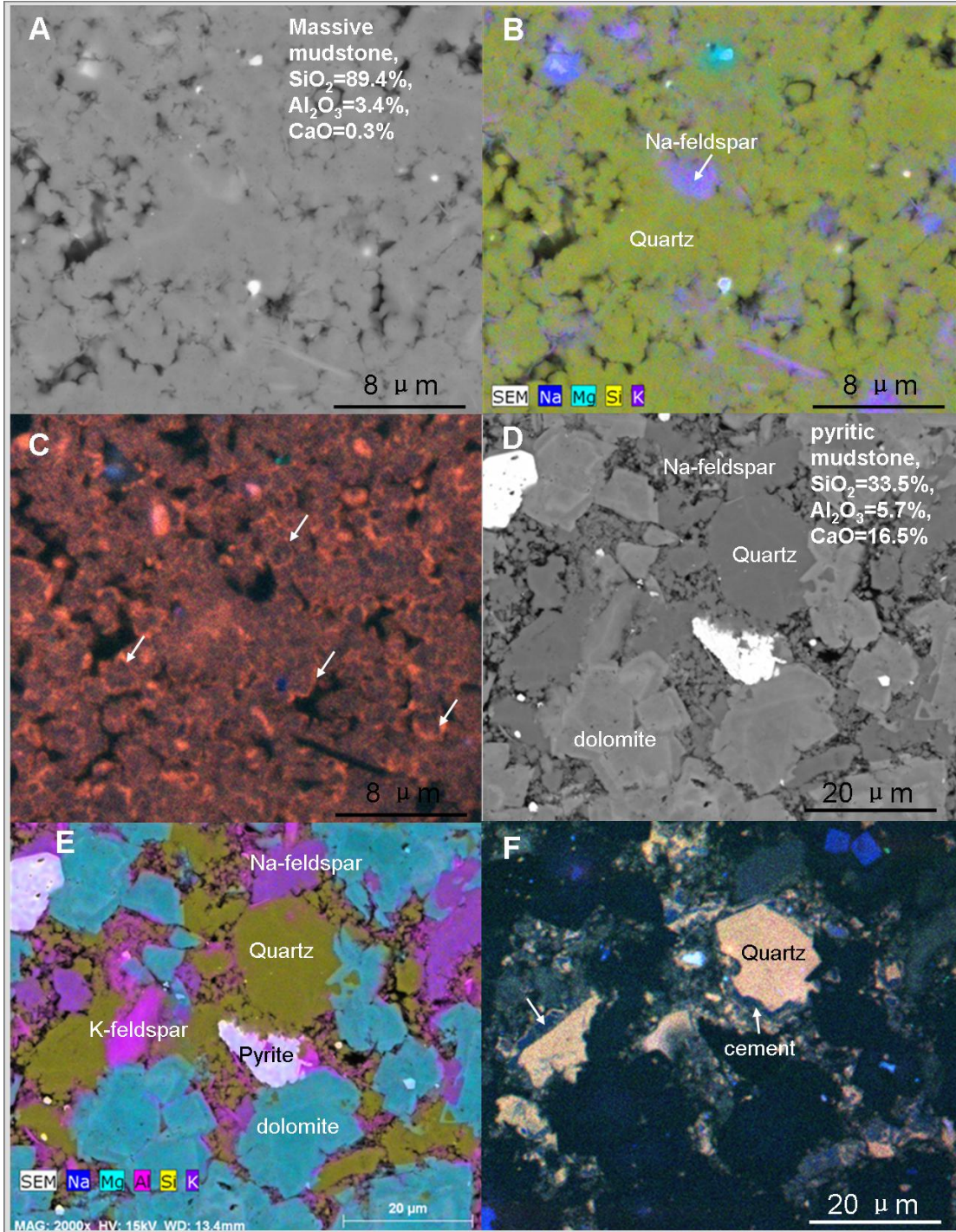


Fig. 5.9. SEM-CL images for massive mudstone (A, B, C) and pyritic mudstone (D, E, F)

samples. A) SEM image of a massive mudstone sample (ConocoPhillips McAdam C-87-K/094-O-7, 2742.3m). B) EDS map of the massive mudstone sample, green color represents quartz minerals. C) SEM-CL image of the sample, white arrow refers to authigenic quartz. D) SEM image of a pyritic mudstone sample (Imperial Komie D-069-K/094-O-02, 2346.08m). E) EDS map of the pyritic mudstone sample, green, blue, pink color represents quartz, dolomite and feldspar minerals, respectively. F) SEM-CL image of the sample, white arrow refers to quartz cements.

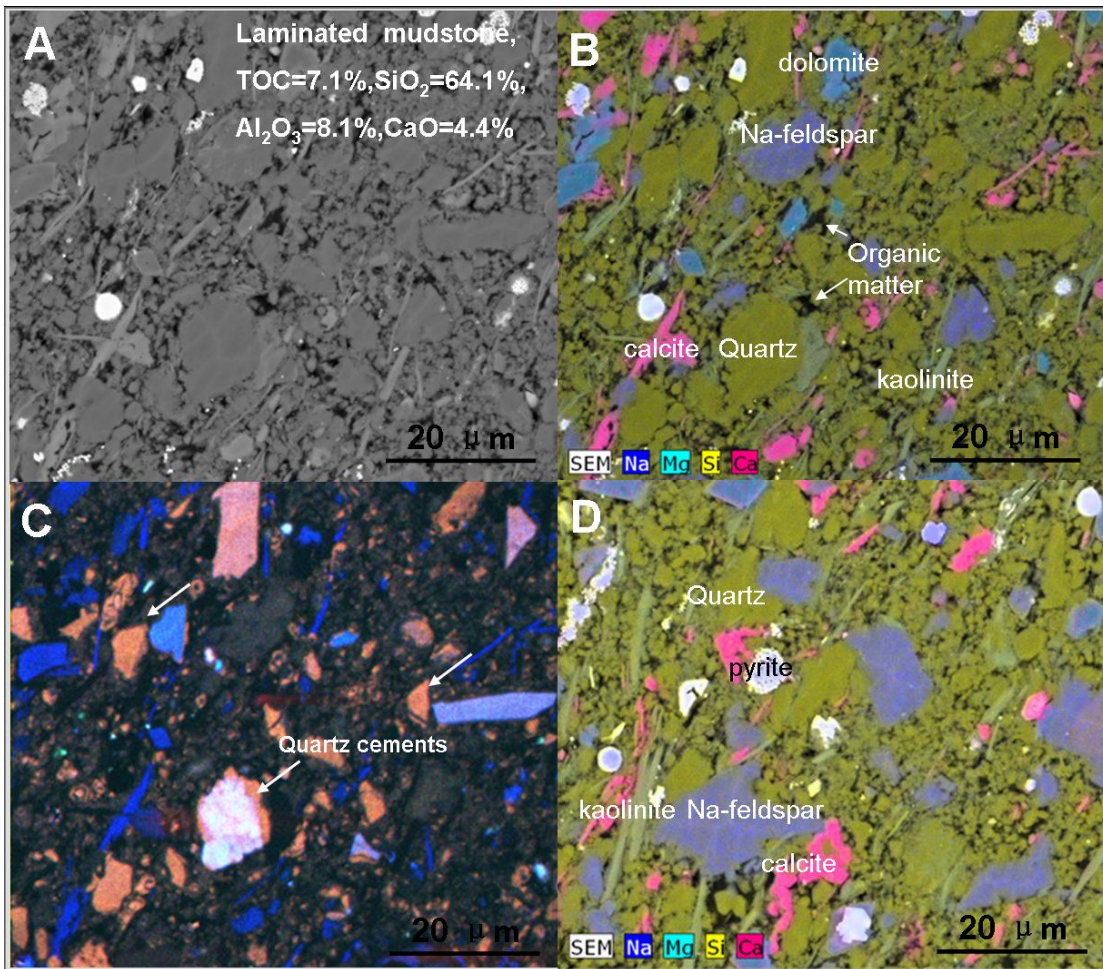


Fig. 5.10. SEM-CL images for the laminated mudstone(Nexen Gote A-27-I/094-O-8, 2501.03m). A) SE-SEM image show the lamination (lower left to upper right). B) EDS map showing the presence of quartz, feldspar, kaolinite, calcite, dolomite, pyrite and organic matter. C) CL-SEM image, white arrow refers to the quartz cements. D) EDS

map of another area in the same sample.

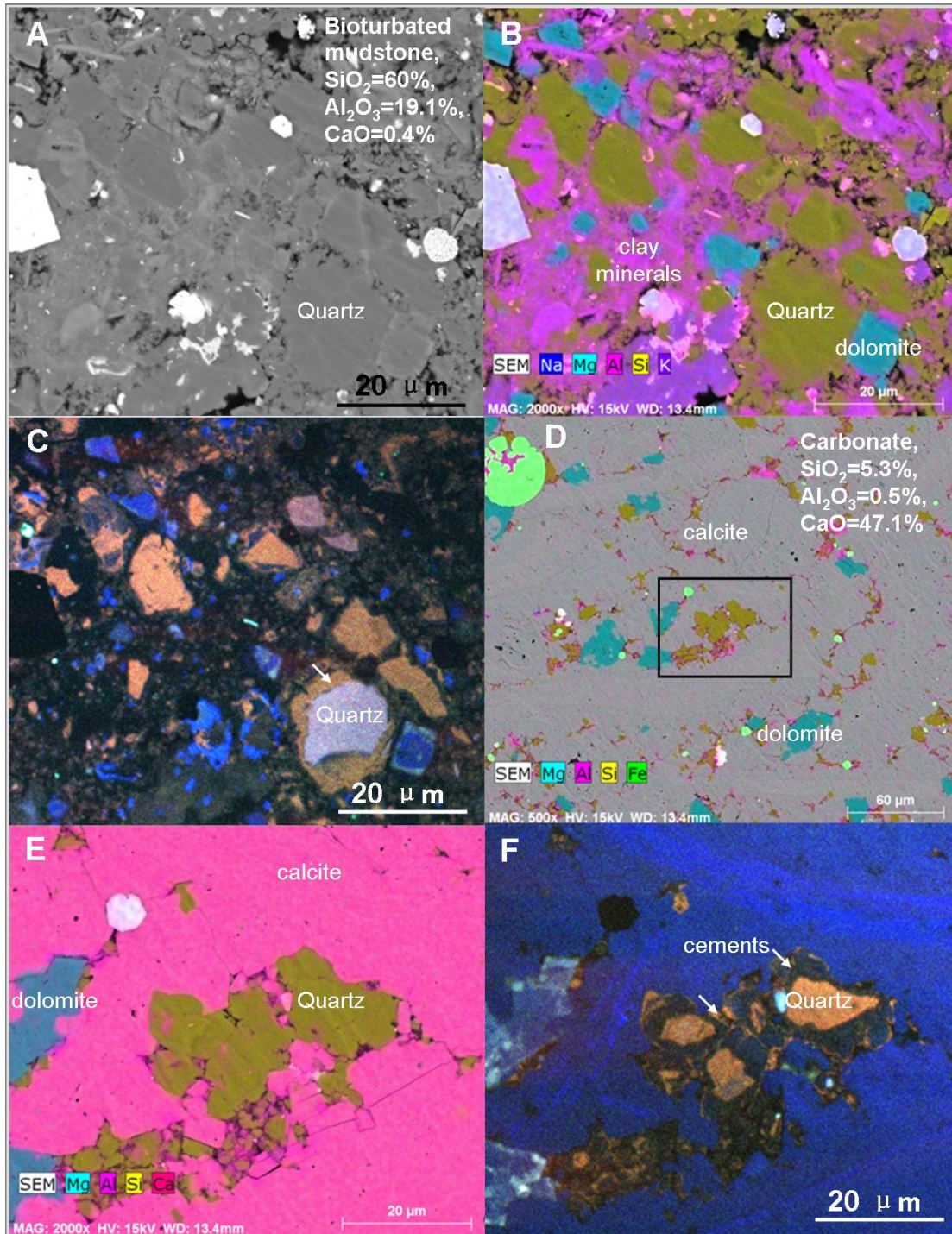


Fig. 5.11. SEM-CL images for a bioturbated mudstone (A, B, C) and carbonate (D, E, F) sample. A) FE-SEM image of a bioturbated mudstone sample (ConocoPhillips McAdam C-87-K/094-O-7, 2866.25m). B) EDS map of the bioturbated mudstone sample, green

and pink area represents quartz and clay minerals, respectively. C) CL-SEM image of the sample, white arrow refers to the quartz cements. D) EDS map of a carbonate sample (ConocoPhillips McAdam C-87-K/094-O-7, 2912.5m). E) Magnified EDS map of the rectangular area in Fig. 11D, green, blue, pink color represents quartz, dolomite and calcite minerals, respectively. F) CL-SEM image of the rectangular area in Fig. 11D, white arrow refers to quartz cements.

#### **5.4.4 Hardness**

Hardness is generally high in the Evie Member, ranging from 371 to 902 with average value of 668 (Figs. 5.4, 5.5, 5.6 and 5.7). Hardness profiles show an abruptly decline just above the contact between the Evie and the Otter Park Member and are characterized by relatively low values in the Otter Park Member (from 114 to 887, averaging 537). Hardness in the Muskwa Formation gradually increases upward, averaging 647 and ranging between 120 and 896. It is noteworthy that in the upper Muskwa Formation, there is a decreasing trend in hardness (Fig. 5.6).

#### **5.4.5 Dynamic rock mechanical properties**

The variations of compressional wave velocity ( $V_p$ ), shear wave velocity ( $V_s$ ) and density from wireline log data are shown in Figs. 5.4 and 5.5.  $V_p$  ranges between 3261 m/s and 6364 m/s, with an average value of 4127 m/s.  $V_s$  ranges from 1831 m/s to 3282 m/s, with an average value of 2484 m/s. The density ranges between 2360 kg/m<sup>3</sup> and 2812 kg/m<sup>3</sup>, with an average value of 2546 kg/m<sup>3</sup>.

Young's modulus is highest in the Evie Member, averaging  $6.58 \times 10^6$  psi, lowest in the Otter Park Member, averaging  $5.27 \times 10^6$  psi, and intermediate in the Muskwa Formation, averaging  $5.35 \times 10^6$  psi. Poisson's ratio is highest in the Otter Park Member, averaging 0.22, and relatively low in the Muskwa Formation and the Evie Member, averaging 0.2 (Figs 5.4, 5.5). Brittleness calculated from waveform sonic data is highest in the Evie Member, averaging 79.87, lowest in the Otter Park Member, averaging 66.5, and intermediate in the Muskwa Formation, averaging 71.32. The brittleness profile is

similar to the profile of hardness measured on core samples (Figs. 5.4 and 5.5) and is characterized by high values in the Evie Member, followed by a sharp decrease at the bottom of Otter Park Member, and then gradually increase in the Muskwa Formation.

Dynamic rock mechanical properties show significant geographic variability. Young's modulus is relatively high in the distal Maxhamish well, averaging  $6.14 \times 10^6$  psi; while the Young's modulus in the proximal Imperial Komie well averages  $5.20 \times 10^6$  psi. The Poisson's ratio is relatively low in the Maxhamish well (averaging 0.16) than the Imperial Komie well (averaging 0.24). Brittleness is relatively high in the Maxhamish well (averaging 83.78) compared to the Imperial Komie well (averaging 61.65).

## **5.5 Discussion**

### **5.5.1 Hardness- a proxy for brittleness in shale formation**

Jarvie et al. (2007) defined brittleness index as the ratio of brittle minerals in weight over ductile minerals in weight in shale reservoirs. In their definition, 
$$\text{brittleness index} = \frac{\text{quartz}}{\text{quartz} + \text{carbonate} + \text{clay}} \quad (6)$$

Quartz is considered to be the only brittle mineral. Wang and Gale (2009) identified dolomite as an additional significant contributor to brittleness, modifying the equation to: 
$$\text{brittleness index} = \frac{\text{quartz} + \text{dolomite}}{\text{quartz} + \text{dolomite} + \text{limestone} + \text{clay} + \text{TOC}} \quad (7)$$

Rickman et al. (2008) defined brittleness from rock physics properties rather than from mineral composition, combining Young's modulus and Poisson's ratio based on dipole sonic and density log, which has been described in the methodology section. In this study, we propose that another proxy -hardness- effectively describes the elastic behavior of shale rocks.

The calculated Young's modulus and Poisson's ratio for the Horn River Shale are in the reasonable range by comparing with other shale formations. Aoudia et al. (2010) reported that in the Woodford shale, Young's modulus ranges between  $6 \times 10^6$  psi -  $2.6 \times 10^7$  psi and Poisson's ratio between 0.05-0.36. Labani and Rezaee (2015) documented

that in the Kockatea Shale and Carynginia Shale from the Perth Basin, Young's modulus ranges between  $2.9 \times 10^6$  psi -  $7.3 \times 10^6$  psi and Poisson's ratio between 0.24-0.32.

A general positive correlation between the measured hardness and dynamic Young's modulus has been observed for both Maxhamish well (Fig. 5.12A) and Imperial Komie well (Fig. 5.12C), yielding correlation coefficients of 0.48 and 0.56, respectively. Samples from both Maxhamish and Imperial Komie wells exhibit negative correlations between dynamic Poisson's ratio and hardness, yielding correlation coefficient of 0.47 (Fig. 5.12B) and 0.55 (Fig. 5.12D), respectively.

Correlations between core-derived hardness and log-derived brittleness for the Maxhamish and Imperial Komie wells are higher than the correlation coefficients between the hardness and either dynamic Poisson's ratio or Young's modulus (Fig. 5.13), yielding correlation coefficients of 0.71 (Fig. 5.13A; Maxhamish well) and 0.75 (Fig. 5.13B; Imperial Komie). The profiles of hardness and brittleness in the Maxhamish and Imperial Komie wells display similar trends in both wells (Figs. 5.4 and 5.5). Small discrepancies between the hardness and brittleness may be due to small mis-ties between core and log depths or to the fact that density log and dipole sonic logs sample a larger depth range than the core samples; hardness measurements target a small area on core samples and are therefore more sensitive to small-scale variations in mineralogy. The good correlation between hardness and brittleness suggest that hardness measurements are a useful proxy for brittleness.

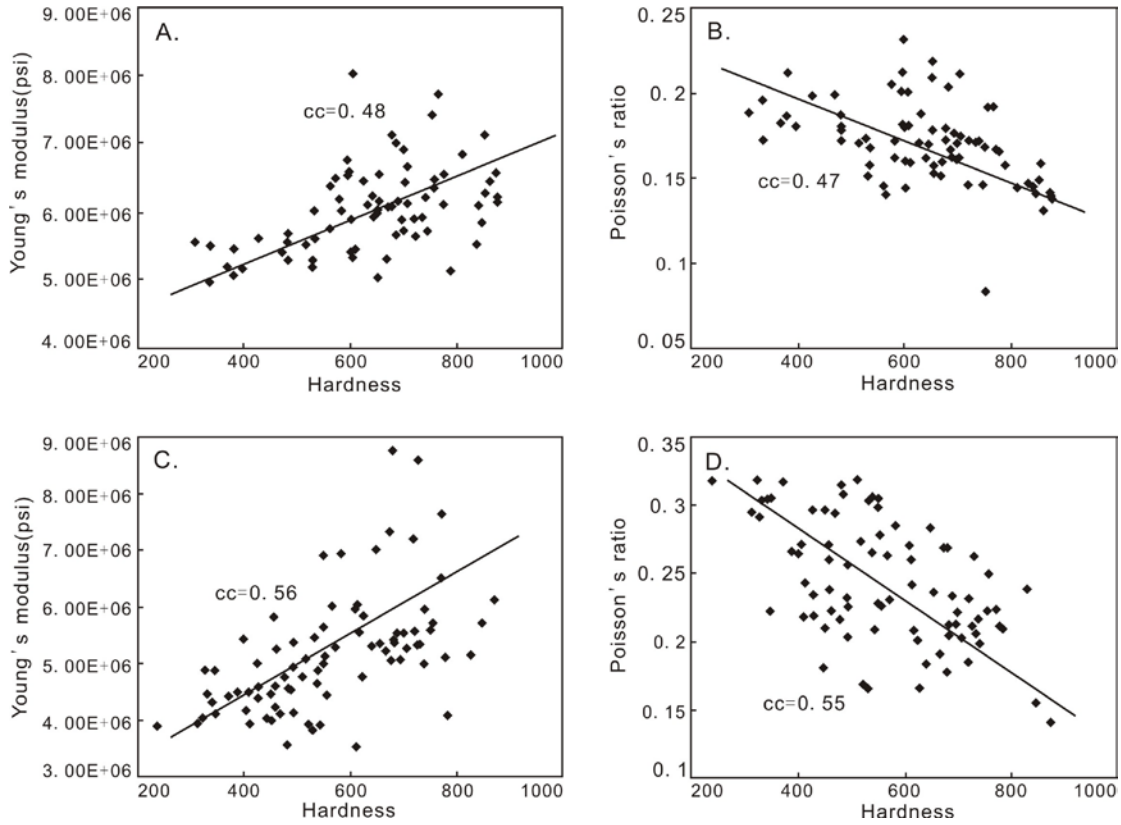


Fig. 5.12. Cross-plot of hardness versus dynamic Young's modulus and Poisson's ratio, calculated from wire-line log data, for samples from EOG Maxhamish D-012-L/094-O-15 core (A, B) and Imperial Komie D-069-K/094-O-02 core (C, D). cc: correlation coefficient.

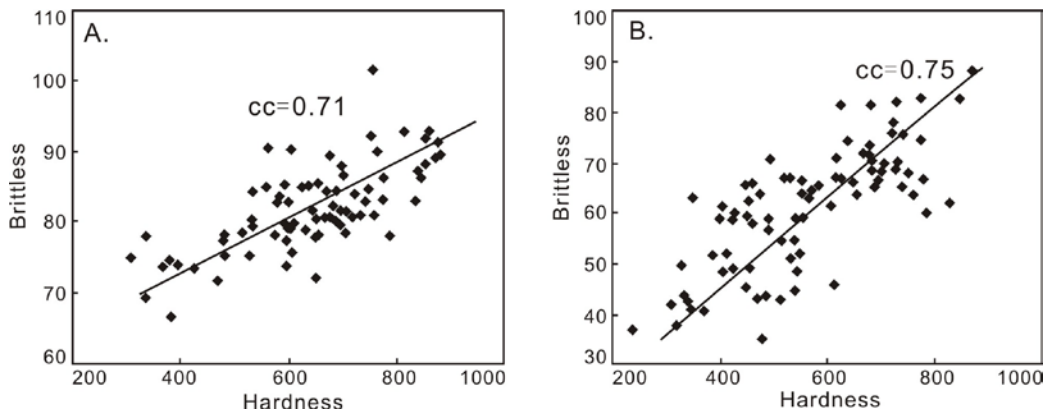


Fig. 5.13. Cross-plot of brittleness versus hardness for EOG Maxhamish D-012-L/094-O-15 core (A) and Imperial Komie D-069-K/094-O-02 core(B).

### **5.5.2 Effect of shale composition on rock geomechanical properties**

A key objective of this study is to determine the effect of shale composition, including organic matter enrichment, on geomechanical properties. We have shown that hardness is an effective proxy for the brittleness of shale formations; therefore, we test the relationship between hardness and TOC content and the major element oxides, which are reliable proxies for minerals.

Organic matter has relatively low bulk density (Okiongbo et al., 2005) and low sonic velocity compared to minerals, such as quartz, calcite, dolomite and clay minerals (Passey et al., 2010; Vernik and Milovac, 2011). Organic matter has been shown to have a significant effect on the geomechanical properties of mudrocks, increasing the ductility of shale formation by decreasing Young's modulus and increasing Poisson's ratio (Aoudia et al., 2010; Prasad et al., 2011; Labani and Rezaee, 2015; Eliyahu et al., 2015). However, in shale samples from both Maxhamish (Fig. 14A), Imperial Komie (Fig. 5.15A), Nexen Gote (Fig. 5.16A) and McAdam (Fig. 5.17A) cores, no negative relationship between the hardness and TOC content was observed. This indicates that organic matter is not a major factor affecting Young's modulus at very high thermal maturities, which are approximately 1.6 - 2.5%  $R_o$  in the Horn River basin (Ross and Bustin, 2008; Ross and Bustin, 2009a). Kerogen is thought to undergo significant changes in its physical properties during maturation and Zargari et al. (2013) reported that more mature samples have higher Young's modulus. The elastic behavior of organic-rich shales is the composite function of organic matter, clay, quartz, feldspar, carbonate and pyrite. Previous studies report that minerals except clays have Young's modulus above 40 GPa and kerogen has Young's modulus below 15 GPa (Prasad, 2001; Zeszotarski et al., 2004; Zargari et al., 2013). Brittle minerals in the formation can dominate the effect of organic matter on bulk elastic properties.

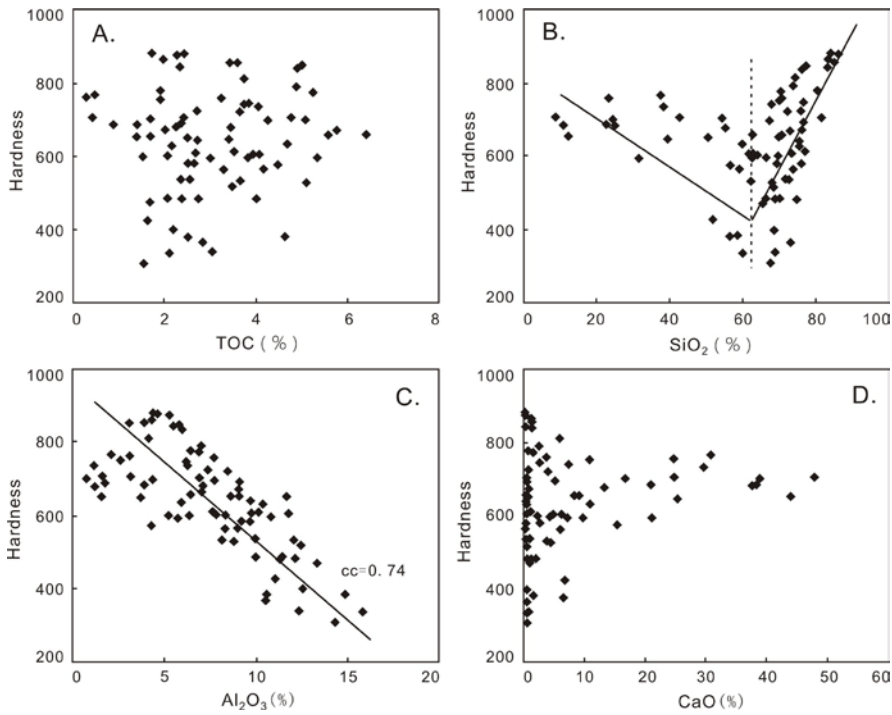


Fig. 5.14. Crossplot of hardness versus TOC content and major oxides for EOG Maxhamish D-012-L/094-O-15 core.

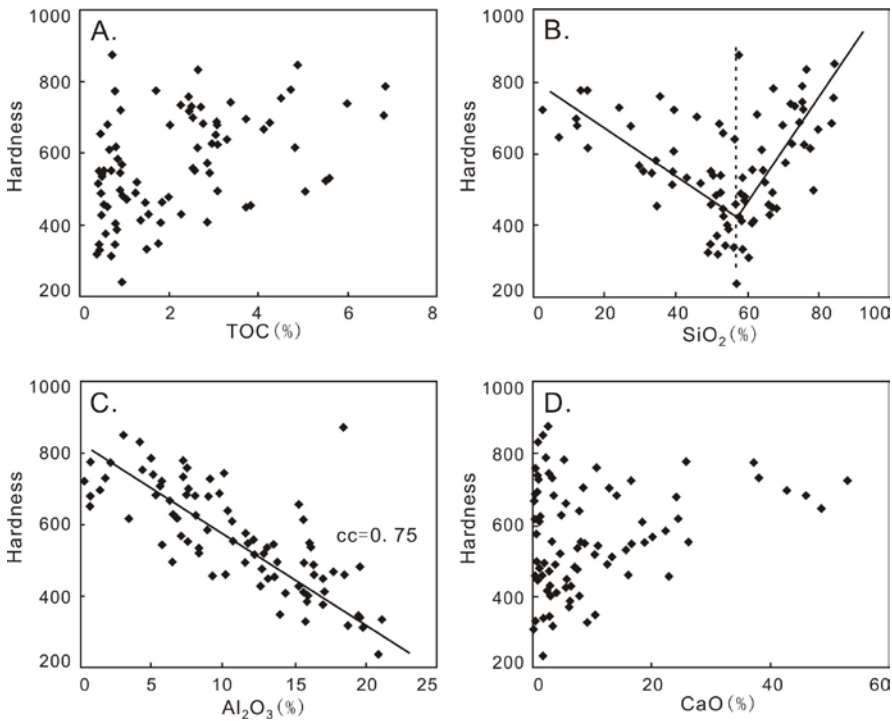


Fig. 5.15. Crossplot of hardness versus TOC content and major oxides for Imperial Komie D-069-K/094-O-02 core.

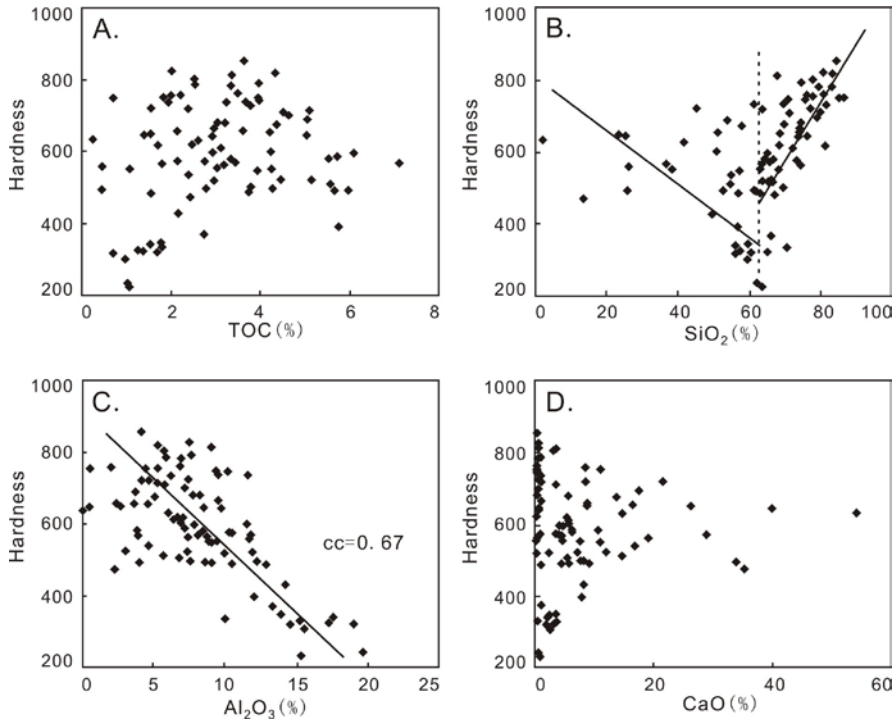


Fig. 5.16. Crossplot of hardness versus TOC content and major oxides for Nexen Gote A-27-I/094-O-8 core.

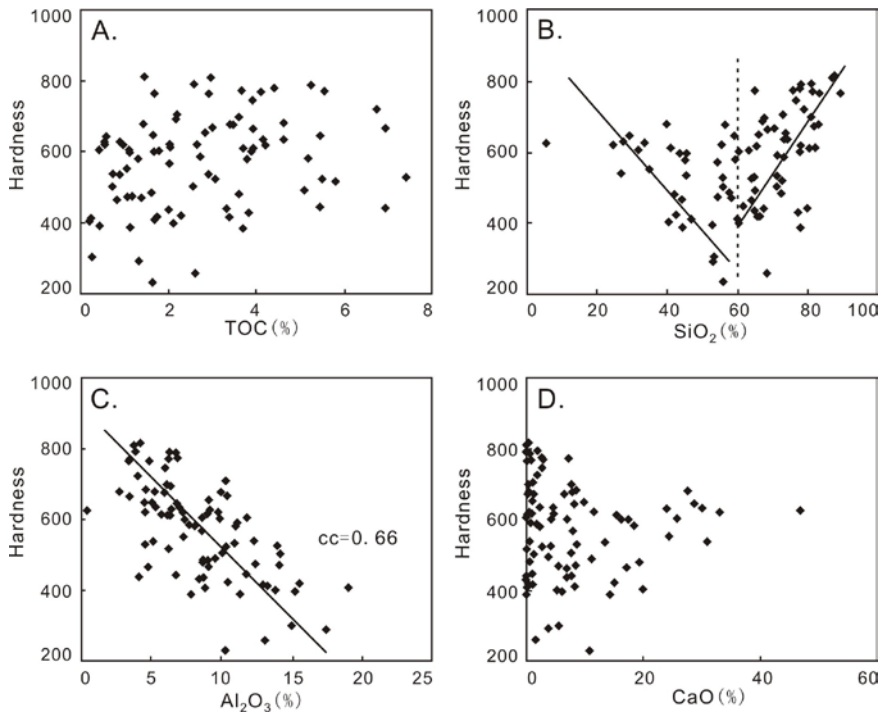


Fig. 5.17. Crossplot of hardness versus TOC content and major oxides for ConocoPhillips McAdam C-87-K/094-O-7 core.

Quartz, clay and carbonate minerals are the predominant minerals in the Horn River Shale, and in this study, we utilize the concentration of SiO<sub>2</sub>, Al<sub>2</sub>O<sub>3</sub> and CaO as proxies for quartz, clay and carbonate, respectively (Wright et al., 2010; Dong et al., 2015). Previous studies demonstrate that clay minerals have much lower sonic velocity and density than carbonate and quartz groups (Pickett, 1963; Mondol et al., 2008). They are usually regarded as ductile minerals and their presence significantly alters the mechanical properties of shale formation (Jarvie et al., 2007; Aoudia et al., 2010; Wang and Carr, 2013). As shown in Figs. 5.14C, 5.15C, 5.16C and 5.17C, Al<sub>2</sub>O<sub>3</sub>, characteristic of clay minerals, has the strongest correlation to hardness, yielding negative correlation coefficients of 0.74, 0.75, 0.67 and 0.66 in Maxhamish, Imperial Komie, Nexen Gote and McAdam cores, respectively. This indicates that in Horn River Shale, the concentration of clay minerals is the most significant factor controlling brittleness of the shale formations.

The relationship between hardness and the concentration of SiO<sub>2</sub> is more complex. For Maxhamish core, a positive correlation between hardness and SiO<sub>2</sub> was observed for samples with SiO<sub>2</sub> concentration exceeding approximately 63 wt.%. However, in samples with SiO<sub>2</sub> concentration less than 63 wt.%, a negative relationship exists between hardness and SiO<sub>2</sub>. Similarly for the Imperial Komie core, a positive correlation between hardness and concentration of SiO<sub>2</sub> was evident in samples in which the abundance of SiO<sub>2</sub> exceeds approximately 57 wt.%; however, for samples with less than 57 wt.% SiO<sub>2</sub>, a negative correlation exists between SiO<sub>2</sub> and hardness. Schieber et al. (2000) reported that in Devonian black shales, a large fraction of quartz is derived from planktonic organisms rather than occurring as detrital grains. The presence of biogenic and detrital quartz in Horn River Shale has been reported previously (Ross and Bustin, 2009b; Hall, 2011; Dong et al., 2015). Wright et al. (2010) proposed that biogenic or detrital silica can be distinguished by plotting SiO<sub>2</sub> concentration versus Zr concentration, which is associated with the heavy mineral zircon and is a proxy for silt-sized detrital

input, where a positive linear relationship between SiO<sub>2</sub> and Zr concentration indicates a detrital quartz trend and a negative association between SiO<sub>2</sub> and Zr implies the presence of biogenic quartz. In the Maxhamish data set (Fig. 5.18A), samples with SiO<sub>2</sub> concentration approximately below 63 wt.% display a positive covariation with Zr, whereas samples with SiO<sub>2</sub> concentrations above of 63 wt.% exhibit negative correlation with Zr. These trends indicate that in samples with low SiO<sub>2</sub> concentrations, quartz primarily has a detrital origin, whereas in samples with high SiO<sub>2</sub> concentrations, it is predominantly biogenic in origin. Similar trends were observed in the Imperial Komie data set (Fig. 5.18B), with a threshold of approximately 57 wt.% SiO<sub>2</sub> separating the biogenic from detrital quartz trends. In the Nexen Gote and McAdam data set, the same correlations between hardness and SiO<sub>2</sub> were observed (Figs. 5.16B and 5.17B). These observations suggest that the simple presence of quartz does not necessarily indicate brittleness and that only biogenic quartz can be regarded as a brittle component. This model is supported by our SEM-CL work which is discussed in the following section. We suggest that the negative correlation between hardness and SiO<sub>2</sub> at low SiO<sub>2</sub> content is in fact caused by clay content, as SiO<sub>2</sub> varies positively with Al<sub>2</sub>O<sub>3</sub> in the range of SiO<sub>2</sub> in which a detrital origin is indicated for quartz. In other words, the negative correlation between hardness and SiO<sub>2</sub> is not the causal relationship.

Carbonate minerals are commonly regarded as brittle because of their high density and sonic velocity. In our datasets, CaO is not positively correlated with hardness (Figs. 5.14D, 5.15D, 5.16D and 5.17D), indicating that the presence of carbonate minerals has limited effect on the brittleness of shale formations.

Factor analysis was carried out on a dataset that included hardness, Young's modulus, Poisson's ratio, brittleness and the geochemical data in order to test the bivariant relationships described above and to identify additional relationships between shale composition and rock geomechanical properties. Factor analysis aims to reduce the number of variables in a given data set and to detect structure in the relationships

between the variables. It identifies lower numbers of unobserved variables, termed factors, which represent the variability in the original data. The strength of associations between new factors and original variables is expressed by correlation coefficients. High values suggest that the original variables are strongly associated with the new single factor.

Table 5.3. Factor analysis results showing the first two factors.

% of variance	Factor 1 46.5%		Factor 2 15.7%	
+	Al <sub>2</sub> O <sub>3</sub>	0.94	SiO <sub>2</sub>	0.6
	Fe <sub>2</sub> O <sub>3</sub>	0.57	TOC	0.79
	Na <sub>2</sub> O	0.69		
	K <sub>2</sub> O	0.93		
	TiO <sub>2</sub>	0.96		
-	Hardness	0.71	Poisson's ratio	0.62
	Young's modulus	0.75		
	Brittleness	0.69		
	CaO	0.61		

Factor 1 is strongly and positively correlated with Al<sub>2</sub>O<sub>3</sub>, Na<sub>2</sub>O, and K<sub>2</sub>O and explains 46.5% of total variance in the data set (Table 5.3). Hardness, Young's modulus, brittleness and CaO are negatively correlated with factor 1, indicating that Young's modulus, brittleness and hardness generally increase as clay minerals decrease or as carbonate minerals increase. Factor 2 is positively correlated with SiO<sub>2</sub> and TOC, and negatively correlated with Poisson's ratio and accounts for 15.7% of the variance in the total data set. This association indicates that Poisson's ratio generally decreases as TOC content and SiO<sub>2</sub> concentrations decrease. In sum, the brittleness of shale rock samples is significantly reduced by the content of clay minerals and enhanced by the abundance of

biogenic quartz and carbonate.

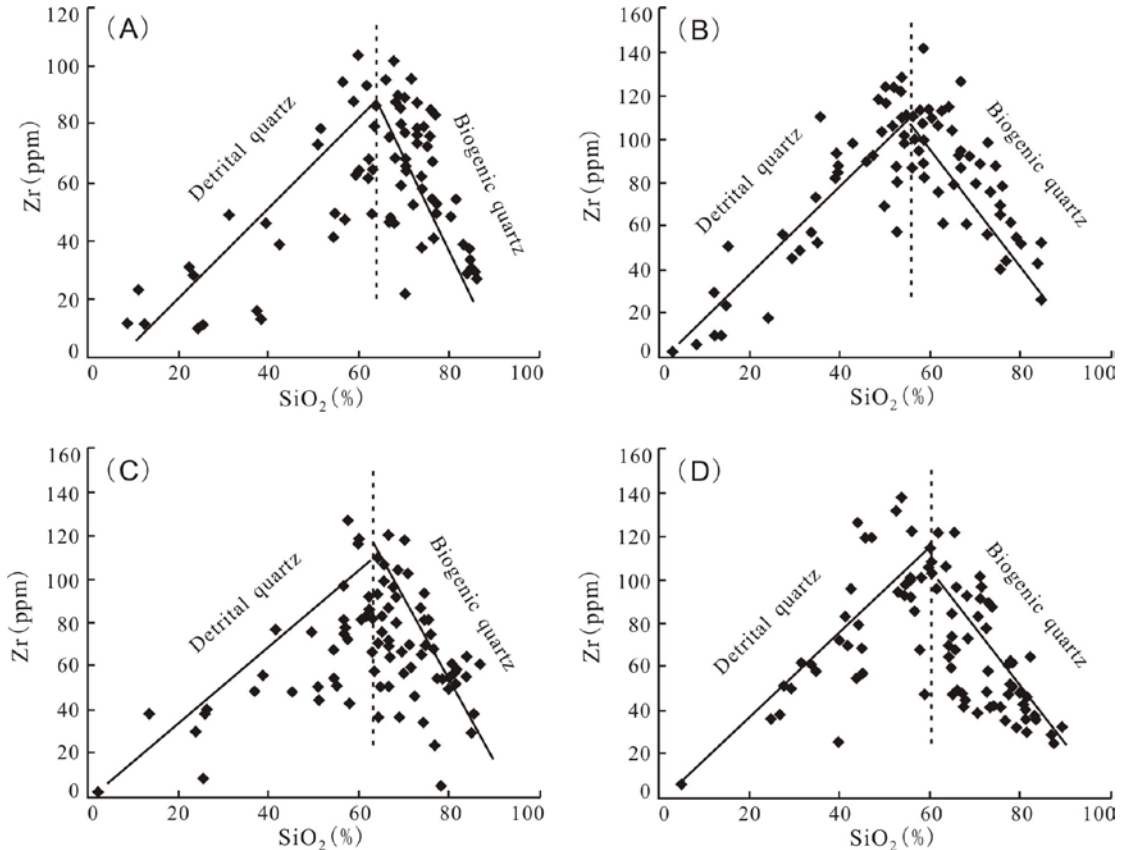


Fig. 5.18. Cross- plot of Si versus Zr for samples from Maxhamish (A), Imperial Komie (B), Nexen Gote (C) and McAdam cores (D). Biogenic quartz is distinguished from detrital quartz by the slope (positive versus negative).

### 5.5.3 Links between lithofacies and mechanical properties

Lithofacies studies in shale reservoirs improve our understanding of spatial variations in mineralogy, organic matter richness and geomechanical properties (Wang and Carr, 2012; 2013). Five lithofacies are present in the Horn River Shale: massive mudstone, pyritic mudstone, laminated mudstone, bioturbated mudstone and carbonates. These lithofacies display variable proportions of quartz, clay and carbonate, as shown in Fig. 5.19. The massive mudstone and pyritic mudstone lithofacies are characterized by relatively high silica contents and plotted in the silica-rich region of the ternary diagram. The laminated mudstone and bioturbated mudstone facies are characterized by relatively

high proportions of clay minerals but can be distinguished from each other by higher amounts of quartz and carbonate minerals in the laminated mudstone lithofacies (Fig. 5.19). The carbonate lithofacies has the highest concentration of carbonate minerals.

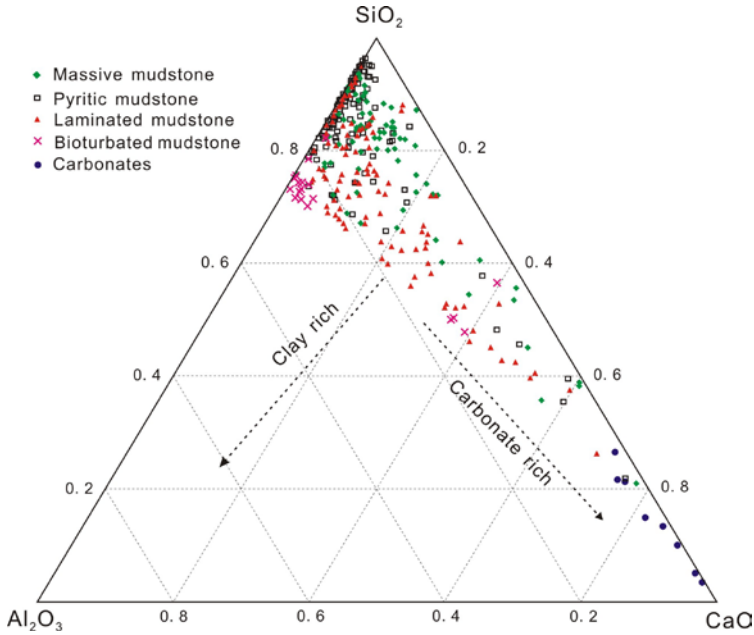


Fig. 5.19. Ternary plot of SiO<sub>2</sub>, Al<sub>2</sub>O<sub>3</sub> and CaO of samples belonging to different lithofacies for EOG Maxhamish D-012-L/094-O-15 and Imperial Komie D-069-K/094-O-02 wells.

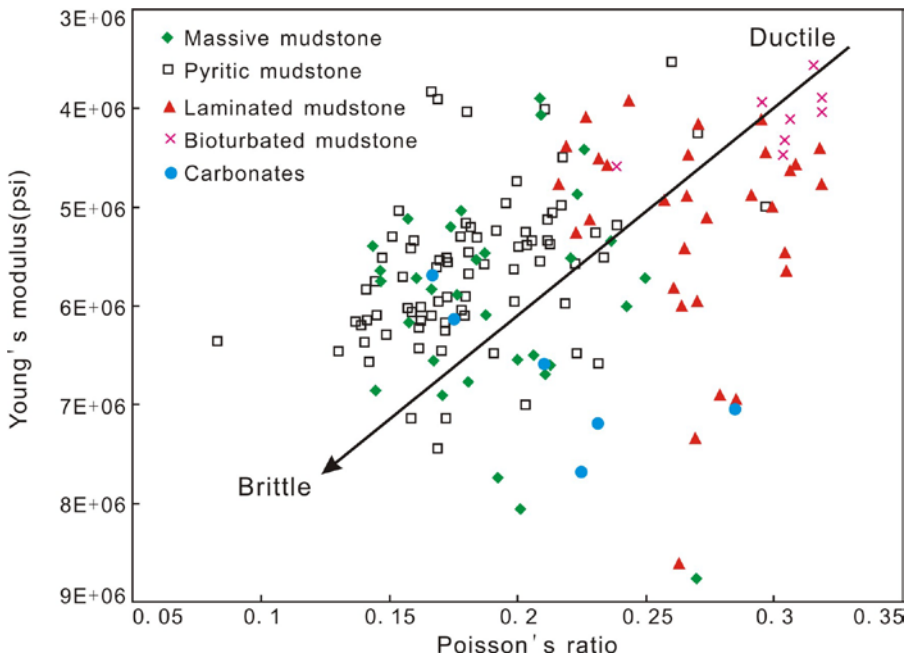


Fig. 5.20. Crossplot of Young's modulus versus Poisson's ratio of samples from different

lithofacies for EOG Maxhamish D-012-L/094-O-15 and Imperial Komie D-069-K/094-O-02 wells.

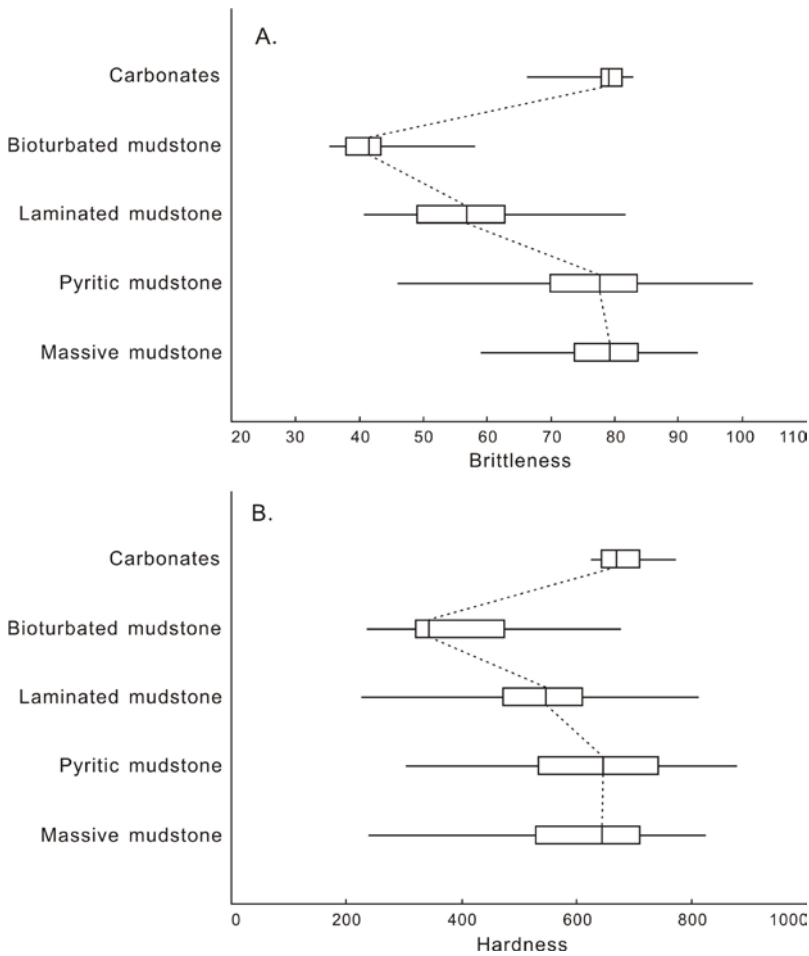


Fig. 5.21. Box and whisker plots showing brittleness (A) and hardness (B) for shale samples differentiated by lithofacies. From left to right, different segments of the box and line represent minimum, quartile Q=0.25, median, quartile Q=0.75 and maximum values, respectively.

The different proportions of mineral components in the five lithofacies are strongly reflected in the geomechanical properties (Figs. 5.20 and 5.21). Fig. 5.20 shows the Young's modulus and Poisson's ratio measurements for the five lithofacies. The massive mudstone, pyritic mudstone and carbonate lithofacies have higher Young's modulus and lower Poisson's ratio than laminated mudstone and bioturbated mudstone lithofacies, consistent with increased brittleness. These relationships are consistent with hardness

measurements, distinguished by lithofacies (Fig. 5.21).

SEM and SEM-CL images and EDS maps provide additional insights into links between lithofacies and geomechanical properties. The massive mudstone sample has the highest hardness (Table 5.1), which we attribute to its high amount of quartz cements. Authigenic quartz forms an interconnected network with the fine-grained detrital quartz, making the sample more brittle (Fig. 5.9C). The carbonate sample also has a high hardness value (Table 5.1), probably because this sample has high concentration of calcite (Fig. 5.11D). The pyritic mudstone sample and the laminated mudstone sample examined by SEM-CL have moderate hardness (Table 5.1). Although a large amount of individual brittle grains such as quartz and carbonate are present in the pyritic mudstone sample, these grains are partially disconnected by clay minerals between them (Figs. 5.9E and F). The bioturbated mudstone sample with highest clay content has the lowest hardness. EDS map and SEM-CL images suggest that this sample contains abundant detrital quartz grains and a moderate amount of quartz cement. Most of the quartz grains are surrounded by clay minerals, which prevent detrital quartz grains from becoming interconnected (Figs. 5.11B and C).

#### **5.5.4 Depositional environment and its influence in the geomechanical properties**

Interpretations of depositional processes and paleoenvironmental conditions of mudstones are challenging due to the predominant massive texture of these formations. However, in the Horn River Basin, sedimentological and ichnological characteristics along with geochemical analysis provide insights into potential depositional environments and conditions. We interpret massive mudstone and pyritic mudstone lithofacies to represent relatively deep-water basin floor sediments deposited under dysoxic to anoxic conditions. These lithofacies display little evidence of fluctuations in the depositional conditions (e.g. rare micro-scale starved current ripple and rare burrowed intervals). Reduced oxygen levels are suggested by well-preserved and undisturbed fossil-rich laminae and by geochemical results suggesting anoxic conditions

with little or no terrestrial input. The massive mudstone and pyritic mudstone lithofacies predominate in the Evie Member and the Muskwa Formation, which are interpreted to have been deposited during a second-order highstand and transgressive system tract stage, respectively.

Laminated to heterolithic bedded mudstones and bioturbated mudstones indicate the most significant fluctuations in depositional energy. Amalgamated current ripples, silty current ripples, climbing ripples, double mud-drapes, and alternating thin-thick laminae set are interpreted as the deposits of deep-water currents (e.g., contourites) (Dykstra, 2012; Rebesco et al., 2014; Shanmugam et al., 2009). Bioturbated mudstones are interpreted to represent oxygenated to dysoxic conditions and were deposited in relatively proximal and shallower water settings than the massive and pyritic mudstones, possibly located at the distal end of a deltaic system. The laminated mudstone and bioturbated mudstone lithofacies, which represent deposition in the shallowest water, are more common in Imperial Komie well than the Maxhamish well. Pervasive bioturbation indicates at least moderate oxygen levels, while the dominance of surface deposit feeding behavior and lack of robust trace fossils suggests low nutrient levels.

Because organic matter and mineral components show stratigraphic and geographic variation, we would expect to see concomitant variation in the geomechanical properties. At the formation scale, the vertical profile of geomechanical properties corresponds to mineralogical variability, including clay, carbonate and biogenic silica. The relatively clay-rich Otter Park Member is more ductile than the Evie Member and the Muskwa Formation. The relatively large amount of carbonate in the Evie Member and the high concentrations of authigenic quartz in the Muskwa Formation result in much higher values of brittleness in those units than in the Otter Park Member. At the second-order scale, high sea level (Evie and Muskwa) is favorable for deposition of brittle lithofacies, while low sea level (Otter Park) is favorable for deposition of ductile lithofacies.

Geographic variability in Young's modulus, Poisson's ratio and brittleness (averaging

values) is shown in Figure. 5.22. The biggest challenge in mapping the geomechanical properties in Horn River Basin is the scarcity of wells with dipole sonic log data. In the Evie Member, Young's modulus generally decreases towards the northwest (Fig. 5.22C), while no obvious trend was observed in Poisson's ratio (Fig. 5.22F). The brittleness in the Evie Member is relatively high in southeast and northwest areas (Fig. 5.22I). The high Young's modulus and brittleness in the southeastern area of the basin results from carbonate detritus shed from the Presqu'ile reef (see location in Fig. 5.1), situated to the south and east of the basin. We suggest that the high brittleness in northwestern parts of the basin results from biogenic silica, as the  $\text{SiO}_2$  content in Maxhamish core is higher than that is in the Imperial Komie well.

In the Otter Park Member and the Muskwa Formation, Young's modulus increases, Poisson's ratio decreases and brittleness increases towards the northwest (Fig. 5.22) In the Otter Park Member, laminated mudstone and bioturbated mudstone are most common in Imperial Komie well, less common in the McAdam and Nexen Gote wells and least common in the distal the Maxhamish well. The trend of increasing of Young's modulus and brittleness towards the northwest is largely controlled by variation of clay content, which is sourced from the southeastern margin of the basin. In the Muskwa Formation, the concentration of biogenic  $\text{SiO}_2$ , much higher in the northwest part of the basin, also contributes to increasing brittleness in northwest from southeast.

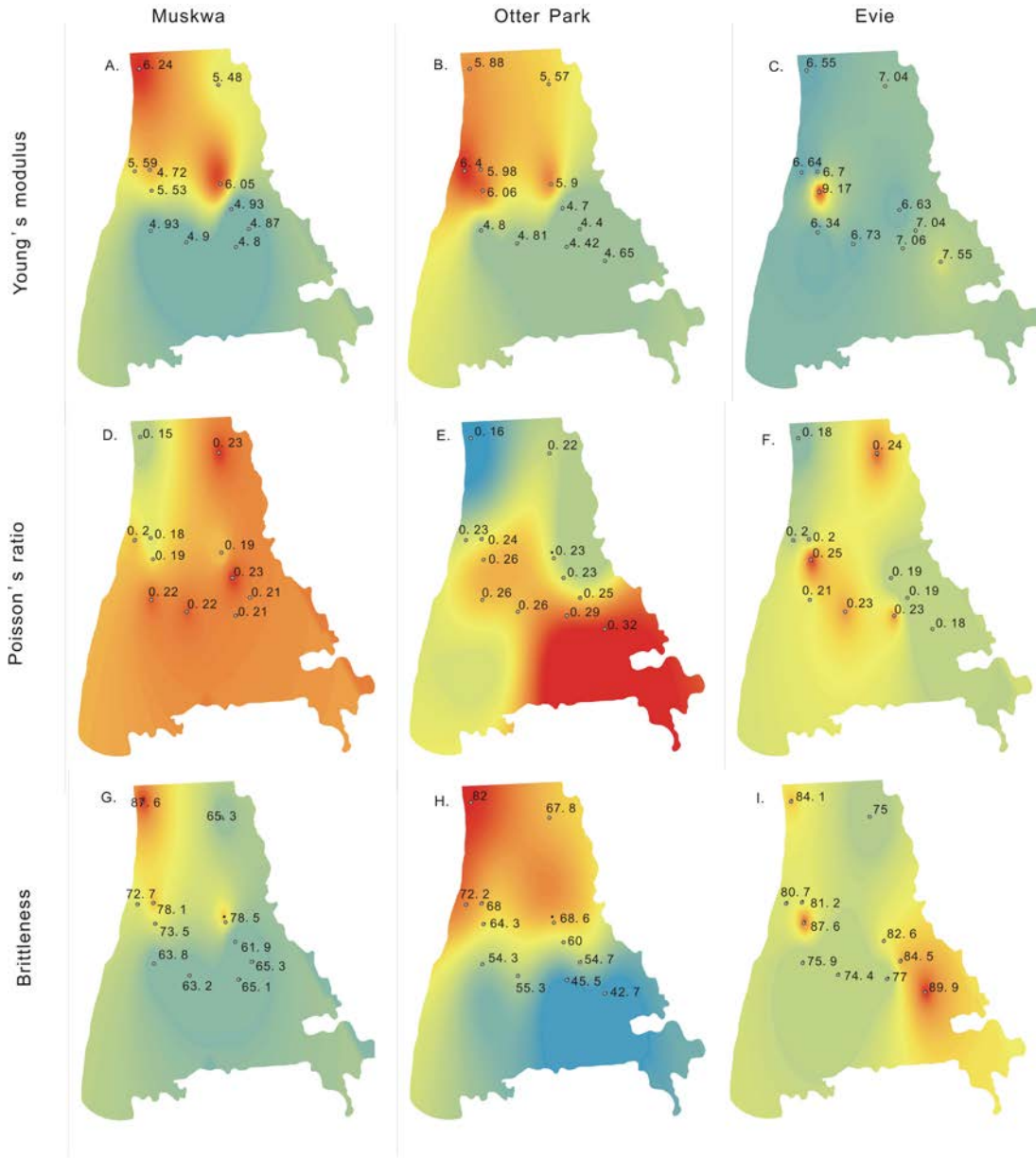


Fig. 5.22. Geographical distribution of Young's modulus ( $\times 10^6$  Psi, A, B, C), Poisson's ratio (D, E, F) and brittleness (G, H, I) for the Muskwa Formation (A, D, G), Otter Park (B, E, H) and Evie Member (C, F, I).

## 5.6 Conclusions

The compositionally diverse suite of Horn River shale units provides insights into controlling factors on geomechanical properties. Specifically, we have shown that:

- (1) Hardness measurements on core samples are an effective proxy for brittleness in shale reservoirs measurement from well logs.
- (2) Rock composition exerts a first order control on brittleness, in particular clay minerals, which result in decreased brittleness. TOC content has only a minor effect on geomechanical properties in the Horn River, at least in part may be due to its high thermal maturity; less mature shales may show a different relationship. Factor analysis demonstrates that a high fraction of carbonate minerals results in increased brittleness, while biogenic quartz enhances brittleness.
- (3) Depositional facies are clearly related to brittleness, because rock composition varies with facies. Quartz- or carbonate-rich massive mudstone, pyritic mudstone and carbonate lithofacies are relatively brittle, whereas relatively clay-rich laminated mudstone and bioturbated mudstone lithofacies are more ductile.
- (4) Geomechanical properties in Horn River Shale show both geographic variation and stratigraphic variation, which can be tied to the variation in mineral composition related to sources of sediment.

### **Acknowledgements**

We thank the British Columbia Ministry of Energy and Mines in Victoria for the access to core data and well files. We are grateful for the funding support from NSERC (grant CRDPJ 445064 – 12) and co-funders ConocoPhillips Canada, Devon Canada, Husky Energy, Imperial, Nexen-CNOOC, and Shell Canada. The authors also thank ConocoPhillips Canada for providing the Equotip Bambino 2 hardness tester, Dr. Chris DeBuhr for carrying out the CL-SEM work in the Department of Geoscience at the University of Calgary.

### **5.7 References**

Al-Zahrani, A.A., 2011, Interpretation of 3D multicomponent seismic data for

investigating natural fractures in the Horn River Basin, northeast British Columbia: M.Sc. thesis, University of Calgary, 118p.

Aoudia, K., J. L. Miskimins, N. B. Harris and C. A. Mnich, 2010, Statistical analysis of the effects of mineralogy on rock mechanical properties of the Woodford shale and the associated impacts for hydraulic fracture treatment design: 44<sup>th</sup> US Rock Mechanics Symposium and 5<sup>th</sup> U.S.-Canada Rock Mechanics Symposium, Salt Lake, 11p.

B.C. Oil and Gas Commission, 2014, Horn River Basin Unconventional Shale Gas Play Atlas, 15p.

Bernet, M., and K. Basset, 2005, Provenance analysis by single-quartz-grain SEM-CL/optical microscopy: *Journal of Sedimentary Research*, v. 75, p. 492-500.

Bowker, K.A., 2007, Barnett Shale gas production, Fort Worth Basin: Issue and Discussion: *AAPG Bulletin*, v. 91, no. 4, p. 523-533.

Bustin, A.M.M., and R.M. Bustin, 2012, Importance of rock properties on the producibility of gas shales: *International Journal of Coal Geology*, v. 103, p. 132-147.

Dong, T., N.B. Harris, K. Ayranci, C.E. Twemlow, and B.R., Nassichuk, 2015, Porosity characteristics of the Devonian Horn River shale, Canada: Insights from lithofacies classification and shale composition: *International Journal of Coal Geology*, v. 141-142, p. 74-90.

Dykstra, M., 2012, Deep Water Tidal Sedimentology, in R. A. Davis Jr., and R. W. Dalrymple, eds., *Principles of Tidal Sedimentology*: Berlin, Springer, p. 371–396.

Eliyahu, M., S. Emmanuel, R.J. Day-Stirrat, and C.I. Macaulay, 2015, Mechanical properties of organic matter in shales mapped at the nanometer scale: *Marine and Petroleum Geology*, v. 59, p. 294-304.

Ferri, F., A.S. Hickin, and D.H. Huntley, 2011, Besa River formation, western Liard Basin, British Columbia (NTS 094N): geochemistry and regional correlations; in

- Geoscience Reports 2011, British Columbia Ministry of Energy, Mines and Natural Gas, p. 1-18.
- Frelinger, S.N., M.D. Ledvina, J.R. Kyle, and D.G. Zhao, 2015, Scanning electron microscopy cathodoluminescence of quartz: Principles, techniques and applications in ore geology: *Ore Geology Reviews*, v. 65, p. 840-852.
- Hall, C. D., 2011, Comparison of the reservoir properties of the Muskwa (Horn River Formation) with other North American gas shales: CSPG CSEG CWLS Convention, 3p.
- Harris, N.B., J.L. Miskimins, and C.A. Mnich, 2011, Mechanical anisotropy in the Woodford shale, Permian Basin: origin, magnitude, and scale: *The Leading Edge*, v. 30(3), p. 284-291.
- Hillier, S., 2003, Quantitative analysis of clay and other minerals in sandstones by X-ray powder diffraction (XRPD): *Int. Assoc. Sedimentol. Special Publication 34*, 213-251.
- Hulsey, K.M., 2011, Lithofacies characterization and sequence stratigraphic framework for some gas-bearing shales within the Horn River basin, Northeastern British Columbia: M.Sc. thesis, University of Oklahoma, 76p.
- Jarvie, D.M., R.J. Hill, T.E. Ruble, and R.M. Pollastro, 2007, Unconventional shale-gas systems: the Mississippian Barnett Shale on north-central Texas as one Model for thermogenic shale-gas assessment: *AAPG Bulletin*, v. 91, no. 4, p. 475-499.
- Labani, M.M., and R. Rezaee, 2015, The importance of geochemical parameters and shale composition on rock mechanical properties of gas shale reservoirs: a case study from the Kockatea Shale and Carynginia Formation from the Perth Basin, Western Australia: *Rock Mechanics and Rock Engineering*, v. 48, p. 1249-1257.
- McPhail, S., W. Walsh, C. Lee, and P.A. Monahan, 2008, Shale units of the Horn River formation, Horn River basin and Cordova Embayment, Northeastern British

- Columbia: Canadian Society of Petroleum Geologists and Canadian Well Logging Society Convention, 14p.
- Melendez-Martinez, J., and D.R., Schmitt, 2016. A comparative study of the anisotropic dynamic and static elastic moduli of unconventional reservoir shales: Implications for geomechanical investigations. submitted to Geophysics.
- Milliken, K.L., W.L. Esch, R.M. Reed, and T.W. Zhang, 2012, Grain assemblages and strong diagenetic overprinting in siliceous mudrocks, Barnett Shale (Mississippian), Fort Worth Basin, Texas: AAPG Bulletin, v. 96, no. 8, p. 1553-1578.
- Mondol, N.H., J. Jahren, and K. Bjørlykke, 2008, Elastic properties of clay minerals: The Leading Edge, v. 27, no. 6, p. 758-770.
- O'Connell, S.C., 1994, Geological history of the Peace River Arch; in Geological Atlas of the Western Canada Sedimentary Basin: Canadian Society of Petroleum Geologists and Alberta Research Council, Special Report 4.
- Okiongbo, K.S., A.C. Aplin, and S.R. Larter, 2005, Changes in type II kerogen density as a function of maturity: evidence from the Kimmeridge Clay formation: Energy and Fuels, v. 19, no. 6, p. 2495-2499.
- Oldale, H.S. and R.J. Munday, 1994, Devonian Beaver Hill Group of the Western Canada Sedimentary Basin; in Geological Atlas of the Western Canada Sedimentary Basin: Canadian Society of Petroleum Geologists and Alberta Research Council, Special Report 4.
- Omotoso, O., D.K. McCarty, S. Hillier, R. Kleeberg, 2006, Some successful approaches to quantitative mineral analysis as revealed by the 3rd Reynolds cup contest: Clays and Clay Minerals, v. 54, no. 6, p. 748-760.
- Passey, Q.R., K.M. Bohacs, W.L. Esch, R. Klimentidis, and S. Sinha, 2010, From oil-prone source rocks to gas-producing shale reservoir - Geologic and petrophysical characterization of unconventional shale-gas reservoir: SPE Paper 131350, International Oil and Gas Conference and Exhibition, Beijing, 29p.

- Pickett, G.R., 1963, Acoustic character logs and their applications in formation evaluation: *Journal of Petroleum Technology*, v. 15, no. 6, p. 659-667.
- Prasad, M., 2001, Mapping impedance microstructures in rocks with acoustic microscopy: *The Leading Edge*, v. 20(2), p. 172-179.
- Prasad, M., K. Mba, T.E. McEvoy, and M.L. Batzle, 2011, Maturity and impedance analysis of organic-rich shales: *SPE Reservoir Evaluation & Engineering*, v. 14, p. 533-543.
- Rebesco, M., F.J. Hernández-Molina, D. Van Rooij, and A. Wåhlin, 2014, Contourites and associated sediments controlled by deep-water circulation processes: State-of-the-art and future considerations: *Marine Geology*, v. 352, p. 111-154.
- Rickman, R., M. Mullem, E. Petre, B. Grieser, and D. Kundert, 2008, A practical use of shale petrophysics for stimulation design optimization: all shale plays are not clones of the Barnett shale: *SPE Paper 115258*, SPE Annual Technical Conference and Exhibition, Colorado, 11p.
- Ross, D.J.K., and R.M. Bustin, 2008, Characterizing the shale gas resource potential of Devonian-Mississippian strata in the western Canada sedimentary basin: Application of an integrated formation evaluation: *AAPG Bulletin*, v. 92, no. 1, p. 87-125.
- Ross, D. J. K., and R.M. Bustin, 2009a, The importance of shale composition and pore structure upon gas storage potential of shale gas reservoirs: *Marine and Petroleum Geology*, v. 26, p. 916-927.
- Ross, D.J.K., and R.M. Bustin, 2009b, Investigating the use of sedimentary geochemical proxies for paleoenvironment interpretation of thermally mature organic-rich strata: examples from the Devonian-Mississippian shales, Western Canadian Sedimentary Basin: *Chemical Geology*, v. 260, p. 1-19.
- Schieber, J., D. Krinsley, L. Riciputi, 2000, Diagenetic origin of quartz silt in mudstones and implications for silica cycling: *Nature*, v. 406, p. 981-985.
- Shanmugam, G., S.K. Shrivastava, and B. Das, 2009, Sandy Debrites and Tidalites of

- Pliocene Reservoir Sands in Upper-Slope Canyon Environments, Offshore Krishna–Godavari Basin (India): Implications: *Journal of Sedimentary Research*, v. 79, p. 736-756.
- Slatt, R. M., and Y. Abousleiman, 2011, Merging sequence stratigraphy and geomechanics for unconventional gas shales: *The Leading Edge*, v. 30(3), p. 274-282.
- Sondergeld, C. H., K. E. Newsham, M. C. Rice and C. S. Rai, 2010, Petrophysical considerations in evaluating and producing shale gas resources: SPE Paper 131768, SPE Unconventional Gas Conference, Pittsburgh, 34p.
- Sone, H., and M.D. Zoback, 2013, Mechanical properties of shale-gas reservoir rocks - Part 1: Static and dynamic elastic properties and anisotropy: *Geophysics*, v. 78, no.5, p. 381-392.
- Vernik, L., and J. Milovac, 2011, Rock physics of organic shales: *The Leading Edge*, v. 30, no. 3, p. 318-323.
- Wang, F.P., and J.F.W. Gale, 2009, Screening criteria for shale-gas systems: *Gulf Coast Association of Geological Societies Transactions*, v. 59, p. 779-793.
- Wang, G.C., and T.R. Carr, 2012, Marcellus shale lithofacies prediction by multiclass neural network classification in the Appalachian Basin: *Mathematical Geosciences*, v. 44, p. 975-1004.
- Wang, G.C., and T.R. Carr, 2013, Organic-rich Marcellus Shale lithofacies modeling and distribution pattern analysis in the Appalachian Basin: *AAPG Bulletin*, v. 97, no. 12, p. 2173-2205.
- Wright, A.M., D. Spain, and K.T. Ratcliffe, 2010, Application of inorganic whole rock geochemistry to shale resource plays: SPE Paper 137946, Canadian Unconventional Resources & International Petroleum Conference, Calgary, 18p.
- Zargari, S., M. Prasad, K.C. Mba, and E.D. Mattson, 2013, Organic maturity, elastic properties, and textural characteristics of self resourcing reservoirs: *Geophysics*, v.

78(4), p. D223-D235.

Zeszotarski, J.C., R.R. Chromik, R.P. Vinci, M.C. Messmer, R. Michels, and J.W. Larsen, 2004, Imaging and mechanical property measurements of kerogen via nanoindentation: *Geochimica et Cosmochimica Acta*, v. 68, p. 4113-4119.

## CHAPTER 6 SUMMARY AND CONCLUSIONS

This thesis is a multi-disciplinary analysis of the Middle and Upper Devonian Horn River Shale, Western Canada Sedimentary Basin, integrating stratigraphy, geochemistry, petrophysics and geomechanics. The objectives of this study are to (1) document the controls of geochemical composition on petrophysical and geomechanical properties and (2) relate shale geochemistry to sea level change.

### 6.1 The effect of sea level change on organic matter accumulation

Chapter 2 documents the effect of sea level fluctuation on detrital flux, redox conditions, productivity and therefore organic carbon enrichment patterns. High resolution geochemical datasets on five long continuous cores provide new insights into the mechanisms and controls on the stratigraphic and geographic variation.

Organic matter accumulation in the Horn River Shale was controlled by multiple factors, including redox conditions, productivity and dilution by detrital input, all of which are directly affected by sea level fluctuation. Three cycles were recorded in the organic matter enrichment, which is preferentially accumulated during transgressions and is depleted during regressions.

Detrital flux is strongly affected by sea level change, which can be used to document transgressive-regressive cycles. Variation of aluminum and titanium concentrations indicates that detrital sediment flux to the basin was higher during regressions than transgressions. Geographic variation in detrital flux provides insights into sediment source. Detrital silica and biogenic silica are identifiable in crossplots of Zr versus Si concentrations.

To document the stratigraphic and geographic redox conditions, three redox-sensitive elements ratios, Mo/Al, Ni/Co, Th/U and C<sub>org</sub>-Fe-S relationships are analyzed in five long cores. Redox conditions, exhibit a strong correlation to TOC content and is interpreted to have been the primary control on the organic carbon

deposition, although productivity and dilution factors also contributed. Key redox-sensitive trace elements ratios and  $C_{org}$ -Fe-S relationships suggest that water conditions are more anoxic during transgressions than regressions. Variations in biogenic silica concentrations demonstrate a enhanced productivity and depleted productivity during transgression and regression, respectively. Redox conditions also vary geographically, more reducing conditions in distal areas. Redox events, expressed by trace element ratios, is traceable across the basin, which may be a tool for chronostratigraphic correlation in other black shales.

In high maturity shale formations, the use of barium and phosphate concentrations as productivity proxies may be problematic due to the remobilization and remineralization processes. Biogenic silica concentrations may be useful for proxying productivity.

The depositional environments for the Evie and Muskwa intervals, deposited during high sea level, were favorable conditions for organic matter accumulation including anoxic bottom water conditions, high primary productivity and less clastic dilution. The Otter Park Member, deposited during sea level falling stage, has relatively low organic matter concentrations, which may be due to high clastic dilution and dysoxic to oxic bottom water conditions.

## **6.2 The characteristics of porosity and permeability and their controlling factors**

Chapter 3 and 4 explores the influence geochemical composition have in affecting porosity, permeability and pore structure, including pore morphology, pore size and pore throat size distribution. Porosity ranges from 0.62% to 12.04%, while measured matrix permeability ranges between 1.7 and 42.8 nanodarcy and increases with increasing porosity, suggesting that permeability in Horn River Shale samples is largely controlled by porosity.

Five primary shale lithofacies were identified by hand-core and thin section

analyses: massive mudstones, massive mudstones with pyrite streaks, laminated mudstones, bioturbated mudstones and carbonates. Massive mudstones and pyritic mudstones have the highest porosity and permeability; laminated mudstones have moderate porosity and permeability; bioturbated mudstones and carbonates have the lowest porosity and permeability.

TOC content exerts stronger control on porosity and permeability than inorganic composition. A weaker positive correlation between porosity and silica content, and the abundant presence of interparticle pores between quartz grains identified by SEM images indicate that quartz content may be another factor enhancing the porosity.

SEM and TEM images suggest that three pore types, organic matter-hosted pores, intraparticle pores and interparticle pores are present in Horn River shale reservoirs. The former appear to have developed by cracking of kerogen to hydrocarbon, while the latter two types result from carbonate dissolution and rearrangement of phyllosilicate platelets in clay aggregates during mechanical compaction and diagenetic processes. In organic-rich samples, organic matter-hosted pores are the dominant pore type, whereas in quartz-rich samples, the dominant pore type is interparticle pores existing between quartz grains. In clay-rich or carbonate-rich samples, the dominant pore type is intraparticle pores, which are fewer in abundance and smaller in size.

Pore size and pore throat size distribution are strongly associated with TOC content. In organic-rich samples, the dominant pore throat size is less than 10 nm, while in organic-lean samples, pore throat size distribution was characterized by a dominant range of greater than 20 nm. Pores with diameters less than 100 nm are pervasive within the organic matter, while pores with diameters greater than 100 nm typically occur between rigid mineral grains.

Our results indicate that the Muskwa Formation and the Evie Member have higher porosity for shale gas storage, as they mainly consist of massive mudstones and pyritic mudstones with relatively high TOC. The Otter Park is a poorer reservoir, as it primarily

comprises laminated mudstones and bioturbated mudstones with lower TOC.

### **6.3 The impact of geochemical composition on geomechanical properties**

Chapter 5 examines the impact of geochemical composition on geomechanical properties in the Horn River shale formation and their temporal and geographic variation. Rock mechanical properties are of considerable significance because they control the rock's response to hydraulic fracturing; however, the factors controlling geomechanical properties are still unclear. The composition in shale formations is strongly heterogeneous; thus developing models that relate geochemical composition and geomechanical properties is critically important. The availability of many core samples and modern wire-line log data make the Horn River Shale an unparalleled opportunity for such an analysis.

Hardness measurements on core samples are an effective proxy for brittleness in shale reservoirs measurement from well logs. Rock composition exerts a first order control on brittleness, in particular clay minerals, which result in decreased brittleness. TOC content has only a minor effect on geomechanical properties in the Horn River, which at least in part may be due to its high thermal maturity; less mature shales may show a different relationship. Factor analysis demonstrates that a high fraction of carbonate minerals results in increased brittleness, while biogenic quartz enhances brittleness.

Depositional facies are clearly related to brittleness, because rock composition varies with facies. Quartz- or carbonate-rich massive mudstone, pyritic mudstone and carbonate lithofacies are relatively brittle, whereas relatively clay-rich laminated mudstone and bioturbated mudstone lithofacies are more ductile. Geomechanical properties in the Horn River Shale show both geographic variation and stratigraphic variation, which can be tied to the variation in mineral composition related to sources of sediment.

#### **6.4 Recommendations for future studies**

The present-day fabric of mudrocks is the product of diagenetic processes that overprint an initial depositional fabric. Diagenetic reactions are important to a variety of significant rock properties: (1) geomechanical strength, largely dictated by clay minerals and silica cementation; (2) porosity and permeability, in part determined by clay mineralogy and TOC content. Future studies should focus on the diverse diagenetic processes and their effect on the petrophysical and geomechanical properties.

## **Bibliography**

- Abouelresh, M. O., Slatt, R.M., 2012. Lithofacies and sequence stratigraphy of the Barnett shale in east-central Fort Worth basin, Texas. *AAPG Bulletin* 96, 1-22.
- Algeo, T.J., Ingall, E., 2007. Sedimentary C<sub>org</sub>:P ratios, paleovean ventilation, and Phanerozoic atmospheric pO<sub>2</sub>. *Palaeogeography, Palaeoclimatology, Palaeoecology* 256, 130-155.
- Algeo, T.J., Kuwahara, K., Sano, H., Bates, S., Lyons, T., Elswick, E., Hinnov, L., Ellwood, B., Moser, J., Maynard, J.B., 2011. Spatial variation in sediment fluxes, redox conditions, and productivity in the Permian-Triassic Panthalassic Ocean. *Palaeogeography, Palaeoclimatology, Palaeoecology* 308, 65-83.
- Algeo, T.J., Maynard, J.B., 2004. Trace element behavior and redox facies analysis of core shales of Upper Pennsylvanian Kansas-type cyclotherms. *Chemical Geology* 206, 289-318.
- Algeo, T.J., Schwark, L., Hower, J.C., 2004. High-resolution geochemistry and sequence stratigraphy of the Hushpuckney Shale (Swope Formation, eastern Kansas): implications for climato-environmental dynamics of the Late Pennsylvanian Midcontinent Seaway. *Chemical Geology* 206, 259-288.
- Algeo, T.J., Tribovillard, N., 2009. Environmental analysis of paleoceanographic systems based on molybdenum-uranium covariation. *Chemical Geology* 268, 211-225.
- Al-Zahrani, A.A., 2011, Interpretation of 3D multicomponent seismic data for investigating natural fractures in the Horn River Basin, northeast British Columbia: M.Sc. thesis, University of Calgary, 118p.
- Anderson, L.D., Delaney, M.L., 2005. Use of multiproxy records on the Agulhas Ridge, Southern Ocean (Ocean Drilling Project Leg 177, Site 1090) to investigate sub-Antarctic hydrography from the Oligocene to the early Miocene. *Paleoceanography* 20, PA3011, 16p.
- Anderson, R.F., Fleisher, M.Q., LeHuray, A.P., 1989. Concentration, oxidation state, and

particular flux of uranium in the Black Sea. *Geochimica et Cosmochimica Acta* 53, 2215-2224.

Aoudia, K., J. L. Miskimins, N. B. Harris and C. A. Mnich, 2010, Statistical analysis of the effects of mineralogy on rock mechanical properties of the Woodford shale and the associated impacts for hydraulic fracture treatment design: 44<sup>th</sup> US Rock Mechanics Symposium and 5<sup>th</sup> U.S.-Canada Rock Mechanics Symposium, Salt Lake, 11p.

Arthur, M.A. and Sageman, B.B., 2005. Sea-level control on source-rock development: perspectives from the Holocene Black Sea, the mid-Cretaceous Western Interior Basin of North America, and the late Devonian Appalachian Basin, in Harris, N.B., ed., *The deposition of Organic-Carbon-Rich Sediments: Models, Mechanisms, and Consequences*. SEPM Special Publication 82, 35-59.

Arthur, M.A., Sageman, B.B., 1994. Marine black shales: Depositional mechanisms and environments of ancient deposits. *Annual Review of Earth and Planetary Sciences* 22, 499-551.

B.C. Ministry of Energy and Mines, 2011. Ultimate potential for unconventional natural gas in northeastern British Columbia's Horn River Basin. *Oil and Gas Reports*, May 2011 (50 pp).

B.C. Oil and Gas Commission, 2014, *Horn River Basin Unconventional Shale Gas Play Atlas*, 15p.

Barret, E.P., Joyner, L.G., Halenda, P.P., 1951. The determination of pore volume and area distribution in porous substances. I. Computation from nitrogen isotherms: *The Bureau of Chemistry and Soils and George Washington University* 73, 373–380.

Benitez-Nelson, C.R., 2000. The biogeochemical cycling of phosphorus in marine systems. *Earth Science Review* 51, 109-135.

Bernard, S., Wirth, R., Schreiber, A., Schulz, H.M., Horsfield, B., 2012. Formation of nanoporous pyrobitumen residues during maturation of the Barnett Shale (Fort

- Worth Basin). *International Journal of Coal Geology* 103, 3-11.
- Berner, R.A., Raiswell, R., 1983. Burial of organic carbon and pyrite sulfur in sediments over Phanerozoic time: a new theory. *Geochimica et Cosmochimica Acta* 47, 855-862.
- Bernet, M., and K. Basset, 2005, Provenance analysis by single-quartz-grain SEM-CL/optical microscopy: *Journal of Sedimentary Research*, v. 75, p. 492-500.
- Bohacs, K., 2005. Production, destruction, and dilution-the many paths to source-rock development. *SEPM Special Publication* 82, 61-101.
- Bohacs, K.M., Grabowski, G.J., Carroll, A.R., Mankiewicz, P.J., Gerhardt, K.J., Schwalbach, J.R., Wegner, M.B., Simo, J.A., 2005. Production, destruction, and dilution – the many paths to source rock development, in Harris, N.B., ed., *The deposition of Organic-Carbon-Rich Sediments: Models, Mechanisms, and Consequences*. *SEPM Special Publication* 82, 61-101.
- Bonn, W.J., Gingle, F.X., Grobe, H., Mackensen, A., Fütterer, D.K., 1998. Palaeoproductivity at the Antarctic continental margin: opal and barium records for the last 400 ka. *Paleogeography, Paleoclimatology, Paleoecology* 139, 195-211.
- Bowker, K.A., 2007, Barnett Shale gas production, Fort Worth Basin: Issue and Discussion: *AAPG Bulletin*, v. 91, no. 4, p. 523-533.
- Brumsack, H.J., 2006. The trace metal content of recent organic carbon-rich sediments: Implications for Cretaceous black shale formation. *Paleogeography, Paleoclimatology, Paleoecology* 232, 344-361.
- Brumsack, H.J., Gieskes, J.M., 1983. Interstitial water trace-metal chemistry of laminated sediments from the Gulf of California, Mexico. *Marine Chemistry* 14, 89-106.
- Brunauer, B.S., Emmett, P.H., Teller, E., 1938. Adsorption of gases in multimolecular layers: *The Bureau of Chemistry and Soils and George Washington University* 60, 309–319.

- Bustin, A.M.M., and R.M. Bustin, 2012, Importance of rock properties on the producibility of gas shales: *International Journal of Coal Geology*, v. 103, p. 132-147.
- Calvert, S.E., Bustin, R.M. Ingall, E.D., 1996. Influence of water column anoxia and sediment supply on the burial and preservation of organic carbon in marine shales. *Geochimica et Cosmochimica Acta* 60, 1577-1593.
- Calvert, S.E., Pedersen, T.F., 1993. Geochemistry of recent oxic and anoxic marine sediments: implications for the geological record. *Marine Geology* 113, 67-88.
- Caplan, M.L., Bustin, R.M., 1998. Paleooceanographic controls on geochemical characteristics of organic-rich Exshaw mudrocks: role of enhanced primary productivity. *Organic Geochemistry* 30, 161-188.
- Catuneanu, O., Galloway, W.E., Kendall, C.G., Miall, A.D., Posamentier, H.W., Strasser, A. and Tucker, M.E., 2011. Sequence stratigraphy: methodology and nomenclature. *Newsletters on Stratigraphy* 44, 173-245.
- Chalmers, G. R. L., Ross, D. J. K., Bustin, R. M., 2012a. Geological controls on matrix permeability of Devonian gas shales in the Horn River and Liard basins, northeast British Columbia, Canada. *International Journal of Coal Geology* 103, 120-131.
- Chalmers, G. R., Bustin, R. M., Power, L. M., 2012b. Characterization of gas shale pore systems by porosimetry, pycnometry, surface area, and field emission scanning electron microscopy/transmission electron microscopy image analyses: Examples from the Barnett, Woodford, Haynesville, Marcellus, and Doig units. *AAPG Bulletin* 96, 1099-1119.
- Creaney, S., Passey, Q.R., 1993. Recurring patterns of total organic carbon and source rock quality within a sequence stratigraphic framework. *AAPG Bulletin* 77, 386-401.
- Cui, X., Bustin, A.M.M., Bustin, R.M., 2009. Measurements of gas permeability and diffusivity of tight reservoir rocks: different approaches and their applications. *Geofluids* 9, 208-223.

Curiale, J.A., Curtis, J.B., 2015. Organic geochemical applications to the exploration for source-rock reservoirs - A review. *Journal of Unconventional Oil and Gas Resources* (in press).

Curtis, J. B., 2002. Fractured shale-gas systems. *AAPG Bulletin* 86, 1921-1938.

Curtis, M. E., Ambrose, R. J., Sondergeld, C. H., Rai, C. S., 2010. Structural characterization of gas shales on the micro- and nano-scales. *Canadian Unconventional Resources and International Petroleum Conference*, Calgary, Alberta, Canada, October 19-21, 2010, SPE Paper 137693, 15p.

Curtis, M. E., Ambrose, R. J., Sondergeld, C. H., Rai, C. S., 2011. Transmission and scanning electron microscopy investigation of pore connectivity of gas shales on the nanoscale. *Society of Petroleum Engineers Unconventional Gas Conference*, Woodlands, Texas, June 14-16, 2011, SPE Paper 144391, 10p.

Curtis, M.E., Cardott, B.J., Sondergeld, C.H., Rai, C.S., 2012b. Development of organic porosity in the Woodford Shale with increasing thermal maturity. *International Journal of Coal Geology* 103, 26-31.

Curtis, M.E., Sondergeld, C.H., Ambrose, R.J., Rai, C.S., 2012a. Microstructural investigation of gas shales in two and three dimensions using nanometer-scale resolution imaging. *AAPG Bulletin* 96, 665-677.

Dean, W.E., Arthur, M.A., 1989. Iron-sulfur-carbon relationships in organic-carbon-rich sequences: I . Cretaceous W  
708-743.

Demaison, G.J., Moore, G.T., 1980. Anoxic environments and oil source bed genesis. *AAPG Bulletin* 64, 1179-1209.

Dewhurst, D.N., Aplin, A.C., Sarda, J.P., Yang, Y.L., 1998. Compaction-driven evolution of porosity and permeability in natural mudstones: An experimental study. *Journal of Geophysical Research* 103, 651-661.

Dewhurst, D.N., Yang, Y.L., Aplin, A.C., 1999. Permeability and fluid flow in natural

- mudstones, in A.C. Aplin et al., *Muds and mudstones: Physical and fluid flow properties*, Geological Society Special Publication 158, 23-43.
- Dong, T., Harris, N. B., 2013. Pore size distribution and morphology in the Horn River shale, Middle and Upper Devonian, northeastern British Columbia, Canada, in W. Camp, E. Diaz and B. Wawak, eds., *Electron microscopy of shale hydrocarbon reservoirs*. AAPG Memoir 102, 67-79.
- Dong, T., Harris, N.B., Ayranci, K., Twemlow, C.E., Nassichuk, B.R., 2015a. Porosity characteristics of the Devonian Horn River shale, Canada: Insights from lithofacies classification and shale composition. *International Journal of Coal Geology* 141-142, 74-90.
- Dong, T., Harris, N.B., Ayranci, K., Yang, S., 2015b. The impact of rock composition on geomechanical properties in a shale formation: Middle and Upper Devonian Horn River Shale, Northeast British Columbia. submitted to AAPG Bulletin.
- Dykstra, M., 2012, *Deep Water Tidal Sedimentology*, in R. A. Davis Jr., and R. W. Dalrymple, eds., *Principles of Tidal Sedimentology*: Berlin, Springer, p. 371–396.
- Dymond, J., Suess, E., Lyle, M., 1992. Barium in deep-sea sediment: a geochemical proxy for paleoproductivity. *Paleoceanography* 7, 163-181.
- Eliyahu, M., S. Emmanuel, R.J. Day-Stirrat, and C.I. Macaulay, 2015, Mechanical properties of organic matter in shales mapped at the nanometer scale: *Marine and Petroleum Geology*, v. 59, p. 294-304.
- Ferri, F., A.S. Hickin, and D.H. Huntley, 2011, Besa River formation, western Liard Basin, British Columbia (NTS 094N): geochemistry and regional correlations; in *Geoscience Reports 2011*, British Columbia Ministry of Energy, Mines and Natural Gas, p. 1-18.
- Fishman, N. S., Hackley, P. C., Lowers, H. A., Hill, R. J., Egenhoff, S. O., Eberl, D. D., Blum, A. E., 2012. The nature of porosity in organic-rich mudstones of the Upper Jurassic Kimmeridge clay formation, North Sea, offshore United Kingdom.

- International Journal of Coal Geology 103, 32-50.
- Frelinger, S.N., M.D. Ledvina, J.R. Kyle, and D.G. Zhao, 2015, Scanning electron microscopy cathodoluminescence of quartz: Principles, techniques and applications in ore geology: *Ore Geology Reviews*, v. 65, p. 840-852.
- Ghanizadeh, A., Clarkson, C.R., Aquino, S., Ardakani, O.H., Sanei, H., 2015. Petrophysical and geomechanical characteristics of Canadian tight oil and liquid-rich gas reservoirs: I. Pore network and permeability characterization. *Fuel* 153, 664-681.
- Gregg, S. J., and K. S. W. Sing, 1982, Adsorption, surface area and porosity, 2d: London, Academic Press, 303 p.
- Groen, J. C., Peffer, L. A. A., Pérez-Ramírez, J., 2003. Pore size determination in modified micro- and mesoporous materials. Pitfalls and limitations in gas adsorption data analysis. *Microporous and Mesoporous Materials* 60, 1-17.
- Gupta, N., 2012. Multi-scale characterization of the Woodford shale in west-central Oklahoma: from scanning electron microscope to 3D seismic. PhD thesis, University of Oklahoma, 182p.
- Hall, C. D., 2011, Comparison of the reservoir properties of the Muskwa (Horn River Formation) with other North American gas shales: CSPG CSEG CWLS Convention, 3p.
- Hammes, U, Frébourg, G., 2012. Haynesville and Bossier mudrocks: A facies and sequence stratigraphic investigation, East Texas and Louisiana, USA. *Marine and Petroleum Geology* 31, 8-26.
- Hao, F., Zou, H. Y., Lu, Y. C., 2013. Mechanisms of shale gas storage: implications for shale gas exploration in China. *AAPG Bulletin* 97, 1325-1346.
- Haq, B. U. and Schutter, S.R., 2008. A Chronology of Paleozoic Sea-Level Changes. *Science* 322, 64-68.
- Harris, N.B., Freeman, K.H., Pancost, R.D., White, T.S., Mitchell, G.D., 2004. The

character and origin of lacustrine source rocks in the Lower Cretaceous synrift section, Congo Basin, west Africa. AAPG Bulletin 88, 1163-1184.

Harris, N.B., J.L. Miskimins, and C.A. Mnich, 2011, Mechanical anisotropy in the Woodford shale, Permian Basin: origin, magnitude, and scale: *The Leading Edge*, v. 30(3), p. 284-291.

Harris, N.B., Mnich, C.A., Selby, D., Korn, D., 2013. Minor and trace element and Re-Os chemistry of the Upper Devonian Woodford Shale, Permian Basin, west Texas: insights into metal abundance and basin processes. *Chemical Geology* 356, 76-93.

Hay, W.W., 1995. Paleooceanography of marine organic-carbon-rich sediments, in Huc, A.Y., ed., *Paleogeography, Paleoclimate, and Source rocks*. American Association of Petroleum Geologists, *Studies in Geology* 40, 21-59.

Hemmesch, N.T., Harris, N.B., Mnich, C.A., Selby, D., 2014. A sequence-stratigraphic framework for the Upper Devonian Woodford Shale, Permian Basin, west Texas. AAPG Bulletin 98, 23-47.

Hillier, S., 2003, Quantitative analysis of clay and other minerals in sandstones by X-ray powder diffraction (XRPD): *Int. Assoc. Sedimentol. Special Publication* 34, 213-251.

Hulsey, K.M., 2011. Lithofacies characterization and sequence stratigraphic framework for some gas-bearing shales within the Horn River Basin, northeastern British Columbia. University of Oklahoma, MSc. thesis, 76p.

Jarvie, D. M., Hill, R. J., Ruble, T. E., Pollastro, R. M., 2007. Unconventional shale-gas systems: the Mississippian Barnett shale of north-central Texas as one model for thermogenic shale-gas assessment. AAPG Bulletin 91, 475-499.

Jennings, D. S., Antia, J., 2013. Petrographic characterization of the Eagle Ford shale, south Texas: mineralogy, common constituents, and distribution of nanometer-scale pore types, in W. Camp, E. Diaz, and B. Wawak, eds., *Electron microscopy of shale hydrocarbon reservoirs*. AAPG Memoir 102, 101-113.

- Jones, B., Manning, D.A.C., 1994. Comparison of geochemical indices used for the interpretation of palaeoredox conditions in ancient mudstones. *Chemical Geology* 111, 111-129.
- Jørgensen, B.B., 1982. Mineralization of organic matter in the sea bed—the role of sulphate reduction. *Nature* 296, 643-645.
- Katz, B., 2005. Controlling factors on source rock development – a review of productivity, preservation, and sedimentation rate, in Harris, N.B., ed., *The Deposition of Organic-Carbon-Rich Sediments: Models, Mechanisms, and Consequences*. SEPM Special Publication 82, 35-59.
- Klaver, J., Hemes, S., Houben, M., Desbois, G., Radi, Z., Urai, J.L., 2015. The connectivity of pore space in mudstones: insights from high-pressure Wood's metal injection, BIB-SEM imaging, and mercury intrusion porosimetry. *Geofluids*. doi: 10.1111/gfl.12128.
- Knapp, L.J., McMillan, J.M., Harris, N.B., 2015. Duvernay Formation sequence stratigraphy: integrating sedimentology, geochemistry, and petrophysics. Canadian Society of Petroleum Geologists, Annual convention, Calgary.
- Kwon, O., Kronenberg, A.K., Gangi, A.F., Johnson, B., Herbert, B.E., 2004. Permeability of illite-bearing shale: 1. Anisotropy and effects of clay content and loading. *Journal of Geophysical Research* 109, B10205, 19p.
- Labani, M.M., and R. Rezaee, 2015, The importance of geochemical parameters and shale composition on rock mechanical properties of gas shale reservoirs: a case study from the Kockatea Shale and Carynginia Formation from the Perth Basin, Western Australia: *Rock Mechanics and Rock Engineering*, v. 48, p. 1249-1257.
- Lash, G. G. and Engelder, T., 2011. Thickness trends and sequence stratigraphy of the Middle Devonian Marcellus Formation, Appalachian basin: implications for Acadian foreland basin evolution. *AAPG Bulletin* 95, 61-103.
- Lash, G.G., Blood, D.R., 2014. Organic matter accumulation, redox, and diagenetic

- history of the Marcellus Formation, southwestern Pennsylvania, Appalachian Basin. *Marine and Petroleum Geology* 57, 244-263.
- Lei, Y.H., Luo, X.R., Wang, X.Z., Zhang, L.X., Jiang, C.F., Yang, W., Yu, Y.X., Cheng, M., Zhang, L.K., 2015. Characteristics of silty laminae in Zhangjiatan Shale of southeastern Ordos Basin, China: Implications for shale gas formation. *AAPG Bulletin* 99, 661-687.
- Lewan, M.D., Maynard, J.B., 1982. Factors controlling enrichment of vanadium and nickel in the bitumen of organic sedimentary rocks. *Geochim. Cosmochim. Acta* 46, 2547-2560.
- Loucks, R. G., and Ruppel, S.C., 2007. Mississippian Barnett shale: lithofacies and depositional setting of a deep-water shale-gas succession in the Fort Worth basin, Texas. *AAPG Bulletin* 91, 579-601.
- Loucks, R. G., Reed, R. M., Ruppel, S. C., and Jarvie, D. M., 2009. Morphology, genesis, and distribution of nanometer-scale pores in siliceous mudstones of the Mississippian Barnett shale. *Journal of Sedimentary Research* 79, 848-861.
- Loucks, R. G., Reed, R. M., Ruppel, S. C., Hammes, U. 2012. Spectrum of pore types and networks in mudrocks and a descriptive classification for matrix-related mudrock pores. *AAPG Bulletin* 96, 1071-1098.
- Luffel, D.L., Hopkins, C.W., Shettler, P.D., 1993. Matrix Permeability measurements of gas productive shales. SPE Paper, 1993 SPE Annual Technical Conference and exhibition, Houston, Texas, US, 10p.
- Lyons, T.W., Werne, J.P., Hollander, D.J., Murray, R.W., 2003. Contrasting sulfur geochemistry and Fe/Al and Mo/Al ratios across the last oxic-anoxic transition in the Cariaco Basin, Venezuela. *Chemical Geology* 195, 131-157.
- Macquaker, J.H.S., Taylor, K.G., Gawthorpe, R.L., 2007. High-resolution facies analyses of mudstones: implications for paleoenvironmental and sequence stratigraphic interpretations of offshore ancient mud-dominated successions. *Journal of*

Sedimentary Research 77, 324-339.

- Mallon, A.J., Swarbrick, R.E., 2008. How should permeability be measured in fine-grained lithologies? Evidence from the chalk. *Geofluids* 8, 35-45.
- Mastalerz, M., Schimmelmann, A., Drobniak, A., Chen, Y. Y., 2013. Porosity of Devonian and Mississippian New Albany shale across a maturation gradient: insights from organic petrology, gas adsorption, and mercury intrusion. *AAPG Bulletin* 93, 1621-1643.
- McManus, J., Berelson, W.M., Klinkhammer, G.P., Johnson, K.S., Coale, K.H., Anderson, R.F., Kumar, N., Burdige, D.J., Hammond, D.E., Brumsack, H.J., McCorkle, D.C., Rushdi, A., 1998. Geochemistry of barium in marine sediments: implications for its use as a paleoproxy. *Geochimica et Cosmochimica Acta* 62, 3453-3473.
- McPhail, S., W. Walsh, C. Lee and P. A. Monahan, 2008. Shale units of the Horn River formation, Horn River basin and Cordova Embayment, Northeastern British Columbia: (abs.), Canadian Society of Petroleum Geologists and Canadian Well Logging Society Convention, 14 p.
- Melendez-Martinez, J., and D.R., Schmitt, 2016. A comparative study of the anisotropic dynamic and static elastic moduli of unconventional reservoir shales: Implications for geomechanical investigations. submitted to *Geophysics*.
- Milliken, K., Day-Stirrat, R., 2013. Cementation in mudrocks: brief review with examples from cratonic basin mudrocks: Critical Assessment of Shale Resource Plays. *AAPG Memoir* 203, 133-150.
- Milliken, K.L., Rudnicki, M., Awwiller, D.N., Zhang, T.W., 2013. Organic matter-hosted pore system, Marcellus Formation (Devonian), Pennsylvania. *AAPG Bulletin* 97, 177-200.
- Milliken, K.L., W.L. Esch, R.M. Reed, and T.W. Zhang, 2012, Grain assemblages and strong diagenetic overprinting in siliceous mudrocks, Barnett Shale (Mississippian), Fort Worth Basin, Texas: *AAPG Bulletin*, v. 96, no. 8, p. 1553-1578.

- Milner, M., Mclin, R., Petriello, J., 2010. Imaging texture and porosity in mudstones and shales: comparison of secondary and ion-milled backscatter SEM methods. Canadian Unconventional Resources & International Petroleum Conference, Calgary, Alberta, June 19-21, 2010, CSUG/SPE Paper 138975, 10p.
- Moghadam, A.A., Chalaturnyk, R., 2015. Laboratory investigation of shale permeability. SPE Paper 175919-MS, 2015 SPE/CSUP Unconventional Resources Conference, Calgary, Alberta, Canada, 30p.
- Mondol, N.H., J. Jahren, and K. Bjørlykke, 2008, Elastic properties of clay minerals: The Leading Edge, v. 27, no. 6, p. 758-770.
- Moore, P.E., 1989. The Kaskaskia Sequence: reefs, platforms, and foredeeps The lower Kaskaskia sequence- Devonian, Western Canada Sedimentary Basin, a case history: Canadian Society of Petroleum Geologist, Special Publication 30, 139-164.
- Morford, J.L., Emerson, S., 1999. The geochemistry of redox sensitive trace metals in sediments. *Geochim. Cosmochim. Acta* 63, 1735-1750.
- Mort, H., Jacquat, O., Adatte, T., Steinmann, P., Föllmi, K., Matera, V., Berner, Z., Stüben, D., 2007. The Cenomanian/Turonian anoxic event at the Bonarelli Level in Italy and Spain: enhanced productivity and/or better preservation? *Cretaceous Research* 28, 597-612.
- Mossop, G.D., Shetsen, I., 1994. Geological atlas of the Western Canada Sedimentary Basin, Canadian Society of Petroleum Geologists and Alberta Research Council, Special Report 4.
- National Energy Board, 2013. The ultimate potential for unconventional petroleum from the Montney Formation of British Columbia and Alberta. 17p. <https://www.neb-one.gc.ca/nrg/sttstc/ntrlgs/rprt/ltmtptntlmntnyfrmtn2013/ltmtptntlmntnyfrmtn2013-eng.pdf>.
- Nelson, P. H., 2009. Pore-throat sizes in sandstones, tight sandstones, and shales. *AAPG Bulletin* 93, 329-340.

- Neuzil, C.E., 1994. How permeable are clays and shales? *Water Resources Research* 30, 145-150.
- O'Connell, S.C., 1994, Geological history of the Peace River Arch; in *Geological Atlas of the Western Canada Sedimentary Basin*: Canadian Society of Petroleum Geologists and Alberta Research Council, Special Report 4.
- Okiongbo, K.S., A.C. Aplin, and S.R. Larter, 2005, Changes in type II kerogen density as a function of maturity: evidence from the Kimmeridge Clay formation: *Energy and Fuels*, v. 19, no. 6, p. 2495-2499.
- Oldale, H.S., Munday, R.J., 1994. Devonian Beaver Hill Group of the Western Canada Sedimentary Basin. *Geological Atlas of the Western Canada Sedimentary Basin*, Canadian Society of Petroleum Geologists and Alberta Research Council, Special Report, 4p.
- Omotoso, O., D.K. McCarty, S. Hillier, R. Kleeberg, 2006, Some successful approaches to quantitative mineral analysis as revealed by the 3rd Reynolds cup contest: *Clays and Clay Minerals*, v. 54, no. 6, p. 748-760.
- Parrish, J. T., 1995. Paleogeography of C<sub>org</sub>-rich rocks and the preservation versus production controversy, in Huc, A.Y., ed., *Paleogeography, Paleoclimate, and Source rocks*. American Association of Petroleum Geologists, *Studies in Geology* 40, 1-20.
- Passey, Q.R., Bohacs, K.M., Esch, W.L., Klimentidis, R., Sinha, S., 2010. From oil-prone source rock to gas-producing shale reservoir-geologic and petrophysical characterization of unconventional shale-gas reservoirs. SPE Paper 131350, 2010 CPS/SPE International Oil & Gas Conference and Exhibition, Beijing, China, 29p.
- Pedersen, T.F., Calvert, S.E., 1990. Anoxia VS. Productivity: What controls the formation of organic-carbon-rich sediments and sedimentary rocks? *American Association of Petroleum Geology Bulletin* 74, 454-466.
- Pickett, G.R., 1963, Acoustic character logs and their applications in formation evaluation: *Journal of Petroleum Technology*, v. 15, no. 6, p. 659-667.

- Piper, D.Z., Perkins, R.B., 2004. A modern vs. Permian black shale- the hydrography, primary productivity, and water-column chemistry of deposition. *Chemical Geology* 206, 177-197.
- Pommer, M., Milliken, K., 2015. Pore types and pore-size distributions across thermal maturity, Eagle Ford Formation, Southern Texas. *AAPG Bulletin* 99, 1713-1744.
- Potma, K., Jonk, R., Davie, M., Austin, N., 2012. A mudstone lithofacies classification of the Horn River Group: integrated stratigraphic analysis and inversion from wireline log and seismic data. 6<sup>th</sup> BC Unconventional Gas Technical Forum, Vancouver, Canada, 26p.
- Prasad, M., 2001, Mapping impedance microstructures in rocks with acoustic microscopy: *The Leading Edge*, v. 20(2), p. 172-179.
- Prasad, M., K. Mba, T.E. McEvoy, and M.L. Batzle, 2011, Maturity and impedance analysis of organic-rich shales: *SPE Reservoir Evaluation & Engineering*, v. 14, p. 533-543.
- Raiswell, R., Berner, R. A., 1987. Organic carbon losses during burial and thermal maturation of normal marine shales. *Geology* 15, 853-856.
- Rebesco, M., F.J. Hernández-Molina, D. Van Rooij, and A. Wåhlin, 2014, Contourites and associated sediments controlled by deep-water circulation processes: State-of-the-art and future considerations: *Marine Geology*, v. 352, p. 111-154.
- ResTech, 1996. Development of Laboratory and Petrophysical Techniques for Evaluating Shale Reservoirs. GRI-95/ 0496, Gas Research Institute, Chicago, Illinois, 279.
- Reynolds, M.M., Munn, D.L., 2010. Development update for an emerging shale gas giant field-Horn River Basin, British Columbia, Canada. *SPE Unconventional Gas Conference*, Pittsburgh, USA, Feb 23-25. SPE Paper 130103, 17p.
- Rickman, R., M. Mullem, E. Petre, B. Grieser, and D. Kundert, 2008, A practical use of shale petrophysics for stimulation design optimization: all shale plays are not clones

- of the Barnett shale: SPE Paper 115258, SPE Annual Technical Conference and Exhibition, Colorado, 11p.
- Rimmer, S. M., Thompson, J. A., Goodnight, S. A., Robl, 2004. Multiple controls on the preservation of organic matter in Devonian-Mississippian marine black shales: geochemical and petrographic evidence. *Palaeogeography, Palaeoclimatology, Palaeoecology* 215, 125-154.
- Rivard, C., Lavoie, D., Lefebvre, R., Séjourné, S., Lamonagne, C., Duchesne, M., 2014. An overview of Canadian shale gas production and environmental concerns. *International Journal of Coal Geology* 126, 64-76.
- Ross, D. J. K., and R. M. Bustin, 2008, Characterizing the shale gas resource potential of Devonian-Mississippian strata in the western Canada sedimentary basin: Application of an integrated formation evaluation: *AAPG Bulletin*, v.92, p. 87-125.
- Ross, D. J. K., and R.M. Bustin, 2009a, The importance of shale composition and pore structure upon gas storage potential of shale gas reservoirs: *Marine and Petroleum Geology*, v. 26, p. 916-927.
- Ross, D.J.K., and R.M. Bustin, 2009b, Investigating the use of sedimentary geochemical proxies for paleoenvironment interpretation of thermally mature organic-rich strata: examples from the Devonian-Mississippian shales, Western Canadian Sedimentary Basin: *Chemical Geology*, v. 260, p. 1-19.
- Russell, A.D., Morford, J.L., 2001. The behaviour of redox-sensitive metals across a laminated-massive-laminated transition in Saanich Inlet, British Columbia. *Marine Geology* 174, 341-354.
- Sageman, B.B., Lyons, T.W., 2004. Geochemistry of fine-grained sediments and sedimentary rocks, In: Mackenzie, F. eds, *Treatise on Geochemistry* 7, 115-158.
- Sageman, B.B., Murphy, A.E., Werne, J.P., Ver Straeten, C.A., Hollander, D.J., Lyons, T.W., 2003. A tale of shales: the relative roles of production, decomposition, and dilution in the accumulation of organic-rich strata, Middle-Upper Devonian,

- Appalachian basin. *Chemical Geology* 195, 229-273.
- Sakhaee-Pour, A., Bryant, S.L., 2011. Gas permeability of shale. SPE Paper 146944, 2011 SPE Annual Technical Conference and Exhibition, Denver, Colorado, USA, 14p.
- Schenau, S.J., Reichart, G.J., De Lange, G.J., 2005. Phosphorus burial as a function of paleoproductivity and redox conditions in Arabian Sea sediments. *Geochim. Cosmochim. Acta* 69, 919-931.
- Schettler, P. D., Parmely, C. R., W. J. Lee, 1989. Gas storage and transport in Devonian shales, SPE Formation Evaluation, p. 371–376.
- Schieber, J., 1998. Deposition of mudstones and shales: overview, problems, and challenges. In: J. Schieber, W. Zimmerle, and P. Sethi, eds. *Shales and Mudstones: Basin Studies, Sedimentology and Paleontology*, Schweizerbart'sche Verlagsbuchhandlung, Stuttgart, 131-146.
- Schieber, J., 1998. Developing a sequence stratigraphic framework for the Late Devonian Chattanooga Shale of the southeastern US: relevance for the Bakken Shales, in Christopher, J. E., Gilboy, C. F., Paterson, D. F., Bend, S. L., ed. *Eighth International Williston Basin Symposium*. Saskatchewan Geological Society, Special Publication 13, 58–68.
- Schieber, J., 2010. Common themes in the formation and preservation of porosity in shales and mudstones: Illustrated with examples across the Phanerozoic. Society of Petroleum Engineers Unconventional Gas Conference, Pittsburgh, Pennsylvania, February 23-25, 2010, SPE Paper 132370, 12 p.
- Schieber, J., D. Krinsley, L. Riciputi, 2000, Diagenetic origin of quartz silt in mudstones and implications for silica cycling: *Nature*, v. 406, p. 981-985.
- Schoepfer, S.D., Shen, J., Weil, H.Y., Tyson, R.V., Ingall, E., Algeo, T.J., 2015. Total organic carbon, organic phosphorus, and biogenic barium fluxes as proxies for paleomarine productivity. *Earth-Science Reviews* 149, 23-52.

- Schroeder, J.O., Murray, R.W., Leinen, M., Pflaum., R.C., Janecek, T.R., 1997. Barium in equatorial Pacific carbonate sediments: terrigenous, oxide, and biogenic associations. *Paleoceanography* 12, 125-146.
- Shanmugam, G., S.K. Shrivastava, and B. Das, 2009, Sandy Debrites and Tidalites of Pliocene Reservoir Sands in Upper-Slope Canyon Environments, Offshore Krishna–Godavari Basin (India): Implications: *Journal of Sedimentary Research*, v. 79, p. 736-756.
- Shen, J., Schoepfer, S.D., Feng, Q.L., Zhou, L., Yu, J.X., Song, H.Y., Wei, H.Y., Algeo, T.J., 2015. Marine productivity changes during the end-Permian crisis and Early Triassic recovery. *Earth-Science Reviews* 149, 136-162.
- Sing, K. S., Everett, D. H., Haul, R.A.W., Moscou, L., Pierotti, R. A., Rouquerol, J., Siemieniewska, T., 1985. Reporting physisorption data for gas/solid systems with special reference to the determination of surface area and porosity. *Pure and Applied Chemistry* 57, 603-619.
- Slatt, R. and Rodriguez, N.D., 2012. Comparative sequence stratigraphy and organic geochemistry of unconventional gas shale: commonality or coincidence? *Journal of Natural Gas Science and Engineering* 8, 68-84.
- Slatt, R. M., Abousleiman, Y., 2011. Merging sequence stratigraphy and geomechanics for unconventional gas shales. *The Leading Edge, special section: shales*, 274-282.
- Slatt, R. M., O'Brien, N. R., 2011. Pore types in the Barnett and Woodford gas shales: contribution to understanding gas storage and migration pathways in fine-grained rocks. *AAPG Bulletin* 95, 2017-2030.
- Slatt, R., 2011. Important geological properties of unconventional resource shales. *Central European Journal of Geosciences* 3, 435-448.
- Slatt, R.M., O'Brien, N.R., 2013. Microfabrics related to porosity development, sedimentary and diagenetic processes, and composition of unconventional resource shale reservoirs as determined by conventional scanning electron microscopy, in W.

- Camp, E. Diaz and B. Wawak, eds., Electron microscopy of shale hydrocarbon reservoirs. AAPG Memoir 102, 37-44.
- Sondergeld, C. H., Ambrose, R. J., Rai, C. S., Moncrieff, J., 2010. Microstructural studies of gas shales. Society of Petroleum Engineers Unconventional Gas Conference, Pittsburgh, Pennsylvania, February 23-25, 2010, SPE Paper 131771, 17p.
- Sondergeld, C. H., K. E. Newsham, M. C. Rice and C. S. Rai, 2010, Petrophysical considerations in evaluating and producing shale gas resources: SPE Paper 131768, SPE Unconventional Gas Conference, Pittsburgh, 34p.
- Sone, H., Zoback, M.D., 2013. Mechanical properties of shale-gas reservoir rocks - Part 1: Static and dynamic elastic properties and anisotropy. *Geophysics* 78, 381-392.
- Taylor, S.R., McLennan, S.M., 1985. *The Continental Crust: Its Composition and Evolution*. Blackwell, Oxford, 312 p.
- Tian, H., Pan, L., Xiao, X. M., Wilkins, R. W. T., Meng, Z. P., Huang, B. J., 2013. A preliminary study on the pore characterization of lower Silurian black shales in the Chuandong thrust fold belt, southwestern China using low pressure N<sub>2</sub> adsorption and FE-SEM methods. *Marine and Petroleum Geology* 48, 8-19.
- Tian, H., Pan, L., Zhang, T.W., Xiao, X.M., Meng, Z.P., Huang, B.J., 2015. Pore characterization of organic-rich Lower Cambrian shales in Qiannan Depression of Guizhou Province, Southwestern China. *Marine and Petroleum Geology* 62, 28-43.
- Tribovillard, N. P., Desprairies, A., Lallier-Verges, E., Bertrand, P., Moureau, N., Ramdani, A., Ramanampisoa, L., 1994. Geochemical study of organic-matter rich cycles from the Kimmeridge Clay Formation of Yorkshire (UK): productivity versus anoxia. *Palaeogeography, Palaeoclimatology, Palaeoecology* 108, 165-181.
- Tribovillard, N., Algeo, T. J., Lyons, T., Riboulleau, A., 2006. Trace metals as paleoredox and paleoproductivity proxies: an update. *Chemical Geology* 232, 12-32.
- Tribovillard, N., Algeo, T. J., Riboulleau, A., 2012. Analysis of marine environmental

- conditions based on molybdenum-uranium covariation-Applications to Mesozoic paleoceanography. *Chemical Geology* 324-325, 46-58.
- Tyson, R. V., 2005. The “productivity versus preservation” controversy: cause, flaws, and resolution. *SEPM Special Publication* 82, 17-33.
- Tyson, R.V., 2001. Sedimentation rate, dilution, preservation, and total organic carbon: some results of a modelling study. *Organic Geochemistry* 32, 333-339.
- Tyson, R.V., Pearson, T.H., 1991. Modern and ancient continental shelf anoxia: an overview, *in* Tyson, R.V., and Pearson, T.H., eds., *Modern and Ancient Continental Shelf Anoxia*. Geological Society of London, Special Publications 58, 1-24.
- U.S. EIA, 2012. Annual Energy Outlook 2012, June 2012, p.252.
- Vaisblat, N., Harris, N.B., Euzen, T., 2015. Petrophysics, geomechanics and rock composition in the Montney Formation. Canadian Society of Petroleum Geologists, Annual convention, Calgary.
- Valenza II, J. J., Drenzek, N., Marques, F. Pagels, M., Mastalerz, M., 2013. Geochemical controls on shale microstructure. *Geology* 41, 611-614.
- Van, W. J. C., Mitchum, R.M., Campion, K.M., Rahmanian, V. D., 1990. Siliciclastic sequence stratigraphy in well logs, cores, and outcrops: concepts for high-resolution correlation of time and facies. *AAPG Methods in Exploration Series*, No.7, 55p.
- Ver Straeten, C. A., Brett, C. E., Sageman, B. B., 2011. Mudrock sequence stratigraphy: a multi-proxy (sedimentological, paleobiological and geochemical) approach, Devonian Appalachian Basin. *Palaeogeography, Palaeoclimatology, Palaeoecology* 304, 54-73.
- Vernik, L., and J. Milovac, 2011, *Rock physics of organic shales: The Leading Edge*, v. 30, no. 3, p. 318-323.
- Wallmann, K., 2003. Feedbacks between oceanic redox states and marine productivity: A model perspective focused on benthic phosphorus cycling. *Global Biogeochemical Cycles* 17, 1084, <http://dx.doi.org/10.1029/2002GB001968>.

- Wang, F. P., Reed, R. M., 2009. Pore networks and fluid flow in gas shales. Society of Petroleum Engineers Annual Technical Conference and Exhibition, New Orleans, Louisiana, October 4-7, 2009, SPE Paper 124253, 8p.
- Wang, F.P., and J.F.W. Gale, 2009, Screening criteria for shale-gas systems: Gulf Coast Association of Geological Societies Transactions, v. 59, p. 779-793.
- Wang, G.C., and T.R. Carr, 2012, Marcellus shale lithofacies prediction by multiclass neural network classification in the Appalachian Basin: Mathematical Geosciences, v. 44, p. 975-1004.
- Wang, G.C., and T.R. Carr, 2013, Organic-rich Marcellus Shale lithofacies modeling and distribution pattern analysis in the Appalachian Basin: AAPG Bulletin, v. 97, no. 12, p. 2173-2205.
- Wedephol, K. H., 1971. Environmental influences on the chemical composition of shales and clays. In: Ahrens, L. H., Press, F., Runcorn, S. K., Urey, H. C. (Eds.), Physics and Chemistry of the Earth. Pergamon, Oxford, pp. 305-333.
- Wei, H.Y., Chen, D.Z., Wang, J.G., Yu, H., Tucker, M.E., 2012. Organic accumulation in the lower Chihhsia Formation (Middle Permian) of South China: Constraints from pyrite morphology and multiple geochemical proxies. Palaeogeography, Palaeoclimatology, Palaeoecology 353, 73-86.
- Weldeab, S., Emeis, K.C., Hemleben, C., Schmiedl, G., Schulz, H., 2003. Spatial productivity variations during formation of sapropels S5 and S6 in the Mediterranean Sea: evidence from Ba contents. Palaeogeography, Palaeoclimatology, Palaeoecology 191, 169-190.
- Wignall, P. B., Twitchett, R. J., 1996. Oceanic anoxia and the end Permian mass extinction. Science 272, 1155-1158.
- Wignall, P.B., 1994. Black Shales: Oxford, U.K., Clarendon, 127p.
- Wood, J.M., Sanei, H., Curtis, M.E., Clarkson, C.R., 2015. Solid bitumen as a determinant of reservoir quality in an unconventional tight gas siltstone play.

- International Journal of Coal Geology 150-151, 287-295.
- Wright, A. M., Spain, D., Ratcliffe, K. T., 2010, Application of inorganic whole rock geochemistry to shale resource plays: SPE Paper 137946, SPE Canadian Unconventional Resources and International Petroleum Conference, Calgary, 18p.
- Xiong, Z.F., Li, T.G., Algeo, T., Nan, Q.Y., Zhai, B., Lu, B., 2012. Paleoproductivity and paleoredox conditions during late Pleistocene accumulation of laminated diatom mats in the tropical West Pacific. *Chemical Geology* 334, 77-91.
- Yan, D.T., Wang, H., Fu, Q.L., Chen, Z.H., He, J., Gao, Z., 2015. Organic matter accumulation of Late Ordovician sediments in North Guizhou Province, China: Sulfur isotope and trace element evidences. *Marine and Petroleum Geology* 59, 348-358.
- Yang, Y.L., Aplin, A.C., 1998. Influence of lithology and effective stress on the pore size distribution and modelled permeability of some mudstones from the Norwegian margin. *Marine and Petroleum Geology* 15, 163-175.
- Yang, Y.L., Aplin, A.C., 2007. Permeability and petrophysical properties of 30 natural mudstones. *Journal of Geophysical research* 112, B03206.
- Yang, Y.L., Aplin, A.C., 2010. A permeability-porosity relationship for mudstones. *Marine and Petroleum Geology* 27, 1692-1697.
- Zahrani, A. A., 2011. Interpretation of 3D multicomponent seismic data for investigating natural fractures in the Horn River Basin, northeast British Columbia. Master thesis, University of Calgary, 118p.
- Zargari, S. Canter, K.L., Prasad, M., 2015. Porosity evolution in oil-prone source rocks. *Fuel* 153, 110-117.
- Zargari, S., M. Prasad, K.C. Mba, and E.D. Mattson, 2013, Organic maturity, elastic properties, and textural characteristics of self resourcing reservoirs: *Geophysics*, v. 78(4), p. D223-D235.
- Zeszotarski, J.C., R.R. Chromik, R.P. Vinci, M.C. Messmer, R. Michels, and J.W. Larsen,

2004, Imaging and mechanical property measurements of kerogen via nanoindentation: *Geochimica et Cosmochimica Acta*, v. 68, p. 4113-4119.

Zhou, L., Algeo, T.J., Shen, J., Hu, Z.F., Gong, H.M., Xie, S.C., Huang, J.H., Gao, S., 2015. Changes in marine productivity and redox conditions during the Late Ordovician Hirnantian glaciation. *Palaeogeography, Palaeoclimatology, Palaeoecology* 420, 223-234.

## APPENDICES

Appendix 1. Major oxides concentrations for Horn River Shale samples from EOG Maxhamish, Nexen Gote, ConocoPhillips McAdam, Imperial

Komie and Arc Snake wells.

Well name	Depth(m)	Formation	SiO <sub>2</sub> (%)	Al <sub>2</sub> O <sub>3</sub> (%)	Fe <sub>2</sub> O <sub>3</sub> (%)	MgO(%)	CaO(%)	Na <sub>2</sub> O(%)	K <sub>2</sub> O(%)	TiO <sub>2</sub> (%)	P <sub>2</sub> O <sub>5</sub> (%)	MnO(%)
Maxhamish	2955.5	Muskwa	84.6	3.11	1.97	0.81	1.29	0.4	0.47	0.14	0.08	0.02
Maxhamish	2956	Muskwa	70.73	6.44	4.36	1.16	1.51	0.56	1.11	0.3	0.09	0.02
Maxhamish	2965.2	Muskwa	85.74	4.42	1.37	0.25	0.22	0.28	0.74	0.14	0.06	0.005
Maxhamish	2967.5	Muskwa	73.92	8.32	3.53	0.42	0.19	0.48	1.53	0.32	0.06	0.02
Maxhamish	2968.3	Muskwa	85.04	3.95	1.7	0.5	0.73	0.31	0.63	0.13	0.06	0.02
Maxhamish	2969.98	Muskwa	77.3	5.76	3.77	0.72	0.89	0.45	1.05	0.2	0.07	0.03
Maxhamish	2970.94	Muskwa	76.27	5.94	2.55	0.74	1.13	0.34	1.13	0.24	0.06	0.02
Maxhamish	2971.91	Muskwa	70.69	8.64	3.78	0.54	0.36	0.57	1.7	0.34	0.07	0.02
Maxhamish	2972.9	Otter Park	72.76	7.04	3.72	0.66	0.61	0.7	1.41	0.36	0.1	0.01
Maxhamish	2973.9	Otter Park	61.47	7.8	4.04	3.52	4.88	1.11	1.51	0.38	0.07	0.04
Maxhamish	2978.16	Otter Park	83.32	5.57	1.85	0.38	0.25	0.33	1.12	0.21	0.05	0.01
Maxhamish	2980.1	Otter Park	84.34	5.33	1.8	0.41	0.28	0.32	1.08	0.19	0.02	0.01
Maxhamish	2982.2	Otter Park	84.05	4.32	1.85	0.91	1.15	0.26	0.84	0.15	0.02	0.02
Maxhamish	2985.61	Otter Park	86.06	4.68	1.29	0.3	0.19	0.34	0.91	0.15	0.02	0.005
Maxhamish	3000	Otter Park	69.63	11.68	3.86	0.76	0.41	0.76	2.5	0.46	0.07	0.01
Maxhamish	3001	Otter Park	72.85	9.94	3.09	1.02	0.98	0.56	2.14	0.4	0.05	0.02
Maxhamish	3002	Otter Park	76.21	9.03	2.17	0.92	0.85	0.52	1.9	0.36	0.04	0.01
Maxhamish	3003	Otter Park	71.84	12.07	2.55	0.82	0.39	0.64	2.54	0.47	0.06	0.01
Maxhamish	3004.1	Otter Park	76.88	9.18	2.07	0.71	0.55	0.6	1.91	0.39	0.04	0.01
Maxhamish	3005	Otter Park	75.93	9.65	2.04	0.69	0.4	0.61	2.02	0.42	0.04	0.005
Maxhamish	3006	Otter Park	50.77	9.07	6.64	5.12	8.41	0.66	1.91	0.36	0.02	0.07
Maxhamish	3007	Otter Park	80.54	6.86	2.38	0.68	0.65	0.46	1.38	0.28	0.02	0.01

Maxhamish	3008	Otter Park	75.59	9.74	2.23	0.65	0.35	0.6	2.06	0.41	0.03	0.01
Maxhamish	3009	Otter Park	75.31	10.34	2.16	0.73	0.41	0.6	2.2	0.41	0.02	0.01
Maxhamish	3010	Otter Park	81.31	6.94	1.6	0.56	0.46	0.49	1.42	0.28	0.01	0.01
Maxhamish	3011	Otter Park	76.51	8.51	2.22	0.87	0.79	0.6	1.78	0.35	0.03	0.02
Maxhamish	3012	Otter Park	69.28	9.25	3.28	2.04	2.69	0.56	1.96	0.39	0.02	0.03
Maxhamish	3013	Otter Park	64.1	11.72	5.61	1.95	2.25	0.68	2.52	0.46	0.04	0.03
Maxhamish	3014.02	Otter Park	65.76	13.35	4.9	1.25	0.93	0.64	2.87	0.52	0.12	0.02
Maxhamish	3015	Otter Park	74.6	10	2.84	0.74	0.4	0.56	2.11	0.4	0.04	0.01
Maxhamish	3016	Otter Park	67.65	14.38	3.74	1.01	0.4	0.61	3.1	0.57	0.07	0.01
Maxhamish	3017.03	Otter Park	22.88	3.91	8.01	11.42	20.92	0.59	0.68	0.15	0.06	0.14
Maxhamish	3018	Otter Park	73.33	10.14	3.53	0.69	0.38	0.58	2.13	0.42	0.05	0.005
Maxhamish	3019.1	Otter Park	68.51	12.61	4.07	0.91	0.48	0.71	2.69	0.52	0.08	0.01
Maxhamish	3020	Otter Park	68.93	11.45	3.78	1.24	1.13	0.67	2.46	0.49	0.06	0.02
Maxhamish	3021.1	Otter Park	60.17	15.82	6.15	1.12	0.5	0.7	3.39	0.64	0.07	0.02
Maxhamish	3022	Otter Park	68.55	12.53	3.74	0.9	0.56	0.73	2.7	0.53	0.08	0.01
Maxhamish	3022.9	Otter Park	51.7	11.13	7.34	3.75	6.84	0.62	2.34	0.43	0.11	0.05
Maxhamish	3024	Otter Park	73.01	10.56	2.8	0.74	0.48	0.73	2.24	0.42	0.06	0.01
Maxhamish	3025	Otter Park	68.97	12.4	3.05	1.01	0.8	0.61	2.68	0.51	0.09	0.01
Maxhamish	3026	Otter Park	77.3	7.7	2.11	0.48	1.08	0.59	1.6	0.31	0.07	0.005
Maxhamish	3027	Otter Park	59.21	9.09	4.19	3.75	6.11	0.69	1.88	0.35	0.06	0.05
Maxhamish	3028	Otter Park	76.8	6.24	1.73	0.45	2.77	0.63	1.21	0.24	0.08	0.005
Maxhamish	3029	Otter Park	72.18	7.44	2.39	0.53	3.92	0.57	1.52	0.31	0.06	0.01
Maxhamish	3030	Otter Park	69.33	8.34	2.29	0.71	4.59	0.58	1.72	0.35	0.08	0.01
Maxhamish	3031	Otter Park	62.19	8.16	8.53	0.71	3.96	0.52	1.75	0.34	0.08	0.01
Maxhamish	3032	Otter Park	73.94	7.05	2.36	0.66	2.55	0.66	1.45	0.31	0.11	0.01
Maxhamish	3033	Otter Park	68.06	8.85	2.56	0.77	4.32	0.58	1.87	0.37	0.09	0.01
Maxhamish	3034	Otter Park	56.67	10.64	4.39	1.59	6.59	1.09	2.36	0.52	0.11	0.02

Maxhamish	3035	Otter Park	31.42	5.26	4.15	7.5	21.17	0.82	1.04	0.25	0.09	0.12
Maxhamish	3036	Otter Park	66.54	11.31	3.39	0.8	2.07	0.71	2.51	0.46	0.15	0.01
Maxhamish	3037	Otter Park	70	12.15	2.96	0.8	1.32	0.52	2.68	0.46	0.05	0.005
Maxhamish	3038.5	Otter Park	58.89	14.92	6.86	1.17	1.52	0.62	3.31	0.58	0.07	0.01
Maxhamish	3039.5	Otter Park	70.42	7.73	2.94	1.18	3.78	0.63	1.75	0.34	0.09	0.01
Maxhamish	3041.2	Evie	74.22	4.2	1.51	0.99	5.87	0.34	0.91	0.19	0.1	0.01
Maxhamish	3044	Evie	24.3	0.73	0.39	0.9	38.7	0.15	0.08	0.03	0.13	0.02
Maxhamish	3047	Evie	70.19	2.59	1.8	0.86	10.67	0.19	0.59	0.12	0.06	0.005
Maxhamish	3048.1	Evie	25.48	1.24	0.87	0.88	37.69	0.18	0.22	0.05	0.09	0.01
Maxhamish	3050	Evie	62.38	9.78	3.22	1.61	6.06	0.62	2.29	0.45	0.05	0.01
Maxhamish	3051.56	Evie	37.72	2.14	1.39	0.85	30.83	0.25	0.5	0.08	0.06	0.02
Maxhamish	3052.4	Evie	66.5	6.36	2.43	1.24	7.08	0.49	1.54	0.31	0.09	0.02
Maxhamish	3053.5	Evie	67.16	7.74	3.21	0.82	5.25	0.39	1.89	0.33	0.06	0.01
Maxhamish	3054.5	Evie	62.81	6.51	2.78	1.47	9.17	0.47	1.58	0.31	0.1	0.02
Maxhamish	3055.37	Evie	67.67	6.22	2.26	0.66	7.27	0.35	1.45	0.28	0.09	0.01
Maxhamish	3056.5	Evie	54.93	7.12	2.73	1.25	13.3	0.44	1.75	0.31	0.1	0.01
Maxhamish	3057.45	Evie	23.62	3.12	1.44	11.88	24.84	0.32	0.73	0.15	0.04	0.08
Maxhamish	3058.4	Evie	12.29	1.52	0.85	2.18	43.8	0.27	0.29	0.07	0.04	0.03
Maxhamish	3059.5	Evie	63.01	10.86	4.44	1.14	4.42	0.63	2.64	0.48	0.08	0.01
Maxhamish	3060.5	Evie	8.8	1.61	0.56	1.06	47.73	0.59	0.18	0.07	0.09	0.03
Maxhamish	3061.49	Evie	56.8	4.32	1.48	0.89	15.54	0.27	1.05	0.22	0.08	0.005
Maxhamish	3062.5	Evie	62.68	5.71	2.11	0.81	9.88	0.34	1.42	0.3	0.11	0.01
Maxhamish	3063.4	Evie	60.2	5.93	2.15	0.75	11.01	0.4	1.47	0.31	0.12	0.01
Maxhamish	3066	Evie	11.09	1.69	0.58	6.75	38.28	0.28	0.36	0.07	0.19	0.04
Maxhamish	3067	Evie	42.8	3.18	1.28	0.88	24.68	0.25	0.84	0.16	0.1	0.01
Maxhamish	3069.31	Evie	38.36	1.12	0.48	1.08	29.52	0.1	0.25	0.05	0.1	0.01
Maxhamish	3071	Evie	54.2	4.36	1.92	1.18	16.74	0.34	1.12	0.19	0.17	0.02

Maxhamish	3072.1	Evie	39.44	3.75	1.65	2.18	25.19	0.08	1.07	0.19	0.08	0.02
Imperial Komie	2224.55	Muskwa	75.98	8.1	2.62	1.06	1.25	0.4	1.63	0.37	0.08	0.02
Imperial Komie	2226.56	Muskwa	15.51	3.41	5.33	13.32	24.43	0.18	0.71	0.18	0.11	0.24
Imperial Komie	2228.54	Muskwa	70.78	11.61	3.65	0.95	0.6	0.64	2.4	0.47	0.08	0.01
Imperial Komie	2230.545	Muskwa	75.74	9.01	2.29	0.97	0.95	0.46	1.77	0.34	0.07	0.01
Imperial Komie	2233.13	Muskwa	74.49	9.75	2.82	0.8	0.63	0.57	1.83	0.41	0.11	0.01
Imperial Komie	2235.03	Muskwa	84.46	4.33	1.43	0.5	0.59	0.23	0.82	0.19	0.07	0.005
Imperial Komie	2237.03	Muskwa	76.79	4.13	7.25	0.63	0.89	0.26	0.74	0.18	0.06	0.005
Imperial Komie	2238.965	Muskwa	78.92	6.38	2.02	0.64	0.63	0.42	1.15	0.27	0.08	0.005
Imperial Komie	2240.96	Muskwa	83.69	5.3	1.65	0.53	0.6	0.53	0.89	0.2	0.06	0.005
Imperial Komie	2242.97	Muskwa	77.97	6.72	2.02	0.63	0.58	0.45	1.25	0.29	0.09	0.01
Imperial Komie	2245.035	Muskwa	80.1	6.22	2.24	0.45	0.34	0.35	1.11	0.25	0.09	0.005
Imperial Komie	2247.05	Muskwa	67.23	13.51	3.21	1.12	0.67	0.71	2.77	0.59	0.15	0.01
Imperial Komie	2249.55	Muskwa	39.69	5.73	3.35	7.69	16.59	0.49	1.11	0.32	0.17	0.1
Imperial Komie	2251.55	Muskwa	75.43	5.01	2.39	0.85	2.14	0.5	0.91	0.26	0.07	0.01
Imperial Komie	2253.53	Muskwa	46.23	7.59	3.14	6.2	12.77	0.65	1.5	0.38	0.13	0.09
Imperial Komie	2257.55	Muskwa	64.18	15.67	3.45	1.33	0.88	0.64	3.29	0.65	0.11	0.02
Imperial Komie	2259.53	Muskwa	35.67	7.5	11.4	5.37	10.81	0.9	1.33	0.41	0.08	0.09
Imperial Komie	2261.55	Muskwa	72.64	10.11	3.3	0.91	0.96	0.63	1.94	0.42	0.09	0.01
Imperial Komie	2263.545	Muskwa	53.5	15.21	4.84	3.24	5.59	0.63	3.23	0.63	0.1	0.06
Imperial Komie	2265.55	Muskwa	53.52	15.26	5.34	3.14	5.65	0.62	3.18	0.68	0.11	0.05
Imperial Komie	2267.53	Muskwa	73.39	7.25	3.56	0.96	3.17	0.46	1.39	0.36	0.09	0.02
Imperial Komie	2269.545	Muskwa	70.1	9.01	3.66	1.11	3.4	0.48	1.75	0.41	0.1	0.02
Imperial Komie	2271.55	Muskwa	64.9	12.05	4.48	1.42	3.23	0.6	2.35	0.55	0.09	0.02
Imperial Komie	2274.05	Muskwa	58.65	17.1	4.68	1.91	2.57	0.85	3.51	0.79	0.1	0.03
Imperial Komie	2276.03	Otter Park	49.8	13.98	3.77	1.85	10.41	0.84	2.86	0.62	0.09	0.04
Imperial Komie	2278.05	Otter Park	39.41	10.7	4.05	2.93	18.39	0.59	2.2	0.48	0.09	0.06

Imperial Komie	2280.05	Otter Park	34.96	8.89	3.53	3.13	22.43	0.53	1.8	0.4	0.09	0.06
Imperial Komie	2282.55	Otter Park	72.62	6.58	2.48	0.83	4.93	0.41	1.25	0.29	0.07	0.02
Imperial Komie	2284.645	Otter Park	39.17	12.09	7.48	4.65	13.09	0.53	2.48	0.53	0.09	0.11
Imperial Komie	2286.55	Otter Park	53.43	17.04	5.68	2.14	5.7	0.65	3.3	0.74	0.1	0.05
Imperial Komie	2288.545	Otter Park	51.77	17.02	6.06	2.34	6.24	0.65	3.34	0.74	0.11	0.06
Imperial Komie	2290.55	Otter Park	51.36	16.38	5.65	2.29	7.16	0.66	3.23	0.73	0.1	0.06
Imperial Komie	2292.55	Otter Park	50.46	16.06	5.66	2.29	7.88	0.63	3.19	0.72	0.1	0.07
Imperial Komie	2294.55	Otter Park	48.95	15.87	5.49	2.33	9.14	0.63	3.06	0.69	0.09	0.06
Imperial Komie	2296.55	Otter Park	50.04	15.93	5.35	2.24	8.73	0.65	3.1	0.68	0.1	0.06
Imperial Komie	2298.54	Otter Park	43.05	13.16	4.24	2.05	15.58	0.6	2.55	0.56	0.1	0.05
Imperial Komie	2300.05	Otter Park	39.53	11.94	3.63	2.01	19.03	0.61	2.33	0.49	0.08	0.05
Imperial Komie	2302.045	Otter Park	27.6	7.97	5.16	4.69	24.27	0.46	1.59	0.33	0.06	0.08
Imperial Komie	2304.54	Otter Park	52.56	11.61	2.71	1.47	12.37	0.76	2.33	0.47	0.09	0.03
Imperial Komie	2306.52	Otter Park	52.53	13.51	2.96	1.58	11.02	0.86	2.77	0.53	0.07	0.03
Imperial Komie	2308.55	Otter Park	31.07	7.62	3.29	2.99	26.07	1	1.39	0.27	0.06	0.05
Imperial Komie	2310.58	Otter Park	58.53	12.72	3	1.39	7.58	0.87	2.55	0.49	0.1	0.02
Imperial Komie	2312.505	Otter Park	61.48	10.64	2.52	1.16	8.31	0.85	2.08	0.42	0.08	0.02
Imperial Komie	2315.055	Otter Park	49.72	10.19	2.26	1.4	15.82	0.77	1.89	0.39	0.09	0.02
Imperial Komie	2317.05	Otter Park	29.69	7.02	6.66	6.47	20.25	0.32	1.39	0.28	0.1	0.1
Imperial Komie	2319.05	Otter Park	66.66	12.69	3.03	1.3	3.04	0.54	2.44	0.54	0.08	0.02
Imperial Komie	2321.05	Otter Park	59.14	17.74	5.04	1.81	2.65	0.64	3.46	0.68	0.09	0.03
Imperial Komie	2322.945	Otter Park	35.01	9.23	3.89	2.37	22.82	0.72	1.74	0.31	0.07	0.06
Imperial Komie	2325.05	Otter Park	54.6	15.86	5.33	2.12	6.31	0.61	3.08	0.64	0.09	0.05
Imperial Komie	2327.075	Otter Park	58.37	15.64	5.82	1.95	3.84	0.63	3.01	0.63	0.1	0.04
Imperial Komie	2329.01	Otter Park	61.48	15.7	4.3	1.61	3.08	0.61	3.13	0.64	0.08	0.03
Imperial Komie	2331.05	Otter Park	54.23	16.02	3.81	1.68	7.69	0.76	3.26	0.59	0.08	0.03
Imperial Komie	2333	Otter Park	47.26	12.86	4.48	3.6	10.41	0.67	2.62	0.52	0.1	0.06

Imperial Komie	2335.05	Otter Park	62.38	14.46	3.13	1.33	3.86	0.72	2.94	0.62	0.1	0.02
Imperial Komie	2337.05	Otter Park	58.03	15.25	3.08	1.55	6.18	0.77	3.13	0.64	0.12	0.03
Imperial Komie	2339.045	Otter Park	67.09	13.77	3.43	1.11	1.79	0.57	2.77	0.54	0.08	0.02
Imperial Komie	2341.555	Otter Park	65.08	8.31	3.34	1.48	4.49	0.61	1.59	0.38	0.08	0.02
Imperial Komie	2344.055	Otter Park	59	8.25	3.54	2.6	7.49	0.79	1.62	0.42	0.09	0.03
Imperial Komie	2346.08	Otter Park	33.54	5.71	6.58	8.05	16.51	0.52	1.09	0.28	0.12	0.17
Imperial Komie	2348.03	Otter Park	68.62	13.29	2.96	1.11	0.63	0.56	2.73	0.51	0.08	0.01
Imperial Komie	2350.06	Otter Park	66.12	16.34	3.1	1.23	0.42	0.63	3.33	0.6	0.05	0.01
Imperial Komie	2352.05	Otter Park	60.54	19.83	4.67	1.45	0.35	0.76	4.05	0.68	0.05	0.01
Imperial Komie	2354.02	Otter Park	59.27	19.65	4.24	1.69	1.09	0.86	4.19	0.7	0.06	0.02
Imperial Komie	2356.95	Otter Park	52.02	18.8	7.01	2.57	3.49	0.47	3.87	0.66	0.08	0.05
Imperial Komie	2359.61	Otter Park	57.14	20.96	3.12	1.87	1.77	0.44	4.69	0.67	0.08	0.04
Imperial Komie	2361.465	Otter Park	54.41	19.54	5.23	2.29	2.59	0.61	4.23	0.65	0.08	0.05
Imperial Komie	2363.515	Otter Park	59.12	21.12	3.1	1.39	0.61	0.75	4.53	0.71	0.08	0.01
Imperial Komie	2365.055	Otter Park	56.58	19.58	4.14	1.86	1.81	0.79	4.17	0.68	0.08	0.03
Imperial Komie	2365.895	Otter Park	57.39	18.56	4.57	1.75	1.54	1.07	4	0.6	0.08	0.02
Imperial Komie	2368.45	Evie	84.49	2.98	1.04	0.33	1.69	0.26	0.48	0.14	0.07	0.005
Imperial Komie	2370.955	Evie	13.85	0.71	1.29	8.14	37.34	0.28	0.07	0.04	0.08	0.09
Imperial Komie	2373.035	Evie	57.94	18.5	4.66	1.92	2.5	0.79	3.87	0.73	0.06	0.02
Imperial Komie	2375.065	Evie	75.6	5.05	1.7	0.56	2.72	0.45	0.97	0.22	0.07	0.005
Imperial Komie	2377.035	Evie	67.8	7.3	2.37	0.85	5.19	0.76	1.51	0.34	0.17	0.01
Imperial Komie	2379.045	Evie	56.32	10.28	3.19	2.3	7.65	0.98	2.2	0.47	0.09	0.02
Imperial Komie	2380.98	Evie	15.25	2.1	2.06	15.19	25.87	0.48	0.23	0.1	0.1	0.09
Imperial Komie	2383.045	Evie	52.47	7.51	2.81	1.8	14.14	0.63	1.46	0.3	0.12	0.02
Imperial Komie	2385.405	Evie	62.91	5.65	1.77	0.99	8.58	0.42	1.1	0.29	0.09	0.01
Imperial Komie	2387.55	Evie	12.29	1.32	0.46	2.3	42.78	0.43	0.07	0.07	0.06	0.02
Imperial Komie	2390.05	Evie	12.53	0.74	0.33	0.95	46.12	0.24	0.09	0.04	0.1	0.01

Imperial Komie	2392.1	Evie	24.02	1.74	0.63	1.3	38.15	0.17	0.48	0.08	0.11	0.005
Imperial Komie	2394.025	Evie	3.05	0.2	0.1	0.57	53.11	0.03	0.005	0.01	0.03	0.005
Imperial Komie	2396.05	Evie	7.58	0.61	0.32	0.85	48.54	0.02	0.11	0.03	0.05	0.005
Nexen Gote	2392.5	Muskwa	63.84	15.36	5.61	1.89	0.63	0.53	2.84	0.63	0.04	0.03
Nexen Gote	2395.25	Muskwa	57.37	15.23	5.09	2.97	3.48	0.51	2.95	0.66	0.04	0.07
Nexen Gote	2397.05	Muskwa	59.4	15.52	5.68	2.63	2.55	0.54	2.94	0.66	0.08	0.06
Nexen Gote	2399.01	Muskwa	67.37	12.88	5.18	1.74	0.99	0.52	2.37	0.53	0.09	0.03
Nexen Gote	2401.05	Muskwa	59.81	13.85	5.16	2.8	3.44	0.56	2.68	0.61	0.08	0.05
Nexen Gote	2403.045	Muskwa	70.74	10.1	4.17	1.8	2.03	0.44	1.97	0.46	0.08	0.03
Nexen Gote	2405.06	Muskwa	73.3	10.39	3.42	1.35	1.03	0.42	2.05	0.44	0.06	0.02
Nexen Gote	2407.045	Muskwa	74.01	9.51	3.22	1.12	0.81	0.44	1.89	0.41	0.08	0.01
Nexen Gote	2409.015	Muskwa	73.75	9.84	3.61	1.03	0.51	0.43	1.9	0.39	0.09	0.01
Nexen Gote	2411	Muskwa	74.54	8.8	4.2	0.75	0.47	0.56	1.71	0.35	0.1	0.01
Nexen Gote	2413.15	Muskwa	81.36	6.7	1.99	0.46	0.27	0.37	1.43	0.27	0.08	0.005
Nexen Gote	2415.065	Muskwa	83.46	5.84	1.86	0.46	0.45	0.44	1.24	0.26	0.1	0.01
Nexen Gote	2417.05	Muskwa	81.45	6.26	2.64	0.7	0.8	0.6	1.31	0.26	0.06	0.01
Nexen Gote	2419.05	Muskwa	80.57	7.51	2.18	0.55	0.4	0.51	1.46	0.31	0.1	0.005
Nexen Gote	2421.045	Muskwa	83.53	5.28	2.88	0.41	0.41	0.43	1.06	0.23	0.08	0.01
Nexen Gote	2423.05	Muskwa	86.36	4.44	1.96	0.35	0.34	0.38	0.91	0.2	0.06	0.01
Nexen Gote	2425.06	Muskwa	68.52	8.98	6.86	0.59	0.33	0.88	1.73	0.41	0.07	0.02
Nexen Gote	2427.14	Muskwa	74.42	8.2	4.35	0.54	0.34	0.61	1.64	0.39	0.08	0.01
Nexen Gote	2429.07	Muskwa	61.54	9.55	11.46	0.67	0.45	0.82	1.86	0.49	0.09	0.02
Nexen Gote	2431.05	Muskwa	75.01	7.71	3.58	0.95	1.02	0.69	1.55	0.35	0.09	0.02
Nexen Gote	2432.995	Muskwa	80.05	5.29	1.94	0.84	1.01	0.61	1.05	0.24	0.06	0.01
Nexen Gote	2435.065	Muskwa	65.11	10.05	4.93	1.84	2.18	1.29	1.87	0.5	0.08	0.02
Nexen Gote	2436.9	Muskwa	84.6	4.15	1.59	0.36	0.3	0.3	0.89	0.16	0.04	0.005
Nexen Gote	2439.05	Muskwa	70.94	10.26	4.52	0.68	0.32	0.85	1.97	0.41	0.08	0.01

Nexen Gote	2441.05	Muskwa	66.33	11.87	5.17	0.81	0.3	1.02	2.34	0.54	0.1	0.02
Nexen Gote	2442.965	Muskwa	85.16	5.33	1.89	0.41	0.29	0.34	1.14	0.2	0.05	0.005
Nexen Gote	2445.05	Muskwa	75.49	9.39	2.57	0.68	0.32	0.52	1.97	0.4	0.04	0.01
Nexen Gote	2447.07	Muskwa	81.22	6.88	2.02	0.52	0.33	0.46	1.47	0.29	0.05	0.005
Nexen Gote	2449.095	Muskwa	76.31	8.43	2.66	0.67	0.47	0.55	1.75	0.37	0.05	0.01
Nexen Gote	2450.95	Muskwa	79.28	7.17	2.45	0.62	0.57	0.62	1.47	0.3	0.06	0.01
Nexen Gote	2453.05	Muskwa	77.1	7.47	3.16	0.65	0.51	0.56	1.42	0.28	0.05	0.005
Nexen Gote	2455.05	Muskwa	79.63	6.86	2.11	0.58	0.54	0.51	1.29	0.26	0.05	0.005
Nexen Gote	2457.05	Muskwa	41.51	6.15	4.21	7.5	14.61	1.26	1.09	0.33	0.06	0.08
Nexen Gote	2459.05	Muskwa	69.73	11.6	3.8	0.84	0.85	0.83	2.29	0.54	0.07	0.01
Nexen Gote	2461.055	Otter Park	63.62	4.66	4.01	3.32	8.37	0.65	0.79	0.22	0.1	0.04
Nexen Gote	2463.01	Otter Park	68.26	7.09	4.39	1.8	5.24	0.78	1.28	0.35	0.09	0.02
Nexen Gote	2465	Otter Park	67.96	9.01	4.99	0.92	3.36	0.79	1.67	0.42	0.08	0.01
Nexen Gote	2467.08	Otter Park	61.2	7.56	4.06	2.56	7.56	0.9	1.42	0.37	0.09	0.04
Nexen Gote	2469.05	Otter Park	78.18	5.69	2.44	0.79	2.89	0.49	1.05	0.25	0.08	0.01
Nexen Gote	2471.055	Otter Park	66.2	10.32	4.09	1.36	3.4	0.78	2.07	0.45	0.08	0.02
Nexen Gote	2473.07	Otter Park	63.69	11.81	3.72	1.24	3.79	0.9	2.48	0.52	0.1	0.02
Nexen Gote	2475.06	Otter Park	66.73	8.46	2.87	1.18	6.17	0.67	1.63	0.35	0.08	0.02
Nexen Gote	2477.075	Otter Park	64.76	11.48	3.72	1.12	4.13	0.72	2.33	0.5	0.1	0.02
Nexen Gote	2479.06	Otter Park	57.07	9.06	7.68	1.2	7.5	0.8	1.73	0.41	0.12	0.02
Nexen Gote	2480.98	Otter Park	69.98	7.76	2.69	0.79	5.41	0.62	1.49	0.35	0.09	0.02
Nexen Gote	2483.05	Otter Park	72.14	6.38	2.21	0.69	5.61	0.6	1.16	0.28	0.09	0.02
Nexen Gote	2485.05	Otter Park	62.94	10.46	3.45	1.51	5.5	0.65	2.15	0.43	0.14	0.03
Nexen Gote	2486.945	Otter Park	62.85	11.7	3.47	1.48	4.68	0.7	2.4	0.48	0.11	0.03
Nexen Gote	2493.05	Otter Park	50.82	6.92	16.4	0.87	5.48	0.55	1.35	0.3	0.07	0.02
Nexen Gote	2495.07	Otter Park	66.2	7.2	2.56	0.98	6.21	0.66	1.39	0.31	0.11	0.02
Nexen Gote	2497.02	Otter Park	64.96	7.85	3.59	1.33	4.62	0.89	1.53	0.38	0.11	0.02

Nexen Gote	2499.05	Otter Park	62.23	8.71	4.55	1.45	4.38	0.95	1.8	0.43	0.09	0.02
Nexen Gote	2501.03	Otter Park	64.11	8.12	2.69	1.45	4.39	0.86	1.64	0.37	0.12	0.02
Nexen Gote	2503.07	Otter Park	56.82	9.17	3.57	1.36	9.05	0.95	1.81	0.41	0.14	0.02
Nexen Gote	2505.05	Otter Park	56.8	11.99	3.5	0.99	7.86	0.69	2.59	0.47	0.13	0.02
Nexen Gote	2507.045	Otter Park	49.31	14.26	4.86	3.16	8.05	0.57	3.12	0.51	0.13	0.05
Nexen Gote	2509.045	Otter Park	66.27	13.33	4.26	1.13	1.13	0.57	2.83	0.52	0.1	0.01
Nexen Gote	2510.95	Otter Park	60.81	14.63	4.61	1.84	2.87	0.57	3.18	0.56	0.08	0.03
Nexen Gote	2513.005	Otter Park	65.14	17.3	2.99	1.11	0.49	0.61	3.73	0.64	0.08	0.01
Nexen Gote	2515.05	Otter Park	62.23	19.69	3.07	1.2	0.4	0.73	4.35	0.67	0.06	0.01
Nexen Gote	2517.05	Otter Park	26.37	7.35	7.78	8.49	19.01	0.51	1.58	0.27	0.06	0.11
Nexen Gote	2519.05	Otter Park	56.43	18.97	5.58	1.72	1.73	0.7	4.28	0.66	0.06	0.03
Nexen Gote	2521.05	Otter Park	56.22	17.61	5.52	1.92	2.32	0.7	3.95	0.59	0.08	0.02
Nexen Gote	2523.06	Otter Park	38.73	9.35	12.88	5.46	10.97	0.52	2	0.35	0.07	0.06
Nexen Gote	2525.305	Otter Park	71.45	5.8	2.97	1.35	3.5	0.56	1.1	0.29	0.1	0.01
Nexen Gote	2526.925	Otter Park	25.62	0.46	0.78	0.88	39.8	0.13	0.06	0.03	0.02	0.02
Nexen Gote	2530.09	Evie	77.84	0.51	0.95	0.26	10.98	0.06	0.08	0.02	0.03	0.005
Nexen Gote	2532.18	Evie	68.85	4.59	1.7	1.08	8.61	0.33	1.04	0.21	0.09	0.005
Nexen Gote	2533.975	Evie	2.1	0.04	0.09	0.67	54.14	0.03	0.01	0.005	0.02	0.01
Nexen Gote	2535.915	Evie	57.91	5.07	1.86	1.01	13.81	0.4	1.14	0.23	0.07	0.01
Nexen Gote	2538.05	Evie	52.48	12.19	4.23	1.68	7.91	0.95	2.91	0.62	0.11	0.02
Nexen Gote	2539.995	Evie	23.84	2.7	1.95	10.42	26.32	0.4	0.56	0.13	0.07	0.07
Nexen Gote	2542.06	Evie	66.19	7.34	2.32	0.87	7.18	0.58	1.56	0.34	0.12	0.01
Nexen Gote	2544.09	Evie	69.31	6.84	2.39	0.77	5.35	0.79	1.28	0.32	0.08	0.005
Nexen Gote	2545.93	Evie	25.84	4.06	1.45	2.01	33.83	0.6	0.86	0.19	0.09	0.02
Nexen Gote	2548.05	Evie	13.42	2.27	0.85	8.2	35.33	0.42	0.48	0.12	0.04	0.05
Nexen Gote	2550.05	Evie	54.12	3.74	1.15	0.96	17.39	0.29	0.85	0.21	0.1	0.005
Nexen Gote	2552.05	Evie	64.47	3.87	1.35	0.66	10.42	0.31	0.9	0.21	0.08	0.005

Nexen Gote	2554.06	Evie	54.25	5.73	2.02	0.95	14.71	0.26	1.41	0.28	0.11	0.005
Nexen Gote	2556.045	Evie	51.23	3.65	1.56	0.67	16.19	0.24	0.95	0.17	0.09	0.005
Nexen Gote	2558.905	Evie	76.57	1.96	1.02	0.5	8.53	0.14	0.47	0.08	0.08	0.005
Nexen Gote	2561.05	Evie	45	4.14	1.71	2.75	21.44	0.32	1.21	0.21	0.12	0.02
Nexen Gote	2564.665	Evie	73.98	2.36	1.24	0.49	8.59	0.18	0.58	0.13	0.07	0.005
Nexen Gote	2566.57	Evie	36.81	3.95	1.53	0.86	28.9	0.34	1.15	0.21	0.09	0.005
Nexen Gote	2568.94	Evie	54.96	4.58	1.73	1.4	16.78	0.3	1.31	0.23	0.08	0.01
Nexen Gote	2577.215	Evie	64.15	3.02	1.45	0.71	12.19	0.21	0.74	0.15	0.1	0.005
McAdam	2719.59	Muskwa	61.97	13.21	5.65	2.11	1.77	0.55	2.56	0.57	0.09	0.03
McAdam	2721.66	Muskwa	70.92	11.45	3.84	1.42	0.94	0.42	2.09	0.46	0.08	0.02
McAdam	2723.66	Muskwa	63.19	9.92	4.14	3.1	4.54	0.46	1.98	0.48	0.07	0.05
McAdam	2725.7	Muskwa	72.81	10.38	2.8	1.29	1.12	0.42	2.03	0.45	0.08	0.02
McAdam	2728.19	Muskwa	71.23	10.99	3.08	1.1	0.77	0.46	2.18	0.45	0.08	0.01
McAdam	2730.44	Muskwa	70.96	10.05	3.09	1.41	1.48	0.41	1.98	0.45	0.1	0.02
McAdam	2733.95	Muskwa	77.96	7.81	2.42	0.52	0.28	0.34	1.45	0.32	0.08	0.005
McAdam	2736.2	Muskwa	58.97	4.99	3.62	5.25	8.33	0.26	0.95	0.23	0.08	0.06
McAdam	2739.45	Muskwa	82.33	5.72	1.88	0.72	0.91	0.38	1.06	0.26	0.08	0.01
McAdam	2742.3	Muskwa	89.38	3.37	1.03	0.28	0.26	0.2	0.61	0.14	0.05	0.005
McAdam	2744.58	Muskwa	78.24	7.25	2.47	0.7	0.8	0.52	1.38	0.29	0.07	0.01
McAdam	2746.9	Muskwa	87.26	4.18	1.23	0.46	0.54	0.25	0.75	0.15	0.04	0.005
McAdam	2748.96	Muskwa	81.01	6.37	2.46	0.53	0.53	0.45	1.16	0.21	0.07	0.005
McAdam	2751.35	Muskwa	87.22	3.79	1.3	0.23	0.2	0.24	0.64	0.14	0.05	0.005
McAdam	2753.78	Muskwa	80.6	6.17	1.96	0.38	0.26	0.42	1.09	0.22	0.09	0.005
McAdam	2755.8	Muskwa	59.51	11	6.71	1.95	2.34	1.28	2.01	0.54	0.08	0.02
McAdam	2758.06	Muskwa	81.61	5.93	1.36	0.49	0.43	0.34	1.08	0.25	0.07	0.005
McAdam	2760.34	Muskwa	82.99	5.28	1.45	0.46	0.6	0.5	0.9	0.19	0.08	0.005
McAdam	2762.08	Muskwa	78.17	6.29	3.35	0.33	0.2	0.47	1.06	0.3	0.07	0.01

McAdam	2764.07	Muskwa	77.82	6.8	2	0.68	0.65	0.56	1.25	0.26	0.07	0.01
McAdam	2766.57	Muskwa	72.37	9.05	2.28	0.77	0.61	0.76	1.72	0.39	0.1	0.01
McAdam	2768.53	Muskwa	65.39	12.99	3.89	1.24	1.11	0.87	2.66	0.61	0.19	0.02
McAdam	2770.15	Muskwa	54.36	8.65	3.5	4.88	8.15	0.79	1.69	0.42	0.2	0.08
McAdam	2771.49	Muskwa	79.85	6.73	1.37	0.48	0.32	0.49	1.27	0.28	0.06	0.005
McAdam	2773.61	Muskwa	77.33	8.49	1.67	0.56	0.23	0.52	1.67	0.34	0.07	0.005
McAdam	2775.61	Muskwa	83.35	4.78	1.53	0.64	0.86	0.49	0.84	0.19	0.07	0.01
McAdam	2777.77	Muskwa	68.31	10.45	3.62	1.26	1.38	0.78	2.08	0.41	0.07	0.02
McAdam	2779.79	Muskwa	77.55	8.63	1.93	0.58	0.29	0.69	1.78	0.28	0.07	0.005
McAdam	2781.84	Muskwa	72.42	6.22	6.01	0.46	0.32	0.53	1.22	0.25	0.07	0.005
McAdam	2784.04	Muskwa	73.09	7.78	2.08	0.7	2.14	0.55	1.48	0.29	0.06	0.005
McAdam	2786.13	Muskwa	41.08	6.32	3.87	5.65	15.76	1.02	1.14	0.33	0.07	0.09
McAdam	2788.48	Muskwa	71.43	11.17	2.73	0.9	0.92	0.75	2.25	0.48	0.07	0.01
McAdam	2789.9	Muskwa	73.81	9.17	2.78	0.78	1.18	0.63	1.79	0.39	0.07	0.01
McAdam	2792.15	Otter Park	39.95	8.85	3.64	2.74	19.91	0.57	1.8	0.39	0.09	0.12
McAdam	2794.2	Otter Park	47.04	13.26	6.74	3.73	8.43	0.54	2.81	0.61	0.1	0.06
McAdam	2796.32	Otter Park	52.72	15.22	4.84	2.74	6.08	0.61	3.19	0.71	0.09	0.05
McAdam	2797.81	Otter Park	53.61	15.11	5.94	2.3	5.68	0.63	3.15	0.71	0.1	0.05
McAdam	2807.76	Otter Park	45.54	12.39	4.65	1.96	13.49	0.64	2.55	0.59	0.09	0.05
McAdam	2809.8	Otter Park	43.96	11.37	5.36	2.22	14.44	0.6	2.36	0.57	0.14	0.06
McAdam	2811.8	Otter Park	42.5	10.45	5	2.41	15.25	0.53	2.14	0.5	0.1	0.06
McAdam	2813.75	Otter Park	41.91	8.71	3.14	2.04	19.38	0.72	1.72	0.37	0.08	0.05
McAdam	2815.93	Otter Park	44.78	8.07	3.43	2.13	18.45	0.54	1.65	0.36	0.11	0.04
McAdam	2817.9	Otter Park	34.98	7.31	2.9	2.17	24.43	0.56	1.48	0.31	0.06	0.04
McAdam	2820.05	Otter Park	29.19	6.83	2.28	2.09	28.63	0.67	1.37	0.27	0.06	0.03
McAdam	2822.14	Otter Park	27.63	6.48	1.8	1.82	30.4	0.66	1.3	0.26	0.07	0.03
McAdam	2824.25	Otter Park	24.86	4.64	1.77	1.83	33.09	0.68	0.88	0.19	0.05	0.03

McAdam	2826.02	Otter Park	26.77	5.15	2.25	2.23	30.98	0.73	0.98	0.21	0.05	0.03
McAdam	2827.54	Otter Park	57.64	8.71	2.25	1.36	11.5	0.61	1.78	0.36	0.09	0.02
McAdam	2829.54	Otter Park	43.84	7.39	3.67	3.39	17.55	0.58	1.5	0.3	0.08	0.05
McAdam	2831.51	Otter Park	45.18	7.3	4.17	3.27	16.38	0.45	1.47	0.31	0.09	0.06
McAdam	2833.56	Otter Park	58.22	14.14	3.67	1.67	5.75	0.54	2.94	0.59	0.07	0.03
McAdam	2835.7	Otter Park	55.69	14.15	3.12	1.7	7.72	0.6	2.92	0.57	0.09	0.04
McAdam	2837.49	Otter Park	33.59	9.09	3	2.04	24.19	0.57	1.88	0.34	0.07	0.05
McAdam	2839.4	Otter Park	31.61	8.7	2.92	2.04	25.84	0.57	1.8	0.34	0.07	0.05
McAdam	2841.42	Otter Park	54.31	12.43	4.75	1.64	8.65	0.53	2.54	0.52	0.11	0.05
McAdam	2843.7	Otter Park	56.74	10.02	6.04	1.7	8.12	0.47	2.01	0.43	0.13	0.05
McAdam	2845.86	Otter Park	60.34	13.85	3.24	1.18	5.53	0.6	2.82	0.59	0.12	0.02
McAdam	2847.85	Otter Park	60.43	11.86	2.88	1.08	7.22	0.62	2.36	0.53	0.11	0.02
McAdam	2849.8	Otter Park	55.53	9.73	2.97	1.41	11.71	0.7	1.89	0.45	0.09	0.03
McAdam	2852	Otter Park	43.95	9.09	3.31	2.69	17.26	0.64	1.81	0.41	0.11	0.06
McAdam	2853.91	Otter Park	55.73	10.24	3.23	1.56	10.81	0.65	2.03	0.48	0.12	0.05
McAdam	2855.85	Otter Park	64.83	8.75	2.92	1.18	7.08	0.59	1.72	0.42	0.09	0.03
McAdam	2857.82	Otter Park	68.29	13.19	2.99	0.86	1.56	0.61	2.73	0.52	0.07	0.005
McAdam	2859.78	Otter Park	61.48	11.81	5.78	0.9	1.29	0.83	2.35	0.53	0.08	0.005
McAdam	2862.35	Otter Park	55.89	13.97	4.72	1.6	2.86	1.24	2.94	0.59	0.11	0.02
McAdam	2864.28	Otter Park	66.1	15.58	3.19	1.15	0.47	0.65	3.31	0.58	0.05	0.005
McAdam	2866.25	Otter Park	59.99	19.12	3.92	1.31	0.38	0.78	4.11	0.7	0.05	0.005
McAdam	2868.25	Otter Park	52.86	17.45	4.99	2.78	3.69	0.79	3.8	0.57	0.08	0.03
McAdam	2870.25	Evie	81.07	3.96	1.29	1.15	2.17	0.36	0.85	0.19	0.07	0.01
McAdam	2872.5	Evie	78.9	4.02	1.71	0.84	1.93	0.41	0.79	0.18	0.11	0.005
McAdam	2874.5	Evie	81.53	3.55	1.24	0.65	3.18	0.38	0.73	0.16	0.07	0.005
McAdam	2876.55	Evie	75.58	6.2	1.77	1	2.96	0.58	1.33	0.26	0.08	0.01
McAdam	2878.75	Evie	76.6	6.04	1.56	0.57	2.75	0.46	1.22	0.23	0.1	0.005

McAdam	2880.4	Evie	73.93	6.94	1.81	0.65	2.62	0.5	1.46	0.27	0.06	0.005
McAdam	2882.45	Evie	73.22	5.35	1.72	0.99	5.02	0.57	1.12	0.23	0.1	0.01
McAdam	2884.35	Evie	64.9	9.5	2.75	1.18	3.92	0.76	2.14	0.42	0.08	0.01
McAdam	2889.4	Evie	63.98	10.35	3.84	1.39	4.18	0.67	2.29	0.44	0.1	0.02
McAdam	2891.5	Evie	65.66	9	3.47	1.3	4.68	0.87	1.97	0.39	0.08	0.02
McAdam	2893.45	Evie	64.65	6.79	2.14	0.69	7.4	0.54	1.51	0.32	0.09	0.005
McAdam	2895.55	Evie	67.7	6.16	1.98	0.51	7.79	0.87	1.29	0.26	0.06	0.005
McAdam	2897.59	Evie	67.12	4.11	1.41	0.57	7.86	0.36	0.93	0.21	0.13	0.005
McAdam	2899.6	Evie	64.14	4.8	1.92	0.64	7.11	0.54	1.21	0.25	0.12	0.005
McAdam	2901.6	Evie	70.47	3.37	1.44	0.64	6.73	0.27	0.85	0.16	0.08	0.005
McAdam	2904.1	Evie	64.87	4.61	1.76	0.61	8.83	0.36	1.16	0.2	0.12	0.005
McAdam	2906.03	Evie	39.67	2.73	1	1.16	27.85	0.41	0.62	0.13	0.18	0.01
McAdam	2908.65	Evie	67.27	4.58	1.82	1.2	8.47	0.41	1.16	0.21	0.09	0.01
McAdam	2910.5	Evie	65.96	4.52	1.8	0.84	9.91	0.39	1.13	0.22	0.13	0.005
McAdam	2912.5	Evie	5.27	0.45	0.39	4.45	47.07	0.03	0.12	0.03	0.06	0.02

---

Appendix 2. Petrophysical data for Horn River Shale samples from EOG Maxhamish, Nexen Gote, ConocoPhillips McAdam and Imperial Komie wells.

Well	Depth (m)	Formation	Lithofacies	Porosity (%)	Perm (nd)	TOC (%)	SiO2 (%)	Al2O3 (%)	MgO (%)	CaO (%)	HI (mg/g)	OI (mg/g)
Maxhamish	2958.50	Muskwa	Massive mudstones	6.15	11.48	5.24	70.73	6.44	1.16	1.51	11	8
Maxhamish	2970.84	Muskwa	Pyrite-rich mudstones	6.03	14.61	3.60	85.04	3.95	0.50	0.73	7	7
Maxhamish	2974.45	Muskwa	Pyrite-rich mudstones	5.02	17.22	6.44	70.69	8.64	0.54	0.36	3	5
Maxhamish	2988.16	Otter Park	Pyrite-rich mudstones	4.87	10.11	2.46	86.06	4.68	0.30	0.19	20	8
Maxhamish	3004.56	Otter Park	Pyrite-rich mudstones	5.46	21.18	2.03	76.21	9.03	0.92	0.85	12	11
Maxhamish	3008.55	Otter Park	Pyrite-rich mudstones	3.08	7.12	1.39	50.77	9.07	5.12	8.41	15	19
Maxhamish	3011.55	Otter Park	Pyrite-rich mudstones	6.48	17.72	2.15	75.31	10.34	0.73	0.41	12	8
Maxhamish	3015.56	Otter Park	Pyrite-rich mudstones	6.73	20.01	1.53	64.10	11.72	1.95	2.25	14	10
Maxhamish	3023.65	Otter Park	Pyrite-rich mudstones	5.78	18.83	2.12	60.17	15.82	1.12	0.50	4	8
Maxhamish	3031.55	Otter Park	Massive mudstones	7.39	26.60	3.67	72.18	7.44	0.53	3.92	5	8
Maxhamish	3033.55	Otter Park	Massive mudstones	8.54	28.03	3.66	62.19	8.16	0.71	3.96	7	6
Maxhamish	3035.55	Otter Park	Massive mudstones	8.74	26.80	5.09	68.06	8.85	0.77	4.32	5	5
Maxhamish	3038.55	Otter Park	Pyrite-rich mudstones	8.26	23.59	4.02	66.54	11.31	0.80	2.07	4	5
Maxhamish	3039.55	Otter Park	Pyrite-rich mudstones	6.09	24.91	2.08	70.00	12.15	0.80	1.32	10	10
Maxhamish	3050.65	Evie	Pyrite-rich mudstones	5.40	8.66	2.24	25.48	1.24	0.88	37.69	7	15
Maxhamish	3057.05	Evie	Massive mudstones	8.89	30.15	5.57	62.81	6.51	1.47	9.17	9	6
Maxhamish	3060.01	Evie	Pyrite-rich mudstones	6.61	16.15	0.30	23.62	3.12	11.88	24.84	28	115
Maxhamish	3060.95	Evie	Massive mudstones	3.67	16.00	1.70	12.29	1.52	2.18	43.80	19	25
Maxhamish	3064.04	Evie	Massive mudstones	6.43	16.94	4.51	56.80	4.32	0.89	15.54	11	6
Maxhamish	3065.04	Evie	Massive mudstones	6.39	33.00	5.37	62.68	5.71	0.81	9.88	13	7
Maxhamish	3065.95	Evie	Massive mudstones	8.24	24.19	4.71	60.20	5.93	0.75	11.01	8	8
Maxhamish	3073.55	Evie	Massive mudstones	4.20	29.37	5.09	54.20	4.36	1.18	16.74	7	7

Maxhamish	3077.55	Evie	Carbonates	4.26	12.65	0.32	3.54	0.52	0.49	52.57	38	91
Maxhamish	3078.55	Evie	Massive mudstones	3.80	12.30	1.90	9.88	2.63	1.00	45.48	17	17
Maxhamish	3088.50	Evie	Carbonates	3.71	6.37	0.04	9.18	2.78	1.00	46.26	n.m.	n.m.
Imperial Komie	2226.56	Muskwa	Massive mudstones	2.45	9.34	0.82	15.51	3.41	13.32	24.43	n.m.	n.m.
Imperial Komie	2228.54	Muskwa	Pyrite-rich mudstones	2.99	10.55	2.88	70.78	11.61	0.95	0.60	n.m.	n.m.
Imperial Komie	2238.97	Muskwa	Pyrite-rich mudstones	5.09	13.61	5.07	78.92	6.38	0.64	0.63	n.m.	n.m.
Imperial Komie	2240.96	Muskwa	Pyrite-rich mudstones	4.54	9.25	2.79	83.69	5.30	0.53	0.60	n.m.	n.m.
Imperial Komie	2245.04	Muskwa	Pyrite-rich mudstones	7.57	24.27	4.12	80.10	6.22	0.45	0.34	n.m.	n.m.
Imperial Komie	2251.55	Muskwa	Massive mudstones	9.81	10.59	6.85	75.43	5.01	0.85	2.14	n.m.	n.m.
Imperial Komie	2259.53	Muskwa	Massive mudstones	4.20	10.59	2.45	35.67	7.50	5.37	10.81	n.m.	n.m.
Imperial Komie	2261.55	Muskwa	Pyrite-rich mudstones	5.59	13.36	3.38	72.64	10.11	0.91	0.96	n.m.	n.m.
Imperial Komie	2278.05	Otter Park	Laminated mudstones	2.58	4.73	0.68	39.41	10.70	2.93	18.39	n.m.	n.m.
Imperial Komie	2288.55	Otter Park	Laminated mudstones	7.36	19.78	0.61	51.77	17.02	2.34	6.24	n.m.	n.m.
Imperial Komie	2294.55	Otter Park	Laminated mudstones	3.98	14.13	0.46	48.95	15.87	2.33	9.14	11	39
Imperial Komie	2312.51	Otter Park	Laminated mudstones	8.59	17.49	2.57	61.48	10.64	1.16	8.31	n.m.	n.m.
Imperial Komie	2315.06	Otter Park	Laminated mudstones	4.31	10.29	1.49	49.72	10.19	1.40	15.82	31	12
Imperial Komie	2317.05	Otter Park	Laminated mudstones	5.30	10.76	0.96	29.69	7.02	6.47	20.25	n.m.	n.m.
Imperial Komie	2333.00	Otter Park	Laminated mudstones	5.55	11.19	1.28	47.26	12.86	3.60	10.41	n.m.	n.m.
Imperial Komie	2341.56	Otter Park	Pyrite-rich mudstones	2.43	6.13	5.52	65.08	8.31	1.48	4.49	n.m.	n.m.
Imperial Komie	2346.08	Otter Park	Massive mudstones	7.81	20.76	2.93	33.54	5.71	8.05	16.51	n.m.	n.m.
Imperial Komie	2354.02	Otter Park	Bioturbated mudstones	4.91	15.41	0.99	59.27	19.65	1.69	1.09	n.m.	n.m.
Imperial Komie	2365.06	Evie	Bioturbated mudstones	10.76	28.06	0.47	56.58	19.58	1.86	1.81	88	45
Imperial Komie	2375.07	Evie	Pyrite-rich mudstones	6.79	21.91	5.97	75.60	5.05	0.56	2.72	30	2
Imperial Komie	2383.05	Evie	Pyrite-rich mudstones	3.90	7.36	4.28	52.47	7.51	1.80	14.14	n.m.	n.m.
Imperial Komie	2385.41	Evie	Pyrite-rich mudstones	5.70	8.59	6.81	62.91	5.65	0.99	8.58	6	2
Imperial Komie	2387.55	Evie	Pyrite-rich mudstones	7.55	14.87	3.75	12.29	1.32	2.30	42.78	n.m.	n.m.
Imperial Komie	2390.05	Evie	Massive mudstones	5.86	18.63	2.02	12.53	0.74	0.95	46.12	n.m.	n.m.

Imperial Komie	2396.05	Evie	Massive mudstones	4.03	3.41	3.05	7.58	0.61	0.85	48.54	n.m.	n.m.
Nexen Gote	2395.20	Muskwa	Laminated mudstones	3.13	12.29	1.28	57.37	15.23	2.97	3.48	42	14
Nexen Gote	2397.00	Muskwa	Laminated mudstones	5.75	25.52	0.97	59.40	15.52	2.63	2.55	n.m.	n.m.
Nexen Gote	2408.96	Muskwa	Laminated mudstones	4.66	14.65	2.93	73.75	9.84	1.03	0.51	n.m.	n.m.
Nexen Gote	2423.00	Muskwa	Laminated mudstones	5.49	11.51	2.00	86.36	4.44	0.35	0.34	n.m.	n.m.
Nexen Gote	2432.96	Muskwa	Massive mudstones	7.77	33.12	5.10	80.05	5.29	0.84	1.01	n.m.	n.m.
Nexen Gote	2441.00	Muskwa	Laminated mudstones	1.63	9.09	4.46	66.33	11.87	0.81	0.30	n.m.	n.m.
Nexen Gote	2457.00	Muskwa	Laminated mudstones	4.54	14.41	2.59	41.51	6.15	7.50	14.61	n.m.	n.m.
Nexen Gote	2473.02	Otter Park	Laminated mudstones	4.16	20.69	3.43	63.69	11.81	1.24	3.79	n.m.	n.m.
Nexen Gote	2485.00	Otter Park	Laminated mudstones	4.66	13.55	3.73	62.94	10.46	1.51	5.50	35	6
Nexen Gote	2496.97	Otter Park	Massive mudstones	3.97	13.38	6.09	64.96	7.85	1.33	4.62	n.m.	n.m.
Nexen Gote	2500.98	Otter Park	Laminated mudstones	6.12	10.71	7.09	64.11	8.12	1.45	4.39	n.m.	n.m.
Nexen Gote	2521.00	Otter Park	Bioturbated mudstones	4.35	13.93	1.52	56.22	17.61	1.92	2.32	n.m.	n.m.
Nexen Gote	2523.02	Otter Park	Pyrite-rich mudstones	5.48	13.40	1.10	38.73	9.35	5.46	10.97	n.m.	n.m.
Nexen Gote	2525.26	Otter Park	Massive mudstones	6.29	21.08	4.50	71.45	5.80	1.35	3.50	n.m.	n.m.
Nexen Gote	2526.88	Otter Park	Massive mudstones	2.32	4.69	1.39	25.62	0.46	0.88	39.80	n.m.	n.m.
Nexen Gote	2535.87	MDC	Massive mudstones	7.17	25.49	4.36	57.91	5.07	1.01	13.81	42	6
Nexen Gote	2542.02	Evie	Massive mudstones	6.29	22.41	2.98	66.19	7.34	0.87	7.18	n.m.	n.m.
Nexen Gote	2544.04	Evie	Massive mudstones	6.11	25.72	3.80	69.31	6.84	0.77	5.35	n.m.	n.m.
Nexen Gote	2545.88	Evie	Laminated mudstones	4.95	11.07	0.46	25.84	4.06	2.01	33.83	n.m.	n.m.
Nexen Gote	2548.00	Evie	Laminated mudstones	7.69	21.65	2.40	13.42	2.27	8.20	35.33	n.m.	n.m.
Nexen Gote	2550.00	Evie	Massive mudstones	4.45	13.39	5.04	54.12	3.74	0.96	17.39	n.m.	n.m.
Nexen Gote	2554.02	Evie	Massive mudstones	6.82	38.71	5.57	54.25	5.73	0.95	14.71	n.m.	n.m.
Nexen Gote	2558.87	Evie	Massive mudstones	1.80	1.69	2.21	76.57	1.96	0.50	8.53	n.m.	n.m.
Nexen Gote	2566.53	Evie	Laminated mudstones	4.69	13.88	1.80	36.81	3.95	0.86	28.90	n.m.	n.m.
Nexen Gote	2577.17	Evie	Massive mudstones	1.76	13.29	5.16	64.15	3.02	0.71	12.19	n.m.	n.m.
Mcadam	2723.66	Muskwa	Massive mudstones	2.84	8.54	1.10	63.19	9.92	3.10	4.54	n.m.	n.m.

Mcadam	2742.3	Muskwa	Pyrite-rich mudstones	3.24	11.52	1.68	89.38	3.37	0.28	0.26	n.m.	n.m.
Mcadam	2751.35	Muskwa	Pyrite-rich mudstones	4.19	13.00	2.97	87.22	3.79	0.23	0.20	n.m.	n.m.
Mcadam	2755.8	Muskwa	Pyrite-rich mudstones	2.87	10.37	3.78	59.51	11.00	1.95	2.34	20	12
Mcadam	2762.08	Muskwa	Pyrite-rich mudstones	12.04	42.81	5.24	78.17	6.29	0.33	0.20	n.m.	n.m.
Mcadam	2768.53	Muskwa	Laminated mudstones	4.87	8.30	3.38	65.39	12.99	1.24	1.11	n.m.	n.m.
Mcadam	2779.79	Muskwa	Massive mudstones	2.80	8.30	3.90	77.55	8.63	0.58	0.29	n.m.	n.m.
Mcadam	2786.13	Muskwa	Laminated mudstones	8.46	26.38	3.69	41.08	6.32	5.65	15.76	14	7
Mcadam	2792.15	Otter Park	Laminated mudstones	4.94	19.97	0.24	39.95	8.85	2.74	19.91	n.m.	n.m.
Mcadam	2807.76	Otter Park	Laminated mudstones	2.59	10.42	0.91	45.54	12.39	1.96	13.49	n.m.	n.m.
Mcadam	2815.93	Otter Park	Laminated mudstones	2.08	4.73	1.30	44.78	8.07	2.13	18.45	n.m.	n.m.
Mcadam	2824.25	Otter Park	Laminated mudstones	1.95	3.19	0.95	24.86	4.64	1.83	33.09	45	36
Mcadam	2826.02	Otter Park	Laminated mudstones	3.22	5.61	0.73	26.77	5.15	2.23	30.98	n.m.	n.m.
Mcadam	2837.49	Otter Park	Bioturbated mudstones	0.62	3.16	0.56	33.59	9.09	2.04	24.19	n.m.	n.m.
Mcadam	2849.8	Otter Park	Laminated mudstones	3.01	10.34	2.05	55.53	9.73	1.41	11.71	n.m.	n.m.
Mcadam	2862.35	Otter Park	Massive mudstones	4.13	12.47	5.49	55.89	13.97	1.60	2.86	n.m.	n.m.
Mcadam	2866.25	Otter Park	Bioturbated mudstones	2.65	16.24	1.70	59.99	19.12	1.31	0.38	n.m.	n.m.
Mcadam	2868.25	Otter Park	Bioturbated mudstones	3.31	10.20	1.32	52.86	17.45	2.78	3.69	n.m.	n.m.
Mcadam	2870.25	Evie	Pyrite-rich mudstones	3.86	5.21	2.58	81.07	3.96	1.15	2.17	n.m.	n.m.
Mcadam	2872.5	Evie	Pyrite-rich mudstones	5.71	40.15	6.72	78.90	4.02	0.84	1.93	n.m.	n.m.
Mcadam	2882.45	Evie	Pyrite-rich mudstones	4.51	13.21	4.13	73.22	5.35	0.99	5.02	n.m.	n.m.
Mcadam	2897.59	Evie	Massive mudstones	4.01	6.85	6.91	67.12	4.11	0.57	7.86	32	8
Mcadam	2899.6	Evie	Massive mudstones	4.49	16.63	8.25	64.14	4.80	0.64	7.11	n.m.	n.m.
Mcadam	2904.1	Evie	Massive mudstones	2.89	11.68	7.38	64.87	4.61	0.61	8.83	n.m.	n.m.
Mcadam	2912.5	Evie	Carbonates	2.61	10.76	0.56	5.27	0.45	4.45	47.07	n.m.	n.m.